Experimental investigation and thermodynamic modeling of the Al-Cr-Mo-Ni system and its sub-systems

zur Erlangung des akademischen Grades

Doktor der Ingenieurwissenschaften

der Fakultät für Maschinenbau
Karlsruher Instituts für Technologie (KIT)

genehmigte

Dissertation

von

Jian Peng

aus Hubei, China

Tag der mündlichen Prüfung: 15. 12. 2016
Hauptreferent: Prof. Dr. Hans Jürgen Seifert
Korreferent: Prof. Dr. Rudy J.M. Konings

Abstract

The intermetallic compound NiAl with B2 structure received much attention because of its outstanding physical and chemical properties, compared to Ni-based superalloys. However, its poor ductility and fracture toughness at room temperature as well as insufficient strength and creep resistance at elevated temperatures prevents its application as a high temperature structural material. These disadvantages can be compensated by manufacturing an *in-situ* composite with NiAl matrix strengthening with embedded refractory metals, such as Cr and Mo, respectively. The systems NiAl-Cr, NiAl-Mo and NiAl-Cr-Mo offer the opportunity for an *in-situ* preparation of this composite with an unprecedented level of microstructural alignment and regularity by directional solidification of alloys with eutectic composition. The mechanical properties of these materials are considerably improved, compared to NiAl. Therefore, NiAl-based composites are proposed to be promising alternative materials for high temperature structural applications.

In the present work, experimental investigation and thermodynamic modeling of the Al-Cr-Mo-Ni system were performed. It particularly focused on the binary Al-Ni and Al-Mo, ternary Al-Ni-Cr, Al-Mo-Ni and Cr-Mo-Ni, and quaternary NiAl-Cr-Mo systems. The thermodynamic descriptions of the Al-Ni and Al-Mo systems from the literature were refined. The liquidus and solidus temperatures of the NiAl-Mo system up to 40 at.% Mo were measured by a laser heating-fast pyrometry apparatus. The results agree well with literature data. A new thermodynamic modeling and dataset of the Al-Mo-Ni system was established. The ordered B2 phase and its disordered A2 (bcc) parent phase were described by a single Gibbs energy function as well as the ordered $L1_2$ phase and its disordered A1 (fcc) parent phase. Very good agreement between the calculated phase diagram and the experimental data is obtained. The description of the section NiAl-Mo is considerably improved and we conclude that this section does not represent a quasi-binary phase diagram. The Al-Ni-Cr database from literature was modified by considering the contribution of the compound energy of vacancies and re-optimizing the liquid phase. The description of the NiAl-Cr system was improved. The Cr-Mo-Ni system was adjusted according to the up-to-date binary datasets. The primary solidification surface of the system NiAl-Cr-Mo has been investigated experimentally. Using own experimental results and additional data from the literature, the liquidus surface of the system NiAl-Cr-Mo was modeled using the CALPHAD approach. The optimization for the NiAl-Cr-Mo system focused on the eutectic equilibria between the liquid, NiAl (B2) and the (Cr, Mo) (A2) phases. The calculated eutectic trough of the NiAl-Cr-Mo system agrees well with our experimental results and literature data. Other regions of the Al-Cr-Mo-Ni system other than the NiAl-Cr-Mo system were also calculated. Satisfactory agreement between the calculation and experimental results were obtained. The present thermodynamic description can further support the selection of alloy compositions and simulations of the Al-Cr-Mo-Ni system and play an important role in the development of the NiAl-based and Ni-based superalloys.

Kurzfassung

Die intermetallische Verbindung NiAl mit der B2-Struktur hat wegen ihrer hervorragenden physikalischen und chemischen Eigenschaften im Vergleich zu Ni-basierten Superlegierungen viel Aufmerksamkeit erlangt. Ihre schwache Duktilität und Bruchfestigkeit bei Raumtemperatur wie auch die unzureichende Festigkeit und der Kriechwiderstand bei hohen Temperaturen verhindert ihre Anwendung als Hochtemperaturwerkstoff. Diese Nachteile können dadurch kompensiert werden, indem ein in-situ Komposit bestehend aus einer NiAl-Matrix hergestellt wird, die durch ein Refraktärmetall, z.B. Cr oder Mo, gestärkt wird. Die Systeme NiAl-Cr, NiAl-Mo und NiAl-Cr-Mo bieten sich für eine Präparation solcher in-situ Komposite an mit einem beispiellosem Maß an mikrostruktureller Anordnung und Regularität durch gerichtete Erstarrung dieser Legierungen mit eutektischer Zusammensetzung. Die mechanischen Eigenschaften dieser Materialien sind deutlich verbessert im Vergleich zu NiAl. Daher sind NiAl-basierten Zusammensetzungen vielversprechende Alternativen für Hochtemperaturanwendungen.

In dieser Arbeit wird das Al-Cr-Mo-Ni System experimentell untersucht und thermodynamisch modelliert. Insbesondere liegt der Fokus auf den binären Al-Ni- und Al-Mo-Systemen, den ternären Al-Ni-Cr-, Al-Mo-Ni- und Cr-Mo-Ni-Systemen sowie dem quaternären NiAl-Cr-Mo-System. Die thermodynamischen Beschreibungen der Al-Ni- und Al-Mo-Systeme aus der Literatur wurden verfeinert. Die Liquidus- und Solidustemperaturen des NiAl-Mo-Systems bis zu 40 at.% Mo wurden mithilfe einer (lasergeheizten Schnelltemperaturmessungsanlage) gemessen. Die Resultate stimmen gut mit der Literatur überein. Es wurde eine neue thermodynamische Modellierung und ein neuer Datensatz für das Al-Mo-Ni-System geschaffen. Die geordnete B2 Phase und ihre ungeordnete A2 (bcc) Phase wurden durch eine einzelne Gibbs-Energiefunktion beschrieben wie auch die geordnete L12 Phase und ihre ungeordnete A1 (fcc) Phase. Eine sehr gute Übereinstimmung zwischen dem berechneten Phasendiagramm und den experimentellen Daten wurde erzielt. Die Beschreibung des Bereiches NiAl-Mo ist deutlich verbessert und wir schließen daraus, dass dieser Bereich kein quasi-binäres Phasendiagramm wiederspiegelt. Die Al-Ni-Cr Datenbank aus der Literatur wurde modifiziert unter Berücksichtigung des Anteils der Verbindungsenergie der Leerstellen und der Re-Optimierung der flüssigen Phase. Die Beschreibung des NiAl-Cr-Systems wurde verbessert. Das Cr-Mo-Ni-System wurde bezüglich der aktuellen Binärdatenbanken angeglichen. Die Primärerstarrungsfläche des Systems NiAl-Cr-Mo wurde experimentell untersucht. Eigene experimentelle Resultate und zusätzliche Daten aus der Literatur wurden zur Modellierung der Liquidusfläche des Systems NiAl-Cr-Mo herangezogen unter Zuhilfenahme des CALPHAD-Ansatzes. Die Optimierung des NiAl-Cr-Mo-Systems stützt sich auf die eutektischen Gleichgewichte zwischen den flüssigen Phasen NiAl (B2) und (Cr,Mo) (A2). Die berechnete eutektische Rinne des NiAl-Cr-Mo-Systems stimmt gut mit unseren experimentellen Ergebnissen und den Literaturdaten überein. Andere Regionen des Al-Cr-Mo-Ni-Systems, die sich vom NiAl-Cr-Mo-System unterscheiden, wurden auch berechnet. Eine zufriedenstellende Übereinstimmung zwischen der Berechnung und den experimentellen

Resultaten wurde erreicht. Die aktuelle thermodynamische Beschreibung kann ferner die Wahl der Legierungszusammensetzung und die Simulationen des Al-Cr-Mo-Ni-Systems unterstützen und spielt eine bedeutende Rolle in der Entwicklung der NiAl-basierten und Ni-basierten Superlegierungen.

Acknowledgements

This work was performed during my PhD study at the Institute for Applied Materials-Applied Material Physics (IAM-AWP), Karlsruhe Institute of Technology (KIT), Karlsruhe, Germany and is financially supported by the Initiative and Networking Fund of the Helmholtz Association (VH-KO-610). I would like to acknowledge all people who have directly and indirectly contributed to this work.

Firstly, I would like to deeply acknowledge my supervisors, Prof. Dr. Hans Jürgen Seifert and Dr. Peter Franke, who taught me everything I know about CALPHAD modeling, thermodynamics and phase equilibria. Prof. Seifert gave me the chance to study in Germany. Without the constant help, most valuable advices, patient guidance and encouragement of Prof. Dr. Hans Jürgen Seifert and Dr. Peter Franke, it will be not possible for me to finish this work.

I am sincerely and deeply thankful to my wife, parents, parents-in-law and other relatives. They have always motivated and encouraged me heartily and enthusiastically and gave me tremendous support and consideration in my life.

I appreciate the help on laser heating experiments from Dr. Dario Manara, Prof. Rudy J.M. Konings, Tyson Watkins, Dr. Konstantinos Boboridis of the European Commission, Joint Research Centre, Institute for Transuranium Elements (JRC-ITU), Karlsruhe, Germany. Dr. Dario Manara spent lots of time on patiently teaching me the background about this wonderful experimental method and how to interpret the experimental results. The laser heating experiments are a very important part of this work.

I acknowledge all members of the Helmholtz Research School on "Integrated Materials Development for Novel High-Temperature Alloys": Prof. Dr. Hans Jürgen Seifert, Prof. Oliver Kraft, Prof. Martin Heilmaier, Prof. Anton Möslang, Prof. Thomas Böhlke, Prof. Britta Nestler, Dr. Heinz Riesch-Oppermann, Dr. Daniel Weygand, Ioannis Sprenger, Michael Kellner, Amritesh Kumar, Antje Krüger, Jürgen Albiez and other members. We have had valuable discussions and good cooperation with each other.

Special gratitude goes to Dr. Dajian Li of the Institute for Applied Materials-Applied Materials Physics (IAM-AWP), Karlsruhe Institute of Technology (KIT), Karlsruhe, Germany, and to Dr. Yuan Yuan of the department of Metallurgy and Materials Engineering, University of Leuven, Leuven, Belgium. They always patiently answered my questions on thermodynamic modeling and experiments. I have learned a lot from them.

Special acknowledgements go to Dr. Damian M. Cupid, Dr. Thomas Bergfeldt, Dr. Harald Leiste, Judith Jung, Alexandra Reif, Petra Severloh, of IAM-AWP, KIT, for the help on experiments.

Furthermore, I would like to give my special thanks to Prof. Chuanbin Wang, Prof. Qiang Shen and Prof. Lianmeng Zhang of the State Key Lab of Advanced Technology for Materials Synthesis and Processing, Wuhan University of Technology, Wuhan, China. They always encourage and support me to pursue my dream.

I also would like to acknowledge my landlord and his family for the continuous help, support and encouragement. They made my stay in Karlsruhe so pleasant.

I am very grateful to all my friends in China and in Germany.

Jian Peng

Karlsruhe, October, 2016

List of publications

Peer-reviewed articles

1. J. Peng, P. Franke, D. Manara, T. Watkins, R.J.M. Konings and H.J. Seifert, Experimental Investigation and Thermodynamic Re-assessment of the Al-Mo-Ni System, Journal of Alloys and Compounds 674 (2016) 305-314.

2. J. Peng, P. Franke and H.J. Seifert, Experimental Investigation and CALPHAD Assessment of the Eutectic Trough in the System NiAl-Cr-Mo, Journal of Phase Equilibria and Diffusion 37 (2016) 592-600.

3. J. Peng, P. Franke, D. Manara, T. Watkins, R.J.M. Konings and H.J. Seifert, Experimental Investigation and CALPHAD Modelling of the NiAl-Mo System, in: Y. Murata, T. Ohmori, M. Igarashi, K. Kimura, M. Takeyama, (Eds.), Proceedings of the 123HiMAT-2015, The 123rd Committee of Japan Society for the Promotion of Science, Tokyo, 2015, pp. 354-357.

4. J. Peng, P. Franke and H.J. Seifert, Thermodynamic modeling of the Al-Cr-Mo-Ni system with the refined description of the Cr-Mo-Ni system, to be submitted.

MSIT (Materials Science International Team) database

1. L. Cornish, A. Fabuyide and J. Peng, Nb-Ni Binary Phase Diagram Evaluation, in MSI Eureka, G. Effenberg (Ed.), MSI, Materials Science International, Stuttgart (2015), Document ID: 20.23791.1.4.

2. A.V. Khvan, A.T. Dinsdale, B. Odera, N. Solak, A. Akhmetova and J. Peng, Cu-Ge-O Ternary Phase Diagram Evaluation, in MSI Eureka, G. Effenberg (Ed.), MSI, Materials Science International, Stuttgart (2016), Document ID: 10.22330.1.9.

3. J. Peng, Cr-Mo Binary Phase Diagram Evaluation, in MSI Eureka, G. Effenberg (Ed.), MSI, Materials Science International, Stuttgart, submitted.

4. J.C. Schuster updated by J. Peng, Al-Mo Binary Phase Diagram Evaluation, in MSI Eureka, G. Effenberg (Ed.), MSI, Materials Science International, Stuttgart, submitted.

Conference presentations

1. J. Peng, P. Franke, H.J. Seifert, Experiment and Thermodynamic Assessment of the AI-Ni-Mo System, Modelling and Simulation of Superalloys International Workshop, 15-17 September, 2014, Bochum, Germany.

2. J. Peng, P. Franke, H.J. Seifert, Thermodynamics and Microstructure Development in Alloys of Ni-Al-Cr-Mo System, 28th Annual MSIT Meeting, International Seminar on Heterogeneous Multicomponent Equilibria, 09-14 March, 2014, Schloss Ringberg, Tegernsee, Germany.

3. J. Peng, P. Franke, H.J. Seifert, Thermodynamic Assessment of the Al-Mo System and of the Al-Ni-Mo System, Advanced High-Temperature Materials Technology for Sustainable and Reliable Power Engineering (123HiMAT-2015), 29 June-3 July, 2015, Sapporo, Japan.

4. J. Peng, P. Franke, D. Manara, T. Watkins, R.J.M. Konings, H.J. Seifert, Thermodynamic Assessment of the Al-Mo-Ni System and Its Quaternary Extension with Cr, European Congress and Exhibition on Advanced Materials and Processes, 20-24 September, 2015, Warsaw, Poland.

5. J. Peng, P. Franke, D. Manara, T. Watkins, R.J.M. Konings, H.J. Seifert, Thermodynamic Assessment of the Al-Mo-Ni System and Its Extension into the NiAl-Cr-Mo System, 4th Japanese-German Seminar on Energy Materials Science, 26-28 January, 2016, Karlsruhe, Germany.

6. J. Peng, P. Franke, D. Manara, R.J.M. Konings, H.J. Seifert, Experimental investigation and thermodynamic modeling of the Al-Cr-Mo-Ni system, Materials Science and Engineering Congress (MSE), 27-29 September, 2016, Darmstadt, Germany.

Contents

List of Tables

List of Figures

1. Motivation

With the development of Ni-based superalloys in the last few decades, the engine manufacturers have considerably increased the combustion temperature and, as a consequence, the thermodynamic efficiency. However, nowadays the operating temperatures of the engines are around 80 % of melting points of the materials [1] and almost reach the upper limit. Therefore, alternative materials with higher operating temperature are in great demand for higher engine efficiency, better performance and lower greenhouse gas emissions. NiAl-based alloys have been investigated and are proposed as promising alternative materials for high temperature structural applications, such as turbine blade. The intermetallic compound NiAl with B2 structure received much attention because of its outstanding physical and chemical properties, compared to Ni-based superalloys. It exhibits high melting point (1911 K), lower density (5.7 g/cm^3), superior oxidation resistance at temperature above 1273 K and good thermal conductivity (70-80 W/m·K at the range of 300-1400 K) [2–5]. Although NiAl has poor ductility and fracture toughness at room temperature as well as insufficient strength and creep resistance at elevated temperatures [6], these disadvantages can be overcome by manufacturing a metal-matrix composite of NiAl strengthened by embedded refractory metals such as Cr and Mo [7–13]. The systems NiAl-Cr, NiAl-Mo and NiAl-Cr-Mo offer the opportunity for an *in-situ* preparation of this composite with an unprecedented level of microstructural alignment and regularity by directional solidification of alloys with eutectic composition and the mechanical properties are substantially improved [7–10, 14], compared to NiAl. Moreover, this kind of composite exhibits good thermodynamic stability and chemical compatibility between the NiAl matrix and the strengthening phase.

In the NiAl-Cr-Mo system, the eutectic trough connects the NiAl-Cr eutectic and NiAl-Mo eutectic. If the eutectic trough of the NiAl-Cr-Mo system is continuous, the mole fraction of the strengthening phase (bcc phase) along the eutectic trough will vary from ~10 at.% (NiAl-Mo eutectic) to ~34 at.% (NiAl-Cr eutectic). Then, the mechanical properties of the *in-situ* composite can be adjusted by adjusting the mole fraction of the strengthening phase. Therefore, determining the eutectic compositions in the NiAl-Cr-Mo system is extremly important for the development of this *in-situ* composite by directional solidification.

Nowadays, the CALPHAD method has reached maturity. Compared to the traditional experimental method, it possesses the following advantages: (1) The thermodynamic database can be created only using experimental data from key experiments. Therefore, it is money-saving and time-saving. (2) The database can not only reproduce the experimental data but also predict the phase behaviors and thermodynamic properties in experimentally uninvestigated regions by extrapolation method. More importantly, the phase behavior and thermodynamic properties of the multicomponent systems can be obtained by extrapolation of the lower-order systems. (3) With the database, the phase diagrams as well as the thermodynamic properties can be obtained. (4) The Gibbs energy

functions determined by CALPHAD type modeling can be used to support other simulations, such as Phase Field Method.

The objective of this thesis is to investigate the Al-Cr-Mo-Ni system and its sub-systems with own key experiments, thermodynamically model them with CALPHAD method and establish a reliable thermodynamic database to support the research and development of alloys in this system. Specifically, the experiments focus on the determination and characterization of pseudobinary systems and eutectic sections in the ternary and quaternary systems, respectively. Phase transformation temperatures, solubilities and primary solidification surface will be determined by experiments. To model the Al-Cr-Mo-Ni system satisfactory, modeling particularly focuses on the binary systems Al-Ni and Al-Mo, ternary systems Al-Cr-Ni, Al-Mo-Ni and Cr-Mo-Ni, and the quaternary system NiAl-Cr-Mo. The results will provide comprehensive understanding of the phase behavior and thermodynamic properties of the Al-Cr-Mo-Ni system and its sub-systems. Additionally, the present work is an indispensable part of the Helmholtz Research School "Integrated Materials Development for Novel High Temperature Alloys" (home page: http://www.imd.kit.edu/66.php) performed at the Karlsruhe Institute of Technology (KIT), Karlsruhe, Germany. This project includes the following research areas: (1) (Present work) experimental investigation and thermodynamic modeling of the eutectic alloys. (2) Preparation and mechanical properties of directionally solidified eutectic alloys; (3) 3D phase-field modeling of eutectic microstructure in the presence of a compression load; (4) Multiscale mechanical testing of directionally solidified eutectic alloys; (5) Discrete dislocation dynamics (DDD) simulation of the eutectic alloys; (6) TEM analyses of matrix fiber interfaces, creep deformation and fracture mechanisms; (7) Microstructural analysis of creep deformation mechanisms of DS eutectic alloys by Transmission Electron Microscopy (TEM). The outcomes of the present work will support for other research areas of this project. The calculated diagrams were provided to support for the selection of alloys composition for directional solidification. The Gibbs free energy functions for all phases in this system were provided as input data for microstructure modeling by phase field simulations.

2. Introduction of the CALPHAD method

CALPHAD, the acronym for the CALculation of PHAse Diagrams, is a technique that all available experimental and theoretical data are used to assess the parameters of the Gibbs energy models selected for each phase [15] and consequently, the obtained Gibbs energy functions of phases are used to represent and predict the phase equilibria and thermodynamic properties of a system and to support further application. Traditional experimental determination of phase diagram with trial-and-error method is time-consuming and costly, but limited data can be obtained. Particularly in the high-order systems, experimental determination of phase diagrams will be less efficient because numerous experiments are required. With CALPHAD, only key experiments are needed to model the system. As a consequence, phase equilibria and thermodynamic properties of a multicomponent system over a wide compositional and temperature ranges can be obtained from calculation and can further support other simulations. For example, the chemical potentials can be used in diffusion simulations. The driving forces of the phase can be provided to support the simulation of microstructure evolution. The information of the solid phase fraction and energies of metastable states can be applied in the simulation of solidification process. The prominent advantage of the CALPHAD method is that it is the only available method for the calculation of the thermodynamics in multicomponent system that possesses sufficient accuracy for practical applications. CALPHAD has been successfully applied in many fields, such as development of Nickel-based superalloys [16], prediction of bulk metallic glass formation [16], "virtual castings" by Ford company [17]. However, the CALPHAD method also has its limitations: (1) The calculation results from the extrapolation of lower order systems will not be satisfactory if a new phase appears in the higher order system; (2) Once the description of lower order system is updated or replaced by a new database, the related higher order system must be updated. For instance, if one binary system is updated, then n-2 ternary systems in a n-component system should be re-assessed; (3) The modeling of certain intermetallic phases such as the TCP (topologically close-packed) phase in multicomponent system is still not satisfactory [18].

Ab initio calculation or first-principle calculation is another source to obtain the thermodynamic properties of a phase. It is very helpful to get the thermodynamic data of metastable or unstable phases, dangerous elements or compounds and a phase at extreme conditions that are difficult to reach in experiments. However, in most of the case, *ab initio* calculations only consider a unit cell of the crystalline structure. Therefore, it is not possible to simulate disordered alloys, where in the unit cell alloying atoms randomly distribute. Despite of the limitations, reliable results from *ab initio* calculation are valuable for the CALPHAD modeling.

By CALPHAD method, phases are modeled with Gibbs energy functions. The parameters of the model can be assessed with data from critical evaluated data. The reason to model the phase with the Gibbs energy function rather than any other thermodynamic function is that all other important quantities can be derived from the Gibbs energy. For example, the enthalpy, entropy and heat capacity can be obtained with the following functions [15].

Entropy $S = -\left(\frac{\partial G}{\partial T}\right)_{P, N_i}$ (2-1)

Enthalpy $H = G - T\left(\frac{\partial G}{\partial T}\right)_{P, N_i}$ (2-2)

Heat capacity $C_P = -T\left(\frac{\partial^2 G}{\partial T^2}\right)_{P,N_i}$ (2-3)

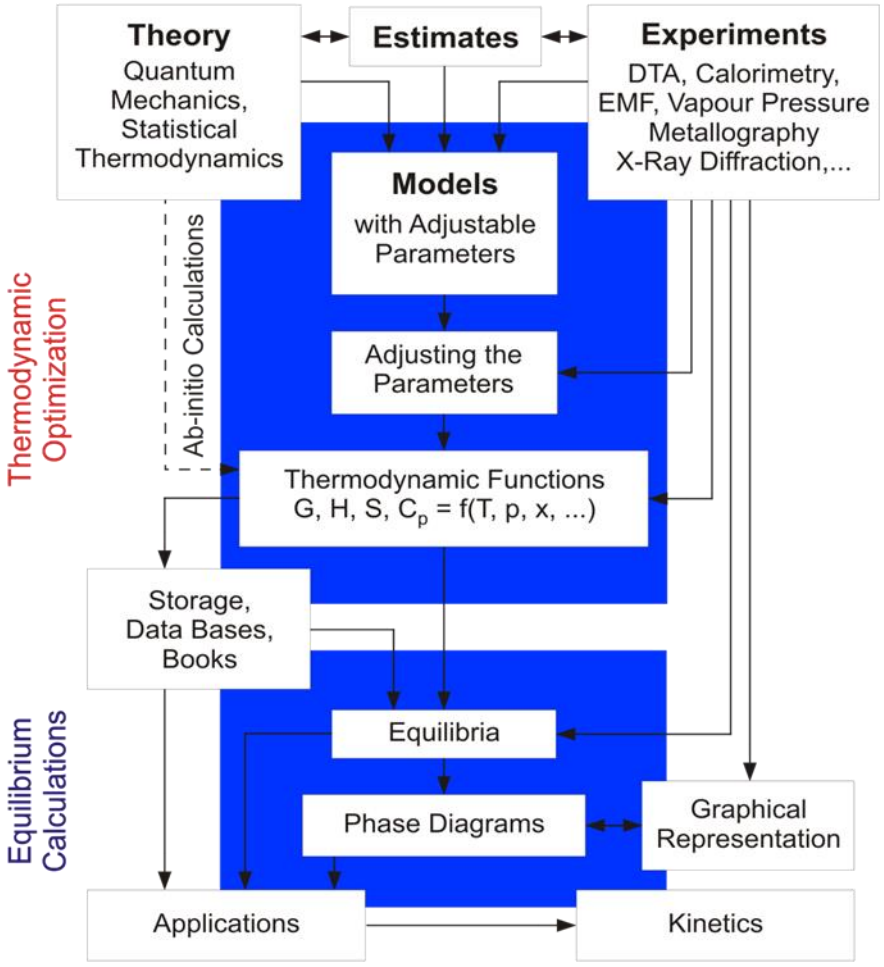

Fig. 2-1 Scheme of the CALPHAD method [19].

The scheme of the CALPHAD method is shown in Fig. 2-1. The core of this method is to determine the Gibbs energy functions of different phases. Firstly, data are collected from experiments, estimates and theoretical calculation, such as phase transformation temperatures from differential thermal analysis (DTA), enthalpies of mixing from calorimetry, vapor pressure measured by a Knudsen cell and enthalpy of formation from first-principles calculation and calorimetry, respectively. These data must be evaluated based on the background information, e.g., the purity

of the raw materials, experimental methods, experimental procedure and the setting of parameters during the calculation. Only reliable data can be adopted in the modeling. Phases are modeled with different Gibbs energy models according to their physical and chemical properties, such as type of bonding between the components, crystal structure, order-disorder transitions and magnetic properties. Then, selected data are used to optimize the parameters in the models (Thermodynamic Optimization). A database is established by saving the obtained Gibbs energy functions of different phases in a specific format. The database can be used for application, such as calculation of phase diagrams and thermodynamic properties, modeling of higher order system and supporting phase field simulation.

2.1. Models

The Gibbs energy of a phase can be expressed as follows:

$$\mathrm{G_m} = {}^{ref}\mathrm{G_m} + {}^{id}\mathrm{G_m} + {}^{E}G_\mathrm{m} + {}^{phy}G_\mathrm{m} \tag{2-4}$$

$${}^{id}\mathrm{G_m} = -T\,{}^{id}S \tag{2-5}$$

Where ${}^{ref}\mathrm{G_m}$ is the "surface of reference", which represents the Gibbs energy of the mechanical mixture of the constituents of the phase. ${}^{id}\mathrm{G_m}$ is the contribution of configuration entropy to the Gibbs energy. T is the absolute temperature in Kelvin and ${}^{id}S$ is the configuration entropy, which is determined by the number of possible arrangements of the constituents in a phase. ${}^{E}G_\mathrm{m}$ is the excess Gibbs energy, the Gibbs energy change from the ideal solution to the real solution. ${}^{phy}G_\mathrm{m}$ represents the Gibbs energy contribution of physical phenomenas, such as magnetic transitions.

2.1.1. Elements

The molar Gibbs energy ${}^{o}G_\mathrm{i}$ of a pure element i in a phase at temperature T and pressure of 10^5 Pa, relative to the "Standard Element Reference" $\mathrm{H}_i^{\mathrm{SER}}$, is described by a power series as follows:

$${}^{o}G_\mathrm{i} - H_i^{SER} = a_0 + a_1T + a_2Tln(T) + a_3T^2 + a_4T^3 + a_5T^{-1} + \cdots, \quad T_1 < T < T_2 \tag{2-6}$$

Where a_1, a_2, $a_{3,\ldots}$ are coefficients. H_i^{SER} is the enthalpy of the pure element i in its reference state. Because the Gibbs energy has no absolute value, it is necessary to refer the Gibbs energy of all phases to the same reference point for each element. In most of the cases, the reference state is the stable state at 298.15 K, 10^5 Pa. The temperatures of T_1 and T_2 determine the validity range of the power series.

In the present work, the molar Gibbs energy of pure elements are adopted from the SGTE (Scientific Group Thermodata Europe) database of pure elements compiled by Dinsdale [20].

2.1.2. Substitutional solution phases

Substitutional model can be used to model substitutional solution phases, such as liquid, gas, fcc and bcc phases. In these phases, constituents can mix randomly with each other.

In special case that no short-range-order (SRO) exists or the contribution of the SRO to the Gibbs energy of the phase can be approximated in ${}^{E}G_{\mathrm{m}}$. Then, the constituents of these phases are the same as the components. To describe the molar Gibbs energies of substitutional solutions, the terms in Eqs. (2-4) and (2-5) are expressed as follows:

$$ {}^{ref}\mathrm{G_m} = \sum_{i=1}^{n} x_{\mathrm{i}}\,{}^{\mathrm{o}}G_{\mathrm{i}} \tag{2-7} $$

$$ {}^{id}S = -R\sum_{i=1}^{n} x_i ln x_i \tag{2-8} $$

The ${}^{id}S$ represents the ideal mixing entropy of the pure elements *i* when the components can randomly mix with each other. R is the gas constant.

${}^{\mathrm{E}}G_{\mathrm{m}}$ is the excess Gibbs energy of mixing. Take a phase with three components for example, the ${}^{\mathrm{E}}G_{\mathrm{m}}$ can be expressed as follows:

$$ {}^{\mathrm{E}}G_{\mathrm{m}} = \sum_{i=1}^{n-1}\sum_{j=i+1}^{n} x_i x_j L_{ij} + \sum_{i=1}^{n-2}\sum_{j=i+1}^{n-1}\sum_{k=j+1}^{n} x_i\, x_j\, x_k L_{ijk} \tag{2-9} $$

Where L_{ij} and L_{ijk} are binary and ternary interaction parameters, respectively. Many excess models such as Lagrange series [15], Quasi-chemical model [15, 21] and Margules model [21] for the binary system are available, but Redlich-Kister polynomial [22] is recommended because it is symmetrical and thus extrapolates well to ternary and higher-order systems. The concentration dependence of the binary interaction parameters are given by Redlich-Kister polynomial [22]:

$$ L_{ij} = \sum_{v=0}^{k} (x_i - x_j)^v \cdot {}^{v}L_{ij} \tag{2-10} $$

The ternary interaction parameters can be expressed as follows:

$$ L_{ijk} = v_i \cdot {}^{i}L_{ijk} + v_j \cdot {}^{j}L_{ijk} + v_k \cdot {}^{k}L_{ijk} \tag{2-11} $$

Where

$$ v_i = x_i + (1 - x_i - x_j - x_k)/3 $$

$$ v_j = x_j + (1 - x_i - x_j - x_k)/3 \tag{2-12} $$

$$v_k = x_k + (1 - x_i - x_j - x_k)/3$$

In most cases, quaternary or higher-order interaction parameters are not necessary because the results from the extrapolation of ternary systems can predict the system well and also normally there is not enough experimental data for the quaternary system available. If the results from the extrapolation of lower-order systems cannot represent the higher-order system satisfactorily, one can adjust the parameters of the lower-order systems to improve it.

In the present work, the Gibbs energy contributions of magnetic transitions, ${}^{Mag}G_{\mathrm{m}}$, are considered. ${}^{Mag}G_{\mathrm{m}}$ can be expressed by the following equation [23]:

$${}^{mag}G_m = nRTf(\tau)\ln(\beta + 1) \tag{2-13}$$

Where n is the number of atoms per formula unit that has the average magnetic moment β. τ equals to T/T^*. $T^*$is the critical temperature for magnetic ordering. For ferromagnetic materials such as Ni, Co and Fe, T^* stands for the Curie temperature T_C. For anti-ferromagnetic materials such as Cr, it stands for Neel temperature T_N. $f(\tau)$ is defined by the following equation [15, 23]:

$$f(\tau) = \begin{cases} 1 - \dfrac{1}{A}\left[\dfrac{79\tau^{-1}}{140p} + \dfrac{474}{497}\left(\dfrac{1}{p} - 1\right)\left(\dfrac{\tau^3}{6} + \dfrac{\tau^9}{135} + \dfrac{\tau^{15}}{600}\right)\right], & \tau < 1 \\ -\dfrac{1}{A}\left(\dfrac{\tau^{-5}}{10} + \dfrac{\tau^{-15}}{315} + \dfrac{\tau^{-25}}{1500}\right) & \tau \geq 1 \end{cases} \tag{2-14}$$

Where

$$A = \frac{518}{1125} + \frac{11692}{15975}\left(\frac{1}{p} - 1\right)$$

p depends on the structure and is an empirical constant, which is defined as the ratio of the contributions due to the long-range order and short-range order to the enthalpy of magnetic transition. For phases with bcc_A2 structure, p is 0.40 while p is 0.28 for other phases.
In other cases that the SRO exists in the solution, then there are more constituents than components. To model the mixing entropy of this solution, models, such as associate-solution model, quasi-chemical model and cluster-variation method, can be applied [15].

2.1.3. Sublattice solution phases

When the SRO is very strong or the long-range order (LRO) exists in the phases, these phases should be modeled as sublattice solution phases. Sublattice solution phases can be envisaged to comprise interlocking sublattices. The compound energy formalism (CEF) [24] was constructed to describe the thermodynamic properties of sublattice solution phases. These phases have two or more sublattices and at least one of these sublattices has a variable composition. Ideal entropy of mixing is assumed on each sublattice. This model is usually used to model crystalline solids, but it can also be extended to model ionic liquid.

Here, a solution phases with two sublattices, $(A,B)_a(C,D)_b$, will be given as an example to illustrate the compound energy formalism. In this model, components A and B can mix randomly on the first sublattice, so do the components C and D on the second sublattice. a and b are the corresponding stoichiometric coefficients.

Site fraction y_i^s is introduced to describe the constitution of the phase and is defined as follows:

$$y_i^s = \frac{n_i^s}{N^s} \tag{2-15}$$

n_i^s is the number of component *i* on sublattice (s) and N^s is the total number of sites on the same sublattice. When vacancies are considered in the model, then the Eq. (2-17) becomes

$$y_i^s = \frac{n_i^s}{n_{Va}^s + \sum_i n_i^s} \tag{2-16}$$

n_{Va}^s is the number of vacancies on sublattice (s). The site fraction can be transferred to mole fraction x_i with the following equation.

$$x_i = \frac{\sum_s n^s y_i^s}{\sum_s n^s (1 - y_{Va}^s)} \tag{2-17}$$

When each sublattice is only ocuppied by one component, then end-members of the phase are produced. In the present case, four end-members exist. They are A_aC_b, A_aD_b, B_aC_b and B_aD_b.

The surface of reference ${}^{ref}\mathrm{G_m}$ is expressed as follows:

$${}^{ref}\mathrm{G_m} = y_A^1 y_C^{2\,o} G_{A:C} + y_A^1 y_D^{2\,o} G_{A:D} + y_B^1 y_C^{2\,o} G_{B:C} + y_B^1 y_D^{2\,o} G_{B:D} \tag{2-18}$$

Fig. 2-2 shows the surface of reference plotted above the composition square for the phase $(A, B)_a(C, D)_b$.

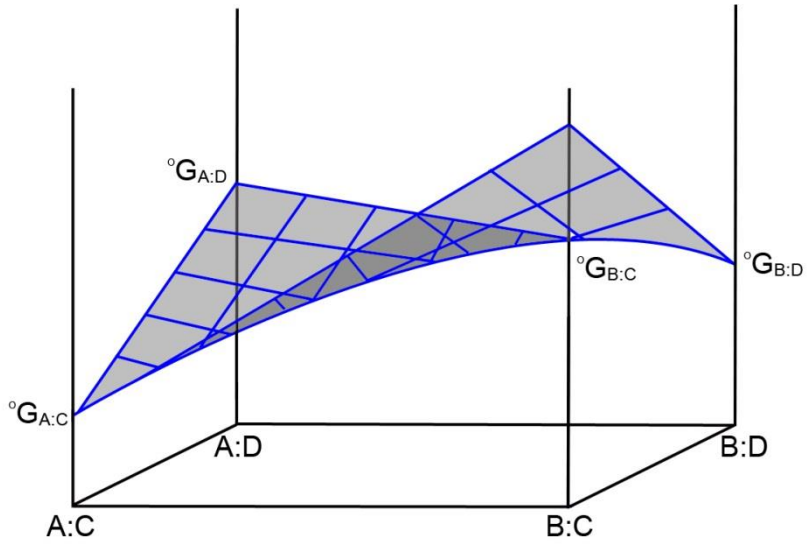

Fig. 2-2 The surface of reference for a phase (A, B)a(C, D)b plotted above the composition square according to the CEF.

The ${}^{id}S_{\mathrm{m}}$ and ${}^{\mathrm{E}}G_{\mathrm{m}}$ are expressed as follows:

$${}^{id}S = -R[a(y_A^1 lny_A^1 + y_B^1 lny_B^1) + b(y_C^2 lny_C^2 + y_D^2 lny_D^2)] \tag{2-19}$$

$${}^{\mathrm{E}}G_{\mathrm{m}} = y_A^1 y_B^1\left(y_C^2 L_{A,B:C} + y_D^2 L_{A,B:D}\right) + y_C^2 y_D^2 (y_A^1 L_{A:C,D} + y_B^1 L_{B:C,D}) \tag{2-20}$$

The binary interation parameters $L_{i,j:k}$ represent the interaction between the constituents *i* and *j* in the first sublattice when the second sublattice is only occupied by constituent *k*. These parameters can be further expanded with Redlich-Kister polynomial as follows:

$$L_{i,j:k} = \sum_v (y_i^1 - y_j^1)^v \cdot {}^v L_{i,j:k} \tag{2-21}$$

Here, an expression of molar Gibbs energy for the phase with three sublattices is also provided as an example.

$$G_{\mathrm{m}} = \sum_i y_i^I \sum_j y_j^{II} \sum_k y_k^{III}\, {}^{\mathrm{o}}G_{i:j:k} + RT \sum_s \sum_i a^s\, y_i^s \ln y_i^s + {}^{\mathrm{E}}G_{\mathrm{m}} \tag{2-22}$$

$${}^{\mathrm{E}}G_{\mathrm{m}} = \sum_i y_i^I \sum_j y_j^{II} \sum_k y_k^{III} \left[\sum_{l>i} y_l^I \sum_v {}^v L_{i,l:j:k}(y_i^I - y_l^I)^v + \sum_{l>j} y_l^{II} \sum_v {}^v L_{i:j,l:k}\left(y_j^{II} - y_l^{II}\right)^v \right.$$

$$+\sum_{l>k} y_l^{III} \sum_v {}^v L_{i:j:k,l}(y_k^{III} - y_l^{III})^v \Bigg] \quad (2\text{-}23)$$

2.1.4. Stoichiometric compounds

Stoichiometric compound can be regarded as a special sublattice phase where each sublattice is occupied by just one element. Therefore, the molar Gibbs energy of the stoichiometric compounds can be deduced from Eq. (2-12) and are expressed as follows:

$$G_{\mathrm{m}} = \sum_i x_i \, {}^{\mathrm{o}}G_{\mathrm{i}} + \Delta G_{i:j} \quad (2\text{-}24)$$

Where $\Delta G_{i:j}$ is the Gibbs energy of formation.

2.1.5. Modeling of the order-disorder transition

For phases where there is an order-disordered transition occuring, such as B2/A2 and $L1_2$/A1 phases, modeling them with a single Gibbs energy function would be a very good choice. This treatment can not only reduce the number of parameters but also give the parameters a sound physical meaning. It ensures the possibility of the ordered phase forming a continuous solution to another binary system where a second-order transition exists. In many previous assessments, ordered phases were modeled as a separate phase with a separate function, like the B2 phase in the Al-Mo-Ni system [25, 26] and the $L1_2$ phase in the Al-Ni-Cr system [27]. However, this treatment loses the advantages mentioned above and also may raise the problem that the ordered phase will never be disordered completely.

Dupin et al. [28, 29] developed a method to model the ordered and disordered phases with a single Gibbs energy function. The ordered B2 phase and its disordered A2 (bcc) parent phase are described by a single Gibbs energy function as well as ordered $L1_2$ and its disordered A1 (fcc) parent phase, which was explained in detail by Dupin et al. [28, 29]. This Gibbs energy function is composed of two parts: One part which represents the thermodynamics of the disordered phase, $G_{\mathrm{m}}^{dis}(x_i)$, and a second part which accounts for the contribution of the ordered state, $G_{\mathrm{m}}^{ord}(y_i)$, to the total Gibbs energy of the phase. At a given temperature and pressure, the Gibbs energy of the disordered state depends on the composition of the phase, given by the mole fractions x_i of its components, while the Gibbs energy of the disordered state is additionally affected by the distribution of the components in two or more sublattices of the ordered phase, which is given by site fractions y_i. In the disordered state, all site fractions are equal to the mole fractions of the corresponding constituents. Therefore, the Gibbs energy contributions of the disordered and ordered states can be separated from each other by the following expression:

$$G_{\mathrm{m}} = G_{\mathrm{m}}^{dis}(x_i) + G_{\mathrm{m}}^{ord}(y_i) - G_{\mathrm{m}}^{ord}(x_i) \quad (2\text{-}25)$$

The first summand provides the Gibbs energy of the disordered state only, while the last two terms give the additional contribution of ordering. In the disordered state, this ordering contribution vanishes, because the site fractions y_i become equal to the mole fractions x_i [28, 29]. In order to make sure the disordered state is always possible, some constraints for the parameters should be employed. A brief introduction of these constraints will be given in the following parts.

2.1.5.1. A2/B2 transition

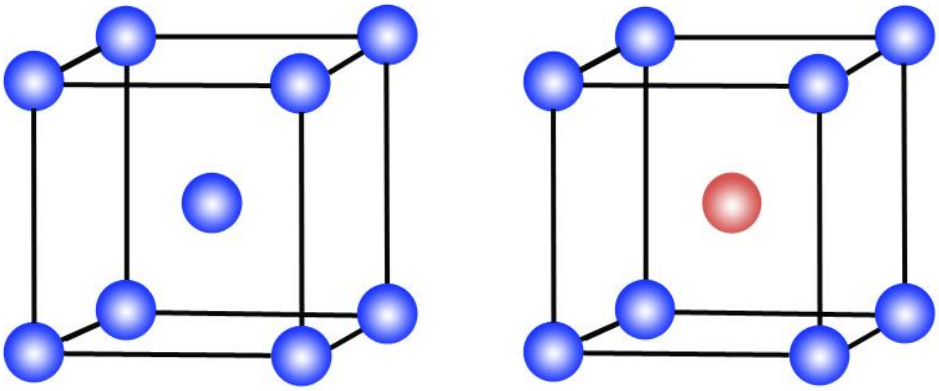

Fig. 2-3 The A2 (left) and B2 (right) lattices.

The difference between the B2 ordered structure and the A2 disordered structure is that the centered atom and 8 corner atoms are not identical. Therefore, the B2 structure can be divided into two sublattices and a two-sublattice model is required to describe the B2 phase. In this model, the two sublattices are equivalent and have the same number of sites. Therefore, the following constraints must be fulfilled in the modeling:

$$^{\circ}G_{i:j} = {}^{\circ}G_{i:j}$$

$$L_{i,j:k} = L_{k:i,j} \qquad (2\text{-}26)$$

$$L_{i,j,k:l} = L_{l:i,j,k}$$

2.1.5.2. A1/$L1_2$ transition

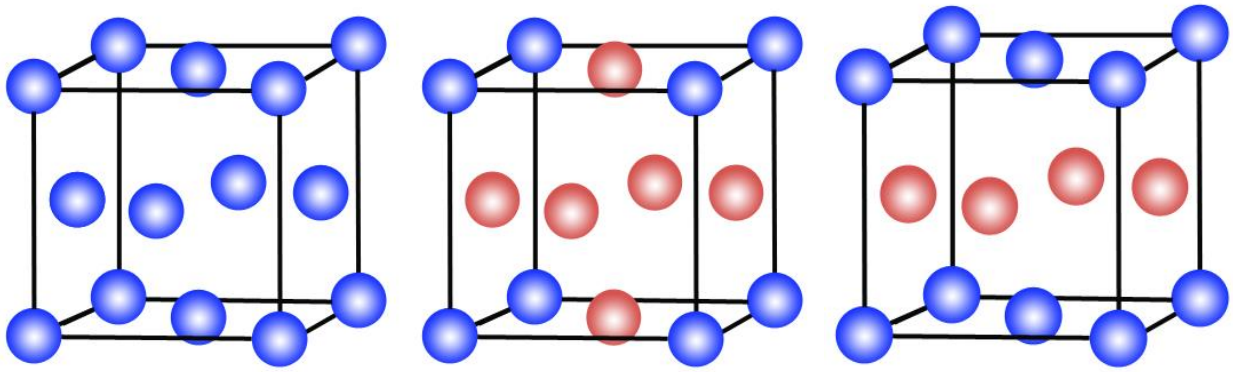

Fig. 2-4 The A1 (left), $L1_2$ (middle) and $L1_0$ (right) lattices.

Fig. 2-4 shows the A1(left), $L1_2$ (middle) and $L1_0$ (right) lattices. The difference of the $L1_2$ ordered structure from the A1 disordered structure is that 6 face center atoms and 8 corner atoms are not identical. In $L1_0$ lattice, 4 face center atoms are different from other atoms.

To model the disordered A1, ordered $L1_2$ and $L1_0$ phases with a single Gibbs energy function, a four sublattice model was developed [29]. When only disordered A1 phase and one ordered $L1_2$ phase exist in the system (More generally, two branches of $L1_2$ can exist, e.g. Cu_3Au and Au_3Cu in the Cu-Au system), the four sublattice model can be converted into a two sublattice model (2SL) by setting the site fractions of three sublattices equal but different from the rest one. The reason to make this conversion is that the calculation with a two sublattice model will be considerably faster. However, after this conversion, it is not possible to reproduce the $L1_0$ transition from calculation.

In order to make sure the disordered state is always possible, some constraints for the parameters should be employed. The following constraints must be fulfilled when a two sublattice model is used to model the $L1_2$ phase in binary, ternary and quaternary systems.

In binary system:

$$^{\circ}G^{2SL}_{A:B} = G_{AB_3}$$

$$^{\circ}G^{2SL}_{B:A} = G_{BA_3}$$

$$^{0}L^{2SL}_{A,B:A} = -1.5\,G_{AB_3} + 1.5\,G_{A_2B_2} + 1.5\,G_{A_3B} + 3L^{0}_{A,B}$$

$$^{1}L^{2SL}_{A,B:A} = 0.5\,G_{AB_3} - 1.5\,G_{A_2B_2} + 1.5\,G_{A_3B} + 3L^{1}_{A,B}$$

$$^{0}L^{2SL}_{A,B:B} = +1.5\,G_{AB_3} + 1.5\,G_{A_2B_2} - 1.5\,G_{A_3B} + 3L^{0}_{A,B} \qquad (2\text{-}27)$$

$${}^{1}L^{2SL}_{A,B:B} = -1.5\ G_{AB_3} + 1.5\ G_{A_2B_2} - 0.5\ G_{A_3B} + 3L^{1}_{A,B}$$

$${}^{0}L^{2SL}_{i:A,B} = L^{0}_{A,B}$$

$${}^{1}L^{2SL}_{i:A,B} = L^{1}_{A,B}$$

In ternary system:

$${}^{0}L^{2SL}_{A,B,C:A} = -1.5\ G_{ABC_2} - 1.5\ G_{AB_2C} + G_{AB_3} + G_{AC_3} + 6\ G_{A_2BC}$$
$$-1.5G_{A_2B_2} - 1.5G_{A_2C_2} - 1.5G_{A_3B} - 1.5G_{A_3C}$$

$${}^{0}L^{2SL}_{A,B,C:B} = -1.5\ G_{ABC_2} + 6\ G_{AB_2C} - 1.5G_{AB_3} - 1.5\ G_{A_2BC}$$
$$-1.5G_{A_2B_2} + G_{A_3B} + G_{BC_3} - 1.5G_{B_2C_2} - 1.5G_{B_3C}$$

$${}^{0}L^{2SL}_{A,B,C:C} = 6G_{ABC_2} - 1.5G_{AB_2C} - 1.5G_{AC_3} - 1.5\ G_{A_2BC}$$
$$-1.5G_{A_2C_2} + G_{A_3C} - 1.5G_{BC_3} - 1.5G_{B_2C_2} + G_{B_3C}$$

$${}^{0}L^{2SL}_{A,B:C} = 1.5G_{AB_2C} + 1.5G_{A_2BC} - 1.5G_{A_3C} - 1.5G_{B_3C} + 3L^{0}_{A,B} \quad (2\text{-}28)$$

$${}^{0}L^{2SL}_{A,C:B} = 1.5G_{ABC_2} + 1.5G_{A_2BC} - 1.5G_{A_3B} - 1.5G_{BC_3} + 3L^{0}_{A,C}$$

$${}^{0}L^{2SL}_{B,C:A} = 1.5G_{ABC_2} + 1.5G_{AB_2C} - 1.5G_{AB_3} - 1.5G_{AC_3} + 3L^{0}_{B,C}$$

$${}^{1}L^{2SL}_{A,B:C} = -1.5G_{AB_2C} + 1.5G_{A_2BC} - 0.5G_{A_3C} + 0.5G_{B_3C} + 3L^{1}_{A,B}$$

$${}^{1}L^{2SL}_{A,C:B} = -1.5G_{ABC_2} + 1.5G_{A_2BC} - 0.5G_{A_3B} + 0.5G_{BC_3} + 3L^{1}_{A,C}$$

$${}^{1}L^{2SL}_{B,C:A} = -1.5G_{ABC_2} + 1.5G_{AB_2C} - 0.5G_{AB_3} + 0.5G_{AC_3} + 3L^{1}_{B,C}$$

$${}^{0}L^{2SL}_{C:A,B} = L^{0}_{A,B} \qquad {}^{0}L^{2SL}_{B:A,C} = L^{0}_{A,C} \qquad {}^{0}L^{2SL}_{A:B,C} = L^{0}_{B,C}$$

$${}^{1}L^{2SL}_{C:A,B} = L^{0}_{A,B} \qquad {}^{1}L^{2SL}_{B:A,C} = L^{0}_{A,C} \qquad {}^{1}L^{2SL}_{A:B,C} = L^{0}_{B,C}$$

In quaternary system:

$${}^{0}L^{2SL}_{A,B,C:D} = G_{A_3D} + G_{B_3D} + G_{C_3D} - 1.5G_{AB_2D} - 1.5G_{AC_2D} - 1.5G_{A_2BD}$$
$$-1.5G_{A_2CD} - 1.5G_{BC_2D} - 1.5G_{B_2CD} + 6G_{ABCD}$$

$${}^{0}L^{2SL}_{A,B,D:C} = G_{A_3C} + G_{B_3C} + G_{CD_3} - 1.5G_{AB_2C} - 1.5G_{ACD_2} - 1.5G_{A_2BC} \quad (2\text{-}29)$$
$$-1.5G_{A_2CD} - 1.5G_{BCD_2} - 1.5G_{B_2CD} + 6G_{ABCD}$$

$${}^{0}L^{2SL}_{A,C,D:B} = G_{A_3B} + G_{BC_3} + G_{BD_3} - 1.5G_{ABC_2} - 1.5G_{ABD_2} - 1.5G_{A_2BC}$$
$$-1.5G_{A_2BD} - 1.5G_{BCD_2} - 1.5G_{BC_2D} + 6G_{ABCD}$$

$${}^{0}L^{2SL}_{B,C,D:A} = G_{AB_3} + G_{AC_3} + G_{AD_3} - 1.5G_{ABC_2} - 1.5G_{ABD_2} - 1.5G_{AB_2C}$$
$$-1.5G_{AB_2D} - 1.5G_{ACD_2} - 1.5G_{AC_2D} + 6G_{ABCD}$$

$L^{v}_{i,j}$ is a short notation for all permutations of the indices of the 4-sublattice parameters

$$L^{v}_{i,j:k:l:m} = L^{v}_{i,j:l:k:m} = L^{v}_{l:i,j:k:m} \cdots\cdots \quad (2\text{-}30)$$

The definitions of the symbols are listed as follows:

$$G_{AB_3} = 3u_{AB} + \Delta u_1$$

$$G_{A_2B_2} = 4u_{AB}$$

$$G_{B_3A} = 3u_{AB} + \Delta u_2$$

$$G_{A_2BC} = u_{BC} + 2u_{AB} + 2u_{AC} + \Delta u_3 \quad (2\text{-}31)$$

$$G_{AB_2C} = u_{AC} + 2u_{AB} + 2u_{BC} + \Delta u_4$$

$$G_{ABC_2} = u_{AB} + 2u_{AC} + 2u_{BC} + \Delta u_5$$

$$G_{ABCD} = u_{AB} + u_{AC} + u_{AD} + u_{BC} + u_{BD} + u_{CD} + \Delta u_6$$

Where u_{ij} is the bonding energy between the pair *i-j*; The coefficient of the u_{ij} stands for the number of the *i-j* bond in each end member. Δu_n are the parameters which are used to correct the deviation of the bonding energy due to the variation of the overall composition and their values can be determined during optimization.

2.2. The software

In the present work, the optimization was performed with the PARROT module [30] of the software package Thermo-Calc [31, 32] and the diagrams and properties were calculated with Thermo-Calc.

3. Experiments and analytics

To determine models for different phases and to assess the parameters of the models, data quantitatively related to any thermodynamic state must be considered. Especially, data determined by experiments are an important resource. In this chapter, the equipment or methods used in the present work for sample preparation and characterization will be briefly introduced.

3.1. Arc melting

Fig. 3-1 Arc-melting furnace (AM0.5, Edmund Bühler) used in the present work.

Arc melting is a technique that electrical energy is used to generate the arc between two electrodes or between electrodes and the materials to melt the materials. According to the type of the electrode, electric arc furnaces can be divided into two types: furnace with consumable electrode and with non-consumable electrode. Both of them are suitable for the preparation of alloys with a high melting point. In an electric arc furnace, the upper electrode is a water-cooled copper pole with a tungsten head, which acts as the cathode. The metal to be melted and the water-cooled copper platform act as the anode. The electric current passing through the electrodes can reach several hundred amperes. Under argon atmosphere, ion plasma is generated because of the electric arc and

melts the samples. By adjusting the current intensity, the output power can be controlled. Usually, alloys are turned over and melted several times to ensure compositional homogeneity.

In this study, the arc-melting furnace (AM0.5, Edmund Bühler) with a non-consumable tungsten electrode was used to prepare the alloys. It can melt samples of up to approx. 500 g and can reach the maximum temperature of up to approx. 3500 °C. A picture of this furnace is shown in Fig. 3-1.

3.2. Quenching furnace

By quenching, the microstructure of the sample at high temperature can be conserved and undesired reactions occurring during slow cooling process can be avoided. Quenching is particularly important for the investigation of the material at high temperature.

Fig. 3-2 Quenching furnace used in the present work.

In this work, a quenching furnace as shown in Fig. 3-2 was used to anneal or quench the samples. It mainly consists of three parts: control cabinet, heating part and pumps. Schematic setup of the sample holding and temperature measurement part is shown in Fig. 3-3. The crucible with the

sample inside is hooked by metal wires. This wire can be used for temperatures as high as approx. 1900 °C. A thermal couple protected by an alumina tube is placed near the crucible to measure the temperature of the sample. The maximum temperature of the furnace can reach up to approx. 1800 °C. For a quenching experiment, direct current will be applied through the wires. Once the wire breaks, the crucible with sample inside will fall down. It takes only a few seconds for the sample to fall from the original position into the water or ice water or liquid nitrogen, so the microstructure changes and undesired reactions can be prevented to the outmost extent.

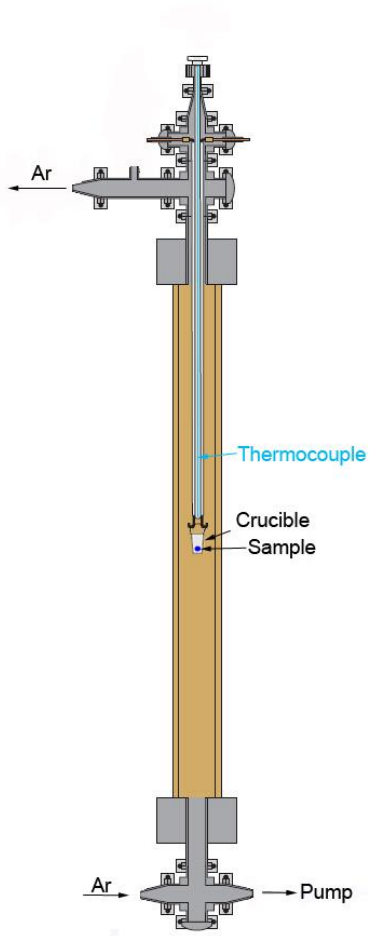

Fig. 3-3 Setup of the sample holding and temperature measurement part.

3.3. X-ray diffraction (XRD)

When the X-rays radiate a sample, the incident X-rays will be diffracted. The diffraction of X-rays by a crystal is in accordance with Bragg's Law. The crystal structure of the material determines the possible diffractions directions and intensities. By recording these diffraction directions and intensities, the diffraction pattern can be obtained. Each crystal has its unique crystal structure and consequently a unique X-ray diffraction pattern.

In the present work, a PADII X-ray diffractometer with a Meteor detector with Cu $K\alpha_{1/2}$ radiation was used. The X-ray diffraction was realized in Bragg-Brentano geometry with a measuring range of 10°-90° with a step size of 0.01° and a counting time of 360 seconds per step. The obtained diffraction patterns in the present work were compared with the standard patterns to identify the phase of the alloys.

3.4. Scanning electron microscope (SEM)

Scanning electron microscope (SEM) is a type of electron microscopes where a focused electron beam is used to scan the samples and produce images. As shown in Fig. 3-4, five types of signals [33]: secondary electrons (SE), back-scattered electrons (BSE), characteristic X-rays, Auger electrons, cathodoluminescence-transmitted electrons and specimen current are produced in a SEM.

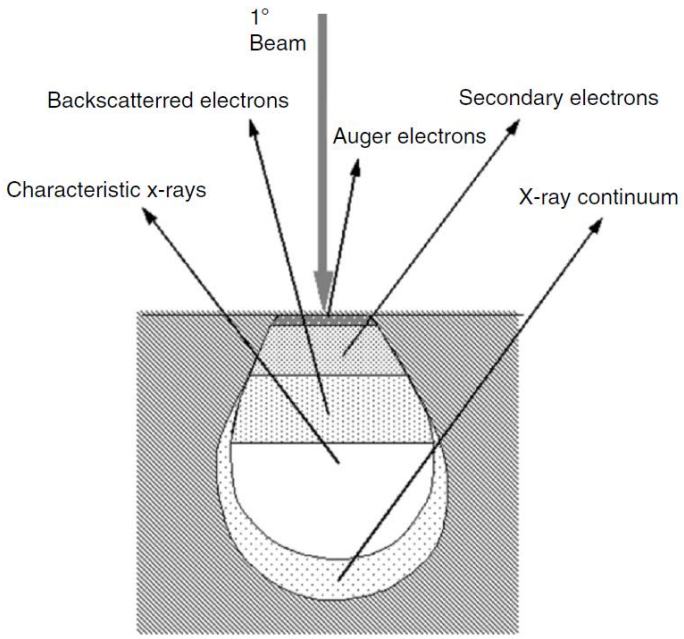

Fig. 3-4 Illustration of the signals generated in the scanning electron microscope [33].

The secondary electrons, back-scattered electrons and characteristic x-rays are the most commonly used signals. The secondary electrons are produced by the inelastic interactions between the incident electrons and the electrons and atoms near the sample surface. The electrons are from the conduction or valence bands of the atoms in the specimen but are ejected by the incident electrons. The secondary electrons can provide the image of the sample surface with a high-resolution. Back-scattered electrons are incident electrons that are reflected from the sample because of elastic collision. They emerge from the area deep beneath the sample surface. Because the intensity of the BSE signal strongly depends on the atomic number, BSE images can provide both compositional and topographic information, such as the distribution of different elements in the sample. Characteristic X-rays are generated when the incident electron displaces an inner shell electron from the sample, causing an outer shell electron to fill the shell and releasing an X-ray photon. The characteristic X-rays are used to identify the composition of the sample.

In the present work, the microstructures of the samples were observed with a SEM (FEI XL30S, PHILIPS).

3.5. Differential thermal analysis (DTA)

Differential thermal analysis (DTA) is a widely used thermal analysis technique. During a measurement, the sample and a reference material are subjected to identical thermal cycles and the temperature difference (ΔT) between the sample and reference is recorded. The ideal reference material is a substance with the same thermal mass as the sample, but with no thermal events occurring over the temperature range of interest. A baseline can be obtained when the signal is recorded without a thermal event taking place. Then the ΔT is plotted against time, or against temperature. Once a thermal event (such as melting, solidification) starts, deviation of ΔT from the baseline occurs. The onset temperature of a thermal event is determined to be the temperature where the first detectable deviation from baseline happens [34].

In the present work, the differential thermal analysis instrument (SETSYS Evolution, SETARAM Instrumentation) was used to measure the solidus temperatures of the samples. The samples were heated up to 1773 K with a heating rate of 10 K/min under an argon atmosphere.

3.6. The laser heating-fast pyrometry apparatus

3.6.1. Setup of the laser heating-fast pyrometry apparatus

The schematic setup of this apparatus [35] is shown in Fig. 3-5. This apparatus consists of two lasers, a heating laser and a probe laser, a pyrometer with two channels, a spectro-pyrometer and a glove box with the sample holder.

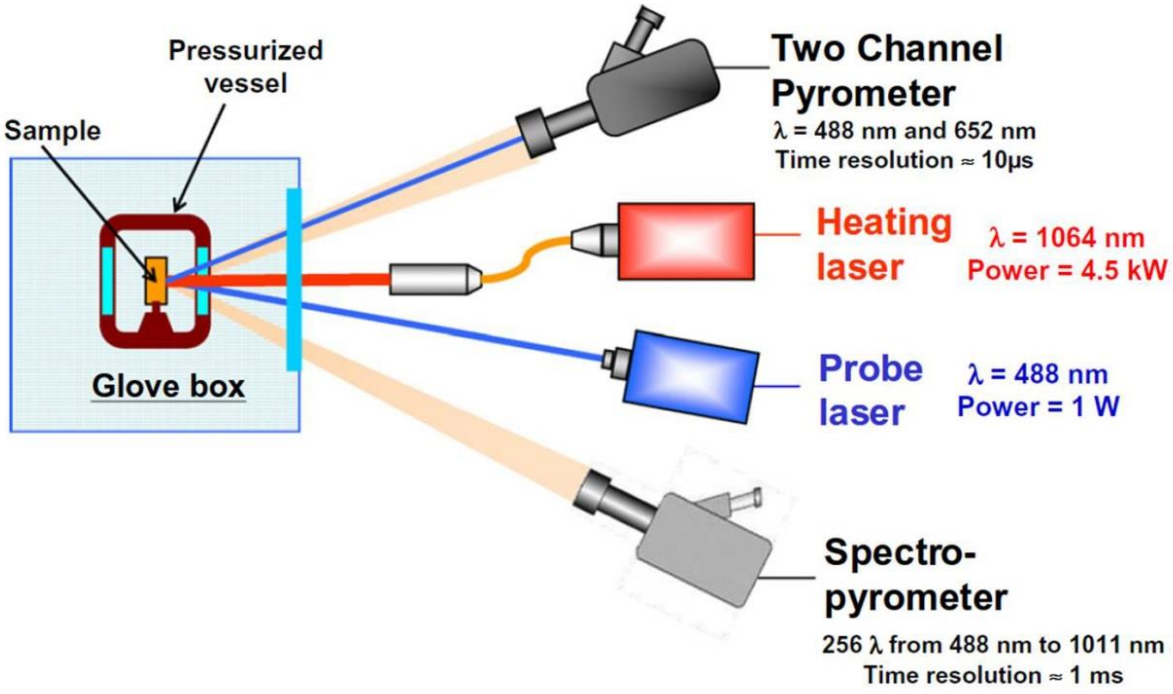

Fig. 3-5 Schematic setup of the laser heating-fast pyrometry apparatus [35] at the European Commission, Joint Research Centre, Institute for Transuranium Elements (ITU), Karlsruhe, Germany.

The heating laser produced by a Nd:YAG cavity of a TRUMPF® HLD 4506 laser apparatus is used to heat the samples. This apparatus is controlled by a computer and can produce continuous laser or laser pulses (shortest duration 1 ms) with the wavelength of 1064 nm and a maximum power of 4.5 kW. The diameter of the spot under direct laser impact on the sample surface can be adjusted between 0.3 and 15 mm.

The probe laser is a lower-power Ar+ laser with the wavelength of 488 nm and the power of 1 W. The probe laser is focused on the same spot as the heating laser on the sample surface during experiments. Reflected laser radiation of the probe laser from the sample surface will be detected by the pyrometer.

One channel of the two-channel pyrometer is working at the wavelength of 652 nm and used to measure the radiance temperature or so-called brightness temperature (T_λ) of the sample surface. This channel was calibrated against a Polaron® standard band lamp up to 2500 K. Above the band lamp calibration temperature, refractory metals such as Molybdenum and Tungsten were used to test this channel. The obtaining results were in acceptable agreement with the recommended data in the literature. The accuracy within 1%, was obtained, which was largely within the extended uncertainty with a coverage factor, k=2 [36].

Another channel is used to detect the intensity of the probe laser, which is reflected from the sample surface. This intensity depends on the angular reflectivity. The morphology of the sample surface under direct laser impact will change when the liquid phase is formed during laser heating or liquid phase completely solidified during cooling. Accordingly, the angular reflectivity of the sample surface will change. Therefore, from the reflected light signal, the moment that phase transformation happens can be determined.

The spectro-pyrometer consists of 256 Si-photodiodes array, which can measure the radiance signal in the wavelength range of 488 to 1011 nm.

During the measurement, the sample is hold by graphite screws and the area under direct laser impact is much smaller in diameter than the typical lateral dimension of the sample. Only a limited area in the interior part of the sample surface is melted. Therefore, any external contamination and reaction with crucible can be avoided. Moreover, the experiment typically only lasts a few seconds and is performed under a reducing atmosphere with a sufficiently high pressure, so the phenomenons, such as oxidation, evaporation or sublimation that may occurred in a differential thermal analysis (DTA) device at a high temperature can also be suppressed under acceptable margins.

3.6.2. Measurement of the emissivity of NiAl

3.6.2.1. Definitions

a) Black body

A black body is an idealized physical body that can absorb all incident electromagnetic radiation, regardless of the frequency or angle of incidence [37].

A black body satisfies the following three features [38]: (1) It is a perfect emitter of energy. At a specified temperature and wavelength, a black body can emit more radiant energy than any other surface at the same temperature. (2) It is the best absorber of energy. It can absorb all energies incident on it from all directions and at all wavelengths. (3) It is a diffuse emitter. The energy radiates from a black body only depend on the temperature and wavelength but is independent of direction.

b) Solid angle

Solid angle is defined as the angle formed by the vortex of a cone or subtended at the point of intersection by three or more planes [38]. The solid angle of an object in steradians equals the area of the segment of a unit sphere, centered at the vertex of the angle, which the object covers.

c) Spectral radiance

The spectral radiance $L_\lambda(\lambda, T)$ is defined as the radiance at a point of a surface at specified temperature T as the radiant power within an infinitesimal wavelength λ interval per unit solid

angle and unit projected area. The radiation of a blackbody follows Planck's radiation law in a medium and can be expressed as follows:

$$L_{\lambda,b}(\lambda,T)=\frac{c_{1L}}{n^2\lambda^5}\left[\exp\left(\frac{c_2}{n\lambda T}\right)-1\right]^{-1} \quad (3\text{-}1)$$

Where c_{1L} is the first radiation constant with $c_{1L}=2hc^2$; c_2 is the second radiation constant with $c_2=hc/k_B$; h is Planck's constant; c is the speed of light in vacuum; k_B is the Boltzmann constant, which equals to 1.3805E-23 J/K. λ is the wavelength. n is the refractive index and was set to be 1 in the present work, because the protective atmosphere we used is close to atmospheric pressure.

d) Emissivity

The emissivity is defined as the ratio of the radiation intensity emitted from a real surface at a given wavelength and temperature in specific direction to the radiation intensity of a black body under the same conditions. For any real surface, the emissivity varies from 0 to 1. Therefore, the spectral directional emissivity in specific direction is expressed as:

$$\varepsilon_{\lambda,T}(\lambda,T)={L_\lambda(\lambda,T)}\Big/{L_{\lambda,b}(\lambda,T)} \quad (3\text{-}2)$$

3.6.2.2 Measurement method

Since the relative position of the sample surfaces and the pyrometers were always fixed, the angle dependence of the emissivity was not considered in the present experiment. Hence, the emissivity obtained was normal spectral emissivity (NSE). The normal spectral emissivity of NiAl (ε_{NiAl}) was firstly determined by measuring the radiance emission of NiAl at its solidification point using the spectro-pyrometer, and then dividing it by Planck radiation intensity function [39] at the established solidification temperature.

3.6.3. Measurement of the $T_{liquidus}$ and $T_{solidus}$

From the measurement, the experimental radiance temperature or so-called brightness temperature (T_λ) can be measured by the two-channel pyrometer. Then the evaluated temperature T can be obtained by correcting the T_λ with the NSE of the corresponding sample within Wien's approximation (Eq. 3-3), according to the procedure described in Refs. [36, 39].

$$\frac{1}{T}=\frac{1}{T_\lambda}+\frac{\lambda}{C_2}ln\left[\varepsilon(x,\lambda,T)\cdot\tau_{eff}(\lambda)\right] \quad (3\text{-}3)$$

Where c_2 is a constant with c_2= 0.014388 mK. $\tau_{eff}(\lambda)$ is the effective total transmittance of the optical elements in this device.

In Eq. (3-3), there are three variables, T, T_λ and $\varepsilon(x,\lambda,T)$. Therefore, to obtain the evaluated temperature T, the $\varepsilon(x, \lambda, T)$ of the samples should be determined firstly. In the present work, the

normal spectral emissivity (NSE) of NiAl (ε_{NiAl}) was successively used as a reference for the other alloys measured in the present work. The evaluated temperature *T* was then obtained for all the investigated compositions by correcting the experimental radiance temperature with the obtained ε_{NiAl} within Wien's approximation. The approximation of neglecting emissivity effects of Mo in the studied alloys resulted in an additional error, which was duly taken into account in the definition of uncertainty bands.

The uncertainties related to the phase transition temperatures measured in the present experiments are determined according to the uncorrelated error propagation law [36]. They derive from the uncertainties in the temperature scale defined in the pyrometer calibration procedure, emissivity of the sample, transmittance factor of the optical elements of the apparatus and the dispersion of the temperatures obtained.

4. The Al-Mo-Ni system

4.1. Review of the binary systems

High quality, reliable binary thermodynamic descriptions are the foundation for establishing reliable databases of ternary and higher order systems. Therefore, before a binary thermodynamic database from previous work is adopted, it is necessary to verify if the available database fits well with the up-to-date experimental data. Only with such action, one can decide if the existing database can be directly adopted or further work to refine or re-assess the system is necessary.

The Al-Mo-Ni system contains three binary sub-systems, Al-Ni, Al-Mo and Mo-Ni. For the Al-Ni and Mo-Ni system, only brief reviews will be given in the following parts, because detailed reviews of these two binary systems have been given by Saltykov et al. [40] and Turchanin et al. [41], respectively. For the Al-Mo system, a controversy on the character of the AlMo phase melting exists. It will greatly influence the selection of the binary dataset, so a detailed review of the Al-Mo system will be given in the following section.

4.1.1. Review of the Al-Ni system

A critical evaluation of the Al-Ni system up to 1990 has been performed by Nash et al. [42]. After that, Okamoto [43] updated the phase diagram of the Al-Ni system with newly released results [44, 45]. Most recent critical evaluation of this system was made by Saltykov et al. [40]. In Ref. [40], the phase Al_4Ni_3 was also included as a stable phase. At atmospheric pressure, there are the eight stable phases in the Al-Ni system. Besides fcc and liquid phases, six intermetallic compounds, $AlNi_3$, NiAl, Al_3Ni_2, Al_3Ni, Al_3Ni_5 and Al_4Ni_3, exist. The crystallographic data of all stable solid phases in this system at atmospheric pressure from Saltykov et al. [40] are summarized in Table 4-1. The critically evaluated phase diagram of the Al-Ni system from Saltykov et al. [40] is given in Fig. 4-1.

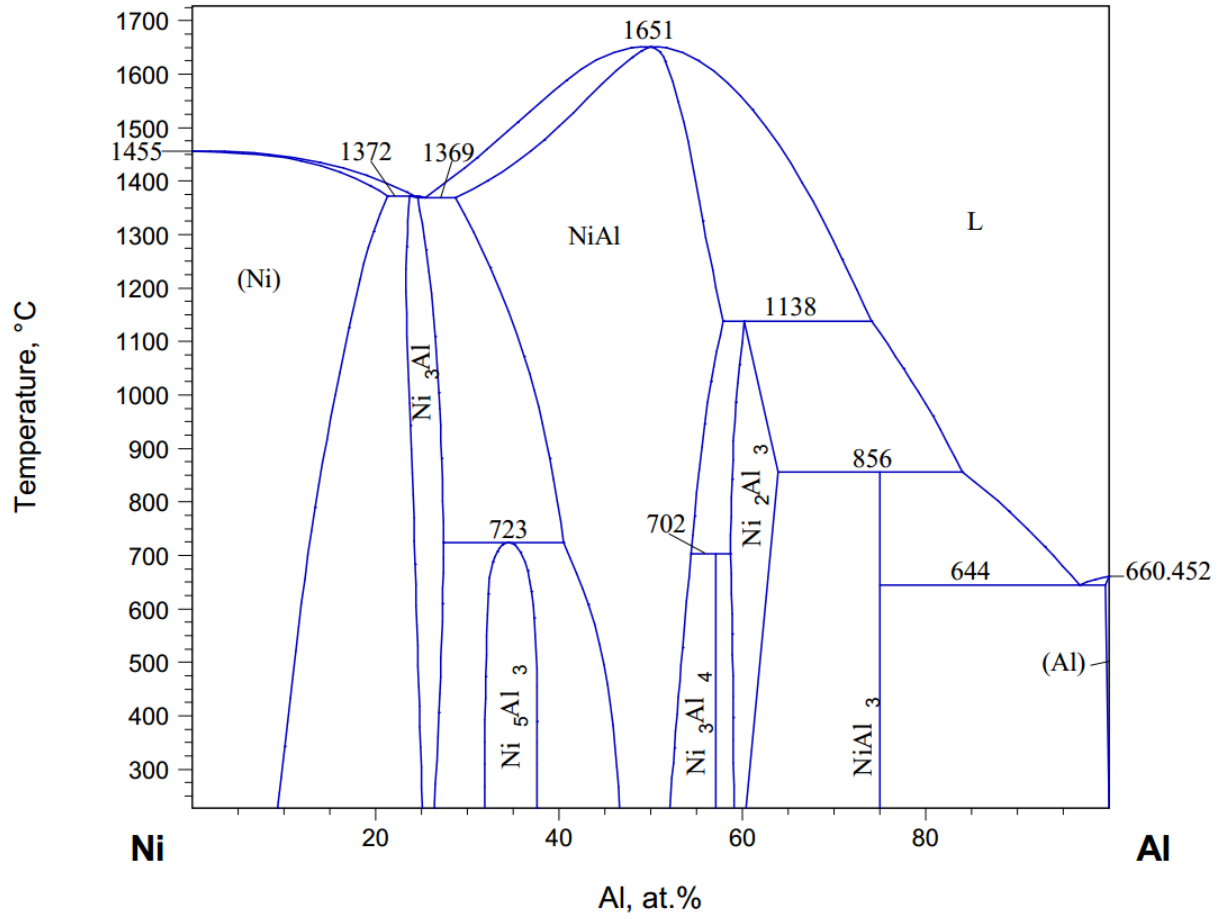

Fig. 4-1 Critically evaluated phase diagram of the Al-Ni system by Saltykov et al. [40].

Table 4-1 Crystallographic data of stable solid phases in the Al-Ni system at atmospheric pressure [40].

Phases	Prototype	Pearson symbol	Space group
fcc	Cu	cF4	$Fm\bar{3}m$
Al_3Ni	Al_3Ni	oP16	Pnma
Al_3Ni_2	Al_3Ni_2	hP5	$P\bar{3}m1$
Al_4Ni_3	Ga_4Ni_3	cI112	$Ia\bar{3}d$
NiAl	CsCl	cP2	$Pm\bar{3}m$
Al_3Ni_5	Ga_3Pt_5	oC16	Cmmm
$AlNi_3$	$AuCu_3$	cP4	$Pm\bar{3}m$

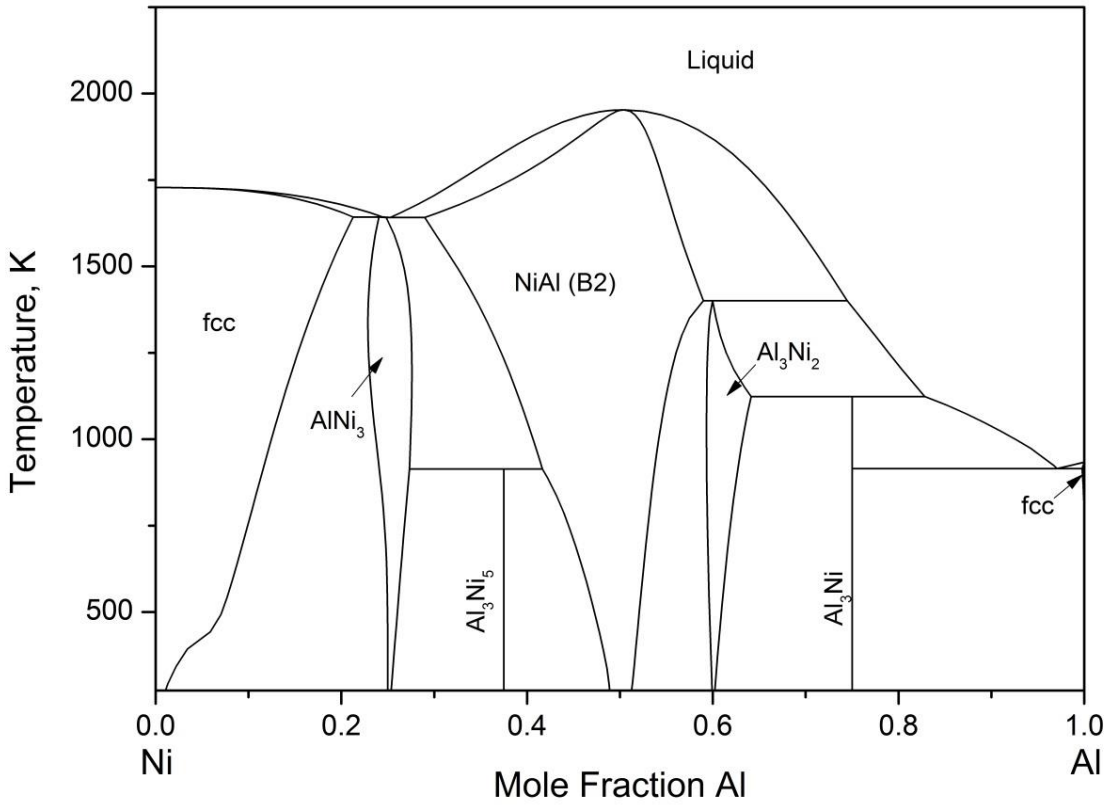

Fig. 4-2 Calculated phase diagram of the Al-Ni binary system by Dupin et al. [28].

Thermodynamic modeling of this system with CALPHAD method was carried out by Kaufman and Nesor [46], Ansara et al. [47], Dupin [29], Du and Clavaguera [48], Ansara et al. [49], Huang and Chang [50, 51], Dupin and Ansara [52] and Dupin et al. [28]. In Ref. [46], the homogeneity range of the intermetallic phases, $AlNi_3$ and Al_3Ni_2, were not considered and significant deviation between the calculated and experimentally determined phase diagrams can be observed. In Ref. [47], the sublattice model was used to describe the thermodynamic properties of the ordering in the ordered $L1_2$ phase. With this model, the order-disorder transition between $L1_2$ and fcc phases was reproduced from calculation for the first time. However, the agreement between the calculated phase diagram and experimentally determined phase diagram was not satisfactory. In Ref. [48], the description for the ordering of the $L1_2$ phase was absent and the associate model was employed to describe the thermodynamic properties of the liquid phase. Ansara et al. [49] further improved the modeling method developed in Ref. [47] for the fcc/$L1_2$ ordering using two sublattice model and four sublattice model, respectively. The improved model was later successfully extended in Ref. [28, 52] to describe the A2/B2 ordering in the Al-Ni system. In Ref. [28], the description of the ordered $L1_2$ phase was revised to get a better agreement with the experimental solvus at low temperature. The calculated phase diagram of the Al-Ni system using the dataset of Dupin et al.

[28] is shown in Fig. 4-2. It shows very good agreement between the calculated and critically evaluated phase diagram except that the homogeneity range of Al_3Ni_5 was not considered and the Al_4Ni_3 phase is not included in the modeling. However, the description developed by Dupin et al. [28] was not yet good enough in regard to the modeling of the Gibbs energy of vacancies in the bcc phase. Therefore, in this work, the thermodynamic assessment of Dupin et al. [28] was adopted after refinement. Details will be discussed in chapter 4.2.

4.1.2. Review of the Al-Mo system

The Al-Mo system has been investigated by many authors. At atmospheric pressure, there are fifteen stable phases in the Al-Mo system. Besides the bcc, fcc and liquid phases, twelve intermetallic compounds, $Al_{12}Mo$, $Al_5Mo(r)$, $Al_5Mo(h_1)$, $Al_5Mo(h_2)$, $Al_{22}Mo_5$, $Al_{17}Mo_4$, Al_4Mo, Al_3Mo, Al_8Mo_3, $Al_{63}Mo_{37}$, AlMo and $AlMo_3$, exist. The crystallographic data of all stable solid phases in this system at atmospheric pressure from Schuster [53] are summarized in Table 4-2.

Table 4-2 Crystallographic data of the stable solid phases in the Al-Mo system at atmospheric pressure [53].

Phases	Prototype	Pearson symbol	Space group
fcc_(Al)	Cu	cF4	$Fm\bar{3}m$
bcc_(Mo)	W	cI2	$Im\bar{3}m$
$Al_{12}Mo$	$Al_{12}W$	cI26	$Im\bar{3}$
$Al_5Mo(r)$	$Al_5Mo(r)$	hP36	$R\bar{3}c$
$Al_5Mo(h_1)$	$Al_5Mo(h_1)$	hP60	P321
$Al_5Mo(h_2)$	Al_5W	hP12	$P6_322$
$Al_{22}Mo_5$	$Al_{22}Mo_5$	oF216	Fdd2
$Al_{17}Mo_4$	$Al_{17}Mo_4$	mC84	C2
Al_4Mo	Al_4W	mC30	C2/m
Al_3Mo	Al_3Mo	mC32	C2/m
Al_8Mo_3	Al_8Mo_3	mC22	Cm
$Al_{63}Mo_{37}$	-	-	-
AlMo	W	cI2	$Im\bar{3}m$
$AlMo_3$	Cr_3Si	cP8	$Pm\bar{3}n$

For the sake of convenience, this review will be divided into two parts. One part focuses on the Al-rich (Al-Al_8Mo_3) region and another part focuses on the Mo-rich (Al_8Mo_3-Mo) region.

4.1.2.1 Review of the Al-rich region

In the Al-rich region, the liquidus line of the Al-rich side is well determined up to 1273 K [54–56]. Based on this and the solubility of Mo in Al reported in Refs. [57, 58], a peritectic reaction between the fcc_(Al), $Al_{12}Mo$ and liquid phases should take place.

The $Al_{12}Mo$ phase is the most Al-rich intermetallic phase in the Al-Mo system. Adam et al. [59] and Walford [60] determined its crystal structure. The experimental results confirmed that $Al_{12}Mo$ formed by a peritectic reaction. The measured peritectic temperatures agree well among different investigation [54, 61–65] and results of Refs. [64, 65] were adopted in present work.

Hexagonal Al_5Mo phase was reported firstly by Yamaguchi and Simizu [54] and confirmed later by many researchers [61, 63–66]. Schuster et al. [65] revealed three Al_5Mo polymorphs, but the highest temperature polymorph was not observed in Ref. [64] and the middle temperature polymorph was concluded to be a meta-stable phase [65]. The peritectic melting temperature (1119 K) of Al_5Mo determined by Eumann et al. [64] was adopted in present work.

The $Al_{22}Mo_5$ and $Al_{17}Mo_4$ phases were reported for the first time by Pötzschke et al. [63]. Later, Tenderloo et al. [67] clarified their stoichiometries. Schuster et al. [65] found the $Al_{22}Mo_5$ phase formed peritectically at 1237 K and a lower temperature stability limit of 1104 K was determined based on X-ray observations and DTA data. However, those results contradicted the most recent experimental work on the Al-rich region performed by Eumann et al. [64]. In Ref. [64], the $Al_{22}Mo_5$ phase was not detected in the diffusion couple equilibrated at 1123 K but in the samples equilibrated at the temperature as low as 873 K. In the present work, the results from Eumann et al. [64] was adopted and the $Al_{22}Mo_5$ phase should melt peritectically at temperature lower than 1123 K and exists as a stable phase as low as room temperature. The $Al_{17}Mo_4$ phase was observed at the as-cast alloys and Schuster et al. [65] determined its melting point to be 1307 K. But later experimental work by Eumann et al. [64] indicated the upper limit temperature for stability of $Al_{17}Mo_4$ should be lower than 1273 K.

The Al_4Mo phase was firstly reported by Wöhler et al. [68] and later confirmed in Refs. [61, 63–65, 69]. Sperner et al. [61] found the Al_4Mo phase existed as a stable phase only above 973 K. Later, Schuster et al. [65] determined the eutectoid decomposition temperature of Al_4Mo to be 1215 K, which was in consistence with the observation of Eumann et al. [64]. The peritectic melting temperature of the Al_4Mo phase was determined to be close to 1423 K by Eumann et al. [64] with DTA data and the observation of heat-treated alloy, which lied between 1403 K determined by Sperner et al. [61] and 1450 K determined by Schuster et al. [65].

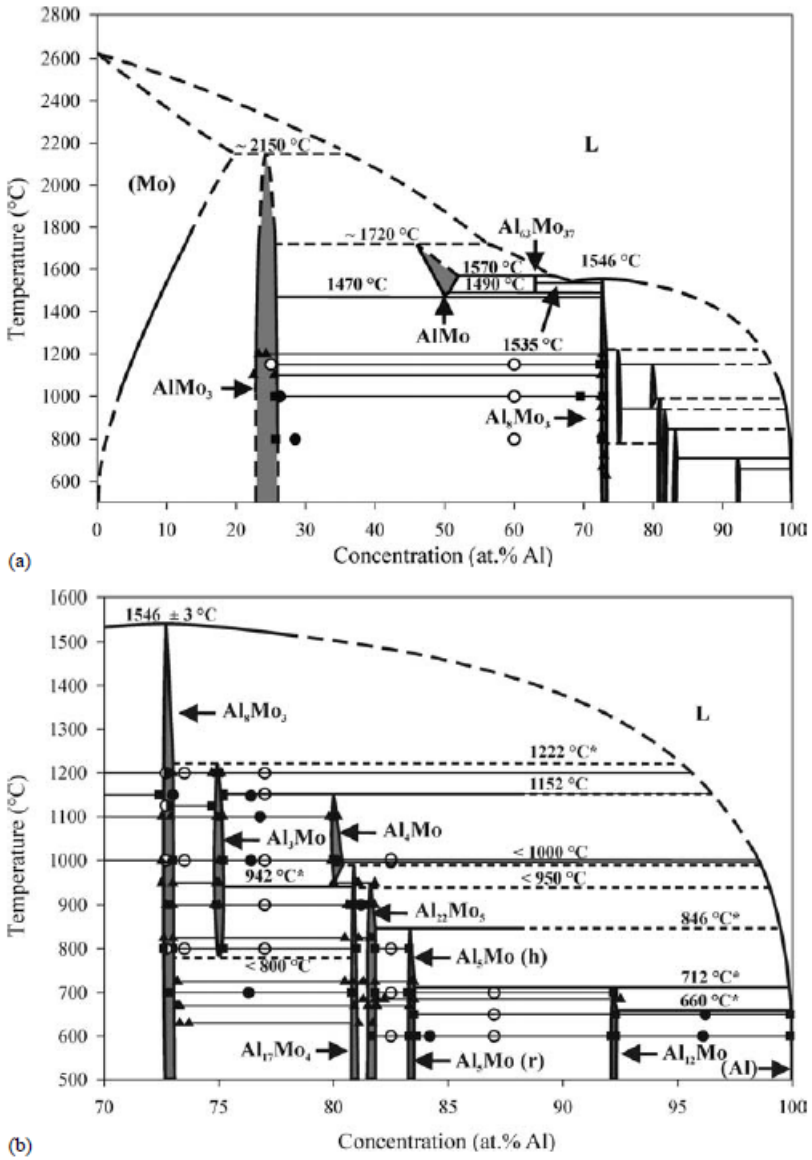

Fig. 4-3 Experimentally determined phase diagrams of the Al-Mo system from Eumann et al. [64].

Schuster et al. [65] firstly reported the $Al_{3+x}Mo_{l-x}$ ($0 \le x \le 0.2$) phase and determined its crystal structure. By DTA, Schuster et al. [65] found this phase existed in the composition range from 21 to 24 at.% Mo. It forms above 1427 K and decomposes by incongruent melting at 1533 K. However, in the most recent experimental work performed by Eumann et al. [64], the $Al_{3+x}Mo_{l-x}$ ($0 \le x \le 0.2$) phase was not detected at alloy with the nominal composition of 23 at.% Mo equilibrated at 1473 K. Therefore, this phase was not considered in the present work.

The Al_3Mo phase was reported to be a stable phase in the range from 1091 to 1495 K by Schuster et al. [65]. Eumann et al. [64] later found the upper limit stability temperature of this phase was 1498 K, which agreed well with the results of Schuster et al. [65]. The experimental results of

Eumann et al. [64] also indicated the temperature of the eutectoid decomposition of Al_3Mo ($Al_3Mo \leftrightarrow Al_{17}Mo_4+Al_8Mo_3$) should be lower than 1073 K.

Sperner et al. [61] mistook Al_8Mo_3 for Al_2Mo and Pötzschke et al. [63] characterized its crystal structure and corrected its stoichiometry as Al_8Mo_3. It was reported that the Al_8Mo_3 phase melted congruently at around 1843K [70, 71], which was consistent with the result of Shilo and Franzen [72]. Ref. [72] reported the melting temperature of the Al_8Mo_3 phase should be higher than 1773 K. Recent work by Schuster et al. [65] and Eumann et al. [64] showed a good agreement with each other. The congruent melting temperatures were determined to be 1828±10 K [65] and 1819±3 K [64], respectively. According to the reports of Refs. [73, 74], a broad homogeneity range of Al_8Mo_3 from ~25 to 31.5 at.% Mo at low temperature was assumed by Saunders [75, 76]. However, it contradicted the results of Eumann et al. [64], because only a narrow homogeneity range with 0.3 at. % Mo width was detected in Ref. [64].

Due to the relatively large numbers of Al-rich intermetallic compounds and the complex reactions between them, the exact sequence of reactions in the Al-Al_8Mo_3 section is not clear until recently. Both Schuster et al. [65] and Eumann et al. [64] reinvestigated the Al-Al_8Mo_3 section thoroughly. The experimentally determined phase diagrams of the Al-Mo system from Eumann et al. [64] is shown in Fig. 4-3. Most of the phases and phase equilibria determined by Schuster et al. [65] were confirmed by Eumann et al. [64]. In Ref. [64], all Al-rich intermetallic compounds exhibited a small homogeneity range with maximum 0.4 at.% Mo widths. Based on the literature survey on the Al-rich region (Al-Al_8Mo_3) above, the experimental results of Schuster et al. [65] and Eumann et al. [64] will be adopted in present study and the Al-rich intermetallic compounds were modeled as stoichiometric compounds because of the narrow homogeneity ranges.

4.1.2.2 Review of the Mo-rich region

Due to the high temperature, few investigations focused on the Mo-rich region (Al_8Mo_3-Mo region).

Rexer [71] investigated the Mo-rich region by thermal analysis and metallographic investigation. Two phases, AlMo and $Al_{63}Mo_{37}$, were detected. The AlMo phase was determined to be an extension of the Mo-rich bcc solid solution into more Al-rich parts with an A2 structure. It decomposes eutectoidally into Al_8Mo_3 and $AlMo_3$ at 1743 K. The eutectic reaction temperature between liquid, AlMo and $AlMo_3$ phases was assumed to be ~1993 K without evidence from thermal analysis. The $Al_{63}Mo_{37}$ phase formed peritectically at 1843 K and decomposed eutectoidally at 1763 K into Al_8Mo_3 and AlMo. The eutectic reaction temperature between liquid, Al_8Mo_3 and $Al_{63}Mo_{37}$ was determined to be 1808 K. Moreover, the homogeneity range of $AlMo_3$ and (Mo) solvus were also determined in range of ~1773 to ~1973 K. Rexer [71] concluded that the AlMo phase melted congruently. The partial phase diagram of the Al-Mo system constructed by Rexer is shown in Fig. 4-4. As we can see, the experiments performed by Rexer only focused

on the vicinity of the 50 at.% Mo, the results cannot exclude the possibility of a peritectic formation of the AlMo phase.

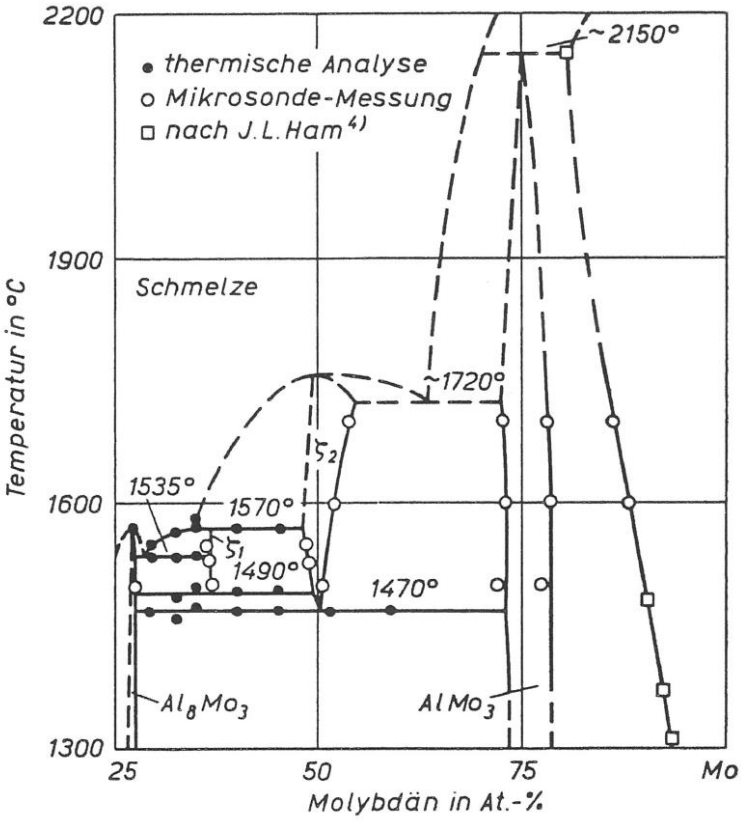

Fig. 4-4 Partial phase diagram of the Al-Mo system determined by Rexer [71].

The (Mo) solvus measured by Shilo and Franzen [72], Rexer [71] and Ham and Herzig [77] are in good agreement with each other. Ham and Herzig [77] estimated the $AlMo_3$ phase formed peritectically at 2423±100 K.

4.1.2.3 Thermodynamics

The earliest experimental thermodynamic data of this system was reported by Belyaeva et al. [78]. In Ref. [78], the derived chemical potential and activities of Al in alloys with 8-75 at.% Mo were determined by an electromotive force (EMF) method. However, Saunders [76] pointed out, a number of thermodynamic inconsistencies existed in Ref. [78]. With a calorimeter method, Dubrovin et al. [79] measured the enthalpies of formation of the Al-Mo system, but the experimental method cannot guarantee the results with high accuracy. The enthalpies of formation of the $AlMo_3$ and Al_8Mo_3 phases were measured by Meschel et al. [80] using a direct reaction calorimetry. Shilo and Franzen [72] measured the enthalpies of formation of the Al_8Mo_3, AlMo and $AlMo_3$ phases and the Mo-rich solid solutions with 89, 92, 96, and 98 at.% Mo by the Knudsen effusion method. The enthalpies of mixing of the liquid phase at 5, 10, 15, and 18 at.% Mo were

measured by Sudavtsova et al. [81] with an isothermal calorimetry. In the present work, the data from Shilo and Franzen [72] and Sudavtsova et al. [81] were adopted.

The thermodynamic assessments of this system were performed by Kaufman et al. [46, 82], Saunders [75, 76], Du et al. [83] and Cupid et al. [84]. Only the Mo-rich region of the phase diagram was optimized by Kaufman et al. [46, 82]. The calculated phase diagrams deviated substantially from the experimental data. Later, two similar thermodynamic descriptions of the Al-Mo system were developed by Saunders [75, 76]. However, none of them include the $Al_{17}Mo_4$, $Al_{22}Mo_5$ and Al_3Mo phases, because not enough information about the stability and the exact sequence of reactions for them was available. The $AlMo_3$ phase was modeled as a stoichiometric compound without considering experimentally determined homogeneity range. Particularly worth mentioning is that the congruent melting of the AlMo phase assumed by Rexer [71] was replaced by a peritectic reaction in the thermodynamic descriptions of Saunders [75, 76], because the congruent melting of the phase is "thermodynamically unlikely". The newly published experimental data from Refs. [64, 65] were adopted in the thermodynamic assessments of Du et al. [61] and Cupid et al. [21]. However, the $AlMo_3$ phase assessed by Du et al. [61] is too stable because it participates erroneously in the equilibria between B2, bcc and liquid phases of the section NiAl-Mo when this binary is extended into the ternary system. An artificial inverted miscibility gap of the liquid phase and an artificial stabilization of the bcc phase above liquidus line were created, but neglected by Cupid et al. [84]. Despite of the artifacts in the description of Cupid et al. [84], the modeling for the solid phases in Ref. [84] can reproduce the corresponding experimental data very well. Therefore, in the present work, the description of the Al-Mo system was refined basing on the dataset of Cupid et al. [84]. The liquid phase and intermetallic compounds was re-optimized. Details are described in chapter 4.3.

4.1.3. Review of the Mo-Ni system

A critical evaluation of the Mo-Ni system up to 1975 has been performed by Brewer and Lemoreaux [85]. Later, Okamoto [86] and Singleton and Nash [87] updated it. The most recent evaluation is available from Turchanin et al. [41]. The critically evaluated phase diagram of the Mo-Ni system from Ref. [41] is given in Fig. 4-5. At atmospheric pressure, there are the eight stable phases in the Mo-Ni system. Besides the fcc, bcc and liquid phases, five intermetallic compounds, MoNi, $MoNi_2$, $MoNi_3$, $MoNi_4$ and $MoNi_8$, exist. The crystallographic data of all stable solid phases in this system at atmospheric pressure from Ref. [41] are summarized in Table 4-3.

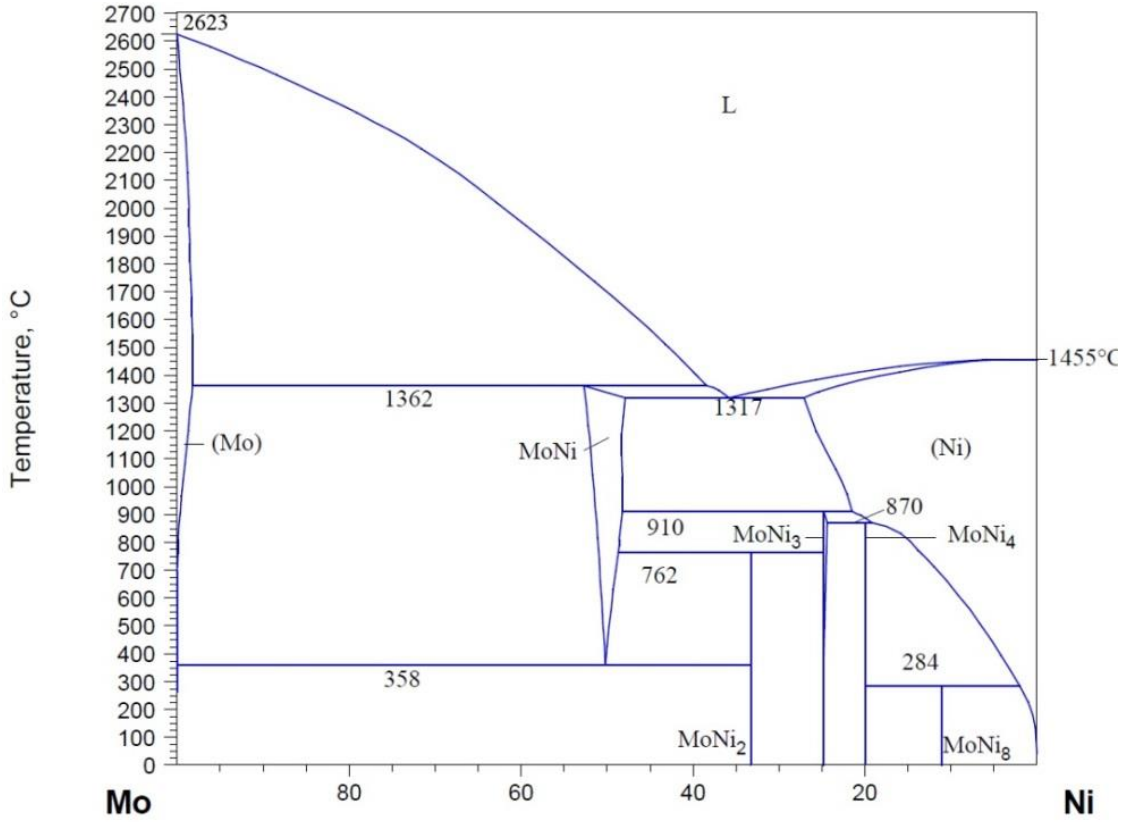

Fig. 4-5 Critically evaluated phase diagram of the Mo-Ni system by Turchanin et al. [41].

Table 4-3 Crystallographic data of stable solid phases in the Mo-Ni system at atmospheric pressure [41].

Phases	Prototype	Pearson symbol	Space group
bcc_(Mo)	W	cI2	$Im\bar{3}m$
fcc_(Ni)	Cu	cF4	$Fm\bar{3}m$
NiMo	NiMo	oP56	$P2_12_12_1$
Ni_2Mo	$MoPt_2$	cI8	Immm
Ni_3Mo	$CuTi_3$	oP8	Pmmm
Ni_4Mo	$MoNi_4$	tI10	I4/m
Ni_8Mo	$TiPt_8$	tI18	I4/mmm

The thermodynamic modeling of the Mo-Ni system was carried out firstly by Kaufman and Nesor [88]. At the time, the stoichiometry of the δ phase was wrongly determined to be Ni_6Mo_7. Both the Ni_3Mo and Ni_4Mo phases were included in the modeling. The calculated phase diagram deviated

considerably from the phase diagram accepted now. Frisk [89] re-assessed this system. The stoichiometry of the δ phase was corrected to be NiMo. Intermetallic compounds, Ni_3Mo and Ni_4Mo, were considered and treated as stoichiometric compounds. To describe the Ni_3Ta and Ni_3Mo phases of the Mo-Ni-Ta system as a single phase, Cui et al. [90] modified the dataset of Frisk [89] and modeled the Ni_3Mo phase with two-sublattice model. Later, Wang et al. [91] calculated the energies of formation of the Ni_2Mo, Ni_3Mo, Ni_4Mo and Ni_8Mo phases with first-principles calculations. At the same year, Zhou et al. [92] further explored the Mo-Ni system with first-principles calculations. The enthalpies of mixing of the fcc and bcc phases were calculated. The first-principles results indicate that the compounds Ni_2Mo and Ni_8Mo are stable besides NiMo, Ni_3Mo and Ni_4Mo whereas the NiMo phase is not stable at 0 K. Therefore, Zhou et al. [92] re-assessed this system and the calculation results fit well with the experimental data and first principle data. The calculated phase diagram from Zhou et al. [92] is shown in Fig. 4-6.

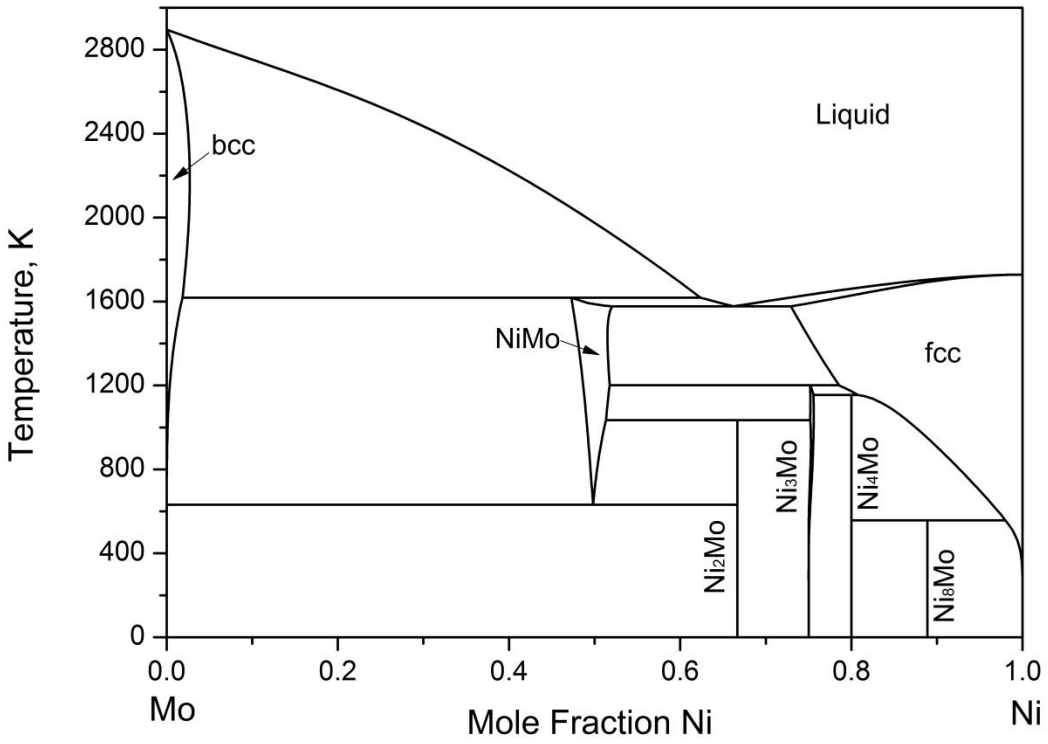

Fig. 4-6 Calculated phase diagram of the Mo-Ni binary system by Zhou et al. [92].

4.2. Refinement of the Al-Ni system

In the modeling of the Al-Ni system performed by Dupin et al. [28], vacancies are also taken into account in the modeling of the A2 and B2 phases. These two phases are related by a second order

transformation. In Ref. [28], the compound energy of thermal vacancies, G_{Va}^{bcc}, was set to zero. Recently, Franke [93] discussed that this choice for G_{Va}^{bcc} prevented the existence of any global minimum of the Gibbs energy for the whole system. The bcc phase can lower its Gibbs energy without limit to minus infinity. It means not only the bcc phase has no stable state of equilibrium, but also the dataset of Ref. [28] cannot have a global equilibrium state, even if all other phases of this dataset are well-behaved. Since in this case all other phases provide equilibrium states with Gibbs energies having minima at finite values, the faulty phase always achieves lower value but without reaching a stable state. This not optimal setting for the compound energy of thermal vacancies can also be found in the assessments of the Ni-Zn [94] and Nb-B [95] systems. The calculated phase diagrams in these cases were not influenced by this not optimal settings, because the software used in these cases can not detect the divergence at high vacancy concentrations [93]. Within the compound energy formalism, the thermodynamics of thermal vacancies was analyzed by Franke [93]. A critical value, G_{Va}^{crit}= (ln2-1/2)RT ≈ 0.193·RT, for the compound energy of thermal vacancies was determined. In order to ensure the existence of unique equilibrium states, the compound energy of thermal vacancies should be set to greater than or equal to this G_{Va}^{crit} and a slightly higher value, G_{Va}^{bcc}=0.2·RT, was recommended by Franke [93]. However, if only this change is applied to the dataset, the calculated phase diagram of the Al-Ni system deviates notably from the previous assessment [28], as shown in Fig. 4-7. The peritectic formation temperature of the Al_3Ni_2 phase increases significantly.

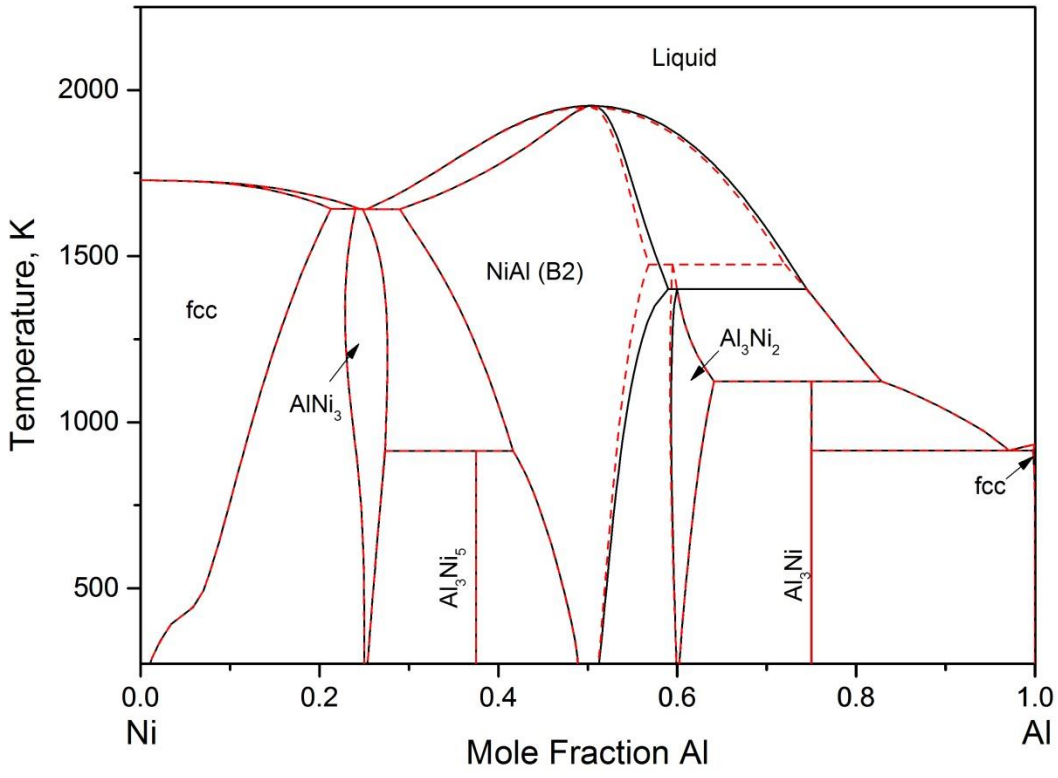

Fig. 4-7 Calculated phase diagram of the Al-Ni binary system before (black solid lines) and after (red dashed lines) G_{Va}^{bcc}=0.2·RT was added in the dataset of Dupin et al. [28].

In order to avoid this change, the contribution of the compound energy of vacancies is compensated by subtracting this value (0.2·RT) in the interaction parameters for vacancies with the atoms. Therefore, we have included a term -0.2·RT into the coefficients $\alpha_{Al,Va}$ and $\alpha_{Ni,Va}$ of the A2 and B2 phases. With this set of parameters, all calculations for the Al-Ni system lead to the same results as the original dataset of Dupin et al. [28]. The corresponding phase diagram is shown in Fig. 4-2 and the corresponding parameters are listed in the appendix.

4.3. Re-optimization of the Al-Mo system

Despite of the artifacts in the description of Cupid et al. [84], the modeling for the solid phases in Ref. [84] can reproduce the corresponding experimental data very well. Therefore, in the present work, the thermodynamic description developed by Cupid et al. [84] was used as the starting dataset for the re-optimization in the present work.

Generally speaking, the methods to eliminate the inverted miscibility gap can be divided into three types. They are: a) finding or creating a physically feasible model, b) adopting the Kaptay's models [96, 97] and c) applying the topological constraint method of Malakhov and Balakumar [98, 99] .

In principle, finding or creating a physically feasible model would be the most reasonable approach to eliminate the inverted miscibility gap. Nevertheless, in practice, it is difficult to find or create a new model. Even though a new model is available, applying the new model to certain phase in certain system may cause the compatibility problems of this system with others.

Kaptay's models [96, 97] are other resources that can be considered to eliminate the inverted miscibility gap. Two models, exponential model [96] and combined model [97], were developed by Kaptay to describe the temperature dependence of the excess Gibbs energy of solutions. The exponential model is shown in Eq. (3-1). Later, Kaptay further improved exponential model to a combined model (Eq. (3-2)) as he realized the exponential model may lead to artifacts at low temperature.

$$^{E}G_{m} = \sum_{i=1}^{n-1}\sum_{j=i+1}^{n} x_i x_j L_{ij} = \sum_{i=1}^{n-1}\sum_{j=i+1}^{n} x_i x_j \, h_e \exp\left(-\frac{T}{\tau_e}\right) \quad (3\text{-}1)$$

$$^{E}G_{m} = \sum_{i=1}^{n-1}\sum_{j=i+1}^{n} x_i x_j L_{ij} = \sum_{i=1}^{n-1}\sum_{j=i+1}^{n} x_i x_j \, (h_c - \mathrm{T}s_c) \exp\left(-\frac{T}{\tau_c}\right) \quad (3\text{-}2)$$

Where subscripts e and c stand for the exponential model and combined model, respectively. h (J/mol) and s (J/mol·K) are the enthalpy- and entropy terms. τ (τ = h/s) is a special temperature, at which the value of interaction parameter will change its sign.

To apply the combined model into the modeling of a phase, a complete CALPHAD assessment using the linear model (L=a-bT) with the temperature-dependent interaction parameters should be

carried out firstly. Next, the τ and z ($z = \tau/T_{exp}$) (T_{exp} is the average experimental temperature) should be calculated to define the type of the system according to the classification defined in Ref. [97]. After that, different strategies to obtain h_c and s_c can be determined. For example, if τ>0, z>1, h_c and s_c can be calculated by the following equations:

$$k = \frac{z}{4} - \frac{1}{2} + \frac{1}{2}\sqrt{\frac{z^2}{4} + z - 1} \tag{3-3}$$

$$\tau_c = k\tau/z \tag{3-4}$$

$$s_c = \frac{s}{k}(1 + k - z)\exp\left(\frac{1}{k}\right) \tag{3-5}$$

$$h_c = \frac{h}{kz}(1 + kz - z)\exp\left(\frac{1}{k}\right) \tag{3-6}$$

The third choice is the topological constraint method of Malakhov and Balakumar [98, 99]. In this method, no new model is required. It makes it possible to take into account not only the critical evaluated data from literature but also the knowledge about the behavior of the Gibbs energies and phase boundaries into the thermodynamic optimization. For example, the constraint, $f(x) = \partial^2 G/\partial x^2, f(x) > 0$, can be applied as hypothetical experimental data in the POP file to suppress the miscibility gap during optimization. The condition $f(x) = \partial^2 G/\partial x^2, f(x) > 0$ means that the liquid phase is stable and a miscibility gap will not be produced [100]. Condition, $f(x) = \partial T/\partial x$, $f(x) < 0$, can be applied in the optimization to ensure that a reasonable shape of the phase boundary can be obtained. The topological constraint method is straightforward, easy-to-use and also effective.

In the following part, both the combined model from Kaptay and the topological constraint method of Malakhov and Balakumar will be tested in the modeling of the liquid phase.

4.3.1. Optimization results and discussion

4.3.1.1. Using combined model from Kaptay

The possibility to reproduce the congruent melting of the AlMo phase but without producing any artifacts in this system will be explored in this part.

With the binary interaction parameters of the liquid phase in Ref. [84], the τ and z were calculated and the requirements, τ>0, z>1, were fulfilled. Therefore, Eqs. (3-3) to (3-6) were adopted to calculate the h_c and s_c (T_{exp} was set to 1800 K). Fig. 4-8 shows the calculated Al-Mo phase diagram using the dataset of Cupid et al. [84], in which original interaction parameters of the liquid phase were converted into the parameters of the combined model developed by Kaptay [97]. As we can see, only the experimental data in the vicinity of 1800 K are well reproduced. The liquid

phase re-stabilizes at low temperature and the calculated peritectic formation temperature (2153 K) of the $AlMo_3$ phase is much lower than the experimental data (2423±100 K).

Thus, further efforts were made to adjust the interaction parameters of the liquid phase to the invariant reaction temperatures and mixing enthalpies of the liquid phase as well as the liquidus lines. Then, the parameters of the liquid phase were fixed and the interaction parameters of the Al-rich intermetallic compounds were optimized to fit the liquidus temperatures and the reaction temperatures. In the final step, all parameters for the system Al-Mo were re-optimized simultaneously.

Figs. 4-9 and 4-10 show the calculated complete phase diagram and partial phase diagrams of the Al-Mo system, respectively. Very good agreement between the calculation results and experimental data was obtained. The congruent melting of the AlMo phase was successfully reproduced. No artifact exists in this system. The corresponding parameters for the liquid phases are listed Table 4-4.

Table 4-4 Interaction parameters of the liquid phases modeled with the combined model from Kaptay [97].

Parameters	Values
${}^{0}L_{Al,Mo}^{Liq}$	(-207561.20+82.87*T)*exp(-T/4825.8)
${}^{1}L_{Al,Mo}^{Liq}$	(-56305.69+478.38*T)*exp(-T/597.5)
${}^{2}L_{Al,Mo}^{Liq}$	-121000.00*exp(-T/1687.3)
${}^{3}L_{Al,Mo}^{Liq}$	60000.00*exp(-T/637.6)

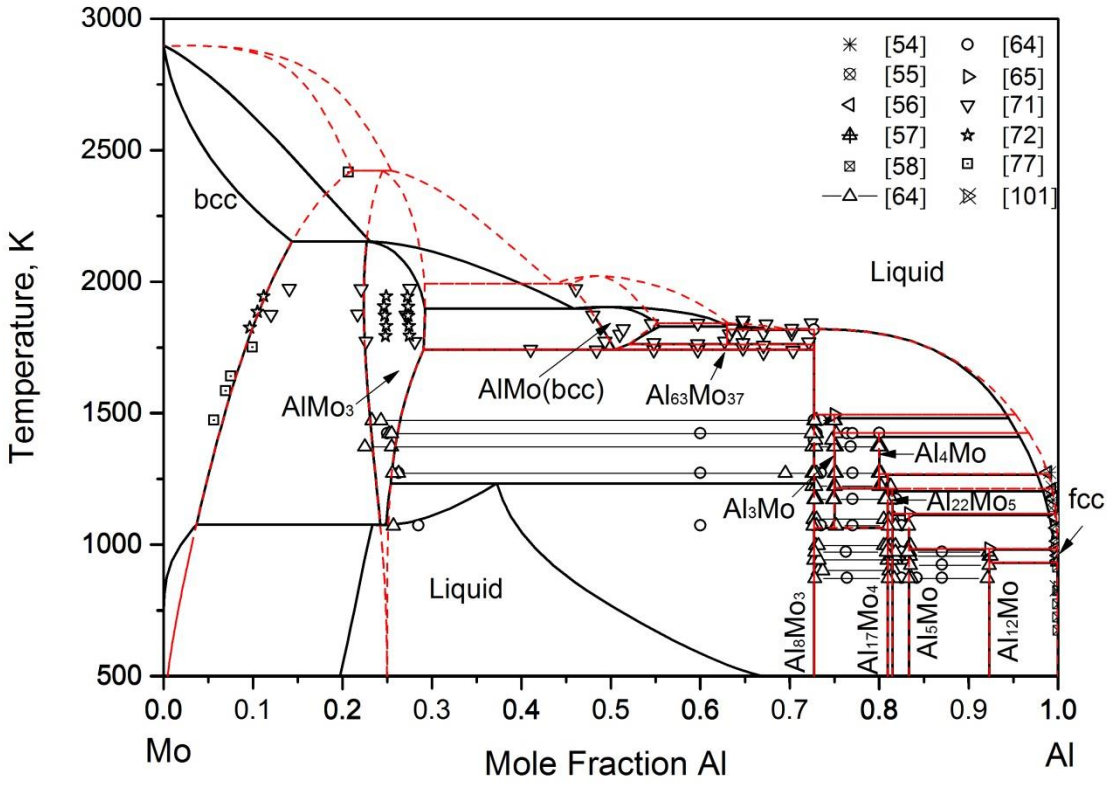

Fig. 4-8 Calculated phase diagram (solid lines) of the Al-Mo system using the dataset of Cupid et al. [84], in which original interaction parameters of the liquid phase was converted into the parameters of the combined model developed by Kaptay [97]. The original description of Cupid et al. [84] (dashed lines) and the experimental data are superimposed.

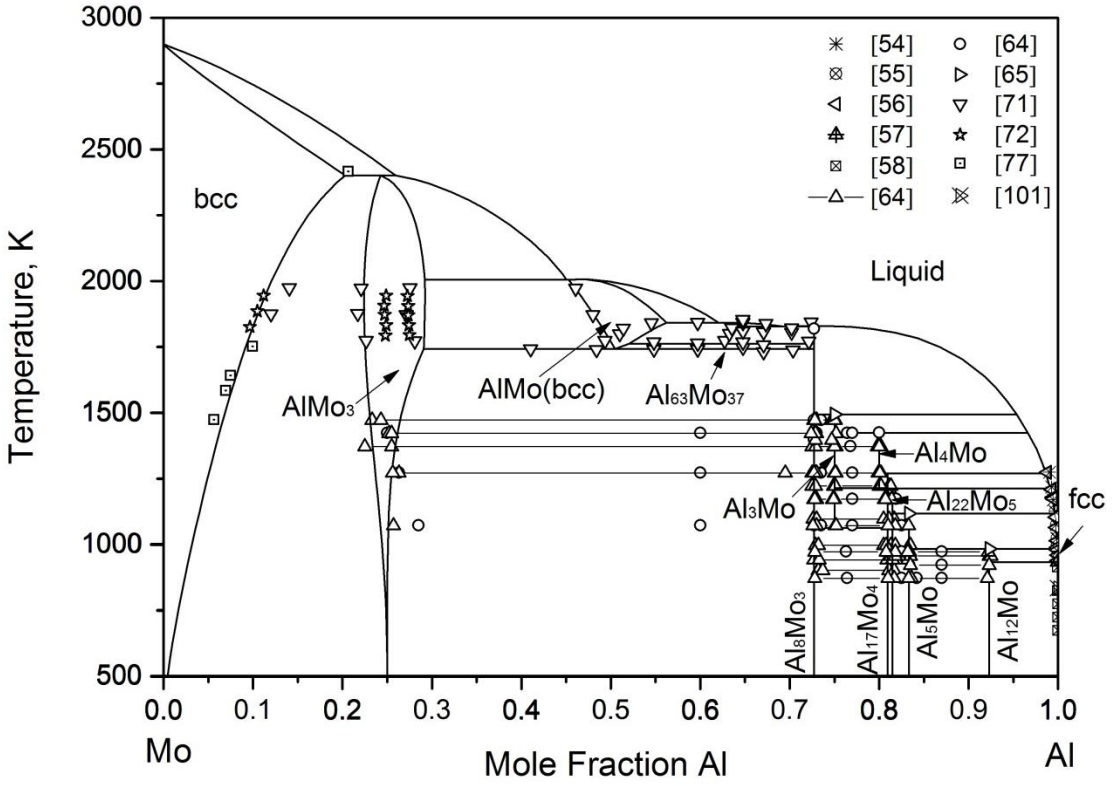

Fig. 4-9 Calculated phase diagram of the Al-Mo system using the present thermodynamic description, in which the liquid phase was remodeled with the combined model from Kaptay [97].

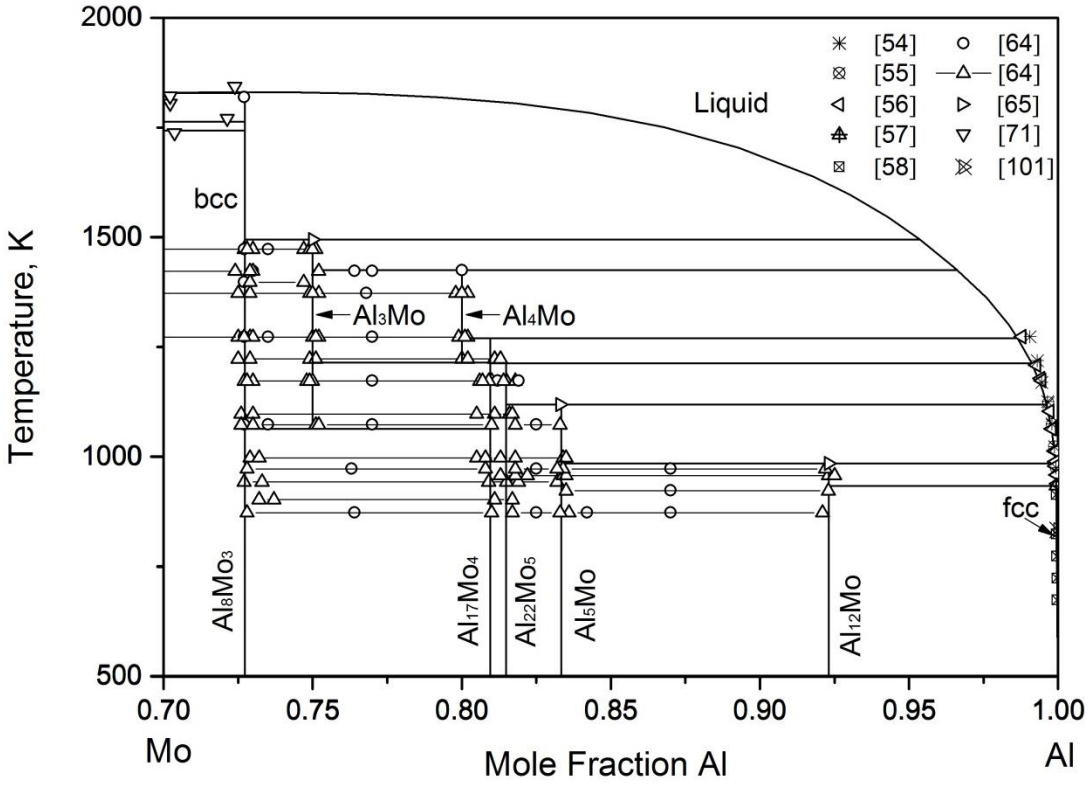

Fig. 4-10 Calculated partial phase diagram (Al-rich region) of the Al-Mo system using the present thermodynamic description, in which the liquid phase was remodeled with the combined model from Kaptay [97].

However, when this dataset was extended into the Al-Mo-Ni system by merging it and the datasets of Dupin et al. [28] (Al-Ni) and Zhou et al. [92] (Mo-Ni), a normal miscibility gap in the ternary system was produced after necessary assessment of the ternary interaction parameters of the liquid phase was performed, as shown in Fig. 4-11. As introduced in chapter 4.5, the liquidus temperatures of the NiAl-Mo alloys with up to 40 at.% Mo were measured, but no miscibility gap in the NiAl-Mo section was detected. Thus, this calculated miscibility gap is an artifact. Tremendous efforts were made to eliminate the miscibility gap but failed, which further supported the conclusion of Saunders [75, 76] that the congruent melting of the AlMo phase was thermodynamically unlikely. A peritectic formation of the AlMo phase seems to be more reasonable.

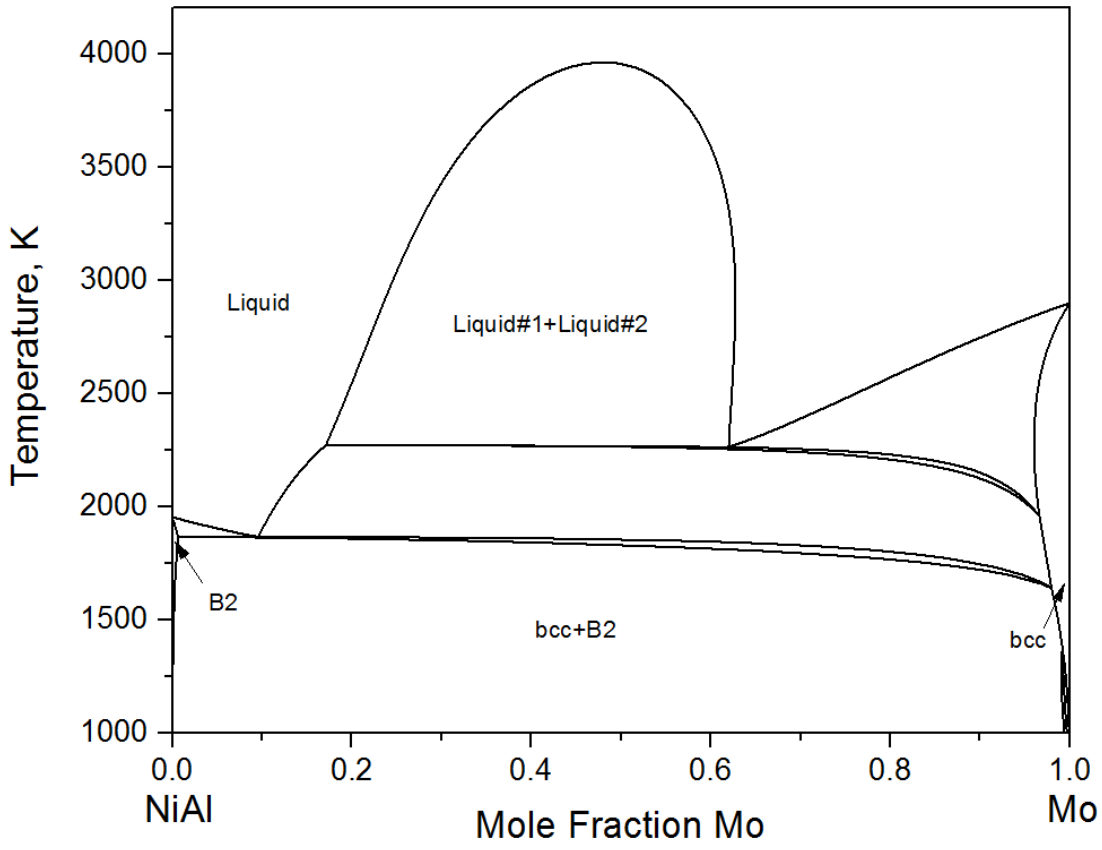

Fig. 4-11 Calculated NiAl-Mo section using the present thermodynamic description, in which the liquid phase was modeled with the combined model from Kaptay [97].

4.3.1.2. Using topological constraint method of Malakhov and Balakumar

In the phase diagram of the Al-Mo system, the bcc phase occurs in two locations: a solid solution extending from the Mo-side and a small region (AlMo) in the vicinity of 50 at.% Mo. Under the condition that both parts of this phase have to be described by the same Gibbs energy function, the congruent melting point for the AlMo phase reported by Rexer [71] seems to be thermodynamically unlikely. This conclusion has already been found by Saunders [76] and the artifacts detected in the previous assessment [84] and in chapter 4.3.1.1 support this argument even more. Therefore, the congruent melting of the AlMo phase was replaced by a peritectic reaction in the present assessment.

In order to avoid the artificial miscibility gap in the liquid phase at high temperatures, we followed the topological constraint method of Malakhov and Balakumar [99]. Despite that it is impossible to directly define the second derivative of the Gibbs energy of a specific phase Φ by defining a function in the software package Thermo-Calc, the phase stability function QF(phase) is available in this software. Since QF(Φ) = $[\partial^2 G^{\Phi}/\partial(x^{\Phi})^2]/[x^{\Phi}(1-x^{\Phi})]$ and the divisor $[x^{\Phi}(1-x^{\Phi})]$, $0 < x^{\Phi} < 1$, always has a positive value, QF(Φ) always has the same sign as $(\partial^2 G/\partial x^2)$.

Therefore, it is convenient to apply the constraint $(\partial^2 G/\partial x^2) > 0$ into the optimization by forcing the QF(liquid) to be positive to suppress the occurrence of the miscibility gap in the liquid phase. In the present work, a grid of auxiliary equilibria in the liquid phase was generated at 6 temperatures between 3000 and 8000 K and at 9 compositions from 10 to 90 at.% Al with equal intervals, as illustrated in Fig. 4-12. In each of these equilibria the variable QF(liquid) was required to be positive. In the POP file of Thermo-Calc, these auxiliary equilibria are formulated as follows:

TABLE HEAD 67

CREATE-NEW-EQUILIBRIUM @@,1

CHANGE-STATUS PHASE LIQ=FIX 1

SET-CONDITION P=101325 X(AL)=@1 T=@2

EXPERIMENT QF(LIQUID)>0.0001:1E-6

TABLE_VALUES

0.10 3000

0.20000 3000.00

0.30000 3000.00

0.40000 3000.00

……..

0.80000 8000.00

0.90000 8000.00

TABLE_END

Under these constraints, the interaction parameters of the liquid phase were re-optimized to fit the temperatures of the invariant reactions in the Mo-rich region. Then, the parameters of the liquid phase were fixed and the interaction parameters of the Al-rich intermetallic compounds were adjusted in the order from Al_8Mo_3 to $Al_{12}Mo$. The liquidus temperatures as well as the invariant reactions temperatures should be reproduced. In the final step, all parameters for the system Al-Mo were re-optimized simultaneously. The revised set of the thermodynamic parameters is given in the appendix.

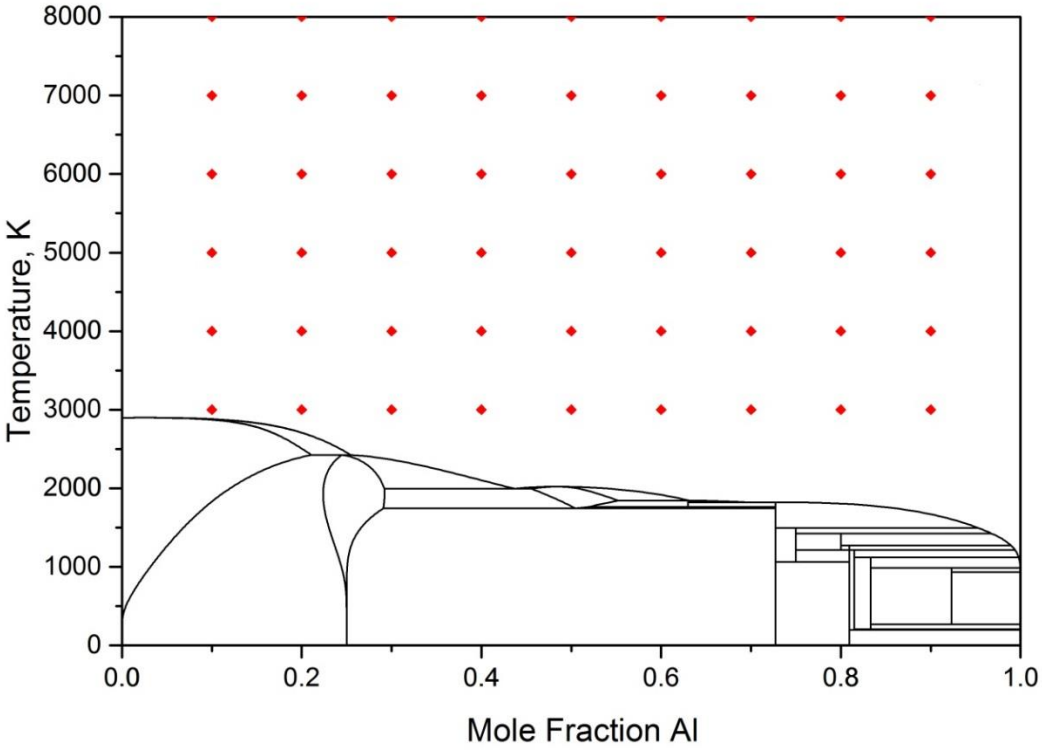

Fig. 4-12 Locations that auxiliary equilibria are applied (red diamonds).

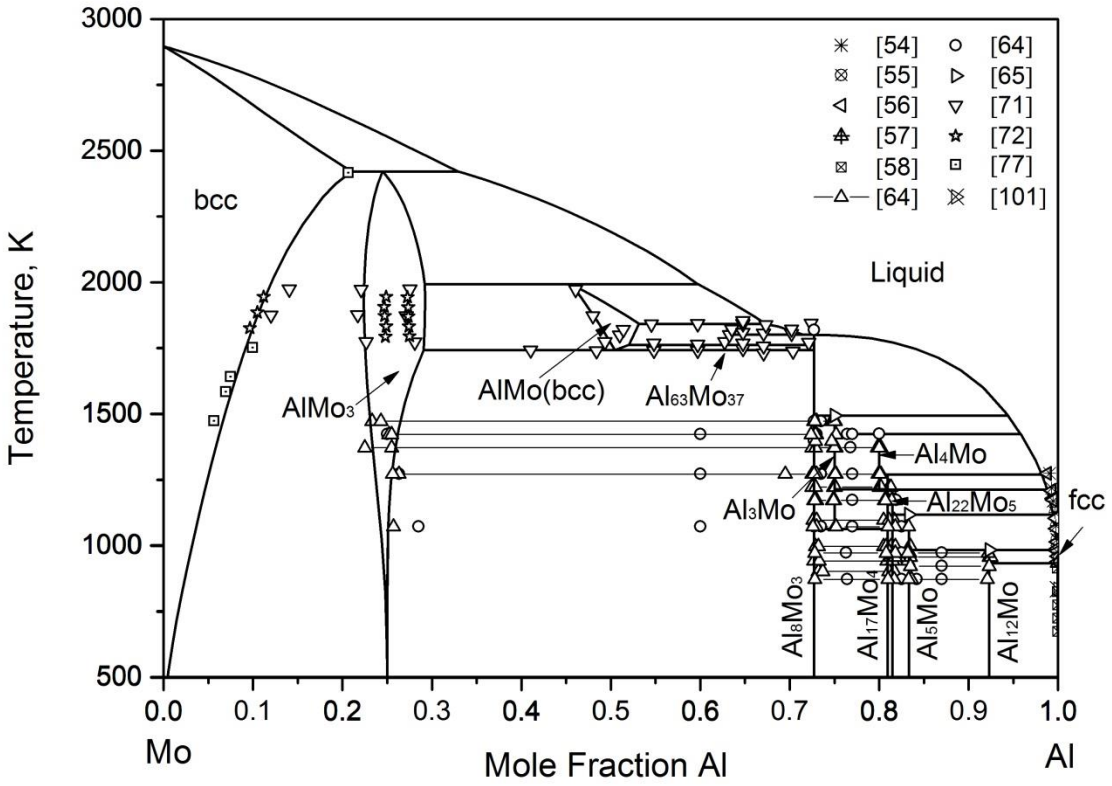

Fig. 4-13 Calculated phase diagram of the Al-Mo system using the present thermodynamic description.

Figs. 4-13 and 4-14 present the calculated complete and partial phase diagram of the Al-Mo system using the present thermodynamic description, in which the thermodynamic parameters of the bcc, $AlMo_3$ and AlMo phases were adopted from Cupid et al. [84]. The experimental data determined by Schuster et al. [65] and Eumann et al. [64] were taken into account in the optimization. The calculated phase diagram agrees well with the experimental data [54–58, 64, 65, 71, 72, 77, 101]. The congruent melting of the AlMo phase in Ref. [84] was replaced by a peritectic reaction. It is worth mentioning that the experimental data of Shilo and Franzen [72] are not correctly cited in previous works [46, 75, 83, 84]. In the present work, the original data from Shilo and Franzen [72] were used.

Fig. 4-15 shows the calculated mixing enthalpies of the liquid phase at 1700 K using the present thermodynamic description in comparsion with the experimental data [81, 81]. Within the uncertainty of the experiment, satisfactory agreement was obtained.

Table 4-5 presents the calculated invariant reaction temperatures in the Al-Mo system. Very good agreement between the calculation results and experimental data was achieved.

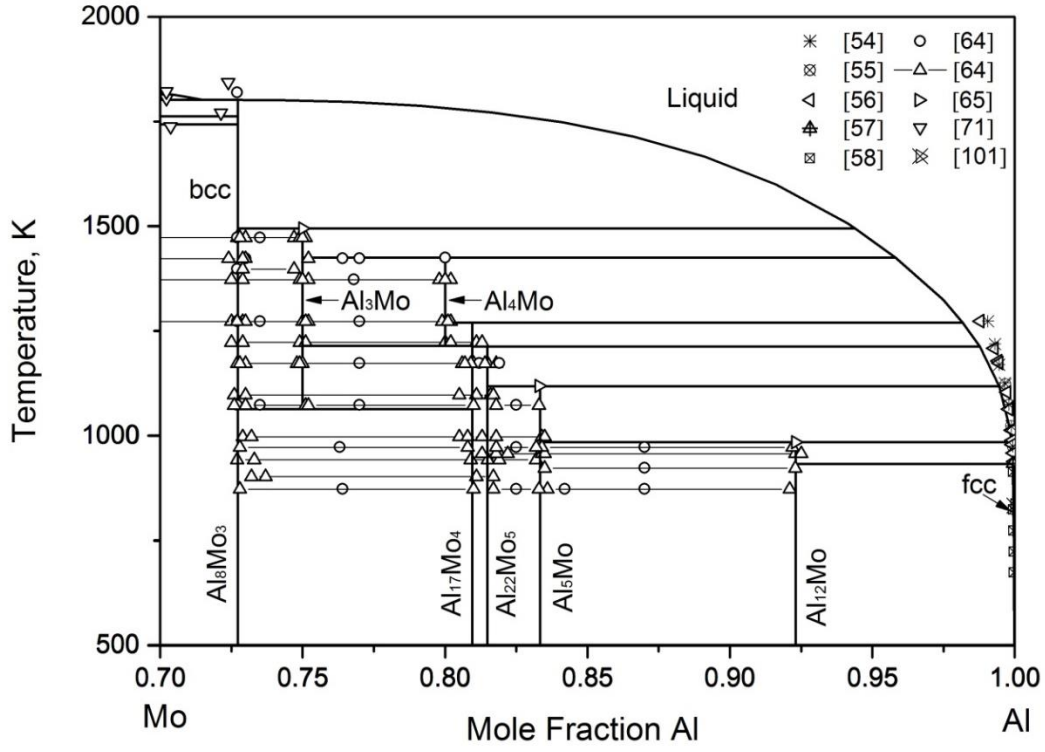

Fig. 4-14 Calculated partial phase diagram (Al-rich region) of the Al-Mo system using the present thermodynamic description.

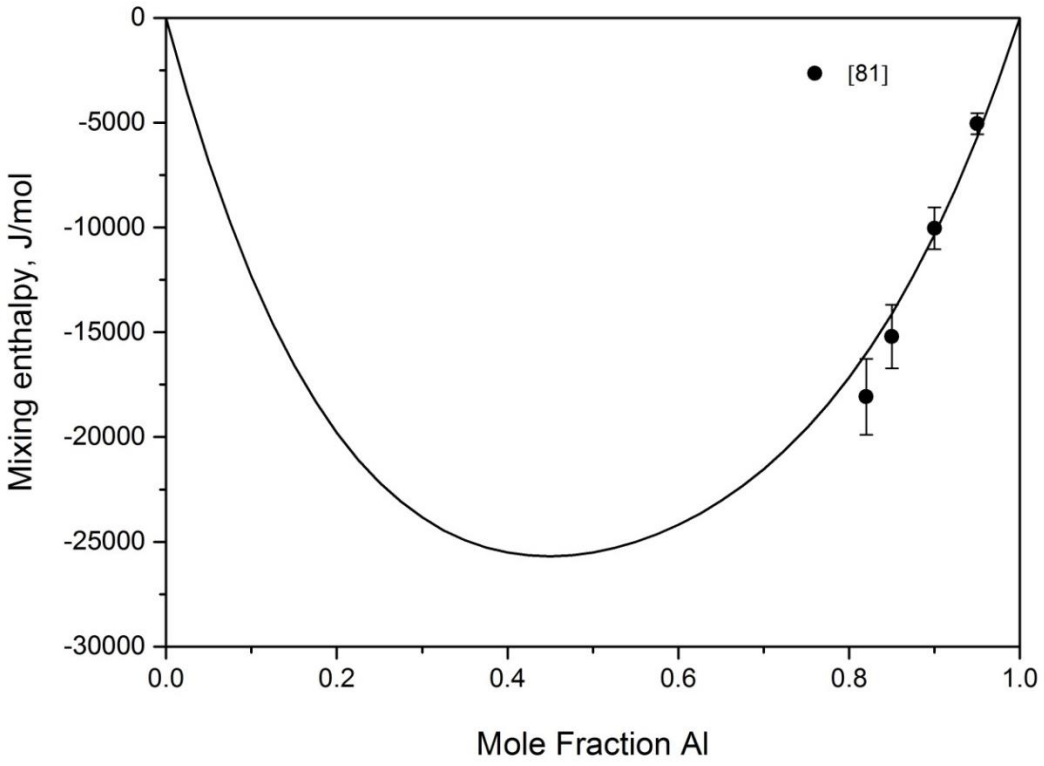

Fig. 4-15 Calculated mixing enthalpies of the liquid phase in the Al-Mo system at 1700 K using the present thermodynamic description in comparison with experimental data [81]

Table 4-5 Invariant reactions in the Al-Mo system.

Reactions	Temperatures, K	
	Present work	Literature
Liquid+bcc_(Mo)↔$AlMo_3$	2422	2423±100 [77]
Liquid+$AlMo_3$↔AlMo	1994	~1993 [71]
Liquid+AlMo↔$Al_{63}Mo_{37}$	1843	1843 [71]
Liquid↔Al_8Mo_3	1832	1828±10 K [65] 1819±3 K [64]
Liquid↔Al_8Mo_3+$Al_{63}Mo_{37}$	1802	1808 [71]
$Al_{63}Mo_{37}$↔AlMo+Al_8Mo_3	1764	1763 [71]
AlMo↔$AlMo_3$ +Al_8Mo_3	1743	1743 [71]
Al_3Mo↔$Al_{17}Mo_4$ +Al_8Mo_3	1065	<1073 [64]
Liquid+Al_8Mo_3↔Al_3Mo	1495	1495 [64]
Liquid+Al_3Mo↔Al_4Mo	1426	1425 [64]
Liquid+Al_4Mo↔$Al_{17}Mo_4$	1272	<1273 [64]
Al_4Mo↔Al_3Mo+$Al_{17}Mo_4$	1214	1215 [64]
Liquid+$Al_{17}Mo_4$↔$Al_{22}Mo_5$	1213	<1223 [64]
Liquid+$Al_{22}Mo_5$↔Al_5Mo	1118	1119 [64]
Liquid+Al_5Mo↔$Al_{12}Mo$	985	985 [64]
Liquid+$Al_{12}Mo$↔fcc_(Al)	934	934 [76]

4.4. Review of the Al-Mo-Ni system

In the Al-Mo-Ni system, most of the investigations focused on the Ni-rich corner and the Al-rich corner was studied less frequently.

Table 4-6 summarizes the experimental data for the isothermal sections and vertical sections of the Al-Mo-Ni system.

4.4.1. Isothermal sections

Complete or partial isothermal sections at 1073 [102], 1153 [103], 1200 [104], 1223 [102], 1273 [102], 1311 [104], 1323 [102], 1366 [104], 1373 [25, 103], 1444 [104], 1473 [103, 105, 106], 1533 [104], 1573 [107], 1613 [107], 1633 [107], 1653 [107] and 1663 [107] K were constructed based on the experimental data in previous works.

Five partial isothermal sections at 1573, 1613, 1633, 1653 and 1663 K were constructed by Maslenkov et al. [107]. Till now, sections at 1613, 1633, 1653 and 1663 K are still the only available isothermal sections at temperature greater than 1573 K. Several alloys with the molar fraction of Ni higher than 55 % were investigated in Ref. [107]. The phase transformation temperatures were measured by DTA and the phases were identified by XRD. Liquid phase started to appear at the Ni rich corner in the isothermal sections at 1613 K. Several tielines between the fcc and $L1_2$ phases were determined by Jia et al. [108] at 1573 K. They agree well with the results of Ref. [107].

Partial isothermal sections with the Al content lower than 40 at.% at 1533, 1444, 1366, 1311, and 1200 K were constructed by Miracle et al. [104] based on the experimental data. Five alloys with 45.1-73.9 at.% Ni were annealed for up to 2500 h. The compositions and phases were determined by EPMA and XRD.

Table 4-6 Experimental data of the isothermal sections and vertical sections of the Al-Mo-Ni system.

References	Experimental data	Experimental methods
[107]	Five partial isothermal sections from 1573 to 1663 K	DTA, XRD
[109]	Three vertical sections with the mole ratio of Al:Mo=4:3, 2:3 and 1:5	DTA, XRD
[25]	Isothermal section at 1373 K	EPMA
[110]	Several Ni-rich alloys at 1273 and 1553 K; 65 at. % Ni isopleth up to 17 at. % Al	TEM/SAD and DTA
[106]	Isothermal sections at 1473 K for 66-77 at.% Ni	XRD, EPMA
[111]	Tielines at 1073, 1273 and 1523 K	EPMA
[104]	Isothermal sections at 1200, 1311, 1366, 1444 and 1533 K	XRD, EPMA
[103]	Isothermal sections at 1153, 1373 and 1473 K	Micro X-ray spectrometric analysis
[112]	14 at. % Al isopleth	DTA, XRD
[113, 114]	fcc and $L1_2$ solvus at 1100, 1200, 1300 and 1400 K	DTA, SEM/EDX
[115]	Single alloy with $L1_2$ and Ni_3Mo at 1073 K	TEM
[108]	Tielines for $L1_2$ and fcc at 1073, 1273, 1373 1473 and 1573K Tielines for $L1_2$ and B2 at 1173, 1373 and 1573 K	EPMA
[116]	Single alloy with $L1_2$ and fcc	SAXS,TEM
[117, 118]	Alloys with $L1_2$ and fcc at 1048, 1115, 1145 and 1176 K	SAXS,TEM
[105]	Isothermal section at 1473 K	EPMA
[102]	Isothermal sections of the Al–AlNi–Al_8Mo_3 compositional range at 1073, 1223, 1273 and 1323 K; Two ternary phases	XRD, TEM, SEM/EDX

Experimentally determined partial isothermal sections of the Al-Mo-Ni system at 1473 K were available from Nash et al. [106], Maslenkov et al. [103] and Cutler [105]. Jia et al. [108] determined several tielines between the $L1_2$ and fcc phases at this temperature. The results of Nash et al. [106], Maslenkov et al. [103] and Jia et al. [108] agreed well with each other, while the homogeneity

range of the fcc phase determined by Cutler [105] was in conflict with the results of other investigations [103, 106, 108]. Therefore, the results of Cutler [105] were excluded in the present work.

Lu et al. [25] prepared two diffusion triples. One triple consisted of pure Mo, pure Ni and $Al_{51}Ni_{49}$ (at.%) alloy and another one was assembled by pure Mo, pure Ni and $Al_{73.4}Mo_{26.6}$ (at.%) alloy. The complete isothermal section at 1373 K was constructed with the tielines between the fcc and $L1_2$, B2 and $L1_2$, NiMo and $L1_2$ and fcc and NiMo as well as fcc, $L1_2$ and NiMo phases. The phase relations determined by both diffusion triples showed good agreement with each other. Partial isothermal section at 1373 K was also constructed by Maslenkov et al. [103] with their own experimental data from micro X-ray spectrometric analysis. The lowest concentrations of Ni of investigated alloys were 55 at.%. Several tielines between the $L1_2$ and fcc phases at 1373 K were also determined by Jia et al. [108]. Experimental data from Refs. [25, 103, 108] agreed well with each other and consequently phase relations in the Ni rich corner of the Al-Mo-Ni ternary system can be determined.

Partial isothermal sections of the Al-AlNi-Al_8Mo_3 compositional range at 1073, 1223, 1273 and 1323 K were determined by Grushko et al. [102]. The investigation [102] mainly focused on the phase relations that the ternary phases N and X involved.

15 alloys were prepared by Wakashima et al. [110] with arc melting and annealed at 1553 K under argon atmosphere for 157 h following by water quenching. After this, these alloys were further annealed at 1273 K for 140 h following by water quenching. The phases of the alloys after both steps were identified by transmission electron microscopy and selected-area diffraction along with optical metallography.

4.4.2. Vertical sections

Maslenkov et al. [109] measured the phase transformation temperatures of several alloys with molar ratios of Al:Mo = 4:3, 2:3 and 1:5. Two vertical sections with the molar ratios of Al:Mo = 4:3 and 2:3 were constructed. However, the liquidus surface derived from these sections is inconsistent with the liquidus surface data from Refs. [110–116]. Maslenkov et al. [109] also proposed the NiAl-Mo system is a quasi-binary system and the corresponding partial phase diagram of the NiAl-Mo section is shown in Fig. 4-16. The maximum solubility of Mo in NiAl was assumed to be ~3.2 at.%.

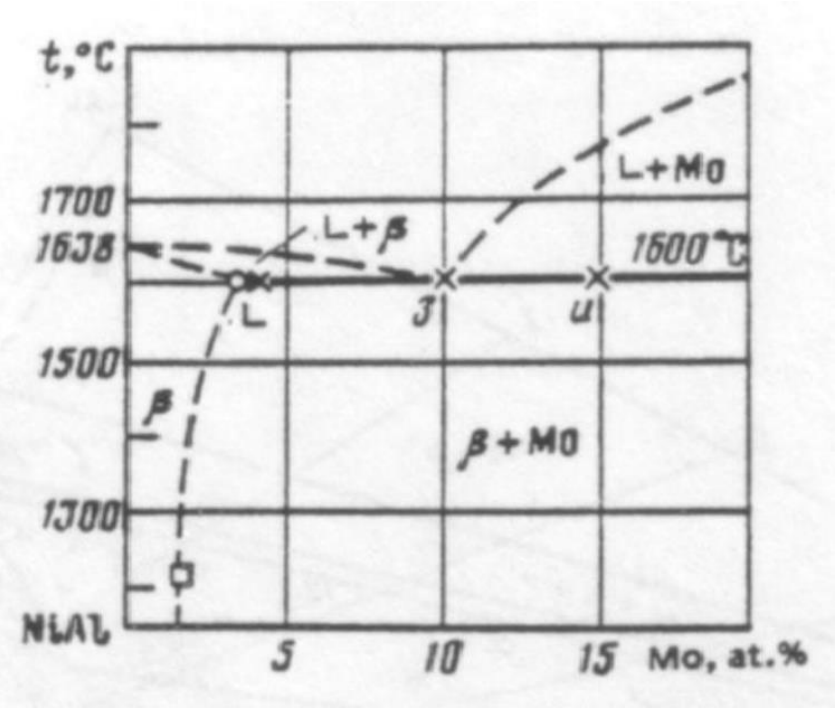

Fig. 4-16 Partial phase diagram of the NiAl-Mo system constructed by Maslenkov et al. [109].

Isopleth with 14 at.% Al was constructed by Maslenkov et al. [112] (Fig. 4-17) and the temperatures of invariant reactions, U_3: bcc+fcc↔$L1_2$+NiMo, U_4: NiMo+fcc↔$L1_2$+Ni_3Mo and U_5: Ni_3Mo+fcc↔$L1_2$+Ni_4Mo, were determined.

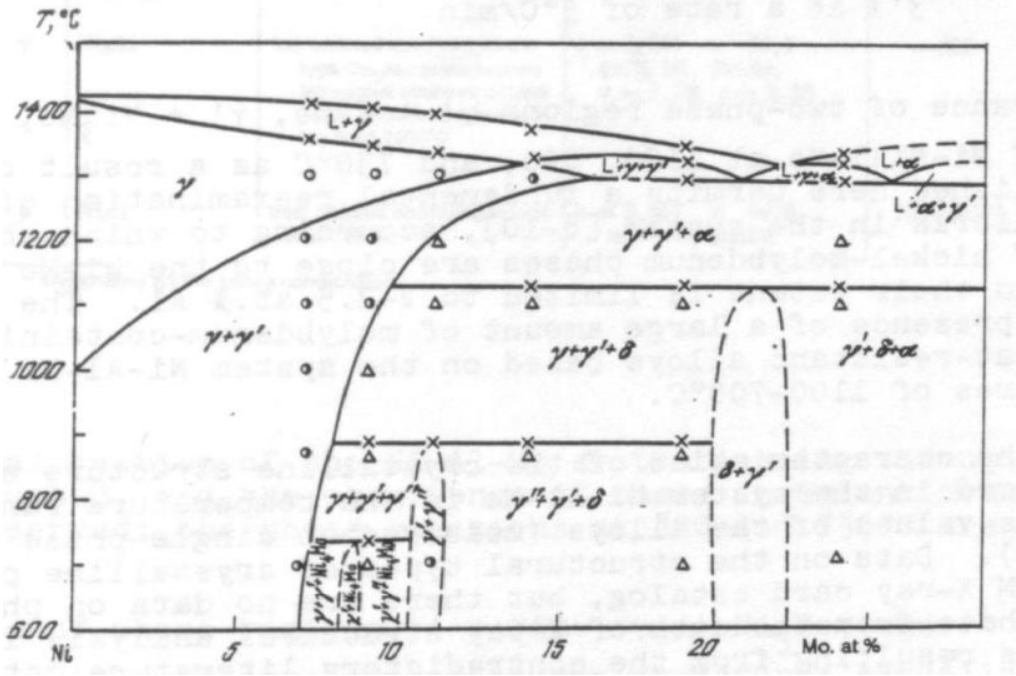

Fig. 4-17 Isopleth with 14 at.% Al was constructed by Maslenkov et al. [112].

Wakashima et al. [110] also measured the $L1_2$ solvus and melting temperatures of these alloys and constructed the 65 at.% Ni isopleth up to 17 at.% Al.

A vertical section up to 12 wt.% Al along the fcc and bcc eutectic trough of the Al-Mo-Ni system was constructed by Pearson and Lemkey [119].

4.4.3. Invariant reactions

So far, seven reactions, of which 6 reactions are invariant reactions, were reported in the subsystem Mo-NiAl-Ni and are listed in Table 4-7. The temperature and liquid composition of the reaction: Liquid↔B2+bcc were reported to be ~1753 K (9 at.% Mo) by Stover et al. [120] and 1538 K (10 at.% Mo) by Pryakhina et al. [121]. Later, the reaction temperature was corrected to be 1873±7 K by Maslenkov et al. [107, 109] and 1868 K by Ferrandini et al. [8]. The compositions of the liquid phase showed good agreement between different authors and determined to be NiAl-10 at.% Mo. The temperature of the invariant reaction U_1: Liquid+B2↔bcc+$L1_2$ was determined by Maslenkov et al. [107, 109] as 1613±10 K by DTA. Yoshizawa et al. [122] firstly reported the temperature of the invariant reaction U_2: Liquid+NiMo↔bcc+fcc as ~1585 K. This temperature was later confirmed by Maslenkov et al. [107, 109] as 1583±10 K. Yoshizawa et al. [122] also reported the temperature of invariant reaction U_3: bcc+fcc↔$L1_2$+NiMo to be ~1468 K, which is considerably higher than that determined later by Wakashima et al. [110] (~1403 K), Miracle et al. [104] (1400±2 K) and Maslenkov et al. [112] (1403±5 K). The reactions U_4: NiMo+fcc↔$L1_2$+Ni_3Mo and U_5: Ni_3Mo+fcc↔$L1_2$+Ni_4Mo were discovered by Maslenkov et al. [112] occurring at 1163±5 and

1003 K, respectively. Pearson and Lemkey [119] reported the ternary eutectic reaction E: Liquid↔fcc+B2+bcc occurring at 1573 K. Aigeltinger [123], Wakashima et al. [110] and Nash et al. [106] accepted this temperature but replaced B2 with $L1_2$. This modification was later confirmed by Maslenkov et al. [107, 109].

4.4.4. Liquidus projection

Pearson and Lemkey [119] investigated a series of alloys with the compositions along the ternary eutectic trough of the Al-Mo-Ni system in the Ni-rich corner. The liquidus and solidus temperatures as well as the $L1_2$ solvus were measured. It was reported, starting from the binary NiMo and fcc_(Ni) eutectics, an eutectic reaction between the fcc and NiMo phases maintained in the ternary system until ~ 2.5 wt.% Al. At this point, the eutectic reaction between the bcc and fcc phases began and persisted until 7.5 wt.% Al. The primary solidification phases of these alloys as well as the eutectic compositions were also determined. Experimental data from DTA indicate the eutectic temperatures along the bcc and fcc eutectic trough keep almost constant as 1573 K. Nesterovich et al. [124], Henry [125], Sprenger et al. [126], Yoshizawa et al. [122], Kovacova [127] and Svetlov et al. [128] also studied the microstructure of several alloys located at or near monovariant lines. The primary phases and eutectic composition were determined. The results from these investigations [119, 122, 124–128] agree well with each other. The eutectic composition and temperature of the NiAl-Mo section determined by Maslenkov et al. [107, 109], Ferrandini et al. [8] are good supplements for the investigation of the liquidus projection in this system. In chapter 4.6, these data together with the experimental results from present work are compared with the calculated monovariant lines of the liquidus surface.

4.4.5. Ternary phases

Three ternary phases were reported in the Al-Mo-Ni system. A ternary phase designated ψ was reported by Guard and Smith [129] having the composition $Al_{34.5}Mo_{7.5}Ni_{58.0}$ (at.%), but it was not observed by Virkar and Raman [130]. They detected this phase in alloys prepared from Ni with a low purity of 99.8% and concluded that the ψ phase should belong to the Mo-Ni-Si system. A $TiAl_3$ type ternary phase, Al_5Mo_2Ni, was firstly observed by Raman and Schubert [131, 132] in the alloy $Al_{50}Mo_{25}Ni_{25}$ (at.%) after the sample was equilibrated at 1173K. Later, it was confirmed by the works of Refs. [102, 130, 133] and denoted as N phase [133]. Virkar and Raman [130] reported the homogeneity range of the N phase was about 4 to 12 at.% Ni along a constant (25 at.%) Mo line, while Grushko et al. [102] found the homogeneity range of the N pahse was between 1.6 and 6.0 at.% Ni in the as-cast samples and this range narrowed after annealing. Another ternary phase, X, with the composition $Al_{77}Mo_5Ni_{18}$ (at.%) was observed by Markiv et al. [133] firstly. Recently, Grushko et al. [102] revised this composition to $Al_{75.1}Mo_{10.7}Ni_{14.2}$ (at.%) and determined its crystal system and lattice parameters. The ternary phase, X, has a very narrow composition range and melts at 1288 K congruently. Fig. 4-18 shows the partial isothermal sections at 1323 K, 1273, 1223

and 1073 K of the Al-Ni-Mo phase diagram constructed by Grushko et al. [102]. The phase equilibria involving the N and X phase were determined.

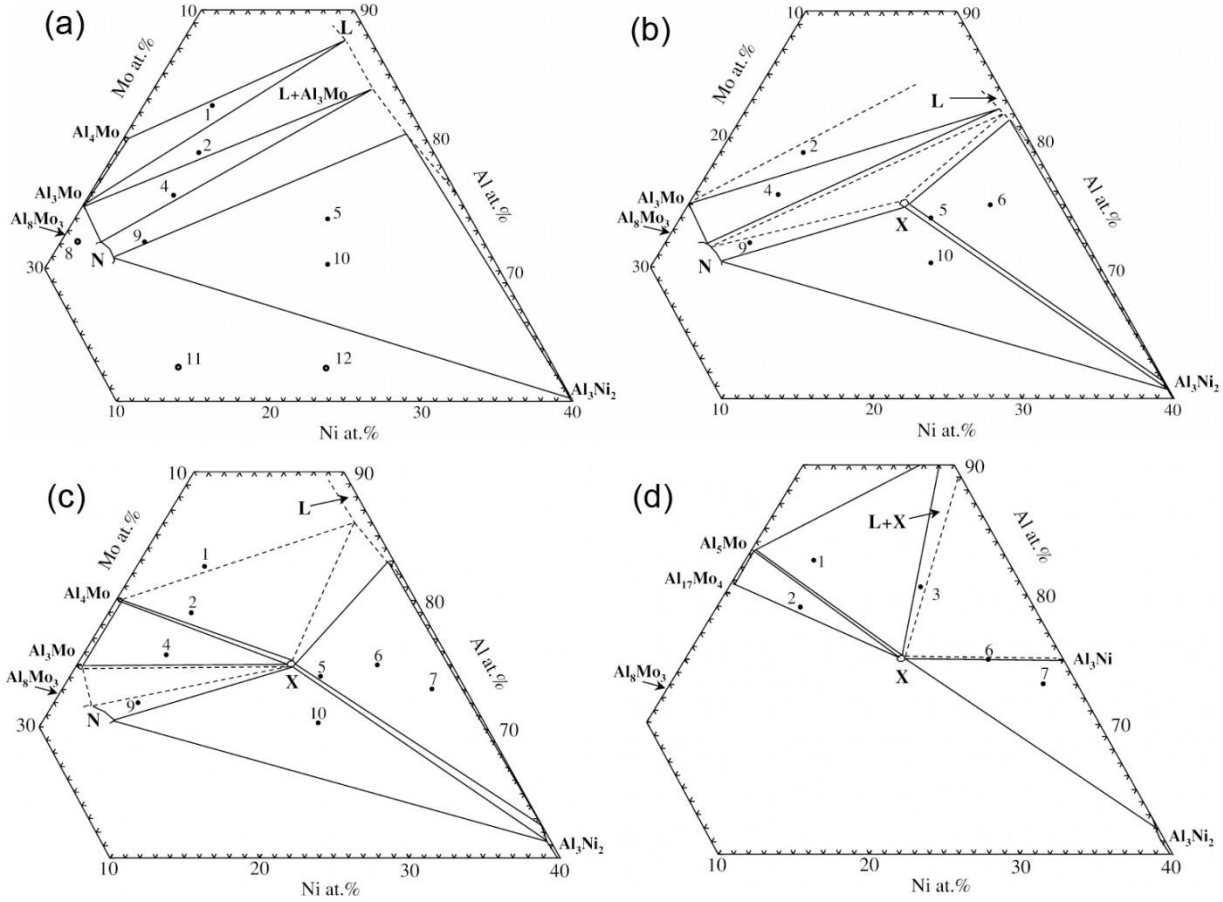

Fig. 4-18 Partial isothermal sections at (a) 1323, (b) 1273, (c) 1223 and (d) 1073 K of the Al-Ni-Mo phase diagram constructed by Grushko et al. [102].

4.4.6. Thermodynamics

No experimental thermodynamic data for the Al-Mo-Ni system are available. Recently, Zhou et al. [26] calculated the zero-Kelvin energies of the N phase and the unstable end-members of the B2 and Ni_3Mo phases as well as the fcc_(Al), fcc_(Ni) and bcc_(Mo) phases with first-principle calculations. Thermodynamic modeling of the Al-Mo-Ni system were performed by Kaufman and Nesor [82], Lu et al. [25] and Zhou et al. [26]. In the pioneering work by Kaufman and Nesor [82], all solid phases were treated as stoichiometric compounds. Later, more sophisticated thermodynamic assessments of the binary systems Al-Ni, Al-Ni and Ni-Mo were published and more experimental data of the ternary system Al-Mo-Ni were available. Based on these improvements, Lu et al. [25] re-assessed the Al-Mo-Ni system and significant improvements were achieved. Recently, Zhou et al. [26] adopted the data from first-principle calculations and

developed a new thermodynamic description for the Al-Mo-Ni system, in which the ternary phases, N and X, were also included. Nonetheless, the phase diagrams calculated with these databases [25, 26] disagreed to some extent with the critical evaluated phase diagram accepted in this work, especially with regard to the liquidus projection and the NiAl-Mo section.

4.5. Experimental investigation

As shown in Fig. 4-11, a normal miscibility gap presents in the calculated phase diagram of the NiAl-Mo section. To clarify if this miscibility gap really exists or not, more experimental investigation on this section must be performed. In addition, to construct the phase diagram of the NiAl-Mo section, the solubility of Mo in NiAl should be determined by experiments.

4.5.1. Sample preparation

High-purity Aluminum shot (99.99 wt.%), Nickel shot (99.95+ wt.%) and Molybdenum wire (99.95 wt.%) from Alfa Aesar GmbH & Co KG, Germany, were used as starting materials.

A series of NiAl-*x*Mo (*x*=0, 0.1 0.3, 3, 6, 10, 15, 20, 25, 30, 35 and 40 at.%) alloys were prepared in an arc-melting furnace (AM0.5, Edmund Bühler) with a non-consumable tungsten electrode under argon atmosphere. To ensure compositional homogeneity, each alloy button was turned over and remelted at least five times. Typically Ingot weights were of about 2 g. Nominal compositions of these alloys were accepted, because the weight loss after melting was less than 0.8 wt. %. All alloys were equilibrated at 1773 K for 50 h under flowing argon. Again, for all the alloys, no significant mass loss occurred. To determine the solubility of Mo in NiAl at 1773 K, alloys NiAl-*x*Mo (*x*=0.1 and 0.3 at.%) were quenched in water. The rest alloys were cooled by furnace cooling and the phase transformation temperatures were measured.

4.5.2. Characterization methods

A scanning electron microscope (SEM)(FEI XL30S, PHILIPS) was used to observe the microstructure of the samples. The normal spectral emissivity (NSE) of NiAl, the liquidus temperature ($T_{liquidus}$) and solidus temperature ($T_{solidus}$) of the alloys were measured with a laser heating-fast pyrometry apparatus under a protective atmosphere of Ar+8 vol.% H_2 of the pressure 0.35 MPa. In the present work, the NSE of NiAl (ε_{NiAl}) was successively used as a reference for the other alloys measured. The evaluated temperature *T* was then obtained for all the investigated compositions by correcting the experimental radiance temperature with the obtained ε_{NiAl} within Wien's approximation. The approximation of neglecting emissivity effects of Mo in the studied alloys resulted in an additional error, which was duly taken into account in the definition of uncertainty bands.

4.5.3. Results of the quenching experiment

Fig. 4-19 shows the microstructure of as-cast NiAl-0.1 at.% Mo and -0.3 at.% Mo alloys and both alloys after equilibrating at 1773 K following by water quenching. In Fig. 4-19a and 4-19c, small amount of primary bcc (Mo) phase can be observed in the as-cast alloys. After equilibrated at 1773 K for 50 h, the bcc (Mo) phase in both alloys did not totally dissolve into the NiAl phase but aggregated into bigger particles (Fig. 4-19b and 4-19d), which indicated the solubility of Mo in the NiAl phase was lower than 0.1 at.% at 1773 K.

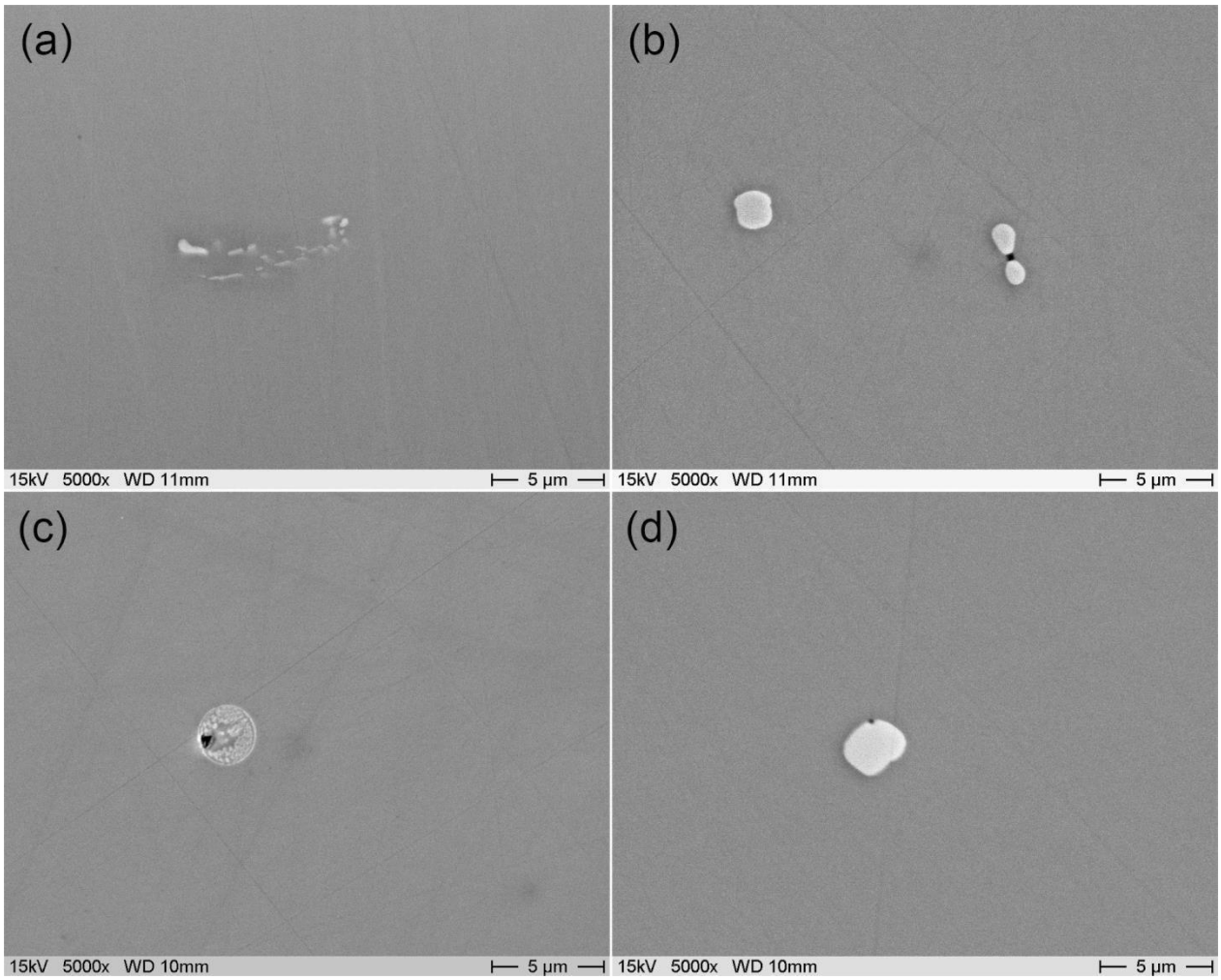

Fig. 4-19 Microstructure of as-cast alloys and alloys after quenching. (a) as-cast NiAl-0.1 at.% Mo alloy, (b) NiAl-0.1 at.% Mo alloy after water quenching, (c) as-cast NiAl-0.3 at.% Mo alloy and (d) NiAl-0.3 at.% Mo alloy after water quenching.

4.5.4. Results of the laser heating experiment

Fig. 4-20 shows the measured normal spectral emissivity of NiAl (ε_{NiAl}) as a function of the wavelength λ. The value obtained for ε_{NiAl} at the pyrometer wavelength (0.652 μm) is 0.48.

Fig. 4-21 shows the surface of the NiAl-6 at.% Mo alloy after laser heating experiment for 3 times. During the measurement, only part of the sample was melted. The heating spot was about 0.35-0.5 mm in diameter and the molten zone was about 4-5 mm in diameter. Fig. 4-22 shows the longitude section of the NiAl-6 at.% Mo alloy. A cone shape molten zone with the depth of about 0.75 mm was formed during the experiment. This molten zone is surrounded by the unmelted alloy. The unmelted area acted as a crucible during measurement, so the influence of external contamination or reaction between the sample and crucible can be eliminated during experiments.

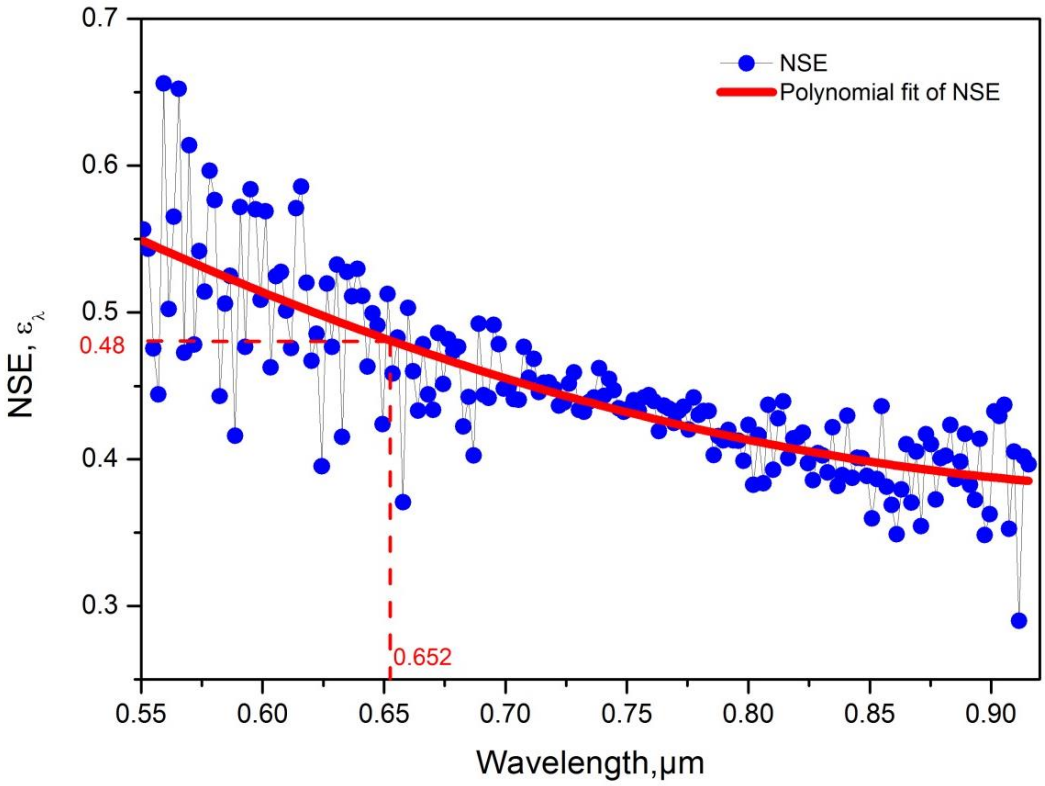

Fig. 4-20 Normal spectral emissivity of NiAl as a function of the wavelength.

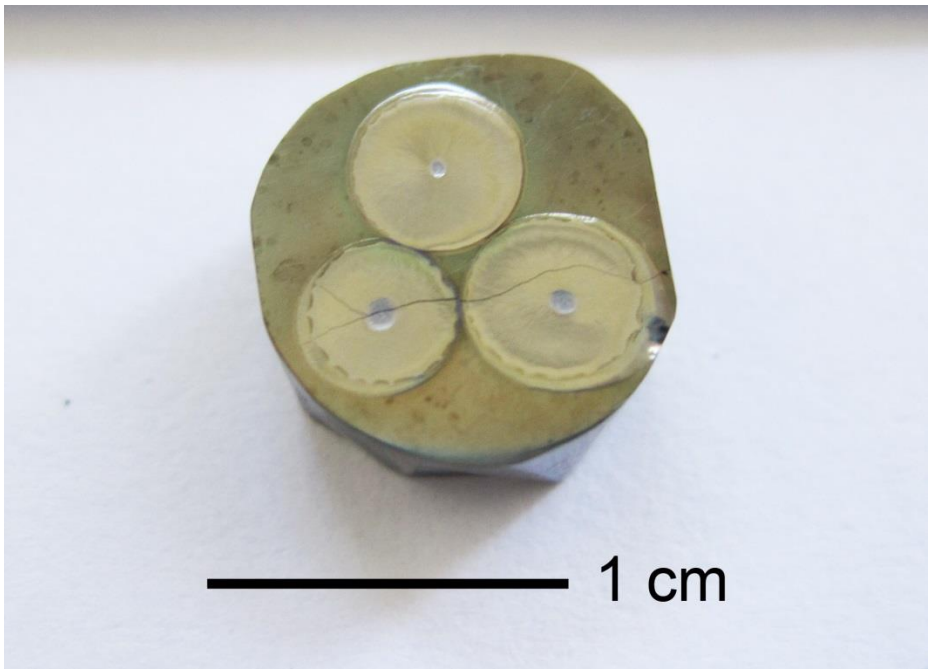

Fig. 4-21 Surface of the NiAl-6 at.% Mo alloy after experiment.

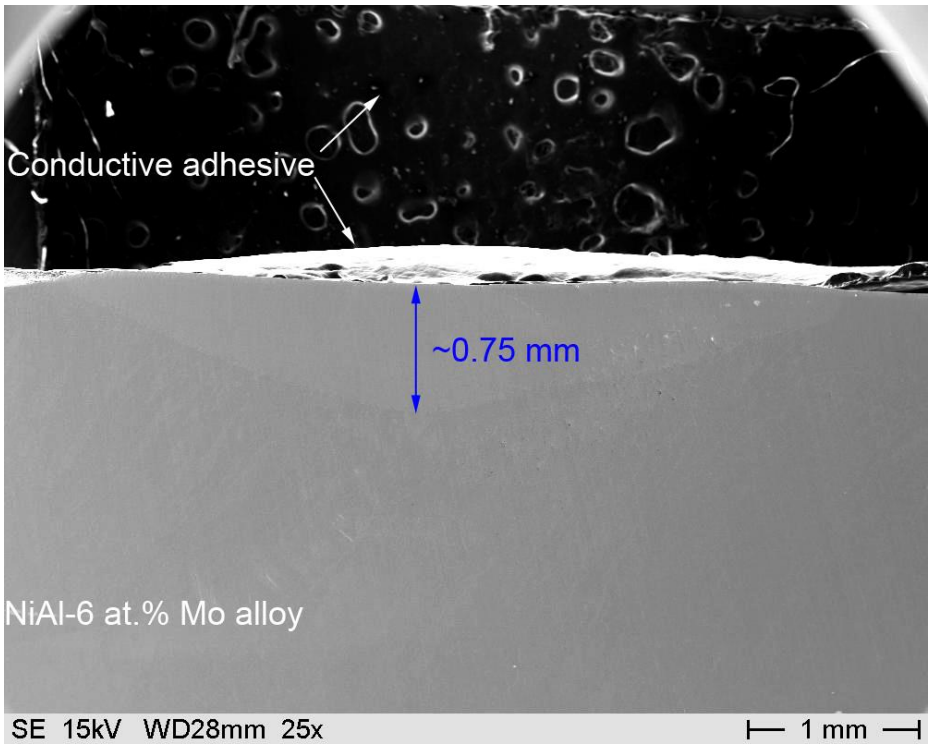

Fig. 4-22 Longitude section of the NiAl-6 at.% Mo alloy after experiment.

Fig. 4-23 shows the reflected light signal (RLS) profile, thermogram and laser power intensity profile of the NiAl-30 at.% Mo alloy measured by the laser heating-fast pyrometry apparatus as an example. Before the laser started, the RLS curve kept constant because the morphology of the sample surface did not change. Once the laser started and the temperature of the sample surface reached the solidus temperature, the sample began to melt, which resulted in a sudden change (a spike) in the RLS profile. After the laser stopped, the sample cooled naturally. When the temperature reached the liquidus temperature, primarily solidified phase formed and extra heat was emitted, which resulted in an inflection in the thermogram. Next, a plateau appeared in the thermogram when the temperature reached the solidus temperature and the second solid phase started to form. After the last drop of liquid solidified, the samples surface froze. Consequently, the RLS curve stabilized again. The $T_{solidus}$ and $T_{liquidus}$ measured in this work are listed in Table 4-7. The results agree well with the experimental data in literature [8, 107, 109]. Due to the small difference between $T_{solidus}$ and $T_{liquidus}$, their signals cannot be separated in the range below 20 at. % Mo in these experiments. Table 4-7 $T_{solidus}$ and $T_{liquidus}$ measured in this work, K. *x* is the mole fraction of Mo in the samples.

x	3	6	10	15	20	25	30	35	40
$T_{solidus}$	1874 ±20	1868 ±23	1862 ±22	1857 ±22	1915 ±24	1912 ±33	1899 ±29	1904 ±26	1914 ±22
$T_{liquidus}$	-	-	-	-	-	1994 ±41	1955 ±46	2035 ±35	2068 ±30

In these experiments, the samples were heated up to around 3000 K, but signals related to the transitions that may occur at about 2250 K (see Fig. 4-11) were not detected for all the samples. Therefore, it can be concluded that the miscibility gap in Fig. 4-11 is an artifact and no miscibility gap exists in the NiAl-Mo section.

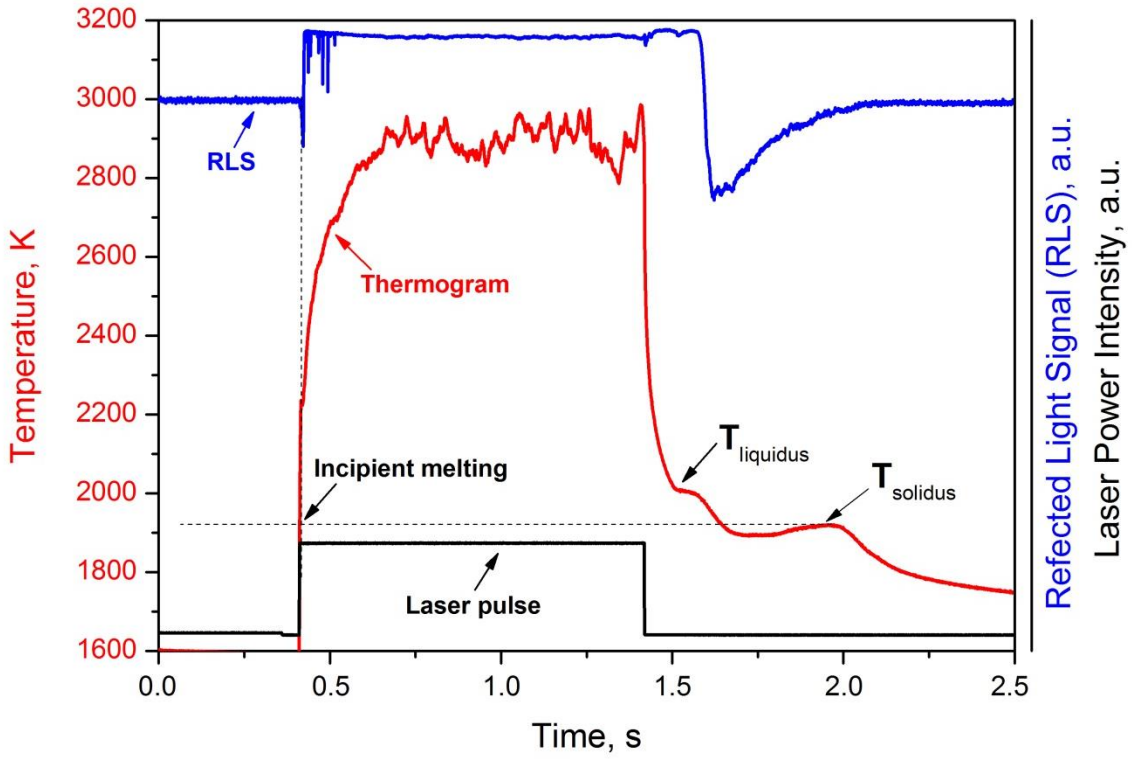

Fig. 4-23 Thermogram, reflected light signal (RLS) profile and laser power intensity profile of the NiAl-30 at.% Mo alloy measured by the laser heating-fast pyrometry apparatus.

4.6. Re-optimization of the Al-Mo-Ni system

4.6.1. Optimization procedure

The starting database is a combination of the Mo-Ni database from Zhou et al. [92], the Al-Ni database developed in chapter 4.2 and the Al-Mo database developed in chapter 4.3.1.2.

Firstly, the ternary interaction parameters, ${}^{0}L_{Al,Mo,Ni}^{fcc-A1}$, ${}^{1}L_{Al,Mo,Ni}^{fcc-A1}$ and ${}^{2}L_{Al,Mo,Ni}^{fcc-A1}$, of the fcc phase without temperature dependence were optimized to fit the equilibria with the NiMo and bcc phases at 1473 K [103]. Then the temperature dependence of the ternary interaction parameters of the fcc phase was considered and the parameters were adjusted to the equilibria with the NiMo and bcc phases at 1373 and 1473 K [25, 103]. Further optimization of these parameters was made to fit the experimental data [110, 117] at other temperatures. Next, the parameters of the fcc phase were fixed. The bonding energies, u_{AlMoNi}^{1}, u_{AlMoNi}^{2} and u_{AlMoNi}^{3} , of the $L1_2$ phase were adjusted to the solubility of Mo in the $L1_2$ phase [25, 103, 106, 111] as well as the equilibria with the $L1_2$ and bcc phases [25, 108]. After that, the ternary interaction parameter, ${}^{0}L_{Al,Mo,Ni}^{bcc-A2}$, of the bcc phase was optimized to fit the solubility of Mo in NiAl (B2) [25, 103, 108], because the B2 phase is the ordered state of the bcc phase. In the following steps, the compound energies, G(NiMo,Ni:Al:Mo),

G(Ni_3Mo,Ni:Ni:Al) and G(Ni_4Mo,Ni:Al) with temperature dependence were optimized in order to reproduce the temperatures of the invariant reactions, U_3 [104, 110, 112], U_4 [103, 112] and U_5 [103, 112] successively. Next, the parameters of the ternary phases N and X developed by Zhou et al. [26] were adopted. The agreement between the calculated results and the experimental data [102, 133] in the Al-rich region was investigated. Then, ternary interaction parameters of the liquid phase, ${}^0L^{Liq}_{Al,Mo,Ni}$, ${}^1L^{Liq}_{Al,Mo,Ni}$ and ${}^2L^{Liq}_{Al,Mo,Ni}$, were optimized to fit the experimental results obtained in the present work as well as the solidus and liquidus temperatures determined by Maslenkov et al. [112] and the temperatures of invariant reactions that the liquid phase involved [107, 109]. To compensate the contribution of the compound energy of vacancies, the coefficients $\alpha_{Mo,Va}$ and $\alpha_{Mo,Va}$ of the bcc and B2 phases as well as the interaction parameters ${}^0L^{bcc-A2}_{Mo,Va}$ were introduced in this system. The same as the treatment in chapter 4.2, the term -0.2·RT was subtracted from the coefficients $\alpha_{Mo,Va}$ to avoid any change to the calculated phase diagram. Finally, all ternary parameters were re-optimized simultaneously to reproduce all available experimental data. The set of the thermodynamic parameters is given in the appendix.

4.6.2. Calculation results and discussion

Figs. 4-25 to 4-29 compare the calculated isothermal sections at 1553, 1473, 1373, 1273 and 1073 K using the present thermodynamic descriptions with the calculations by Zhou et al. [26] and the experimental data.

In the NiAl-Mo-Al section, the calculated isothermal sections from the present description are significantly different in the Al-rich corner from that of Ref. [26]. This is because a different thermodynamic description of Al-Mo system was adopted in Ref. [26]. In Ref. [26], the Al-Mo binary description is from Saunders [46], where only five intermetallic compounds $Al_{63}Mo_{37}$, Al_8Mo_3, Al_4Mo, Al_5Mo and $Al_{12}Mo$ are included. In the present work, three stable intermetallic compounds, Al_3Mo, $Al_{22}Mo_5$ and $Al_{17}Mo_4$, were also taken into account. It is worth mentioning that the ternary phase N was firstly observed by Raman and Schubert [131, 132] after the sample was equilibrated at 1173K for 5 days, but Zhou et al. [26] mistakenly used this data in the isothermal section of 1473 K.

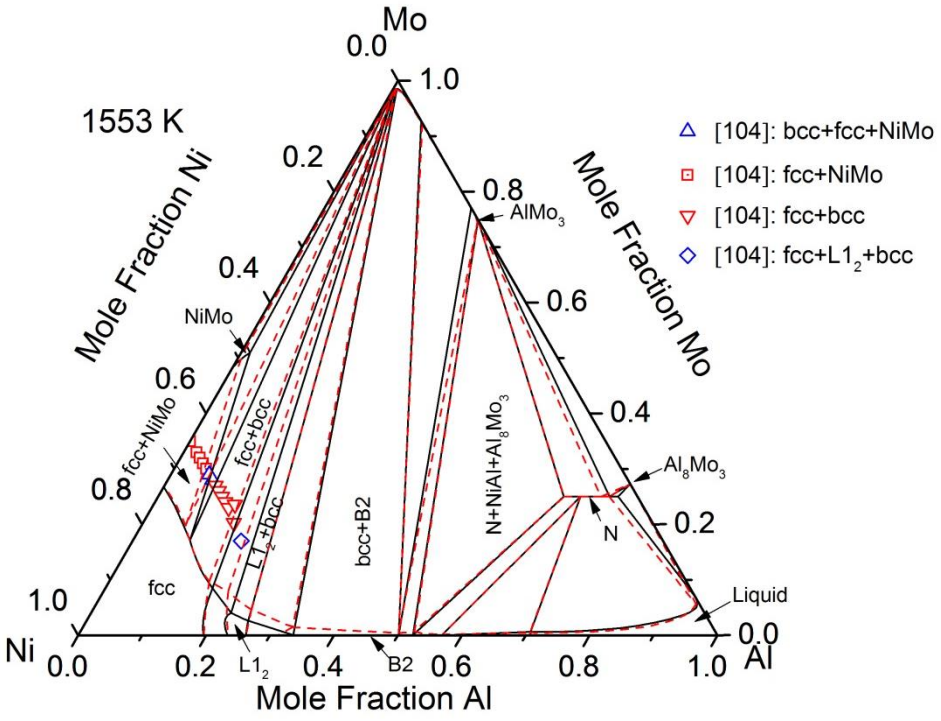

Fig. 4-24 Calculated isothermal section at 1553 K using the present thermodynamic description (solid lines) in comparison with that by Zhou et al. [26] (dashed lines) and the experimental data.

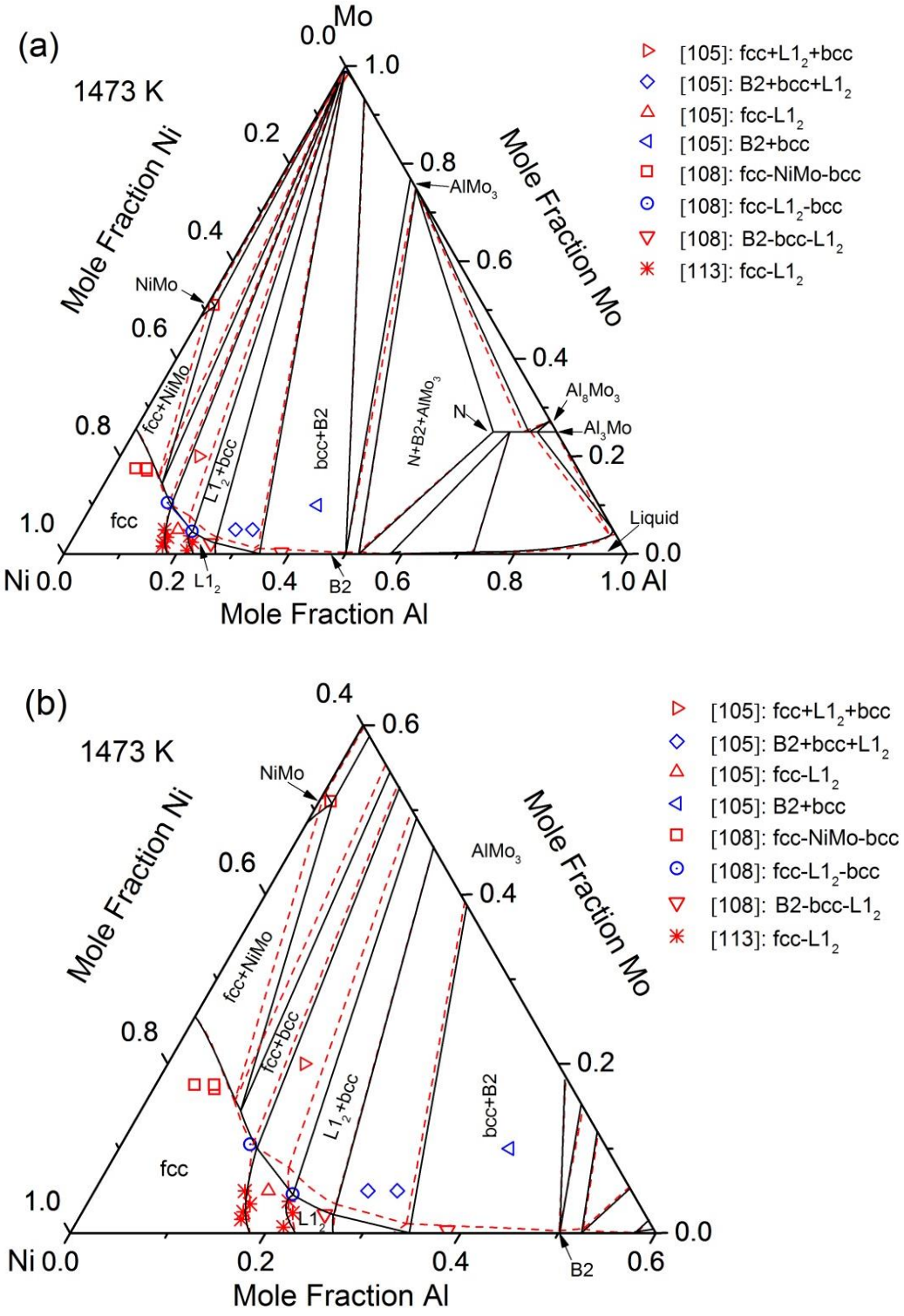

Fig. 4-25 Calculated isothermal section at 1473 K using the present thermodynamic description (solid lines) in comparison with that by Zhou et al. [26] (dashed lines) and the experimental data. (a) overall composition and (b) Ni-rich corner.

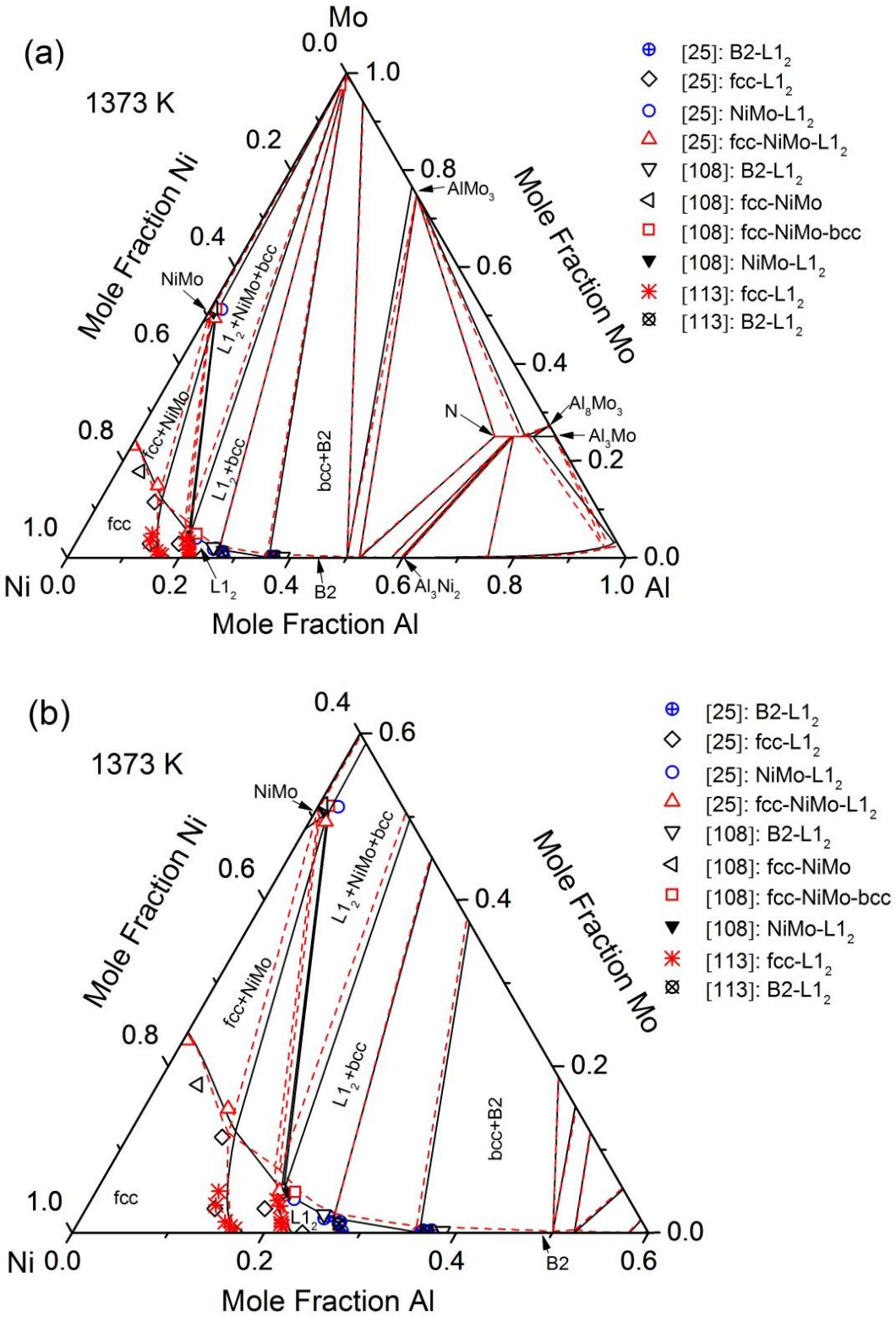

Fig. 4-26 Calculated isothermal section at 1373 K using the present thermodynamic description (solid lines) in comparison with that by Zhou et al. [26] (dashed lines) and the experimental data. (a) overall composition and (b) Ni-rich corner.

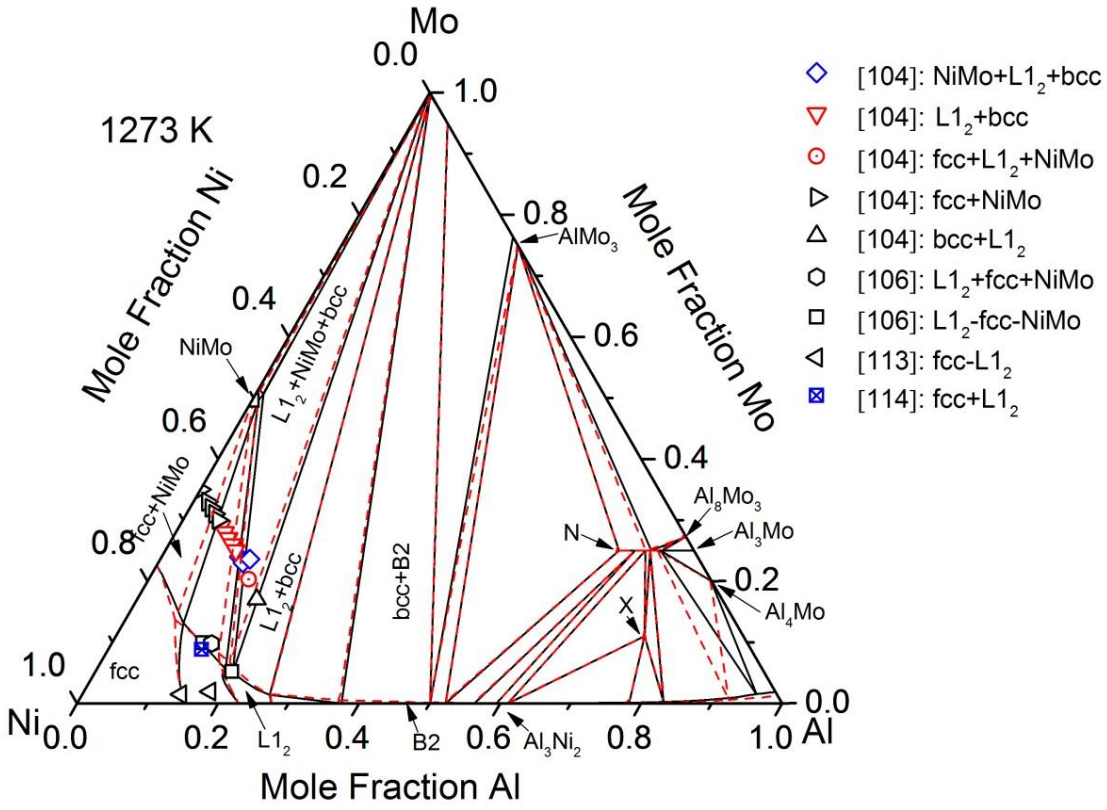

Fig. 4-27 Calculated isothermal section at 1273 K using the present thermodynamic description (solid lines) in comparison with that by Zhou et al. [26] (dashed lines) and the experimental data.

The calculated isothermal sections using the present description agree well with the experimental data except for the X+Al_5Mo+$Al_{17}Mo_4$ and liquid+Al_5Mo+X equilibria at 1073 K (Fig. 4-28). Our calculated results indicate they should be replaced by X+$Al_{22}Mo_5$+$Al_{17}Mo_4$ and Liquid+$Al_{22}Mo_5$+X equilibria, respectively. Probably, this is because Grushko et al. [102] used the phase diagram of Al-Mo system reported by Schuster et al. [65] as a reference. Schuster et al. [65] reported that the $Al_{22}Mo_5$ phase had a lower temperature stability limit of 1104 K so that Grushko et al. [102] did not treat the $Al_{22}Mo_5$ phase as a stable phase at 1073 K. But according to the most recent experimental investigation [64], $Al_{22}Mo_5$ can exist as low as 873 K. Also, in [102], the compositions of the two Al-Mo phases detected were determined by EDX, which made Grushko et al. [102] easily mistake $Al_{22}Mo_5$ for $Al_{17}Mo_4$. Our calculation predicts the X phase melts at 1280 K, which is close to the 1288K determined experimentally by Grushko et al. [102].

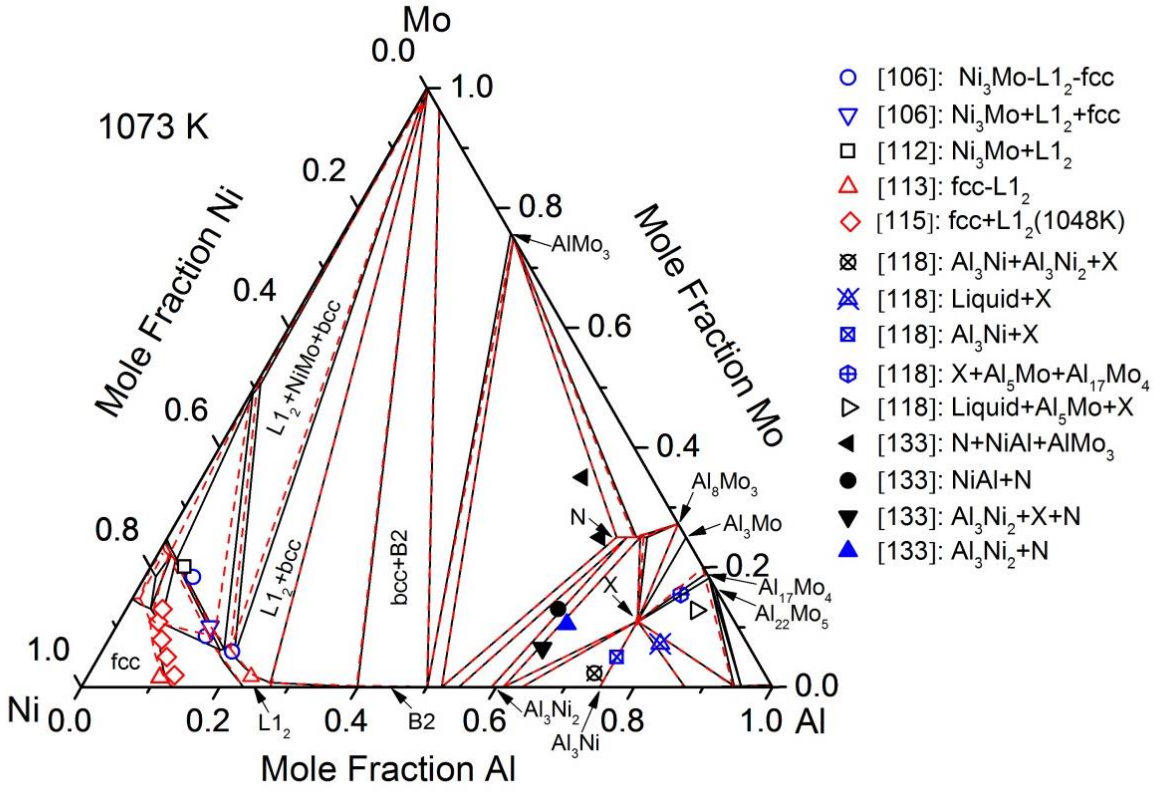

Fig. 4-28 Calculated isothermal section at 1073 K using the present thermodynamic description (solid lines) in comparison with that by Zhou et al. [26] (dashed lines) and the experimental data.

Obviously, in the NiAl-Mo-Ni region, our results are in better agreement with the experimental data. The solubility of Al in the NiMo phase was not considered in the dataset of Zhou et al. [26], but taken into account in the present assessment. In Ref. [26], the solubility of Mo in $L1_2$ is obviously larger than the experimental data (Fig. 4-25 and 4-26). For instance, the description of Zhou et al. [26] indicates the maximum solubility of Mo in $L1_2$ is 7.8 at.% at 1473 K (Fig. 4-25), which deviates significantly from the experimentally determined data (4.6%) by Maslenkov et al. [103].

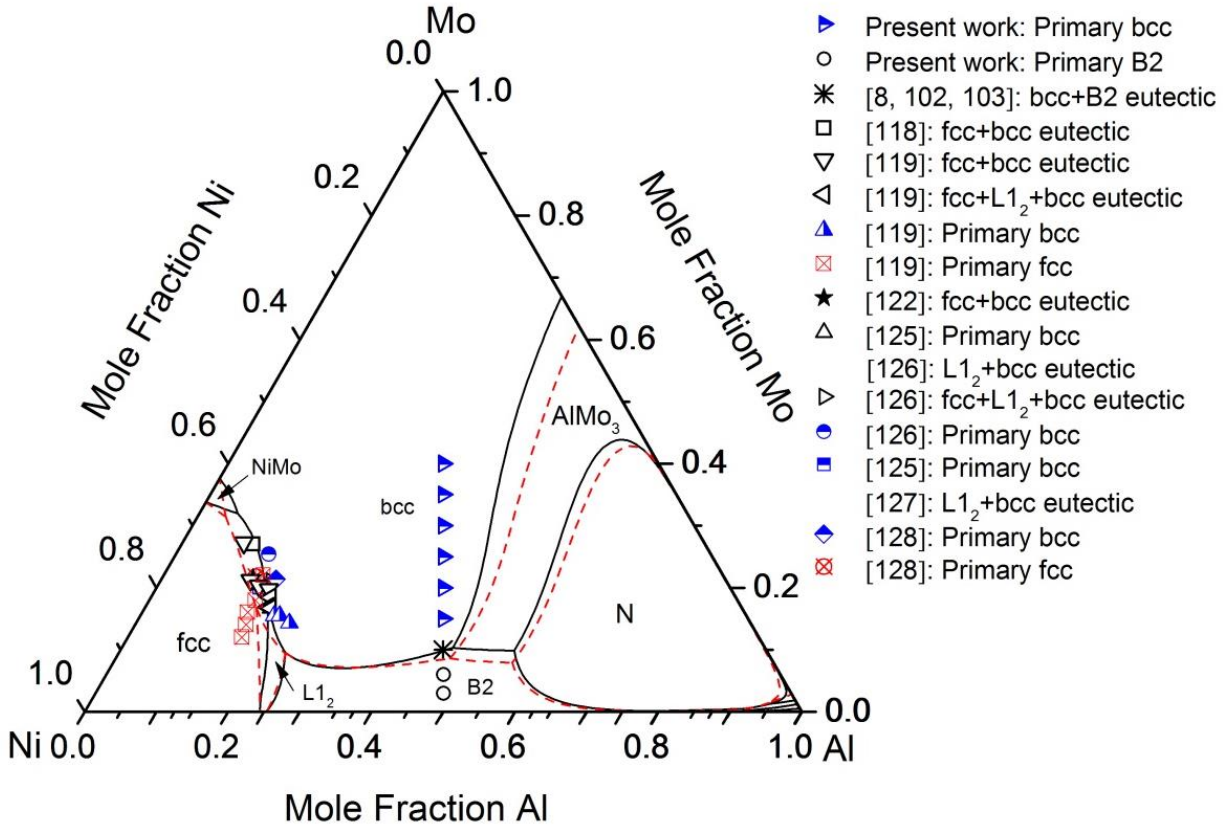

Fig. 4-29 Calculated liquidus surface projection of the Al-Mo-Ni system using the present description (solid lines) in comparison with that from Zhou et al. [26] (dashed lines) and the experimental data.

The clarification of the monovariant eutectic trough in the Al-Mo-Ni system will highly facilitate the selection of alloys composition for manufacturing in-situ composites by directional solidification. Fig. 4-29 compares the calculated liquidus surface projection of the Al-Mo-Ni system using the present description with the experimental data. The calculated liquidus projection by Zhou et al. [26] is also superimposed. Our calculated results are in good agreement with the experimental data. The experimental data reported by Refs.[8, 102, 107, 109, 119, 126] provided valuable information but were neglected by Zhou et al. [26]. Pearson and Lemkey [119] investigated a series of alloys located at and near the bcc and fcc monovariant trough by metallographic examination and DTA. They observed, starting from the binary NiMo and (Ni) eutectics, a eutectic reaction between fcc and NiMo maintained until ~2.5 wt. %. Al, from where the monovariant eutectic reaction between fcc and bcc began and persisted until 7.5 wt.% Al. In our description, the monovariant eutectic reaction between fcc and bcc begins at 2.2 wt.% Al and ends at 7.4 wt.% Al, which is consistent with the experimental data, while the calculated results the description of Zhou et al. [26] indicates it begins at 1.5 wt.% Al and ends at 7.0 wt.% Al.

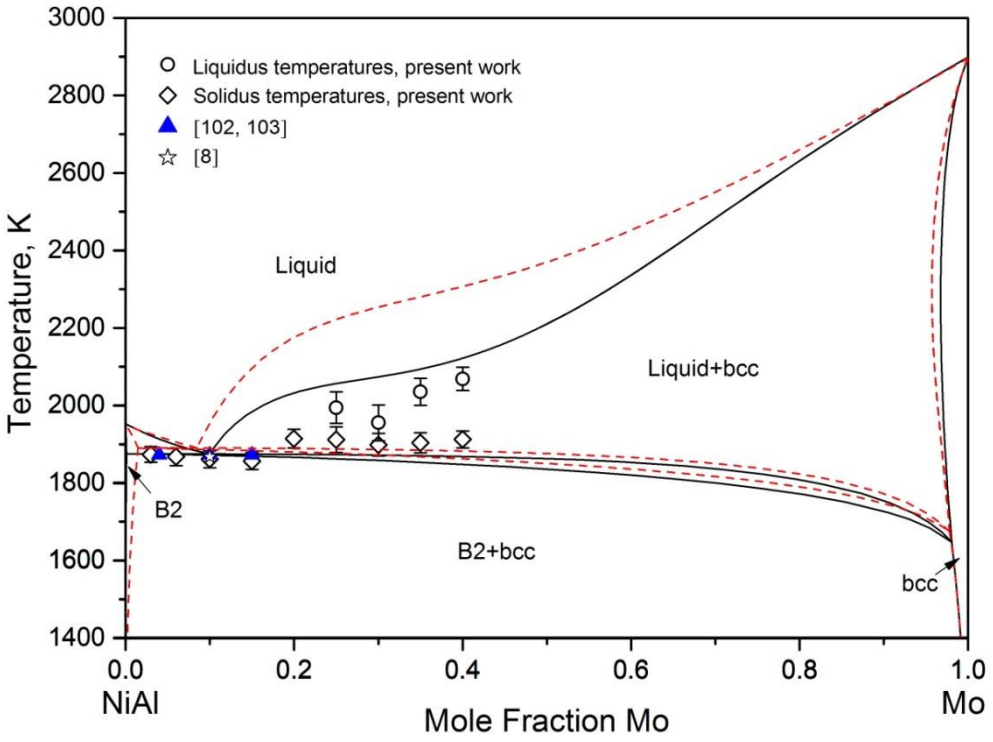

Fig. 4-30 Calculated NiAl-Mo section using the present description (solid lines) in comparison with that by Zhou et al. [26] (dashed lines) and the experimental data.

The calculated NiAl-Mo section using the present thermodynamic description is presented in Fig. 4-30. The experimental data from the literature and the present investigation are also superimposed. Contradicting to the reports by Maslenkov et al. [107, 109], the present calculated NiAl-Mo section reveals deviations from a quasi-binary section. The satisfactory agreement between the calculated phase diagram using the thermodynamic description of the present work and the experimental data is obtained. During the laser heating experiment, certain extent of undercooling may exist because of the fast cooling rate, which results in the lower measured liquidus temperatures than these of calculation in the present work. The calculated NiAl-Mo section using the description of Zhou et al. [26] indicates the eutectic composition and temperature are 8.4 at.% Mo and 1891 K, which shows a significant deviation from the experimental data [8, 107, 109]. Our description indicates eutectic composition and temperature are 9.9 at.% Mo and 1875 K, which agrees well with the experimental data. Better agreement with the liquidus temperatures is obtained using the present thermodynamic description. The calculated solubility of Mo in NiAl at 1773 K in this work is 0.06 at.% (as shown in Fig. 4-31), which is consistent with our experimental result that the solubility of Mo in NiAl should be lower than 0.1 at.% Mo at 1773 K, while the calculated one by Zhou et al. [26] is 1 at.% Mo.

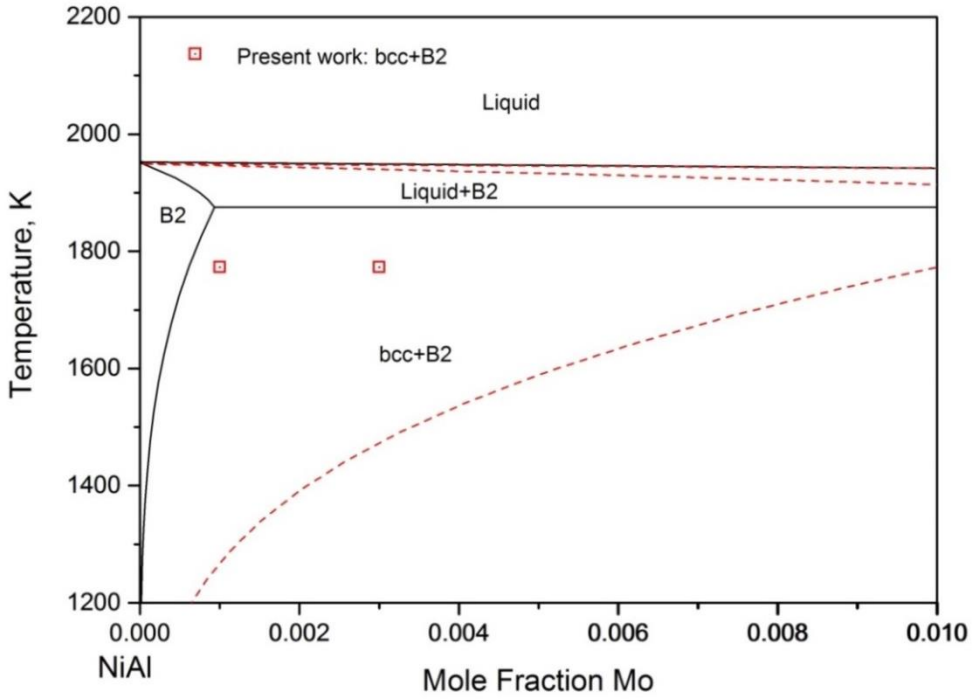

Fig. 4-31 Calculated partial NiAl-Mo section using the present description (solid lines) in comparison with that by Zhou et al. [26] (dashed lines) and the experimental data.

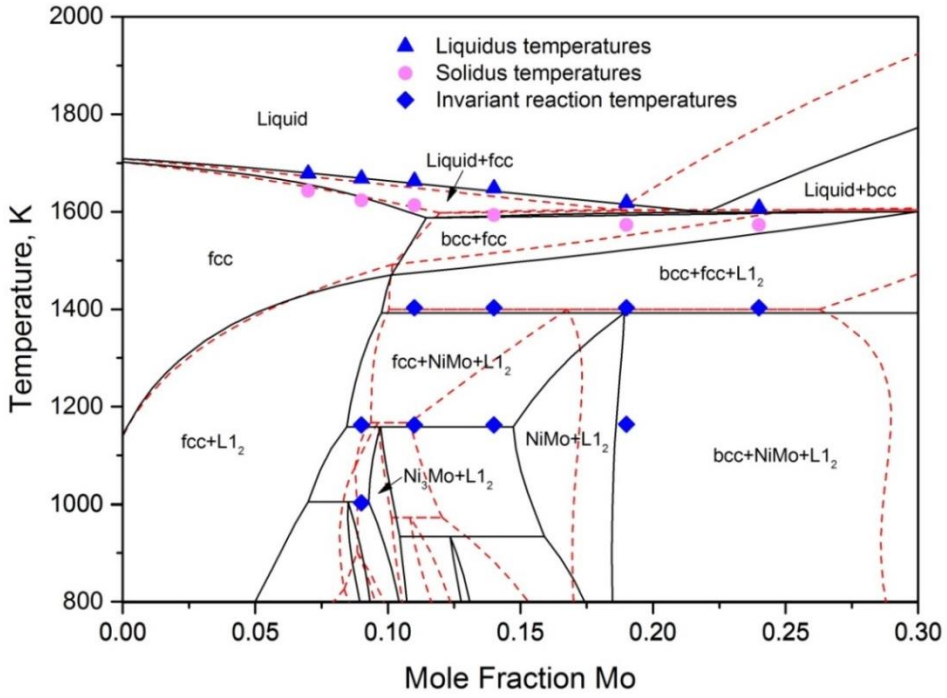

Fig. 4-32 Calculated partial isopleth with 14 at.% Al using the present description (solid lines) in comparison with that by Zhou et al. [26] (dashed lines) and the experimental data [112].

Table 4-8 Temperatures of the reactions in the NiAl-Mo-Ni subsystem.

Reactions	Temperature, K	References
Liquid↔bcc+B2	1875 (9.9 at.% Mo)	Present work
	1873±7 (10.0 at.% Mo)	[107, 109]
	1868 (10.0 at.% Mo)	[8]
	1891 (8.4 at.% Mo)	[26]
U_1: Liquid+B2↔bcc+$L1_2$	1605	Present work
	1613±10	[107, 109]
	1617	[26]
U_2: Liquid+NiMo↔bcc+fcc	1573	Present work
	~1385	[119]
	1583±7	[107, 109]
	1574	[26]
U_3: bcc+fcc↔$L1_2$+NiMo	1400	Present work
	~1468	[119]
	~1403	[110]
	1400±2	[104]
	1403±5	[112]
	1400	[26]
U_4: NiMo+fcc↔$L1_2$+Ni_3Mo	1163	Present work
	1163±5	[103, 112]
	1167	[26]
U_5: Ni_3Mo+fcc↔$L1_2$+Ni_4Mo	1003	Present work
	1003±5	[103, 112]
E: Liquid↔fcc+$L1_2$+bcc	1600	Present work
	~1573	[122]
	~1578	[119]
	~1573±7	[107, 109]
	1604	[26]

Fig. 4-32 shows the calculated partial isopleth with 14 at.% Al (solid lines) using the present description in comparison with that by Zhou et al. [26] (dashed lines) and the experimental data from Maslenkov et al. [112]. Both calculations can well reproduce the liquidus temperatures up to

19 at.% Mo as well as the temperatures of invariant reactions U_3 and U_4. The fcc solvus from both works are very similar. However, the calculated liquidus temperature at 24 at.% Mo at the present work significantly agrees better with the experimental data than that by Zhou et al. [26]. The temperature of invariant reactions U_5 can be well reproduced with the present description, but not with that of Zhou et al. [26].

Table 4-8 presents the calculated reaction temperatures in the NiAl-Mo-Ni subsystem. Very good agreement is obtained except for the temperature of the reaction E.

5. The Al-Cr-Ni system

5.1. Review of the binary systems

The Al-Cr-Ni system consists of three binary sub-systems, Al-Ni, Al-Cr and Cr-Ni. A review of the Al-Ni system has been given in the chapter 4.1.1, so in the following sections, brief reviews of the Al-Cr and Cr-Ni systems will be presented.

5.1.1. Review of the Al-Cr system

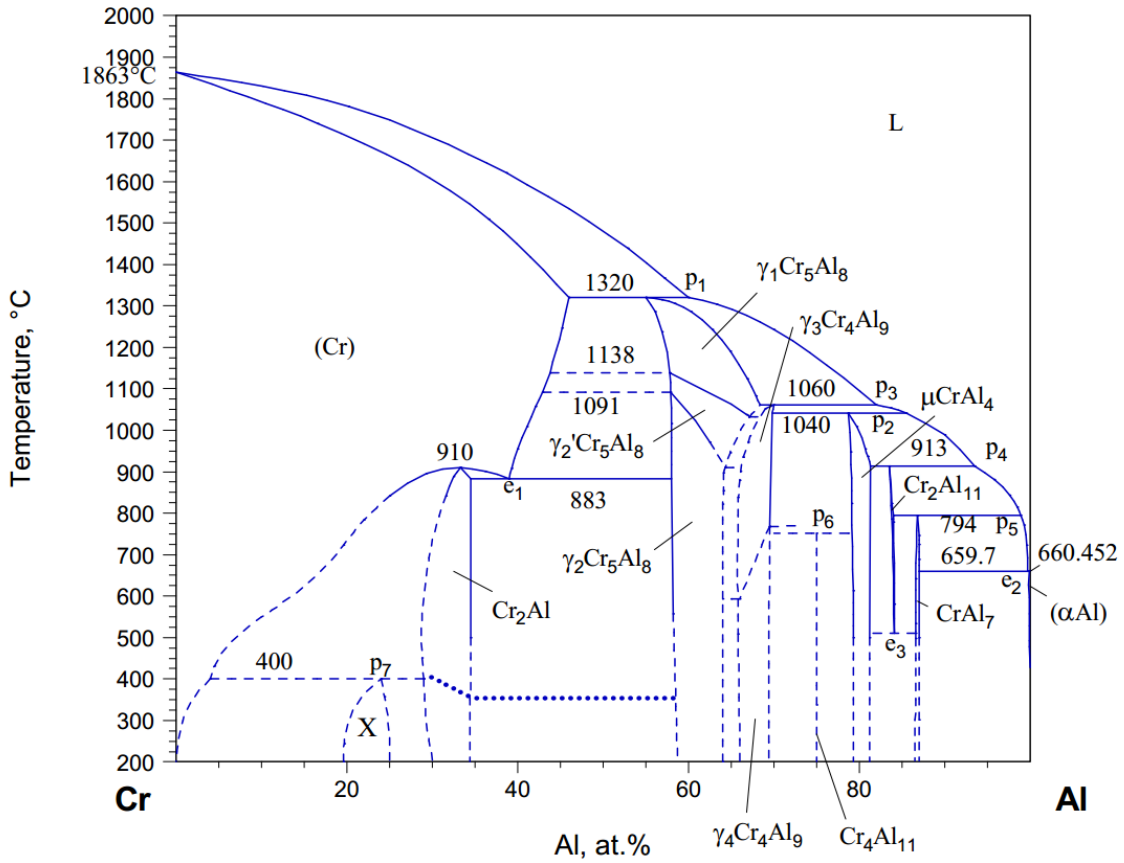

Fig. 5-1 Critically evaluated phase diagram of the Al-Cr system by Khvan and Watson [134].

A critical evaluation of the Al-Cr system up to 1998 has been performed by Murray [135]. Later, it was updated by Okamoto [136] and Chen [137]. The most recent one was given by Khvan and Watson [134] and the corresponding phase diagram of the Al-Cr system from Ref. [134] is shown in Fig. 5-1. At atmospheric pressure, there are thirteen stable phases in the Al-Cr system. Besides fcc, bcc and liquid phases, ten intermetallic compounds Al_7Cr, $Al_{11}Cr_2$, Al_4Cr, γ_1-Al_8Cr_5, γ_2-Al_8Cr_5, γ_2'-Al_8Cr_5, γ_3-Al_9Cr_4, γ_4-Al_9Cr_4, $AlCr_2$ and X, exist. The crystallographic data of all stable solid

phases in this system at atmospheric pressure from Ref. [134] are summarized in Table 5-1. However, the phase diagram of the Al-Cr system is not fully determined yet. Some controversies still exist. The main one is on the structure of the region with 30-42 at.% Cr, the so-called γ phase field. Experimental investigation has been performed by Grushko et al. [138] and Chen [137] on this region, respectively, but their works cannot reach an agreement with each other. Therefore, further investigation on the γ phase field is still necessary.

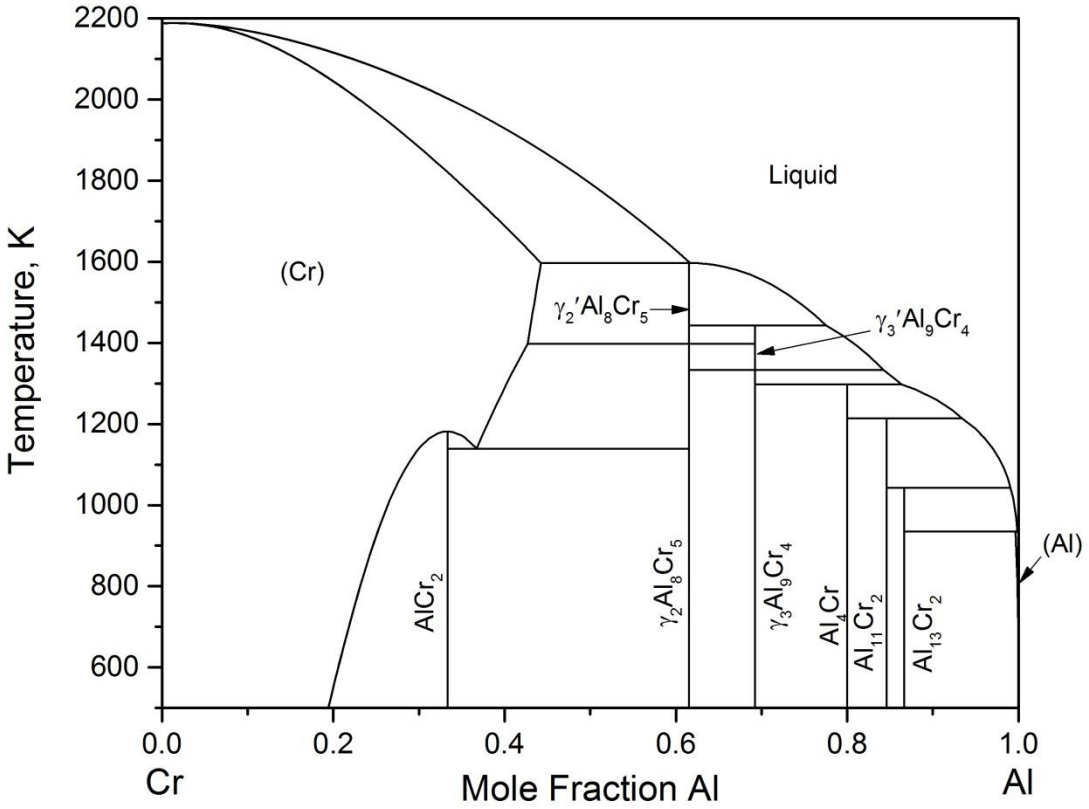

Fig. 5-2 Calculated phase diagram of the Al-Cr system from Saunders and Rivlin [139, 140].

Thermodynamic assessments of this system have been made by Saunders and Rivlin [139, 140], Tokunaga et al. [141], Liang et al. [142], Hu et al. [143] and Witusiewicz et al. [144]. In Refs. [139, 140], all the intermetallic phases were treated as stoichiometric compounds and eight intermetallic phases, $Al_{13}Cr_2$, $Al_{11}Cr_2$, Al_4Cr, γ_1-Al_8Cr_5, γ_2-Al_8Cr_5, γ_3-Al_9Cr_4, γ_4-Al_9Cr_4, $AlCr_2$ were included. This dataset later was included in the COST 507 database [145]. Recently, Tokunaga et al. [141] and Liang et al. [142] re-assessed this system. The calculation results are in consistence with the experimental results from Refs. [138, 146]. In Ref. [142], sublattice models were used to model the intermetallic phases. However, these models were not based on the crystallographic structure of the phases. In addition, the experimentally determined enthalpies of mixing for liquid as well as the activities were not reproduced well in Ref. [142]. Therefore, Hu et al. [143] re-assessed this system and some improvements were achieved. Stein et al. [147] recently investigated the Cr-rich

region (from 49.1 to 79.3 at.% Cr) of the Al-Cr system. Some solidus and liquidus temperatures and reaction temperatures were measured. Taking into account this new experimental data, Witusiewicz et al. [144] re-assessed this system. The new description from Witusiewicz et al. [144] can reproduce the experimental data well.

In the present work, the dataset from Saunders and Rivlin [139, 145] was adopted instead of Witusievicz et al. [144], because we adopted the dataset of the ternary system Al-Cr-Ni from Dupin et al. [28] and the Al-Cr description used in Dupin et al. [28] was from Refs. [139, 145]. The main goal of this work is to determine the location of the eutectic trough in the section NiAl-Cr-Mo. In this section, only three phases, liquid, bcc and B2, were involved. The assessment of Saunders and Rivlin [139, 145] already provides a suitable description for the alloy range of the present work, especially with regard to the liquid phase. Details will be discussed in chapter 5.4. The calculated phase diagram of the Al-Cr system from Saunders and Rivlin [139, 145] is shown in Fig. 5-2.

Table 5-1 Crystallographic data of stable solid phases in the Al-Cr system at atmospheric pressure [134].

Phases	Prototype	Pearson symbol	Space group
fcc_(Al)	Cu	cF4	$Fm\bar{3}m$
bcc_(Cr)	W	cI2	$Im\bar{3}m$
Al_7Cr	$Al_{45}V_7$	mC104	C2/m
$Al_{11}Cr_2$	Al_5Cr	mP48	P2
		C2/c	
		Cmcm	
Al_4Cr	μ-Al_4Mn	hP574	$P6_3/mmc$
γ_1-Al_8Cr_5	Cu_5Zn_8	cI52	$I\bar{4}3m$
γ_2-Al_8Cr_5	Al_8Cr_5	R3m	-
	$D8_{10}$	hR26	$R\bar{3}m$
γ_2'-Al_8Cr_5	-	-	-
γ_3-Al_9Cr_4	-	-	-
γ_4-Al_9Cr_4		cI52	$I\bar{4}3m$
$AlCr_2$	$MoSi_2$	tI6	I4/mmm
X	Al_3Cr_5	-	-

5.1.2. Review of the Cr-Ni system

The Cr-Ni system has been studied extensively. At atmospheric pressure, there are four stable phases in the Cr-Ni system above 773 K. Besides the fcc, bcc and liquid phases, one intermetallic compound Ni_2Cr exists. This system is characterized by the eutectic reaction between the liquid, bcc and fcc phases at 1618 K. The Ni_2Cr phase forms at 863 K [148]. The experimentally determined phase diagram of the Cr-Ni system was constructed by Nash [148], Udovsky and Kozodaeva [149] and Tomiska [150]. These diagram versions agree well with each other, only a few discrepancies resulting from the fluctuations in available experimental data exist. The Cr-Ni phase diagram included in Massaski2 [151] was a replica of that from Nash [148] and it is shown in Fig. 5-3. Thermodynamic data of this system up to 2002 were reviewed by Saltykov et al. [152].

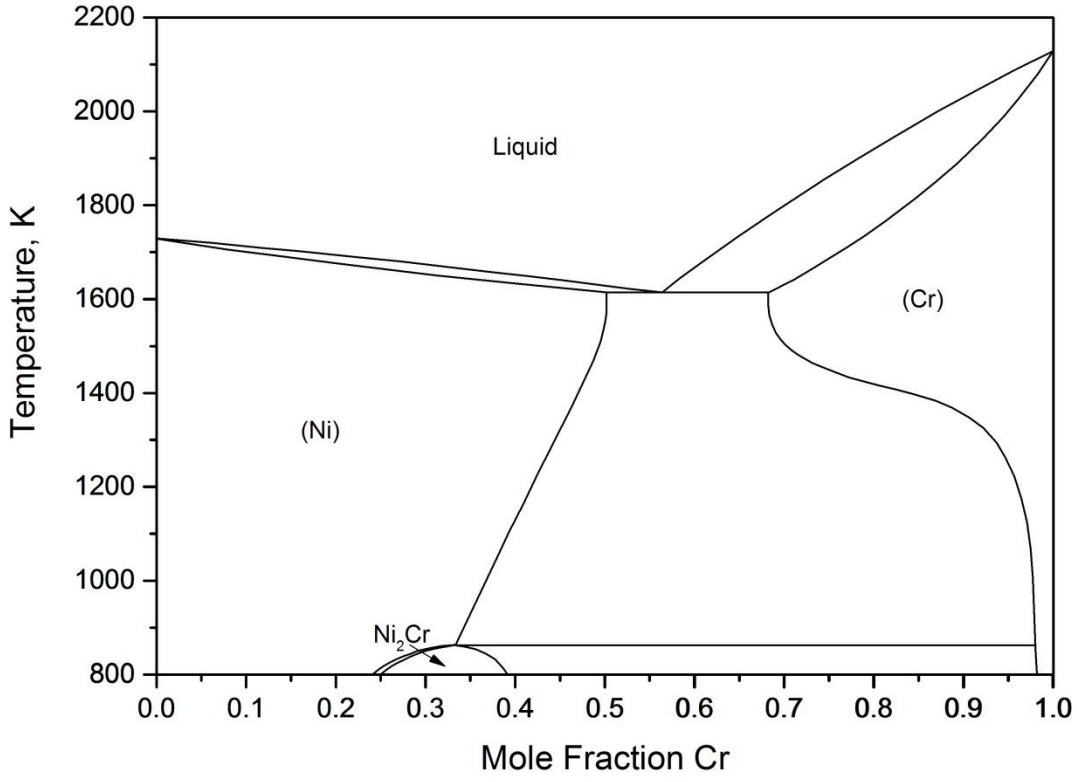

Fig. 5-3 Critically evaluated phase diagram of the Cr-Ni system by Nash [148].

Four thermodynamic assessments of this system are available from Chart [153], Gustafson [154], Lee [155] and Turchi [156]. The unpublished description developed by Chart [153] can be found in Ref. [157]. The assessments of Chart [153], Gustafson [154] and Lee [155] are in good agreement with each other. The dataset of Lee [155] was accepted by the SGTE (Scientific Group Thermodata Europe) SSOL database [39]. However, the Ni_2Cr phase was not included in these assessments. Although Turchi et al. [156] updated the thermodynamic description of Lee [155] by adding the Ni_2Cr phase in the dataset, the Ni_2Cr phase was modeled as a stoichiometric compound without considering its homogeneity range. It forms peritectoidally at 807 K, which is lower than

the experimental result (863 K). In the present work, the dataset from Lee [155] was selected and the corresponding calculated phase diagram of the Cr-Ni system is shown in Fig. 5-4.

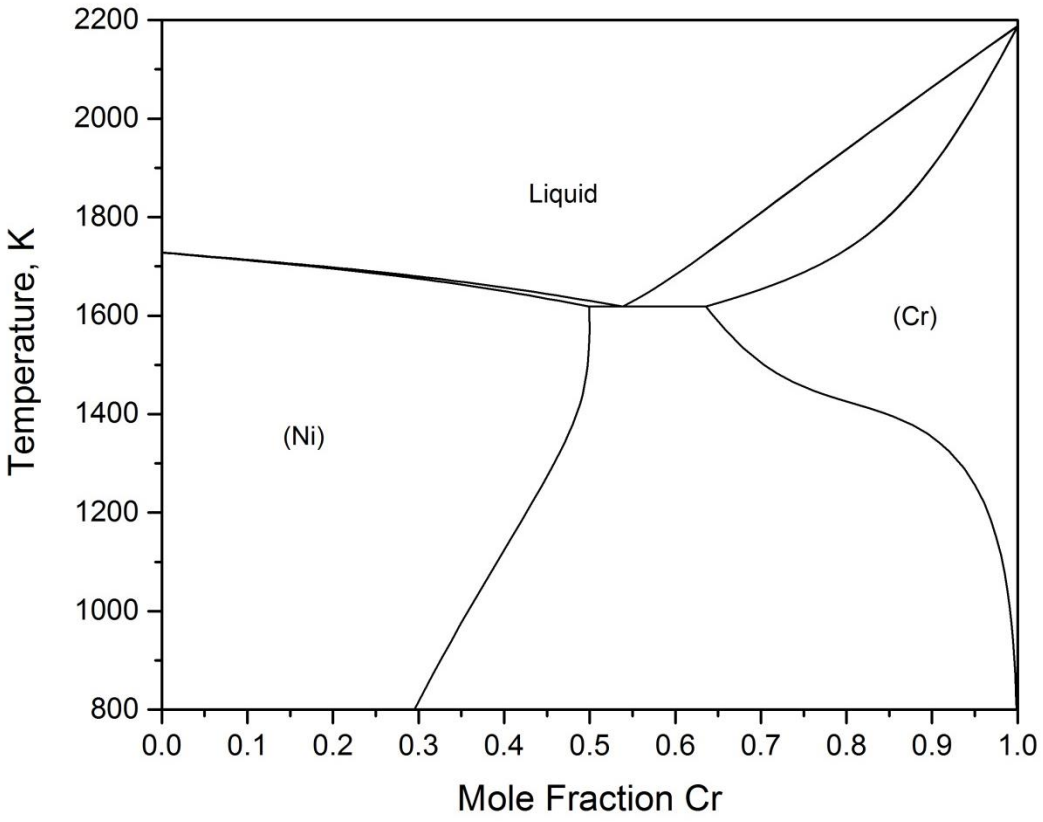

Fig. 5-4 Calculated phase diagram of the Cr-Ni system from Lee [155].

5.2. Review of the Al-Cr-Ni system

A detailed review of the Al-Cr-Ni system up to 2003 was performed by Velikanova et al. [158]. In this system, several ternary phases were reported, but they are not considered in the previous thermodynamic assessments. Thus, a detailed review focusing on the ternary phase will be presented in the following part to clarify the necessity of including the ternary phases in the present assessment.

Table 5-2 summarizes the experimental methods, crystallographic data and the homogeneity ranges of the ternary phases in the Al-Cr-Ni system were summarized. The phases in the same column are the same phase.

Table 5-2 Literature information of the ternary phases in the Al-Cr-Ni system.

Ref.	Methods	Phases						
[159]		$Al_{75}Cr_{15}Ni_{10}$						
[160]	EDX EPMA PAP TEM DTA (as-cast)	Φ		λ		ρ		
						ρ_1	ρ_2	ρ_3
		Monoclinic	Orthorhombic	Orthorhombic	Triclinic	Rhombohedral	Hexagonal	Hexagonal
		$P2_1$ or $P2_1/m$	$Pn2_1a$	*Immm*		$R\bar{3}$ or $R3$	$P6_3$	$P6_3$
		a = 1.34, b =c=1.255, β= 100°	a = 1.255, b=1.255, c = 2.64	a = 1.255 b =1.255 c = 3.075	a = 1.255, b = 2.510 c = 1.775, α=β= 100.7°, γ=90°	a=2.87, α=36° in hexagonal system a=1.77, c=8.04	a=1.77, c=1.24	a=3.07, c=1.24
		$Al_{71.2\text{-}78.5}Ni_{5.8\text{-}10.1}Cr_{15.7\text{-}18.7}$		$Al_{76.8\text{-}79.0}Ni_{8.5\text{-}10.4}Cr_{11.7\text{-}12.8}$		$Al_{79.6}Ni_{1.7}Cr_{18.7}$		
[161, 162]	HREM Calculation (slow cooling)						denoted κ	
							Hexagonal	
							$P6_3$	
							a=1.7674, c=1.2516	
							$Al_{76}Ni_6Cr_{18}$ [161]), $Al_{76.2}Ni_{5.8}Cr_{18.0}$[162])	
[163]	EDX, XRD (as-cast)	Φ confirmed		λ confirmed		ρ confirmed		
[164]	EDX XRD TEM DTA (1173, 1273 K)	ε (not Φ and λ)					denoted ζ	
		a = 1.26, b =3.48, c = 2.02					a=1.77, c=1.24	
		$Al_{76.5}Ni_{2.0}Cr_{21.5}$					$Al_{71.5\text{-}81}Ni_{3\text{-}9}Cr_{14.5\text{-}20.5}$	
		Note: It may be a metastable binary Al-Cr phase stabilized by Ni						
[165]	EDX	denoted τ_2				denoted τ_3	denoted τ_1	

	XRD DTA (973 K)	$Al_{77.5}Ni_{10}Cr_{12.5}$ (±0.5)		$Al_{80}Ni_5Cr_{15}$ (±1)		
[166]	SEM TEM EDX DTA (973, 1073, 1173 K)	Φ	Actually no λ exist	denoted ζ_1	denoted ζ	
		Monoclinic	-			
		$P2_1$ or $P2_1/m$		$R\bar{3}$ or $R3$	$P6_3/m$	
		a = 1.34, b = 1.255 c = 1.255, β= 100°		a=2.87, α=36°; in hexagonal system a=1.77, c=8.04	a=1.7714, c=1.2591	
		~$Al_{80}Ni_9Cr_{11}$		~$Al_{82}Ni_3Cr_{15}$	$Al_{72\text{-}80.5}Ni_{3\text{-}8.5}Cr_{15\text{-}20.5}$	

Note: Compositions are in mole percent.

The existence of a ternary phase in the Al-Cr-Ni system was reported for the first time by Tu and Seigle [159]. The composition of this ternary phase is $Al_{75}Cr_{15}Ni_{10}$ (at. %). Later, three ternary phases Φ, λ and ρ as well as their polytypes were observed by Rosell-Laclau et al. [160]. Their crystal structures were also determined. The Φ phase exhibits monoclinic structure. Because of a periodic multiple of (100) twinning, a polytype of the Φ phases with an orthorhombic structure can form. The composition of the Φ phase varies in the range of $Al_{71.2\text{-}78.5}Ni_{5.8\text{-}10.1}Cr_{15.7\text{-}18.7}$ (at.%). The structure of the λ phase was identified to be orthorhombic and its polytype shows a triclinic structure. The composition of the λ phase varies in the range of $Al_{76.8\text{-}79.0}Ni_{8.5\text{-}10.4}Cr_{11.7\text{-}12.8}$ (at.%). The ρ phase exhibits a rhombohedral structure **(**ρ_1). It has two polytypes (ρ_2 and ρ_3), both of which show hexagonal structures but have different lattice parameters. Li et al. [161] and Sato et al. [162] confirmed the existence of the ternary phase ρ_2 (denoted κ in [161, 162]). It was reported in Refs. [161, 162], the ρ_2 phase is a hexagonal phase with the composition $Al_{76}Cr_{18}Ni_6$ (at.%). Three ternary phases were identified by Compton et al. [163] from microstructure observation and their compositions agree reasonably with the ternary phases Φ, λ and ρ reported in Ref. [160]. The existence of the ρ_2 phase was further confirmed by Grushko et al. [164] (denoted ζ phase) and Weitzer et al. [165] (denoted τ_1 phase). Moreover, two ternary phases, denoted τ_2 and τ_3 in Ref. [165], were found to be stable at 973 K. Their compositions are $Al_{77.5}Cr_{12.5}Ni_{10}$ (at.%) and $Al_{80}Cr_{15}Ni_5$ (at.%), respectively, which are close to the compositions of the Φ and ρ_1 phases reported by Rosell-Laclau et al. [160]. Recently, Grushko et al. [166] reported the monoclinic Φ phase in [160] was stable below 1108 K with the composition around $Al_{80}Ni_9Cr_{11}$ (at.%). In addition, the ρ_1 phase in Ref. [160] was found to be stable at 973 and 1073 K with the composition around $Al_{82}Ni_3Cr_{15}$ (at.%) in Ref. [166]. Grushko et al. [166] also suggested that the λ phase may be the ternary extension of the binary phase monoclinic η phase from the Al-Cr system, but not a ternary phase. From what has been discussed above and the summary in Table 5-2, the following conclusions can be drawn: The τ_2 phase is the same phase as Φ. τ_2, ζ_1 and ρ_1 are the same phase. ζ and ρ_2 are the same phase. Further investigation is required to clarify the existence of the λ and ε phase and the polytypes of the Φ, λ and ρ phases as well as the homogeneity ranges of these ternary phases.

The composition ranges of the ternary phases and their polytypes from different researches were summarized in Fig. 5-5. They exist in low temperature range and locate in the triangular region between the compositions of $Al_{60}Cr_{40}$, $Al_{60}Ni_{40}$ and Al (at.%), which is far away from the NiAl-Cr section that is concerned in the present work. Also, the homogeneity ranges of respective ternary phase from different sources [160, 163–166] are not in good agreement with each other. Therefore, in the present work, ternary phases were not considered in the modeling.

To well describe the eutectic trough of the NiAl-Cr-Mo system, an accurate thermodynamic description of the NiAl-Cr section is essential. Several experimental investigations were carried out to determine the eutectic point of the NiAl-Cr section, but they are not in good agreement with each other. It was reported that the eutectic point locates at 33.6 at.% Cr and 1718 K [167], 40 at.% Cr [168], 28.2-37.4 at.% Cr [169, 170], 35 at.% Cr [171] and 34 at.% Cr [7, 172–174]. Therefore, additional experiments are necessary to clarify the eutectic composition of the NiAl-Cr section.

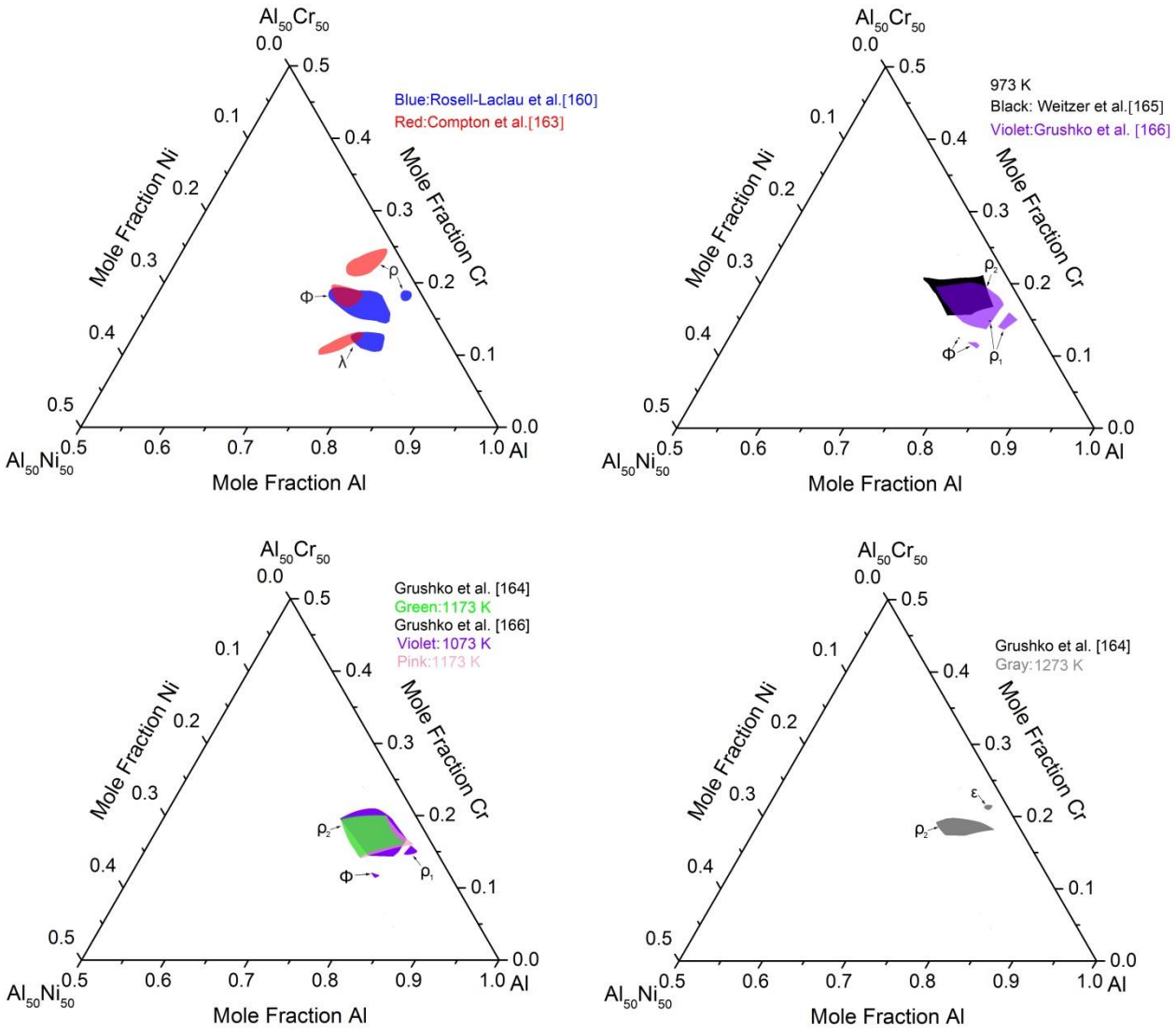

Fig. 5-5 Homogeneity ranges of ternary phases reported by different authors.

Dupin [29] developed the first thermodynamic description of the Al-Cr-Ni system. Later, Huang and Chang [27] argued "the thermodynamic description by Dupin [29] was unnecessarily complicated" and cannot reproduce the experimental data determined by Sung and Poirier [175]. Hence, they established a new thermodynamic description of the Al-Cr-Ni system. The disordered fcc and ordered $L1_2$ phases were modeled using separate Gibbs energy functions as well as the two bcc phases disordered A2 and ordered B2. However, Dupin et al. [28] pointed out: "No real simplification is thus introduced" in Ref. [27] and "in multicomponent systems, a possible competition between stable and metastable disordered phases may occur". Therefore, Dupin et al. [28] re-assessed the Al-Cr-Ni system. The disordered bcc and ordered B2 were successfully modeled using a single Gibbs energy function as well as the disordered fcc and ordered $L1_2$ phases.

Moreover, new experimental data from Tian et al. [176] and Saltykov et al. [177] were also taken into account in Ref. [28]. Significant improvements were achieved. In the present work, the latter dataset [28] was adopted because it provided a good representation of most experimental data and used the most advanced models for the description of ordered phases. However, a few adjustments have to be applied to the parameters of the liquid phase and the A2/B2 phases, as will be discussed in chapter 5.4.

5.3. Experimental investigation

5.3.1. Experimental procedure

Alloys No.1 and No. 2 with the compositions NiAl-31.4 at.% Cr and NiAl-33.5 at.% Cr were prepared with the same preparation procedure introduced in chapter 4.5.1. To better reveal the microstructure, a solution of 80 vol.% H_2O, 10 vol.% HCl (3.8 %) and 10 vol.% H_2O_2 (30 %) was used to selectively etch the NiAl in alloys No. 1 and No. 2. The microstructures of the samples were observed with a scanning electron microscope (FEI XL30S, PHILIPS).

5.3.2. Experimental results

Fig. 5-6 shows the microstructure of the as-cast alloys No. 1 (Fig. 5-6a and 5-6b) and No. 2 (Fig. 5-6c and 5-6d) after etching. Dendrite-like grooves were observed in Fig. 5-6a and small holes uniformly distributed in Fig. 5-6b, which indicated that the alloy No. 1 originally consisted of primary solidified NiAl (B2) phase and eutectic before etching. Alloy No. 2 showed a fully eutectic structure, in accordance with the experimental data in the literature [167]. The calculations with the dataset of Dupin et al. [28] are in conflict with these results since they predict that alloy No.1 should show a fully eutectic structure and primary bcc_(Cr) phase should be observed in alloy No. 2. Recent results from Tang et al. [178] indicate that the eutectic composition of this section should be larger than 33.0 at.% Cr, which further supports the present results. Therefore, the thermodynamic description of the Al-Cr-Ni system by Dupin et al. [28] needs to be modified.

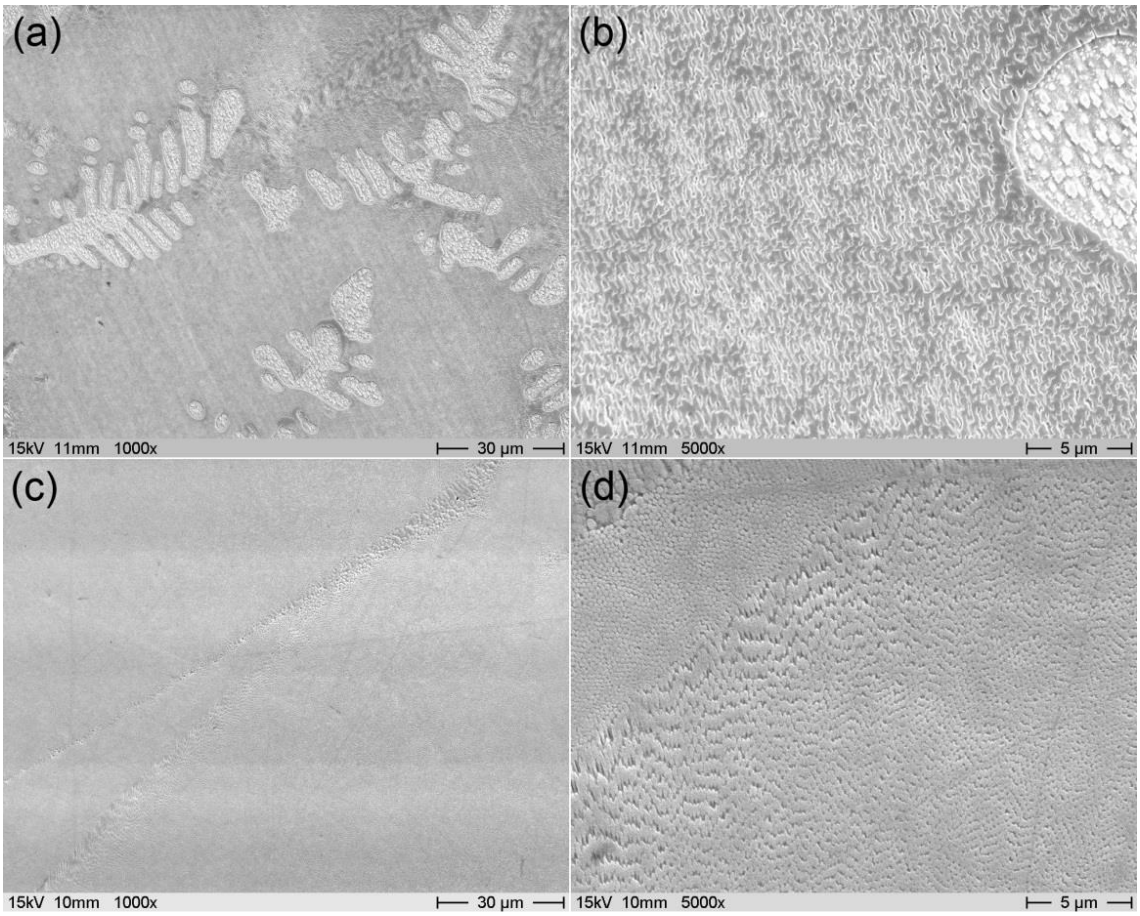

Fig. 5-6 Microstructure of as-cast alloys (a) No. 1, (b) magnified eutectic region of No. 1, (c) No. 2 and (d) magnified eutectic region of No. 2.

5.4. Optimization and calculation results

Two modifications had to be applied to the dataset of Dupin et al. [28]. The first change is related to the modeling of thermal vacancies in the bcc phase. Here, the compound energy of the vacancies has been set to zero (G_{Va}^{bcc} = 0) by Dupin et al. [28]. But this choice prevents the existence of any global minimum of the Gibbs energy for the whole system, as discussed by Franke [93]. In order to assure unique solutions for the equilibrium vacancy concentrations their compound energy has to be larger than the limiting value of (ln2-½)·RT [93]. Therefore, in the refinement of the Al-Ni system (chapter 4.2 as well as in Ref. [179]), we adopted Franke's recommendation, G_{Va}^{bcc}=0.2·RT, and subtracted a term 0.2·RT from the coefficients $\alpha_{\mathrm{Al,Va}}$ and $\alpha_{\mathrm{Ni,Va}}$ of the A2/B2 phases to avoid any change in the calculated phase diagram. With this set of parameters, all calculations for the system Al-Ni lead to the same results as the original dataset of Dupin et al. [28]. Therefore, to compensate the contribution of the compound energy of vacancies in the Al-Ni-Cr system, we followed the method of the author of this thesis (Peng et al. [179]), and subtracted the value 0.2·RT

from ${}^{0}L_{Cr,Va}$. With this modification, all calculations for the binary and ternary sub-systems can completely reproduce the results of Dupin et al. [28].

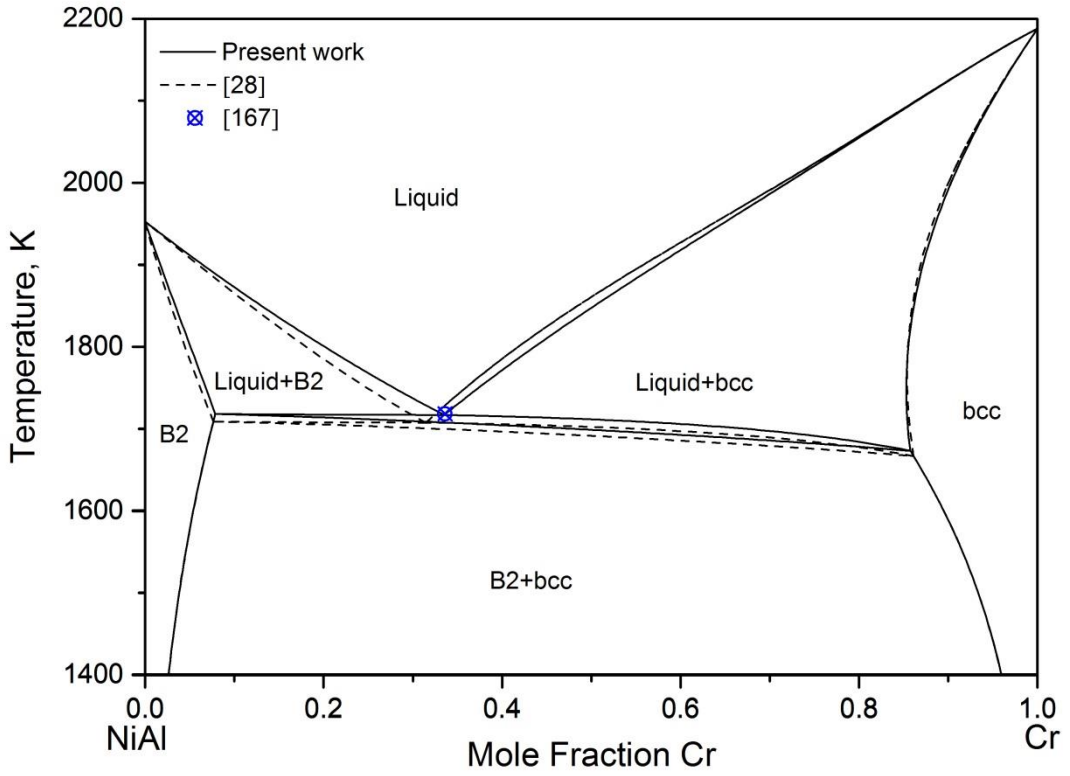

Fig. 5-7 Calculated NiAl-Cr section using the revised description (solid lines) in comparison with that from Dupin et al. [28] (dashed lines).

The second change in Dupin's dataset [28] concerns the liquid phase. As discussed in chapter 5.2, the calculated eutectic point of the NiAl-Cr section by Dupin et al. [28] deviates notably from the experimental data. Therefore, the ternary interaction parameters of the liquid phase in Ref. [28] were re-optimized in order to fit our experimental data (alloys No. 1 & 2 in chapter 5.3.2). Fig. 5-7 shows the calculated NiAl-Cr section from the revised description of the Al-Ni-Cr system in the present work. The resulting calculated eutectic point is located at NiAl-33.5 at.% Cr, 1717 K, which agrees well with our experimental results and the literature data [167, 178].

In Fig. 5-8, the calculated enthalpy of mixing in the liquid is compared with experimental data of Saltykov et al. [152, 177] at 1718-1831 K. The solid lines are calculated with the dataset of the present work whereas the dashed lines represent results of the dataset of Dupin et al. [28]. Both calculated lines are very close to each other throughout the whole composition range. In the binary system Al-Cr (curve 1), the agreement between the calculated curves and the experimental data is quite good which justifies the use of Saunders' dataset for the Al-Cr system [145]. However,

especially in ternary mixtures the diagram reveals certain deviations between the calculations and the experimental data. In order to achieve a better representation of the mixing enthalpies not only the liquid phase but the complete ternary system Al-Cr-Ni would have to be re-optimized which is deferred at the present stage.

Fig. 5-9 compares the calculated liquidus temperatures of the isopleths with chromium contents of 5, 10 and 15 at.% using the revised description of the Al-Cr-Ni system with those from Dupin et al. [28], respectively. The revised description is in reasonable agreement with the calculation results of Dupin et al. [28].

Fig. 5-10 shows the calculated liquidus projection of the Al-Cr-Ni system in the present work. Compared to the calculation of Dupin et al. [28], the B2 primary solidification area expands towards the Cr corner and the bcc primary solidification area shrinks. Accordingly, the ternary eutectic point shifts slightly to the composition $Al_{16.4}Cr_{34.3}Ni_{49.3}$ (at.%). The calculated invariant reaction temperatures of liquid↔fcc+B2+bcc and liquid+$L1_2$↔fcc+B2 are in good agreement with those of Dupin et al. [28]. The largest discrepancy is only 5 K.

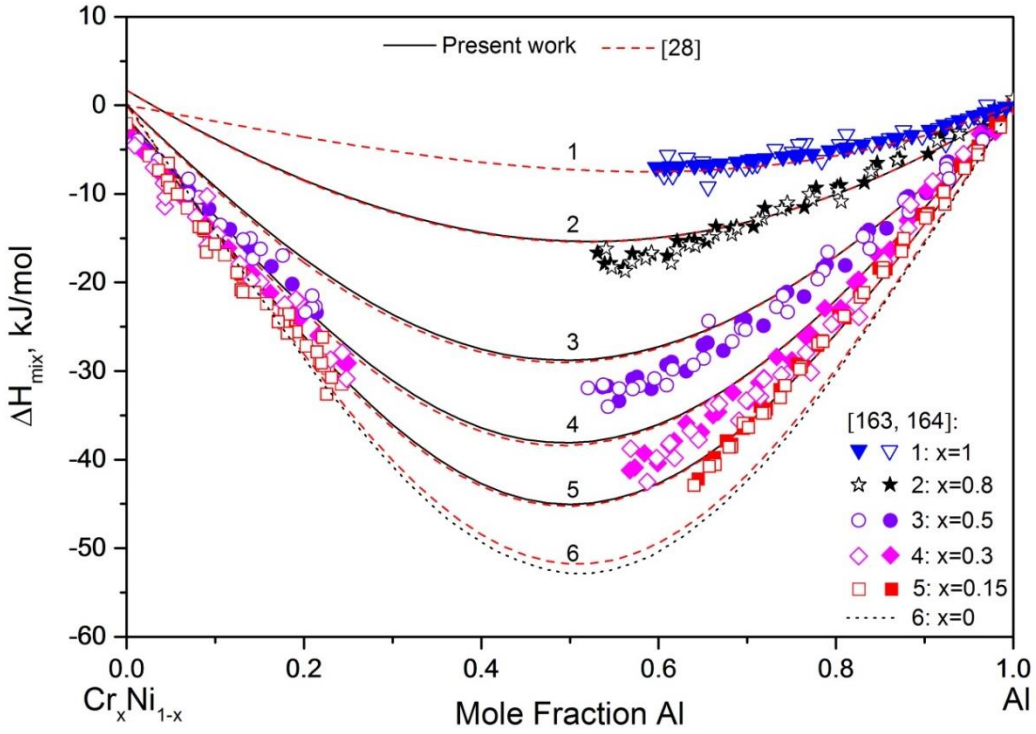

Fig. 5-8 Calculated enthalpies of mixing of the liquid phase in comparison with experimental data of Saltykov et al. [152, 177] at 1718-1831 K.

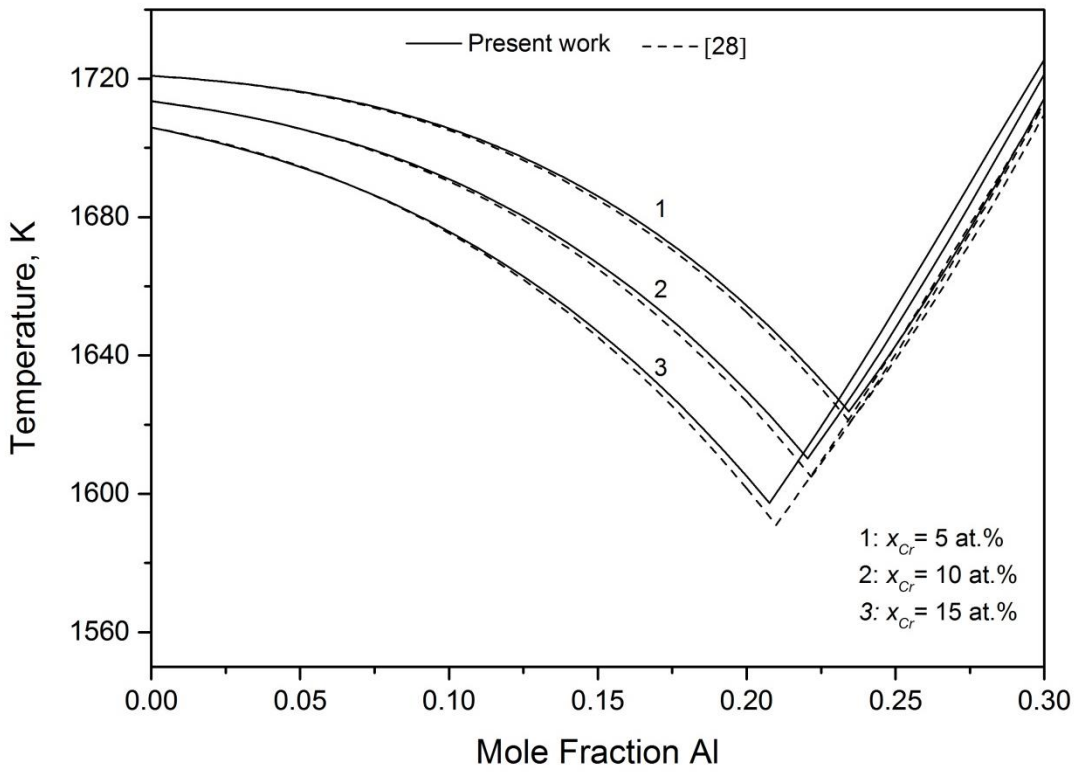

Fig. 5-9 Calculated liquidus temperatures for x_{Cr} = 5, 10, 15 at.% using the revised description of the Al-Cr-Ni system (solid lines) compared to results of Dupin et al. [28] (dashed lines).

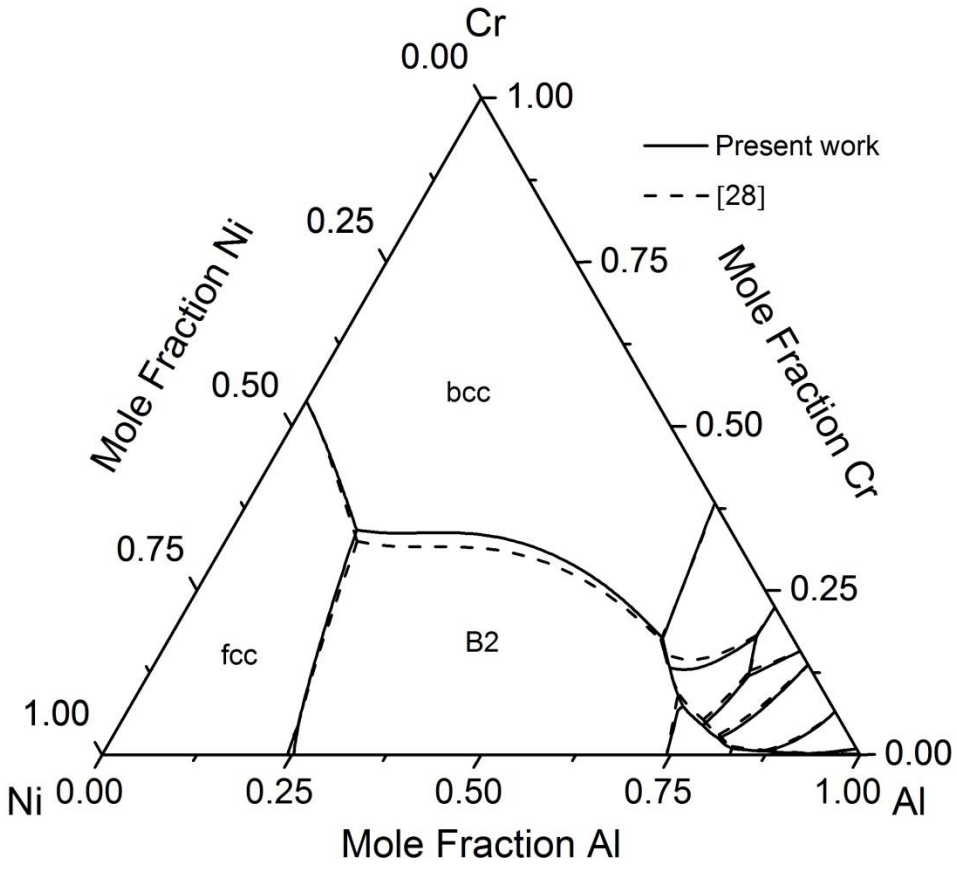

Fig. 5-10 Calculated liquidus surface projection of the Al-Cr-Ni system using the revised description (solid lines) in comparison with that from Dupin et al. [28] (dashed lines).

6. The Cr-Mo-Ni system

6.1 Review of the binary systems

The Cr-Mo-Ni system contains three binary sub-systems, Cr-Mo, Cr-Ni and Mo-Ni. Only a brief review of the Cr-Mo system will be given in the following part, because detailed reviews of the Mo-Ni and Cr-Ni systems have been given in chapters 4.1.3 and 5.1.2, respectively.

6.1.1. Review of the Cr-Mo system

The Cr-Mo system is characterized by continuous solid solution and a miscibility gap in the solid phase at low temperatures. A minimum occurs in the liquidus and solidus lines. An overview of the Cr-Mo system up to 1986 has been performed by Venkatraman and Neumann [180]. The phase diagram from Ref. [180] is shown in Fig. 6-1.

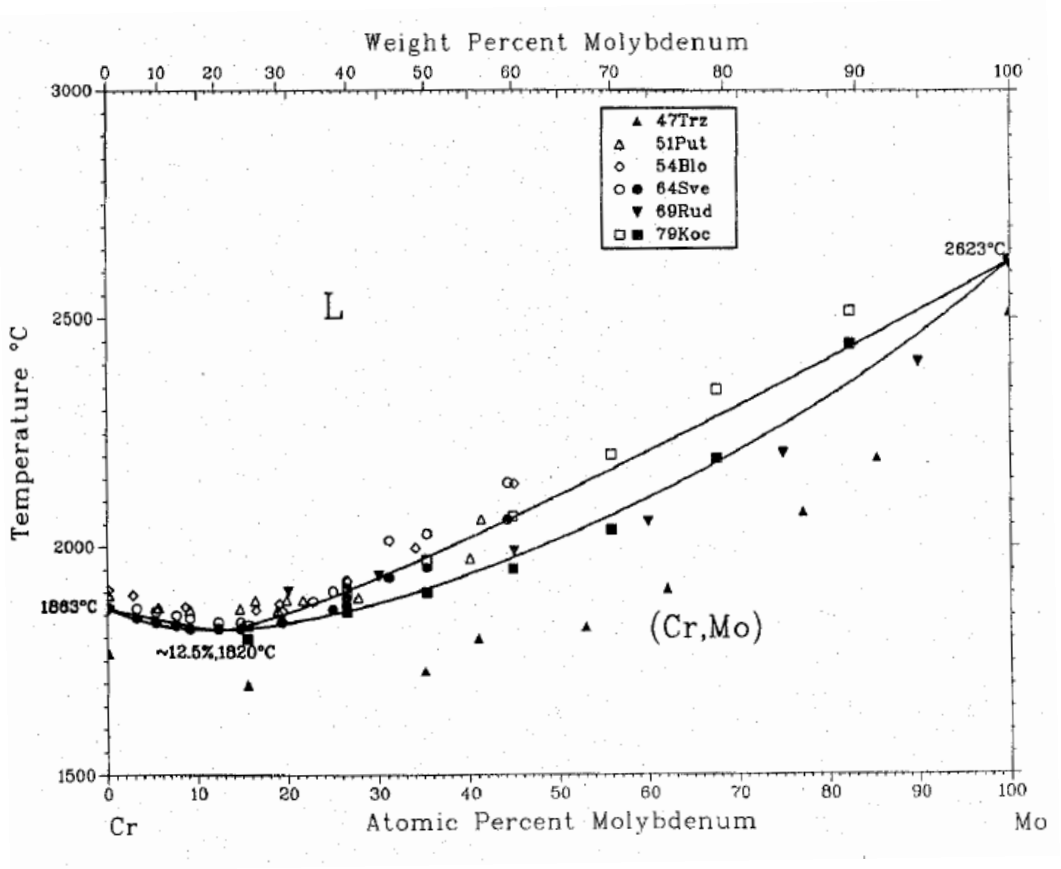

Fig. 6-1 Critically evaluated phase diagram of the Cr-Mo system [180].

The Cr-Mo system has been modeled by Kaufman and Nesor [181], Balakrishna and Mallik [182], Lesnik et al. [183], Frisk and Gustafson [184], Shunyaev [185] and Jindal et al. [186]. The calculated phase diagrams of Refs. [181–183, 185] deviate significantly from the experimental data. The calculated liquidus temperatures of Refs. [181, 185] are obviously lower than the experimental data, while both the calculated liquidus and solidus lines of Ref. [182] are much lower than the experimental data. Good agreement between the calculated liquidus line and the experimental data was obtained in Refs. [184, 186]. Because Rudy [187] did not observe the minimum in the liquidus line, Frisk and Gustafson [184] excluded the data of Ref. [187] and adopted the experimental data from Kocherzhinskii and Vasilenko [188] in the assessment. However, in the assessment by Jindal et al. [186], the experimental data from Rudy [187] were considered, which results in lower solidus temperatures than these of Ref. [184]. Only the calculated miscibility gaps by Frisk and Gustafson [184] and Jindal et al. [186] are consistent with the experimental results from Kubaschewski and Chart [189], who reported the critical temperature of the miscibility gap should lie in between 1173 and 1223 K. In the present work, the dataset from Frisk and Gustafson [184] was adopted and the corresponding diagram is shown in Fig. 6-2.

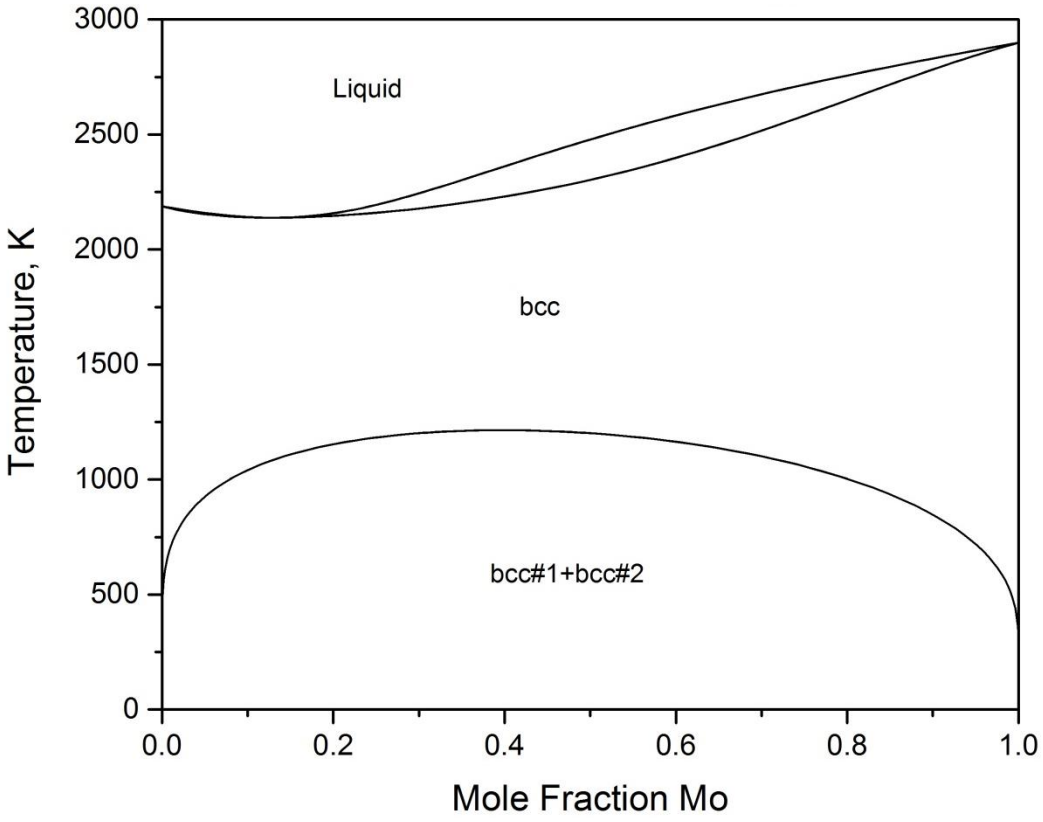

Fig. 6-2 Calculated phase diagram of the Cr-Mo system from Frisk and Gustafson [184].

6.2. Review of the Cr-Mo-Ni system

A detailed review of the Cr-Mo-Ni system has been given by Gupta [190] and Lukas [191]. Besides the phases from the binary systems, three ternary phases, σ, P and μ, were confirmed in this system. The crystallographic data of ternary phases in this system from Refs. [191, 192] are summarized in Table 6-1.

Table 6-1 Crystallographic data of ternary phases in the Cr-Mo-Ni system [191, 192].

Phases	Prototype	Pearson symbol	Space group
σ	CrFe	tP30	$P4_2/mnm$
P	P-CrMoNi	oP56	Pbnm
μ	Fe_7Mo_6	hR39	$R\bar{3}m$

6.2.1. Isothermal sections

Complete and partial isothermal sections of the Cr-Mo-Ni system at 1523 K were determined experimentally by Bloom and Grant [193] and Raghavan et al. [194], respectively. In Ref. [193], the isothermal section comprises bcc, fcc, a ternary extension of the NiMo phase from the Mo-Ni binary system, a ternary extension of a phase denoted β from the Cr-Ni binary system and two ternary phases, σ and P. However, the existence of the β phase contradicts the currently accepted phase diagram of the Cr-Ni system. The isothermal sections at 1523 K constructed in Refs. [193, 194] are in reasonable agreement with each other. The differences are in the solubility of Cr and Mo in the fcc phase as well as the homogeneity ranges of the σ and P phases. Rideout et al. [195] determined the partial isothermal section of the Cr-Mo-Ni system at 1473 K. Similar to the isothermal sections at 1523 K, the ternary phases, σ and P, are also presented. The homogeneity ranges of both phases show better agreement with those reported in Ref. [194] than those in Ref. [193]. Also, the results in Refs. [193–195] indicate that the homogeneity range of the σ phase shrinks with decreasing temperature. Partial isothermal sections at 1473, 1273 and 1073 K with mole fractions of Ni higher than 40 % were constructed by Class et al. [196] based on experimental data. In these isothermal sections, the ternary phases, σ and P, existed. At 1473 K, the results of Refs. [195, 196] are consistent with each other. No μ phase was detected in Ref. [196] at 1073 K, which was inconsistent with the result of Ref. [194], in which the μ phase was observed at 1123 K. Many tielines at 1425 K were determined by Kodentzov et al. [197] using diffusion couples and triples. The isothermal section at 1425 K was constructed. These results show good agreement with the tielines at 1423 K determined by Morizot and Vignes [198]. Tielines at 1373 K determined by Frisk [157] and Selleby [199] are in good consistence with each other. The isothermal section at 873 K is available from Goldschmidt [200]. Besides the σ and P phases, a ternary phase denoted A was also detected. It reported the σ phase existing in a very large area, which contradict results of Refs. [193–195].

6.2.2. Vertical sections

Several partial vertical sections of the Cr-Mo-Ni system were reported by Smiryagin et al. [201]. However, only results in the regions above 1473 K are consistent with these in Refs. [193–195] and significant discrepancy exists in the lower temperature parts.

6.2.3. Liquidus projection

A partial liquidus projection of the Cr-Mo-Ni system was constructed firstly by Siedschlag [202] with the measured melting temperatures of a serials of alloys with less than 50 at.% Mo. However, the reference binary systems were not accurate enough and this projection disagreed considerably with later investigations by Bloom and Grant [193]. In Ref. [193], the melting temperatures of around 100 Cr-Mo-Ni alloys were measured. Based on the experimental data of Ref. [193], a new liquidus projection was constructed by Gupta [190]. It consists of five primary phase regions, NiMo, σ, P, bcc and fcc. Alloys compositions with the melting temperature of 1673 K were available from Smiryagin et al. [201], which showed good agreement with the results of Ref. [193].

6.2.4. Thermodynamics

No experimental thermodynamic data are available for the Cr-Mo-Ni system. The first thermodynamic assessment of this system was developed by Kaufman and Nesor [203]. Later Frisk [157] evaluated a dataset which was based on the element data recommended by SGTE. In addition, the ternary phases, σ and P, were included. SGTE incorporated this assessment into the SSOL database [204], but replaced the binary subset for Cr-Ni with the respective dataset of Lee [155]. However, neither of these databases [157, 204] was adopted in the present work, because the sub-system Mo-Ni differs from the respective choice in the Al-Mo-Ni system [179] (also in chapter 4.6). Therefore, a re-optimization of this system should be performed.

6.3. Re-optimization of the Cr-Mo-Ni system

Only the ternary σ and P phases were considered and the ternary μ phase was excluded in the present work because of the discrepancy at lower temperature.

In the present work, the starting dataset for the re-optimization was a combination of the binary datasets from Lee (Cr-Ni) [155], Zhou et al. (Mo-Ni) [92] and Frisk and Gustafson (Cr-Mo) [184] and original ternary interaction parameters of the ternary phases, σ and P, developed by Frisk [157].

Fig. 6-3 shows the calculated isothermal section of 1523 K using the starting dataset. Apparently, the P phase was too stable that it erroneously extended to the binary Mo-Ni system and the NiMo phase cannot extends to this ternary system. Doubtful homogeneity ranges were obtained for both σ and P phases.

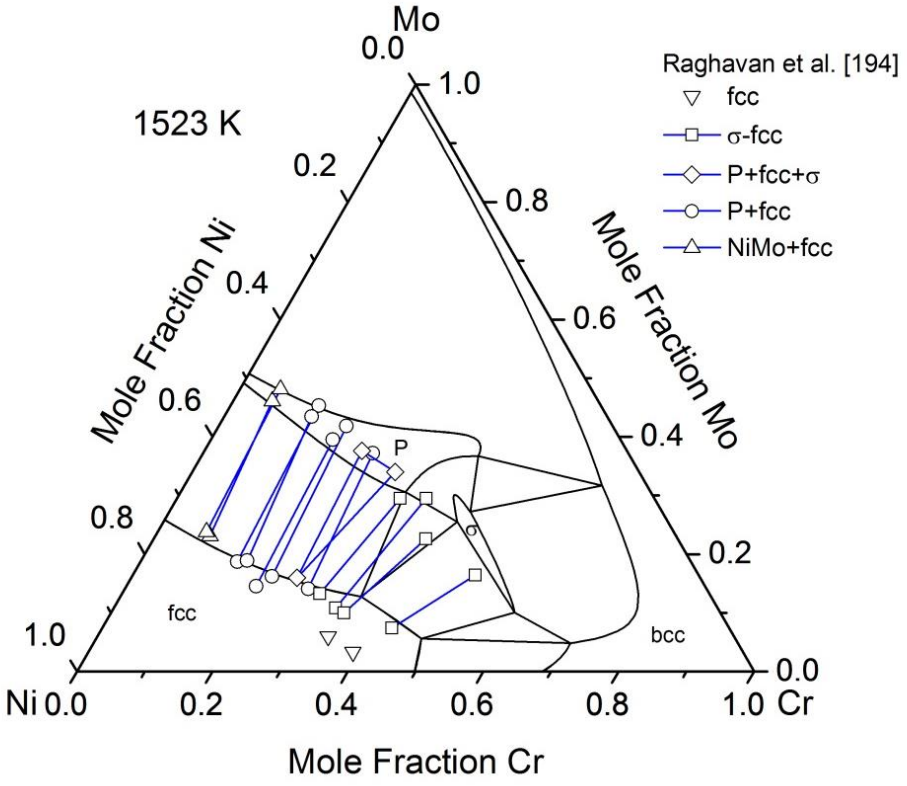

Fig. 6-3 Calculated isothermal section of 1523 K using the starting dataset in comparison with experimental data.

6.3.1. Optimization procedure

At first, the ternary interaction parameters of the P phases were adjusted to destabilize it so that the NiMo phase can extend into the ternary system with the right homogeneity range [193, 194, 196]. Next, the ternary interaction parameters of the σ and fcc phases were optimized to fit the equilibria with the fcc and σ phases [193, 194, 196]. Then, ternary interaction parameters of the liquid phase were assessed to fit the liquidus temperatures determined by Bloom and Grant [193]. To ensure the fcc disordered state is always possible in this system and also after extending this dataset into the quaternary system, the $L1_2$ phase with two sublattices, $(Cr,Mo,Ni)_{0.75}(Cr,Mo,Ni)_{0.25}$ was introduced as a metastable phase in this system and the parameters in Eq. (2-27) and (2-28) were added. The bonding energies u_{CrMo} and corresponding parameters Δu_n in Eq. (2-31) were set to zero. Finally, all ternary parameters were re-optimized simultaneously to reproduce all available experimental data.

6.3.2. Results and discussion

Figs. 6-4 to 6-8 show the calculated isothermal sections at 1523, 1473, 1425 and 1273 K using the present thermodynamic description (solid lines) in comparison with those of Frisk [157] (dashed lines) and the experimental data. Larger solubility of Cr in the NiMo phase is achieved in the present work than in Ref. [157], which is in better agreement with the experimental data [194]. The descriptions of the homogeneity ranges of the bcc and fcc phases are significantly improved. Compared to the calculation of Frisk [157], the homogeneity ranges of the σ phase shifts towards the Ni corner. Fig. 6-7 indicates that the homogeneity ranges of the σ phase at 1425 K should be broader than those predicted in this work. However, the experimental data of Kodentzov [197] are the only available data concerning the equilibria of the σ and bcc phases in the temperature range we considered. Further investigation on the homogeneity ranges of the σ phase is necessary.

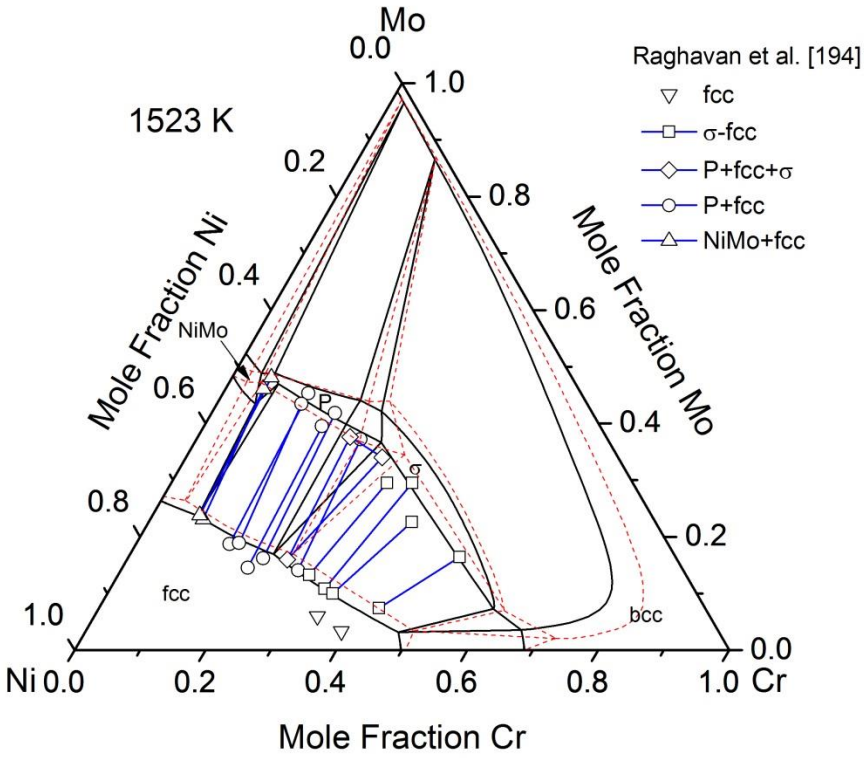

Fig. 6-4 Calculated isothermal section at 1523 K using the present thermodynamic description (solid lines) in comparison with that by Frisk [157] (dashed lines) and the experimental data of Raghavan et al. [194].

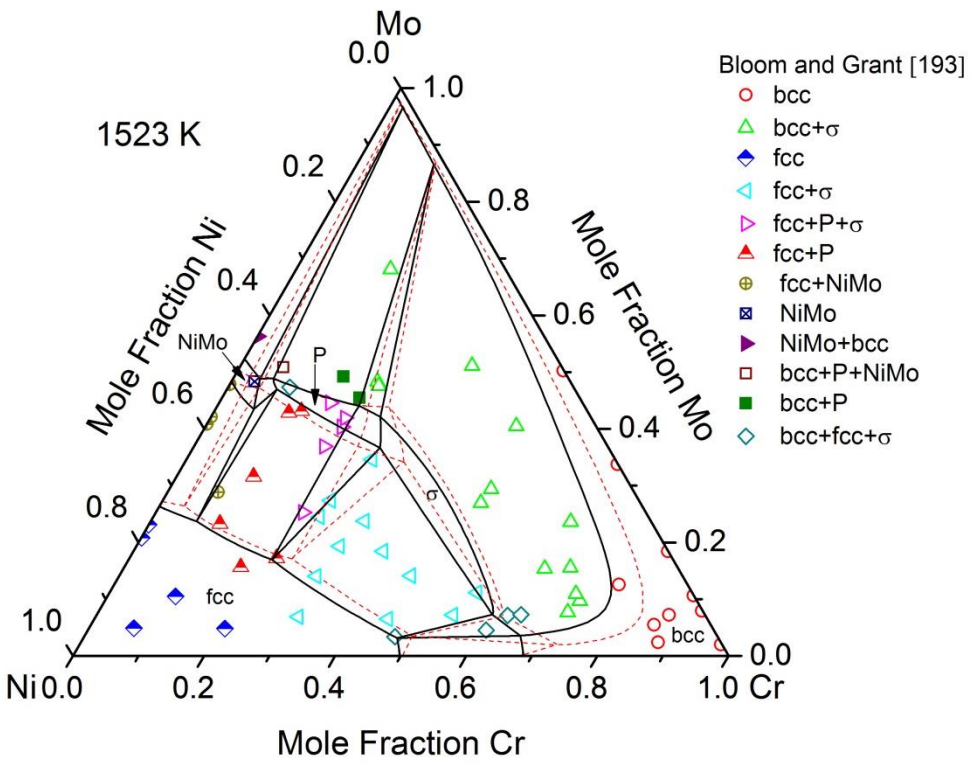

Fig. 6-5 Calculated isothermal section at 1523 K using the present thermodynamic description (solid lines) in comparison with that by Frisk [157] (dashed lines) and the experimental data of Bloom and Grant [193].

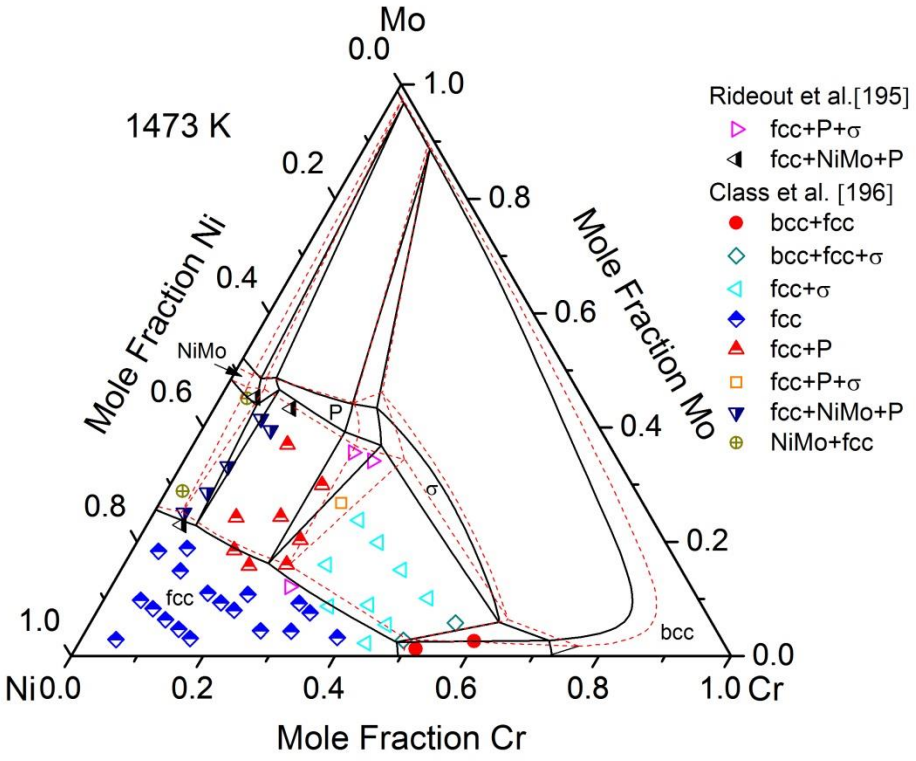

Fig. 6-6 Calculated isothermal section at 1473 K using the present thermodynamic description (solid lines) in comparison with that by Frisk [157] (dashed lines) and the experimental data of Rideout et al [195] and Class et al. [196].

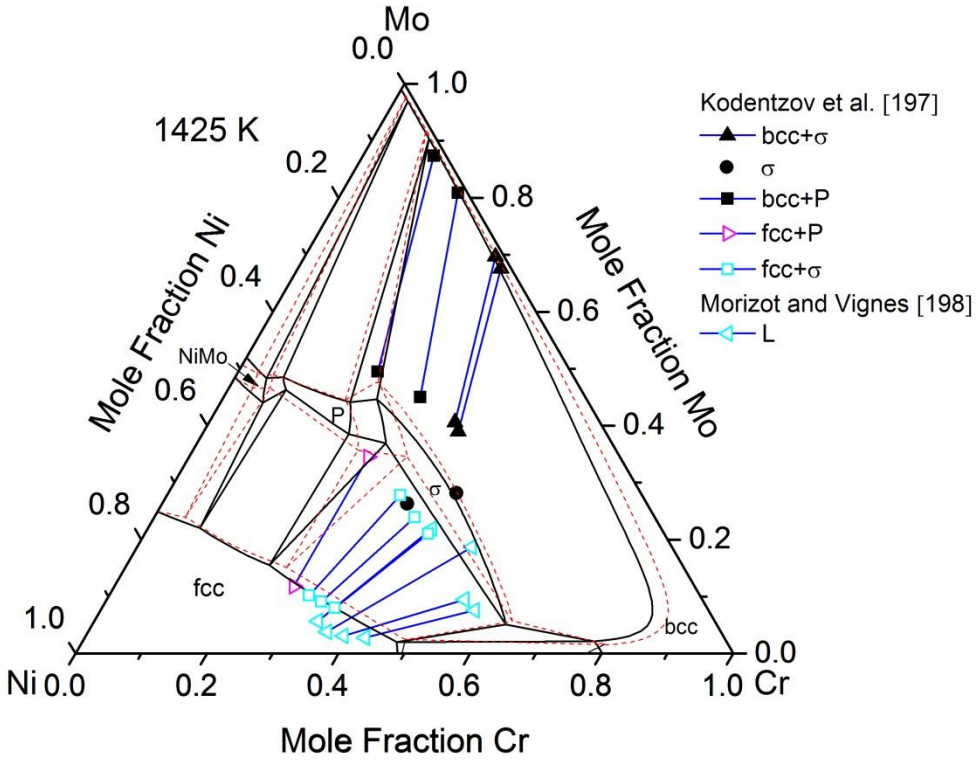

Fig. 6-7 Calculated isothermal section at 1425 K using the present thermodynamic description (solid lines) in comparison with that by Frisk [157] (dashed lines) and the experimental data of Kodentzov [197] and Morizot and Vignes [198].

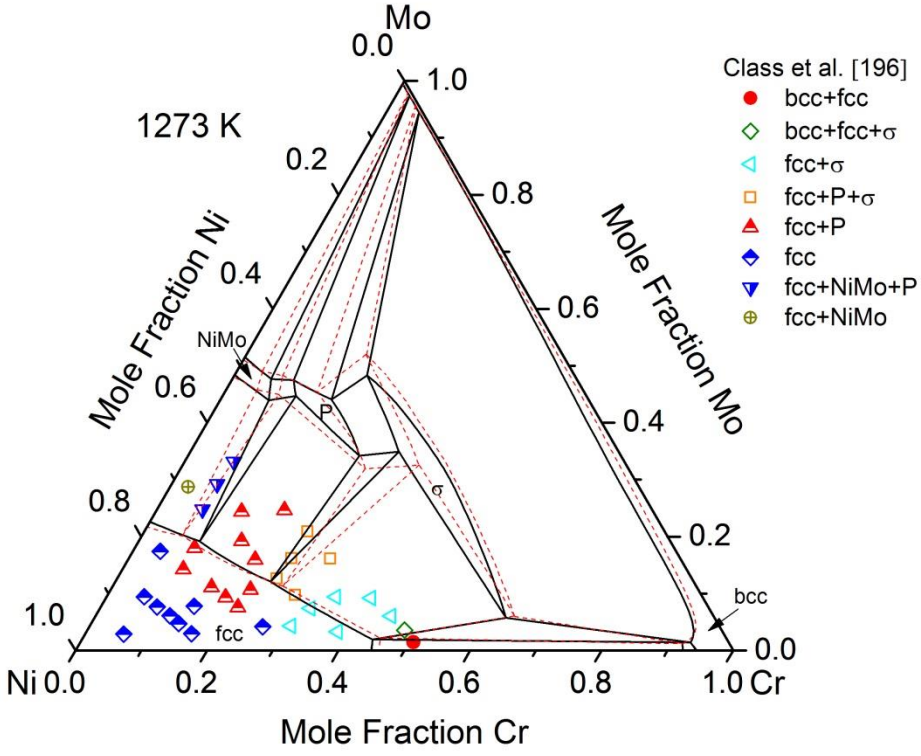

Fig. 6-8 Calculated isothermal section at 1273 K using the present thermodynamic description (solid lines) in comparison with that by Frisk [157] (dashed lines) and the experimental data of Class et al. [196].

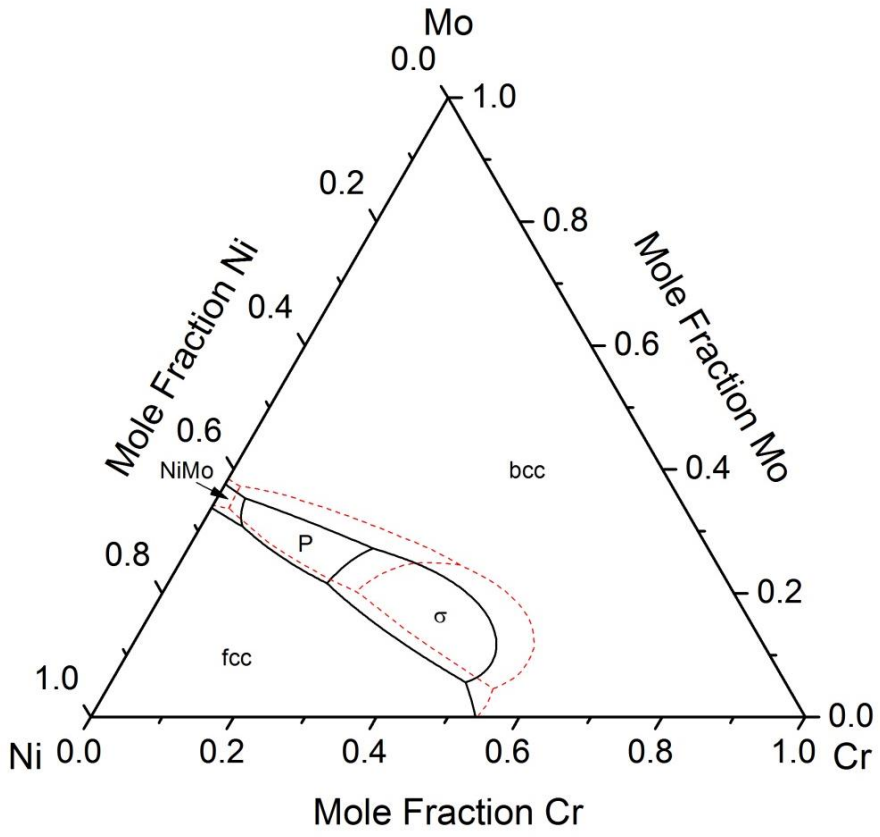

Fig. 6-9 Calculated liquidus projection using the present thermodynamic description (solid lines) in comparison with that by Frisk [157] (dashed lines).

Table 6-2 Calculated invariant reactions temperatures in the Cr-Mo-Ni system in the present work.

Reactions	Temperature, K
Liquid+bcc+σ↔P	1702
Liquid+bcc+P↔NiMo	1620
Liquid↔fcc+bcc+ σ	1604
Liquid↔fcc+P+σ	1604
Liquid+P↔fcc+NiMo	1589

Fig. 6-9 shows the calculated liquidus projection using the present thermodynamic description (solid lines) in comparison with that by Frisk [157] (dashed lines). The primary solidification regions of the NiMo phase expands towards the Cr corner, while that of the P phase shrinks

compared to the calculation of Frisk [157]. The calculated invariant reaction temperatures of the Cr-Mo-Ni system in the present work are listed in Table 6-2.

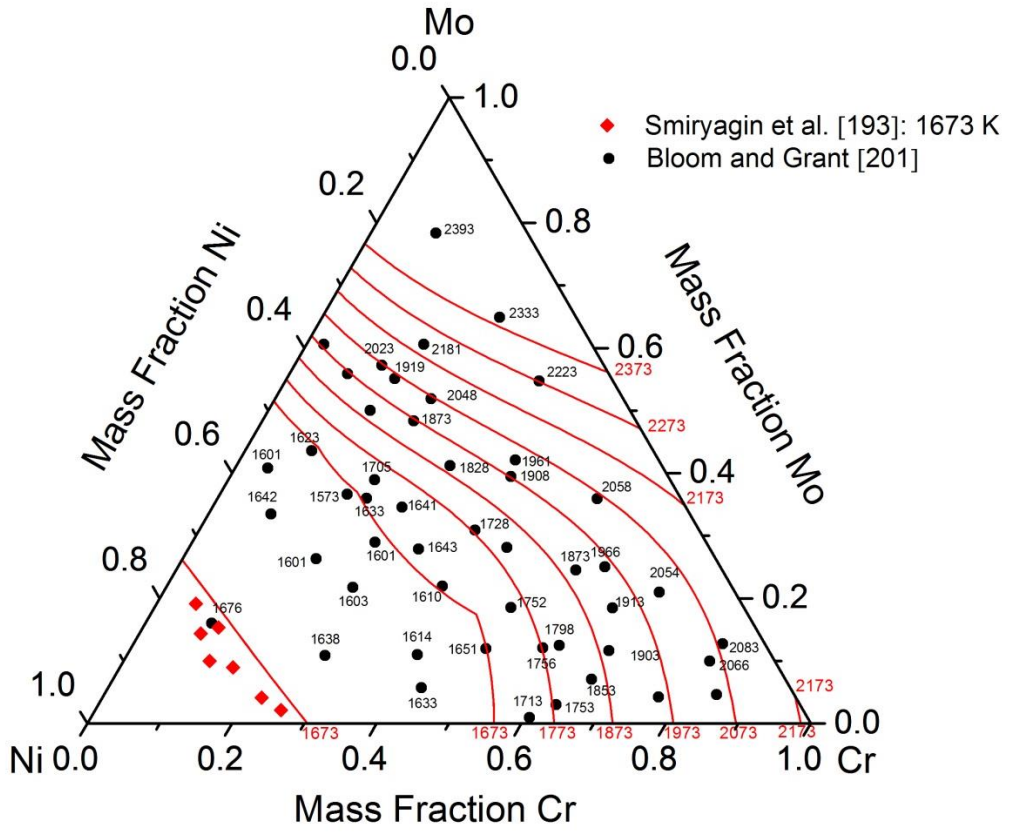

Fig. 6-10 Calculated isothermal lines (solid lines) of the Cr-Mo-Ni system using the present thermodynamic description in comparison with the liquidus temperatures (units, K) measured by Bloom and Grant [193] and Smiryagin et al. [201].

Fig. 6-10 shows the calculated isothermal lines of the Cr-Mo-Ni system using the present thermodynamic description, in which no ternary interaction parameter for the liquid phase was added. The liquidus temperatures determined by Bloom and Grant [193] and Smiryagin et al. [201] were also superimposed for comparison. Since satisfactory agreement between the calculation and the experimental data was obtained, the ternary interaction parameter of the liquid phase was set to zero in the Cr-Mo-Ni system. A similar result was obtained in the assessment of Frisk [157].

7. The Al-Cr-Mo system

7.1. Review of the Al-Cr-Mo system

The Al-Cr-Mo system consists of three binary systems, Al-Cr, Al-Mo and Cr-Mo. Reviews of these systems have been given in previous chapters.

The Al-Cr-Mo system does not attract much attention. Contributions focusing on this ternary system were available from Raman and Schubert [205], Polesya and Stepina [206], Nitischan et al. [207], Escorial et al. [208], Sanchez et al. [209, 210], Akiyama et al. [211] and Kaufman and Nesor [82]. Among them, the experimental works of Natischan et al. [207] and Akiyama et al. [211] focus on the corrosion behavior of the Al-Cr-Mo alloy.

Raman and Schubert [205] prepared five Al-Cr-Mo alloys with ~33 at.% Al with arc melting and the primarily solidified phase, bcc, in the as-cast alloys was determined by XRD.

Supersaturated Al-Cr-Mo ternary solid solutions were studied by some researchers. Polesya and Stepina [206] studied the formation of supersaturated Al-Cr-Mo ternary solid solutions at the cooling rate of 10^6 -10^7 K/s from melts. A solid solution containing 1.66 at.% Cr and 2.10 at.% Mo was obtianed. Melt-spun ribbons of the Al-3 at.% Cr-0.3 at.% Mo were investigated by Escorial et al. [208] in the as-spun condition and after anealing at 623, 673, 723, 773 K for 6 h. When the annealing temperatures were higher than 673 K, $Al_{13}Cr_2$ precipitates were observed in the supersaturated alloys. As the annealing temperature increased, the precipiates coarsed. Microprobe analysis indicated the composition of the precipitates was close to $Al_{13}(Cr_{0.9}Mo_{0.1})_2$ after annealing at 773 K. Powders of Al-3 at.% Cr-0.3 at.% Mo alloys were also prepared by the same group [209, 210] with centrifugal atomisation method and the microsturcture of the powders were observed. Besides the supersaturated Al solid solution, $Al_{13}Cr_2$ also appeared but no $Al_{12}Mo$ was observed.

The thermodynamic calculation of this system were performed by Kaufman and Nesor [82]. Four isothermal sections at 1000, 1500, 2300 and 2500 K were calculated. However, because no experimental data for the ternary system were available at that time, the dataset was just an extrapolation of the binary systems. More recent experimental investigations of the phase diagram and the thermodynamics of this system are very limited. Therefore, it is not possible to thermodynamically assess this system. In the present work, the ternary interaction parameter of the liquid phase in the Al-Cr-Mo system will be optimized to fit the experimental data of the NiAl-Cr-Mo quaternary system. Details are given in chapter 8.2.2.

7.2. Calculation results

Compared with the binary datasets adopted in Ref. [82], the present binary subsets provide better descriptions for the respective binary systems. The descriptions of the binary system are from: Saunders (Al-Cr) [139, 145], Frisk and Gustafson (Cr-Mo) [184] and Peng et al. [179] (also in chapter 4.3.1.2). Thus, in this section, some isothermal sections as well as the liquidus projection will be calculated to provide a better understanding of this system and act as a guide for the experimental investigation of this system in the future. The ternary interaction parameters of the liquid phase and the $L1_2$ phase determined in chapter 8 were included in the Al-Cr-Mo description of the present work. The calculated results will be compared with the available experimental data.

Figs. 7-1 to 7-3 show the isothermal sections at 1000, 1500 and 2000 K, respectively. At 1000 K, the miscibility gap of the binary Cr-Mo system extends into the ternary system. The Al-rich corner is dominated by ternary phase regions which consist of the intermetallic compounds from the binary systems. At 1500 K, the bcc phase region covers almost half of the diagram. At 2000 K, the bcc, liquid and their two phase region dominate the diagram. A two phase region comprising bcc and $AlMo_3$ phases also exists.

Fig. 7-4 shows the calculated liquidus projection of the Al-Cr-Mo system. The experimental data from Raman and Schubert [205] are also superimposed for comparison. The calculation results agree well with the experimental data except the alloy with 7 at.% Mo (red square). Judging from the binary boundary of the Al-Cr system accepted nowadays, the $AlCr_2$ phase is not possible to solidify primarily. The $AlCr_2$ phase appearing in the alloy may be caused by the insufficient cooling rate. In this alloy with 7 at.% Mo, the primary phase should be the bcc phase, which is consistent with the present calculation.

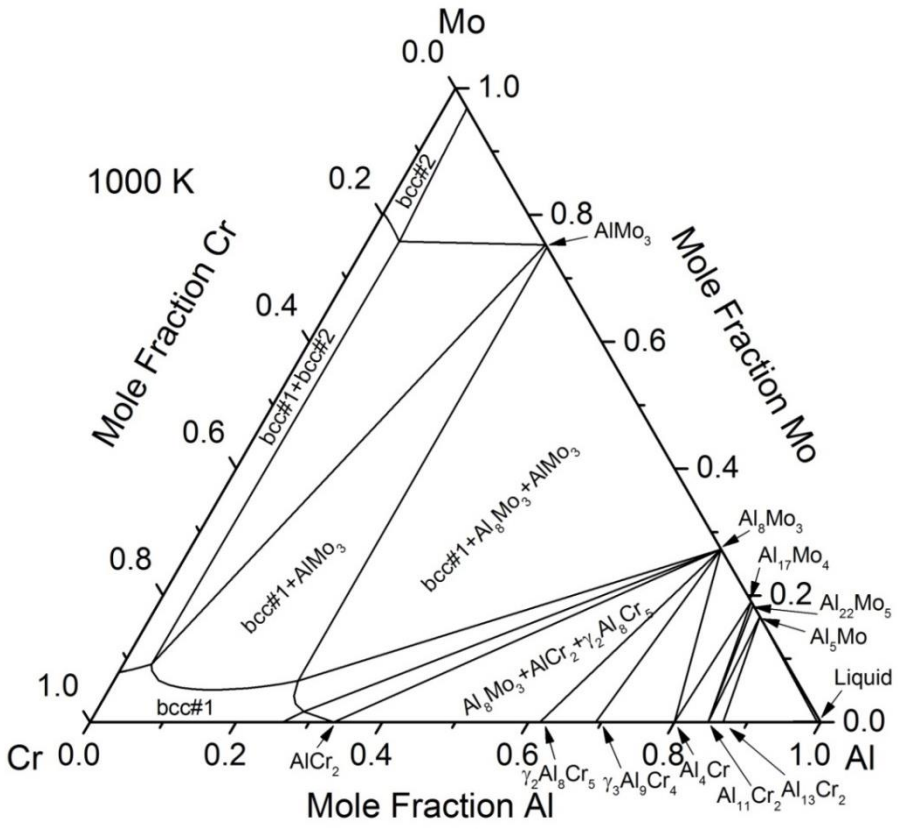

Fig. 7-1 Calculated isothermal section at 1000 K using the present thermodynamic description, in which the ternary interaction parameter of the liquid and $L1_2$ phases determined in chapter 8 were included.

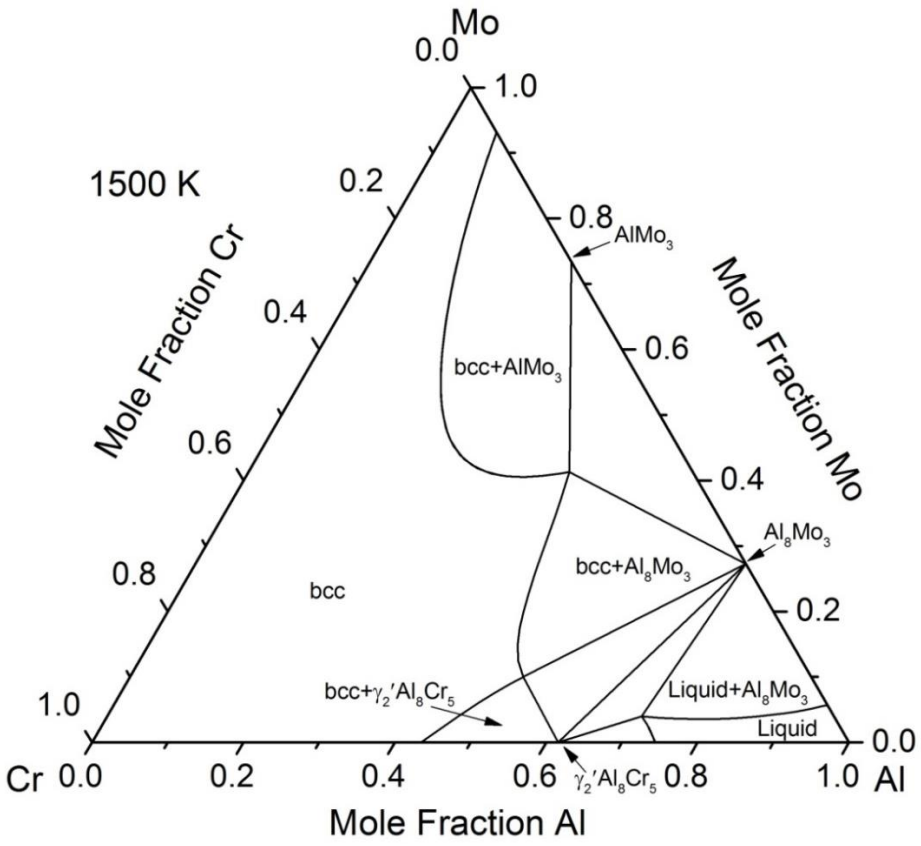

Fig. 7-2 Calculated isothermal section at 1500 K using the present thermodynamic description, in which the ternary interaction parameter of the liquid and $L1_2$ phases determined in chapter 8 were included.

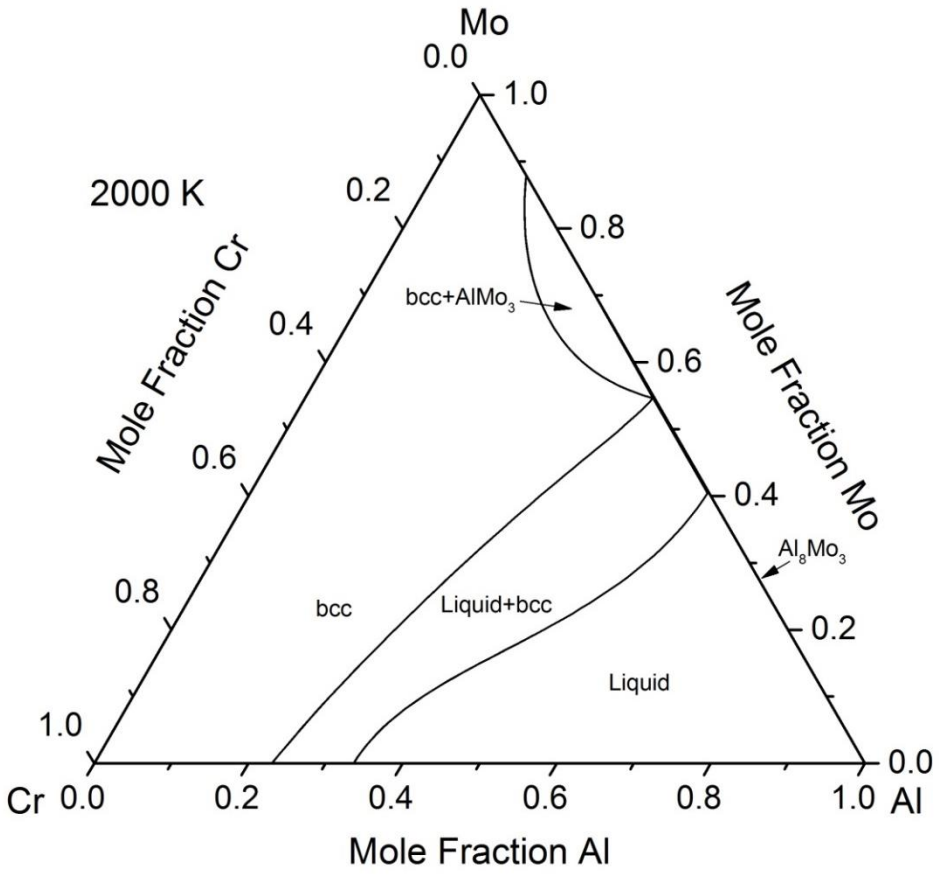

Fig. 7-3 Calculated isothermal section at 2000 K using the present thermodynamic description, in which the ternary interaction parameter of the liquid and $L1_2$ phases determined in chapter 8 were included.

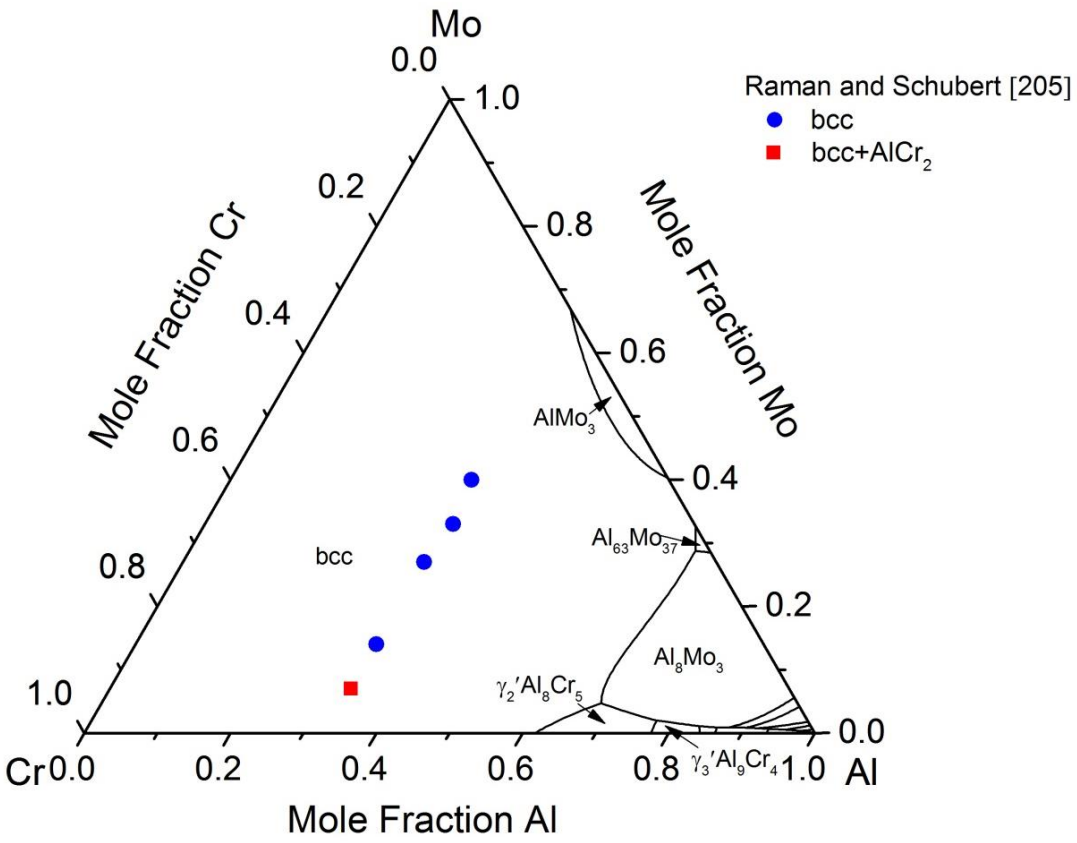

Fig. 7-4 Calculated liquidus projection of the Al-Cr-Mo system using the present thermodynamic description, in which the ternary interaction parameter of the liquid and $L1_2$ phases determined in chapter 8 were included. Experimental data from Raman and Schubert [205] were superimposed for comparison.

8. The Al-Cr-Mo-Ni system

8.1. Review of the Al-Cr-Mo-Ni system

The Al-Cr-Mo-Ni system has been investigated by many researchers, but they mainly focus on the structure and mechanical properties of directional solidified alloys. Limited experimental data (Table 8-1) are available for the thermodynamic modeling of this system.

Table 8-1 Experimental data for the thermodynamic modeling of the Al-Cr-Mo-Ni system.

References	Experimental data	Experimental methods
[111]	75 at. % Ni isopleths at 1073, 1273 and 1523 K	SEM, EDX, XRD, EPMA
[212]	50, 60 at. % Ni isopleths at 1523 K	TEM, EPMA, SEM, EDX, XRD
[213]	50, 60 at. % Ni isopleths at 1073 and 1273 K	TEM, SEM, EDX, XRD
[214]	70 at. % Ni isopleth at 1173 K	TEM, SEM, EDX
[215]	Primary phase of solidified NiAl-Cr-Mo alloys	Light optical techniques
[216]	Primary phase of solidified NiAl-Cr-Mo alloys	SEM, EDX, XRD
[217]	Primary phase of solidified NiAl-Cr-Mo alloys	SEM,TEM
[218]	Primary phase of solidified NiAl-Cr-Mo alloys	OM, TEM, SEM
[219]	Four alloys with 70 at.% Ni annealed at 873 and 1073 K	SEM, TEM, EDX

8.1.1. NiAl-Cr-Mo system

In the as-cast alloy $Ni_{32.51}Al_{32.99}Cr_{33.33}Mo_{1.03}$ (at.%) prepared by Whittenberger et al. [215] using induction melting, primary solidified B2 dendrites were found. The $Ni_{33}Al_{33}Cr_{30}Mo_4$ (at.%) alloy prepared by Zhang et al. [216] with arc melting showed a fully eutectic structure. Wang et al. [217] prepared alloy $Ni_{33}Al_{33}Cr_{31}Mo_3$ (at.%) by induction melting and primary solidified B2 phase was observed. Recently, Shang et al. [218] prepared three alloys, $Ni_{33}Al_{33}Cr_{28}Mo_6$, $Ni_{31}Al_{31}Cr_{32}Mo_6$ and $Ni_{29}Al_{29}Cr_{36}Mo_6$ (at.%), with induction melting. The as-cast $Ni_{33}Al_{33}Cr_{28}Mo_6$ (at.%) alloy showed fully eutectic structure and primary bcc dendrites were observed in the other alloys.

8.1.2. Other sections

Chakravorty and West [111] prepared three Al-Cr-Mo-Ni alloys by arc melting. All these alloys have around 75 at.% Ni and equimolar amounts of Cr and Mo. The alloys were annealed at 1523

for 1 week and quenched in ice water. Then they were heat-treated for 1 week at 1273 K followed by quenching in ice water. After that, the alloys were further heated at 1073 for 1 week and quenched in ice water again. The phases and lattice parameters were identified by XRD and the phase compositions were measured by EPMA. The partial isopleths with 75 at.% Ni at 1073, 1273 and 1523 K were also constructed.

Later, the Al-Cr-Mo-Ni alloys were further studied by Chakravorty et al. [212, 213]. Similar to Ref. [111], alloys were annealed at 1073, 1273 and 1523 K. Four alloys with 60 at.% Ni and equimolar amounts of Cr and Mo and one with 50 at.% Ni were investigated. The phases and lattice parameters and phase compositions were determined. Two partial isopleths with 60 and 50 at.% Ni at 1523 K were constructed.

Experimental information for this quaternary system are also available from Bursik and Svoboda [219]. Four Al-Cr-Mo-Ni alloys containing 70 at.% Ni and different ratios of (Mo+Cr)/Al and Mo/Cr were investigated. The alloys were annealed at 873 or 1073 K up to 3000 h. It was observed that the P and $Ni_2(Cr,Mo)$ phases existed in some of the alloys.

Havránková et al. [214] prepared five quaternary alloys with around 70 at.% Ni. The molar fraction of elements, Al, Cr and Mo, were lower than 15 at.%. The alloys were produced with an induction furnace under argon atmosphere. After annealing for 300 h at 1173 K, the microstructures of the alloys were observed by SEM and the crystal structures were identified by TEM. STEM/EDX was used to measure the composition of the phases. Havránková et al. [214] also performed thermodynamic calculation for this system. The calculated composition of each phase agrees reasonably well with the experimental data. However, The database used in Ref. [214] is just a simple combination of databases from Lu et al. [25] (Al-Mo-Ni), Frisk [157] (Cr-Mo-Ni) and Dupin et al. [29] (Al-Ni-Cr) and Huang and Chang [27] (Al-Ni). No new parameters were added and optimized. It cannot reproduce the experimental data in Refs. [215–218], so it is not capable of supporting the selection of NiAl-Cr-Mo eutectic alloys for directional solidification and other simulations. It also has to be mentioned that the constraints for the ordered $L1_2$ phase were included in modeling of the Al-Cr-Ni [29] and Al-Mo-Ni [25] systems to ensure that the disordered state is always possible, but Havránková et al. [214] did not introduce these constraints into the binary Cr-Mo, ternary Cr-Mo-Ni and Al-Cr-Mo, and Al-Cr-Mo-Ni systems. Thus, the thermodynamic description of the disordered fcc phase in Ref. [214] was not correct because the fcc phase was actually not properly disordered.

In the chapter 8.3, the constraints for the $L1_2$ phase will be introduced into the binary Cr-Mo, ternary Cr-Mo-Ni and Al-Cr-Mo, and quaternary systems. Calculation results will be compared with the experimental data to validate the dataset of the Al-Cr-Mo-Ni system established in the present work.

8.2. The NiAl-Cr-Mo system

8.2.1. Experimental investigation

To determine the eutectic trough of the NiAl-Cr-Mo by solidification experiments, alloys with the compositions listed in Table 8-2 were prepared with the procedure introduced in chapter 4.5.1. The crystallographic data of the phases in samples No. 6, 7 and 8 were identified by a PADII X-ray diffractometer. The microstructures of the samples were observed with a scanning electron microscope (FEI XL30S, PHILIPS). The solidus temperatures of samples No. 6 and 7 were measured by a differential thermal analysis instrument (SETSYS Evolution, SETARAM Instrumentation). The samples were heated up to 1773 K with a heating rate of 10 K/min under an argon atmosphere.

Table 8-2 Alloy compositions (at. %) and primary phases.

Alloy No.	Al	Ni	Mo	Cr	Primary phases
3	34.0	34.0	0.5	31.6	B2
4	36.1	36.1	0.6	27.2	B2
5	35.2	35.2	2.9	26.8	B2
6	34.2	34.2	4.5	27.2	B2
7	33.3	33.3	6.3	27.1	eutectic
8	32.8	32.8	7.5	26.9	bcc
9	38.2	38.2	4.4	19.3	B2
10	37.5	37.5	6.0	19.0	B2
11	35.9	35.9	9.3	18.9	B2
12	35.7	35.7	9.8	18.9	bcc
13	34.5	34.5	12.1	18.9	bcc
14	40.3	40.3	4.4	15.1	B2
15	40.8	40.8	8.9	9.5	B2
16	40.1	40.1	10.3	9.6	eutectic
17	39.0	39.0	12.1	9.9	bcc
18	36.1	36.1	15.5	12.4	bcc
19	44.9	44.9	8.8	1.5	B2
20	43.5	43.5	11.6	1.5	bcc

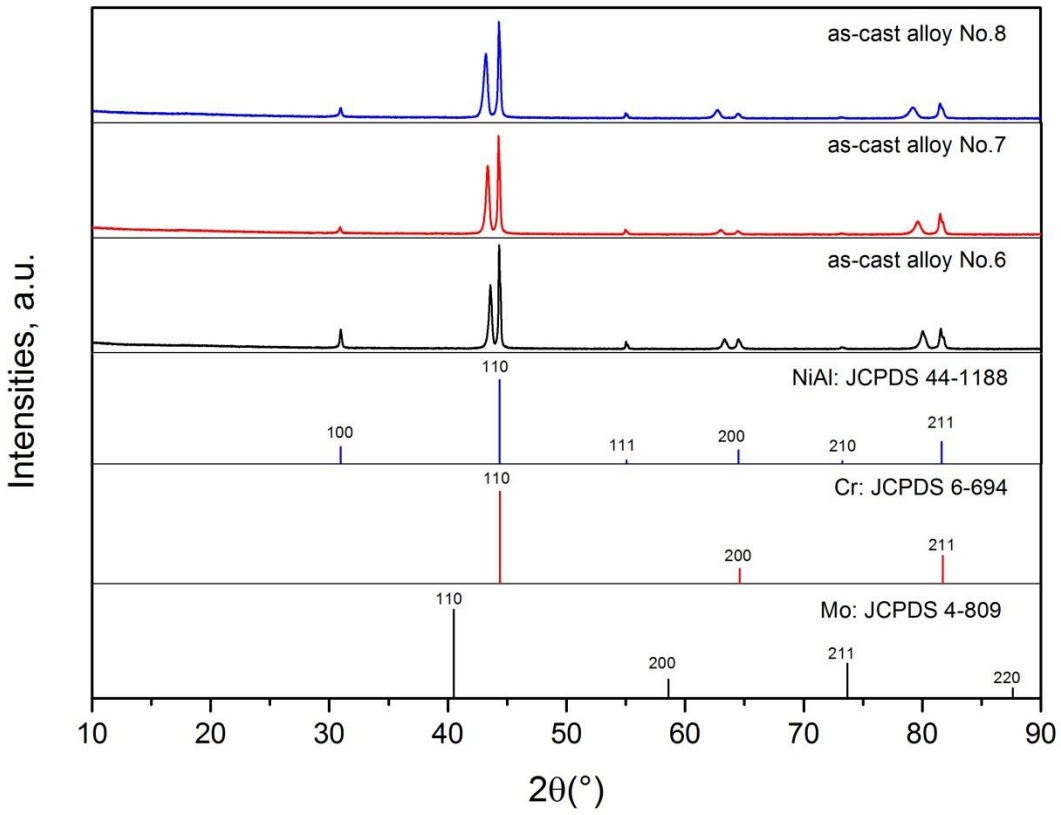

Fig. 8-1 XRD patterns of (a) JCPDS 4-809 data, (b) JCPDS 6-694 data, (c) JCPDS 44-1188 data, (d) as-cast alloy No. 6, (e) as-cast alloy No. 7 and (f) as-cast alloy No. 8.

Fig. 8-1 shows the XRD patterns of as-cast alloys No. 6, 7 and 8. The standard patterns of Cr (JCPDS 6-694), Mo (JCPDS 4-809) and NiAl (JCPDS 44-1188) are also presented for comparison. The peaks of NiAl can be identified well in the patterns of the alloys. It is observed in Fig. 8-1 that three peaks alloys close to the (110), (200) and (211) peaks of NiAl shift towards lower angle side with increasing Mo content in alloys No. 6, 7 and 8. As introduced in section 6.1.1, Cr and Mo can form continuous solid solution. Adding Mo into the bcc_(Cr) unit cell will result in larger lattice parameters, which has been experimentally proved in previous works, as reviewed in Ref. [180]. According to the Bragg's Law, the larger the lattice parameter is, the smaller the diffraction angle will be. So it is safe to conclude that the three peaks close to the (110), (200) and (211) peaks belongs to the bcc_(Cr, Mo) solid solution and the alloys No. 6, 7 and 8 only consist of two phases, NiAl (B2) and bcc.

The results of the microstructural investigations of all alloys are summarized in Table 8-2. Fig. 8-2 presents the microstructures of alloys No.10, 11, 12 and 13 as an example. These alloys have a constant Cr content of around 18.9 at.%. Primary B2 dendrites and eutectic regions were observed in the micrographs of alloys No. 10 and 11. With the addition of more Mo, small amounts of button-like bcc phase appeared in alloy No.12. Dendrites of the bcc phase were also observed in alloy

No.13 as the Mo content further increased. Therefore, the eutectic trough must be located between 9.3 and 9.8 at.% Mo at a chromium concentration of 18.9 at.%. In the same way, the position of the eutectic trough at other compositions can be narrowed to small concentration ranges.

Alloys No. 6 and 7 were investigated by DTA and the respective heating curves are shown in Fig. 8-3. Broad endothermic peaks with widths of about 50 K were detected for both alloys. The onset temperature was determined at the point where the first deviation from the baseline was detected [34]. The onset (solidus) temperatures of alloys No. 6 and 7 were 1710 K and 1713 K, respectively. Because of the broad peaks, the liquidus temperature cannot be determined.

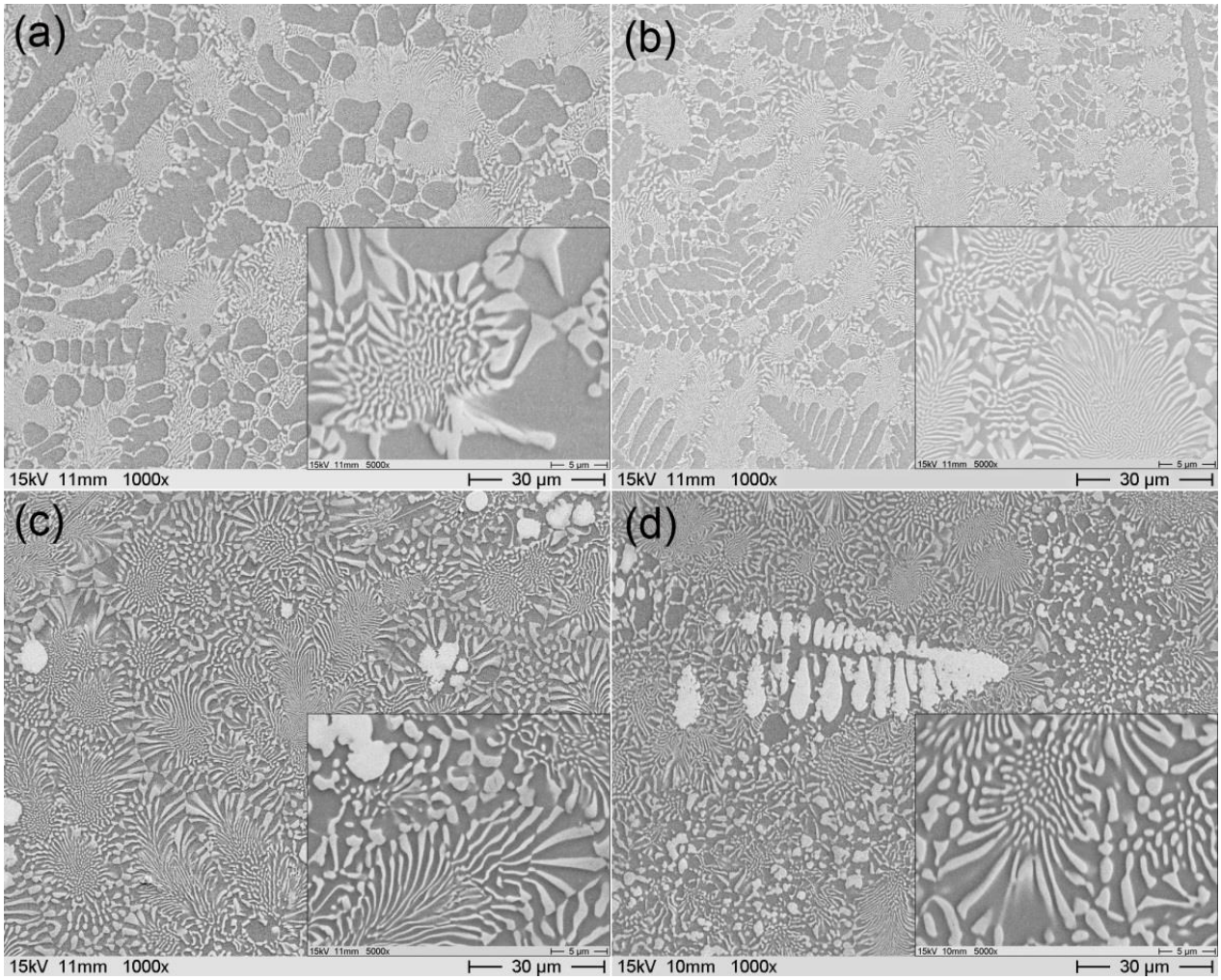

Fig. 8-2 Microstructure of as-cast alloys (a) No. 10, (b) No. 11, (c) No. 12 and (d) No. 13.

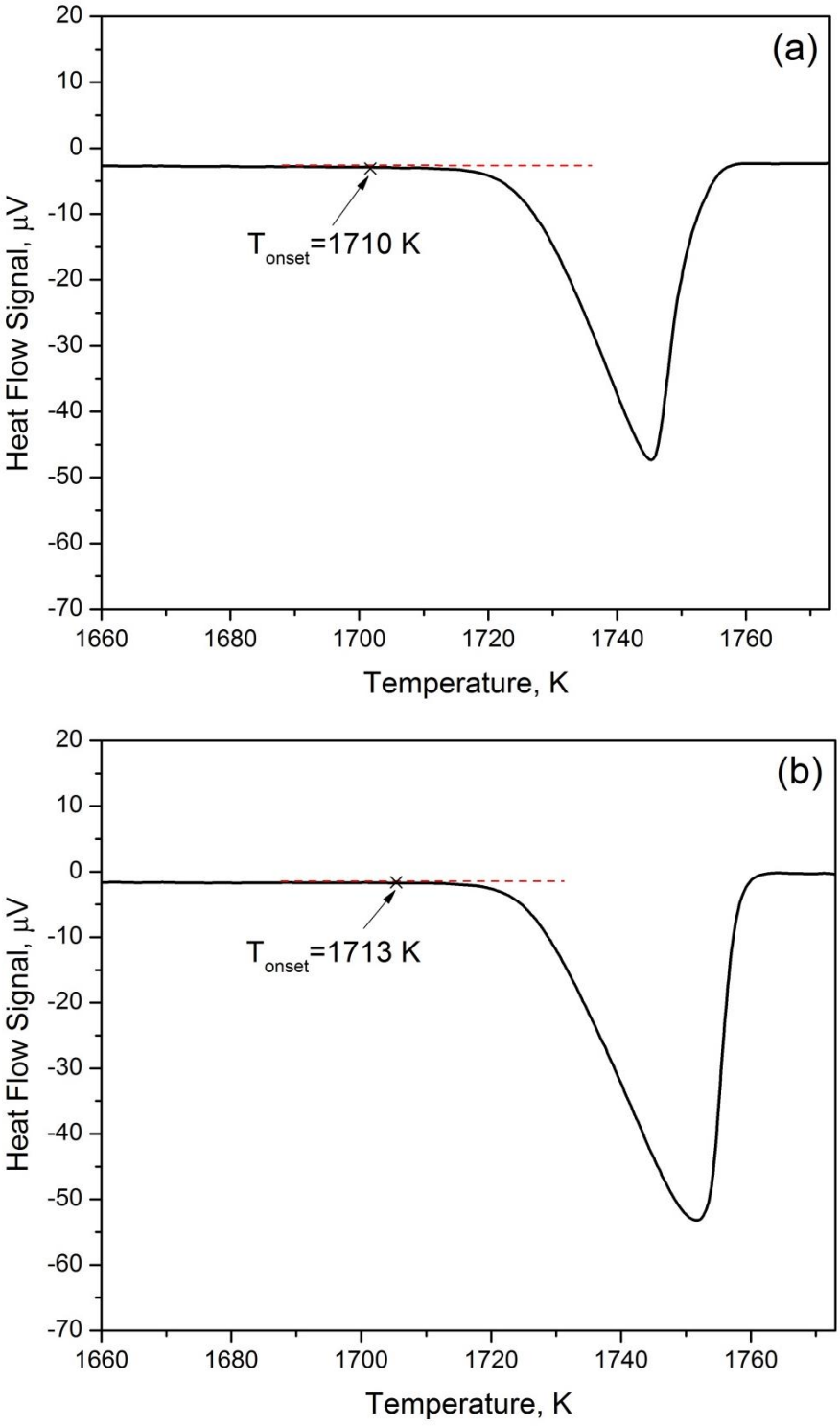

Fig. 8-3 Heating curves of samples (a) No. 6 and (b) No. 7.

8.2.2. Optimization results and discussion

A thermodynamic evaluation of the phases and transformations which are relevant for the formation of NiAl-composites with embedded metal fibers has to consider just three phases: the liquid, the refractory metal based bcc-phase, and the NiAl phase with B2 structure. In both ternary systems, Al-Ni-Cr and Al-Ni-Mo, there is a compositional range with stable phase equilibria involving only the mentioned phases and the same holds for the quaternary system.

The quaternary system NiAl-Cr-Mo includes four ternary sub-systems, Al-Cr-Ni, Al-Cr-Mo, Al-Mo-Ni and Cr-Mo-Ni. In the present work, the ternary datasets are selected from Peng et al. (Al-Mo-Ni) [179] (also in chapter 4.6), Peng et al. (Al-Cr-Ni) [220] (also in chapter 5.4. The assessment is based on the work of Dupin et al. [28], but the liquid phase is re-optimized) and assessment of the Cr-Mo-Ni system in chapter 6.3. The available data on the thermodynamic properties and phase equilibria of the Al-Cr-Mo system are so limited that it is not possible to perform a reasonable assessment for this system. However, one interaction parameter of the liquid phase of the Al-Cr-Mo system was considered in the present work, because it can contribute to the behavior of the liquid phase in the NiAl-Cr-Mo quaternary system.

To obtain the thermodynamic description of the NiAl-Cr-Mo system, the selected and revised ternary databases in the present work were merged. One ternary interaction parameter of the liquid phase in the Al-Cr-Mo system was optimized to fit the experimental data in Table 8-2.

Fig. 8-4 shows the calculated partial liquidus surface of the NiAl-Cr-Mo system using the present thermodynamic description in comparison with the experimental data of the present work and from the literature [215–218]. It can be seen that our results are consistent with the experimental data in the literature. The calculated eutectic trough proceeds through the eutectic compositions and it separates the symbols for the primary solidified phases B2 and bcc, which indicates a good agreement between the calculation and the experimental data.

To further verify the reliability of our database, the solidus temperatures of samples No. 6 and 7 were measured and compared with the calculation. Fig. 8-5 shows the calculated isopleth through the system NiAl-Cr-Mo at 27.1 at.% Cr including the solidus temperatures of samples No. 6 and 7. Our calculated solidus temperatures fit well with the experimental data, which further indicates the reliability of the NiAl-Cr-Mo database of the present work. The calculation reveals only a small difference between the liquidus and solidus temperatures in this isopleth, which explains the appearance of only one signal in the heating curves of samples No. 6 and 7.

Fig. 8-6 shows the calculated eutectic temperatures along the eutectic trough. It can be seen that the eutectic temperatures decrease almost continuously from the NiAl-Mo side to NiAl-Cr. Close to the latter end a shallow minimum is located at 1716 K and 32 at.% Cr.

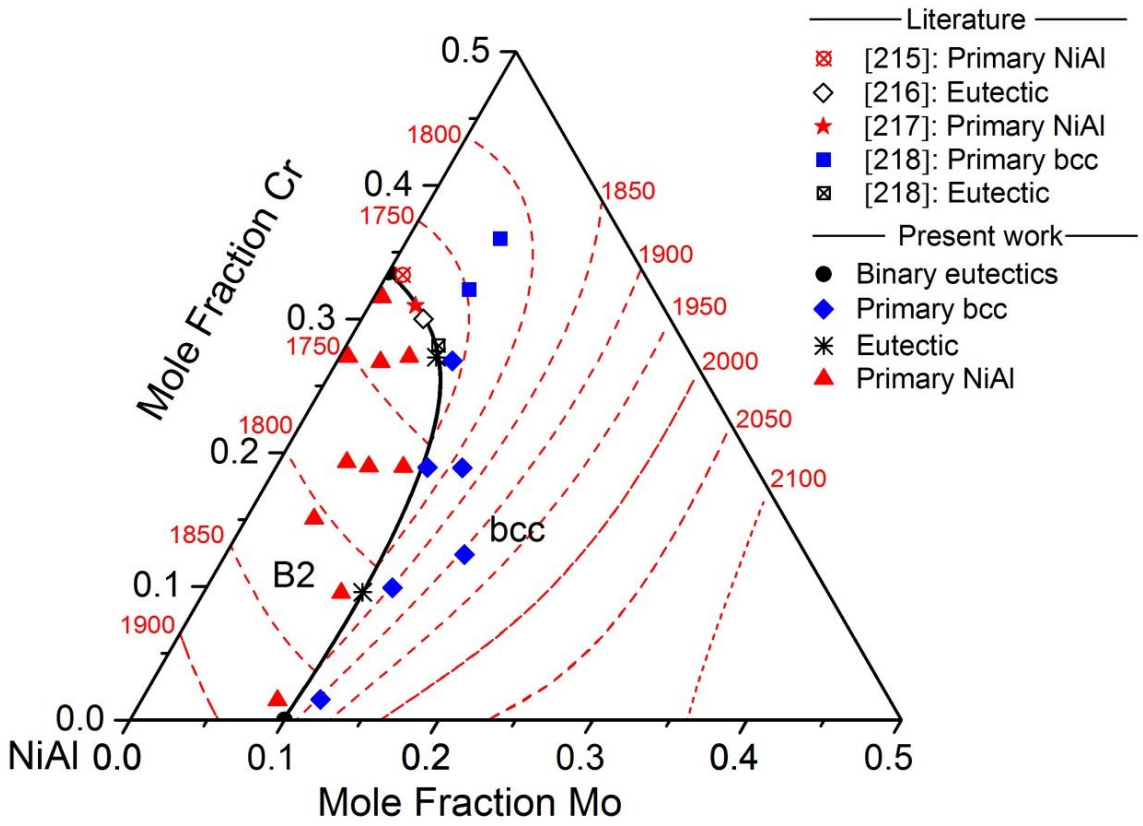

Fig. 8-4 Calculated partial liquidus surface of the NiAl-Cr-Mo system using the present thermodynamic description in comparison with the experimental data (temperatures in K).

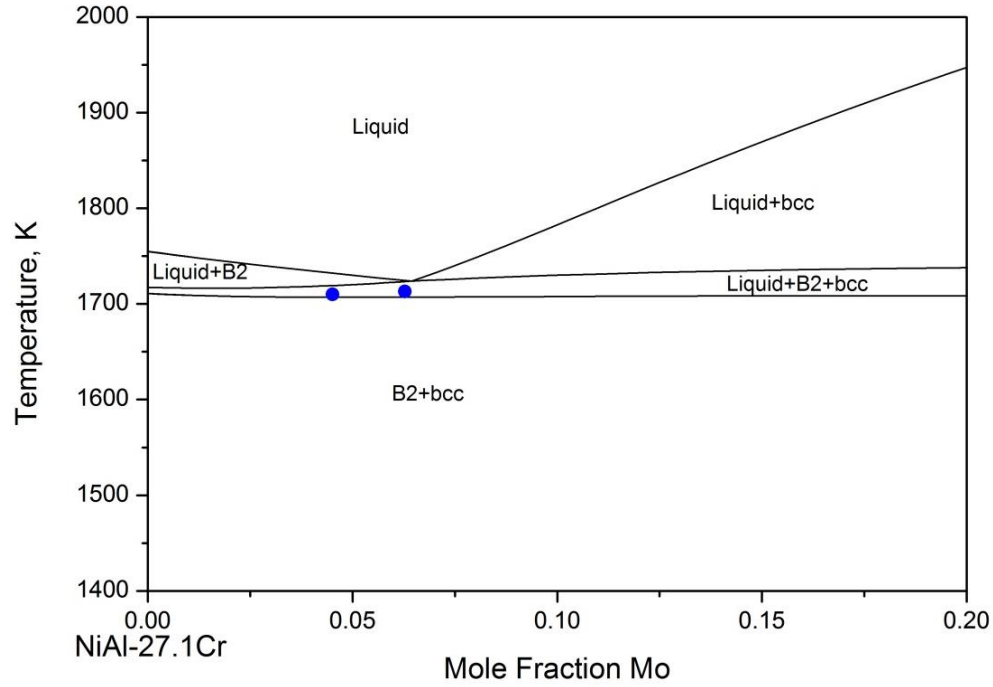

Fig. 8-5 Calculated partial isopleth through the system NiAl-Cr-Mo at 27.1 at.% Cr including experimental data.

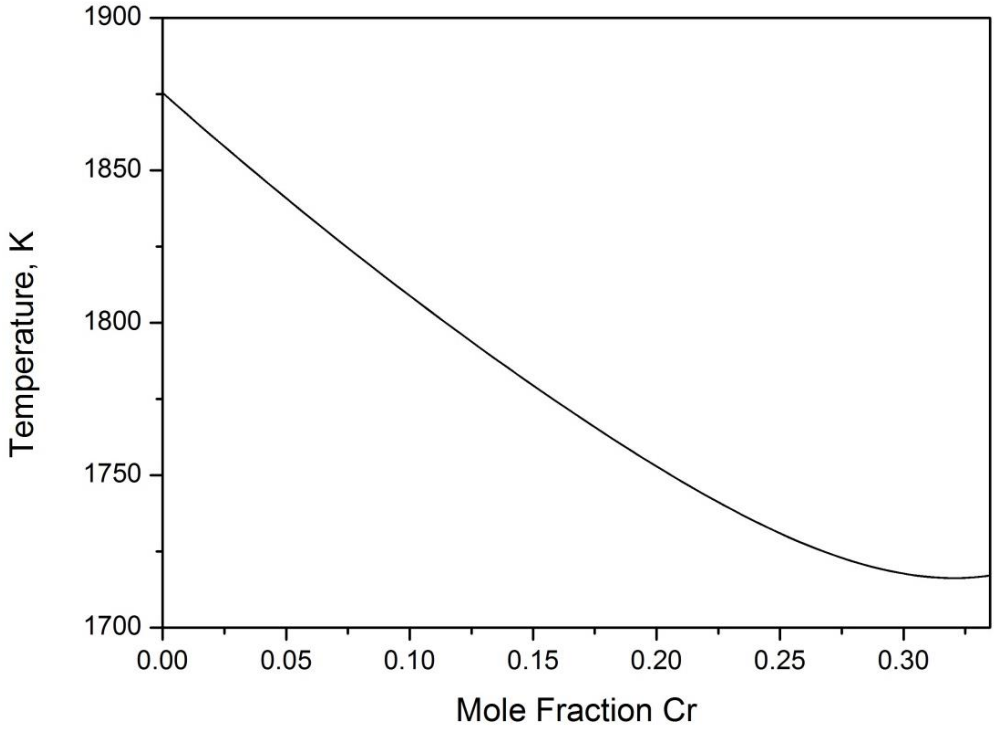

Fig. 8-6 Calculated eutectic temperatures of the NiAl-Cr-Mo system along the eutectic trough.

Fig. 8-7 presents the calculated atomic ratio of Ni to Al in the B2 phase along the eutectic trough. Across the whole range, the B2 phase contains an excess of Ni over Al. The ratio varies only slightly between 1.003 and 1.012 with a maximum at 26.5 at% Cr. Since the ratio of Ni:Al is always close to 1:1, the projection of the eutectic trough on the plane of NiAl-Cr-Mo is feasible, as shown in Fig. 8-3.

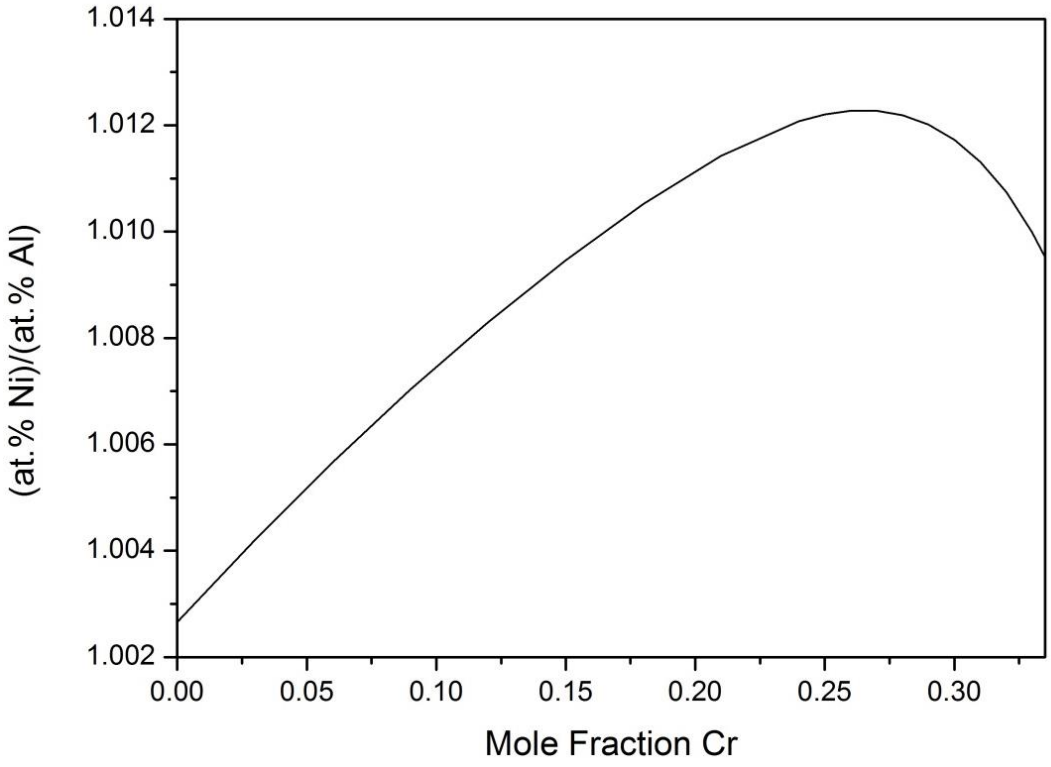

Fig. 8-7 Calculated atomic ratio of Ni to Al in the B2 phase of the NiAl-Cr-Mo system along the eutectic trough.

Fig. 8-8 shows the calculated mole fraction of the bcc phase along the eutectic compositions. It is well-known that the phase fraction of the strengthening phase has significant influence on the mechanical properties of the *in-situ* composite [218]. The diagram reveals that the molar amount of the bcc phase embedded in the NiAl-(Cr,Mo) composite can be varied continuously from 10.7 % at the NiAl-Mo side to 33.2 % at the NiAl-Cr side. In-between, the amount of bcc phase proceeds through a maximum of 34.6 % at 30 at.% Cr.

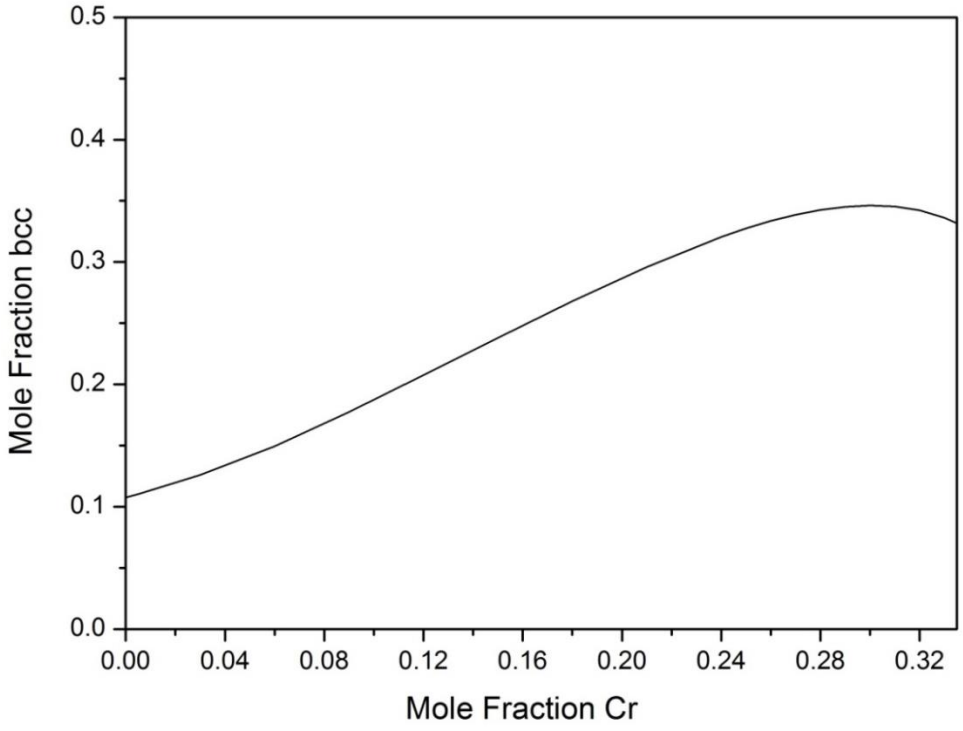

Fig. 8-8 Calculated mole fraction of the bcc phase of the NiAl-Cr-Mo system along the eutectic composition.

8.3. Other sections of the Al-Cr-Mo-Ni system

8.3.1. Thermodynamic modeling

No thermodynamic data of this quaternary system were available. To further extend the application range of the present thermodynamic description to other regions of the Al-Cr-Mo-Ni, especially for the Ni-rich region, the descriptions of the fcc and $L1_2$ phases (the γ and γ′ phases in Ni-based superalloys) in this system were completed. The established database presents correct and better descriptions of the fcc and $L1_2$ phases. In the thermodynamic descriptions of the ternary Al-Cr-Ni [28, 220] (also in chapter 5.4), Al-Mo-Ni [179] (also in chapter 4.6) and Cr-Mo-Ni (present work, chapter 6.3) systems, the fcc and $L1_2$ phases were modeled with a single Gibbs energy function and the constraints for the $L1_2$ phase introduced in chapter 2.1.5 were included to ensure the fcc phase can be properly disordered in this systems. Thus, to ensure the fcc phase can also be properly disordered in the Al-Cr-Mo-Ni system, the $L1_2$ phase was also introduced as a metastable phase into the Al-Cr-Mo system under the constraints of Eq. (2-28). Quaternary parameters in Eq. (2-29) were assessed for the $L1_2$ phase in the Al-Cr-Mo-Ni system. The corresponding parameters Δu_3 to Δu_6 were set to zero. The set of the thermodynamic parameters is given in the appendix.

8.3.2. Calculation results and discussion

Fig. 8-9 compares the calculated 71.3 at.% Ni section of the system Al-Cr-Mo-Ni at 1173K with the experimental data from Havránková et al. [214]. Good agreement is obtained between the calculations and experimental data. Table 8-3 compares the calculated phase compositions and phase fractions with the experimental data [214]. Not only the composition of each phase fits reasonably well with the experimental data, but also satisfactory agreement between the phase fractions (*f*) is obtained. The phase compositions cannot be depicted in the diagram because the tie-lines are not in the plane of the section in Fig. 8-9. Al is not considered in the modeling of the P phase, so the calculated mole fraction of Al is 0 in all alloys. However, the experimentally determined solubility of Al in the P phase is small, so the calculated results are acceptable.

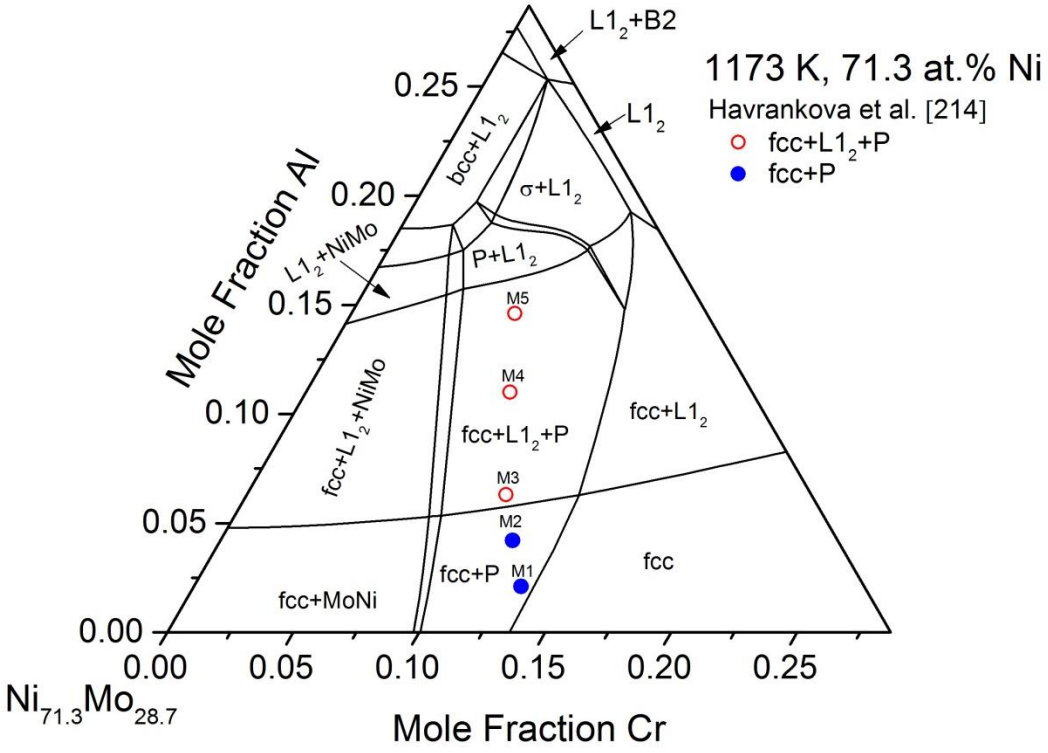

Fig. 8-9 Calculated 71.3 at.% Ni section of the system Al-Cr-Mo-Ni at 1173 K in comparison with the experimental data from Havránková et al. [214].

Table 8-3 Calculated phase compositions and their phase fraction (at.%) at 1173 K in comparison with experimental data from Havránková et al. [214].

Alloys	Phases	Calculated results					Experimental results				
		Al	Ni	Cr	Mo	*f*	Al	Ni	Cr	Mo	*f*
M1	fcc	2.2	71.6	12.8	13.4	**95.5**	1.7	71.0	12.4	15.0	**99.0**
	P	0	42.7	17.3	40.0	**4.5**	0.8	43.3	11.5	44.4	**1.0**
M2	fcc	4.3	72.3	11.4	12.0	**96.8**	3.6	72.4	11.4	12.5	**99.0**
	P	0	42.4	16.8	40.8	**3.2**	0.9	44.3	11.7	43.1	**1.0**
M3	fcc	6.1	72.8	10.3	10.8	**89.4**	5.4	70.6	11.7	12.3	**87.4**
	$L1_2$	18.0	74.8	3.7	3.5	**4.9**	16.7	73.9	2.9	6.6	**11.4**
	P	0	42.3	16.2	41.5	**5.7**	1.5	42.2	11.6	44.7	**1.2**
M4	fcc	6.1	72.6	10.7	10.6	**46.9**	5.6	70.1	13.5	10.8	**47.3**
	$L1_2$	18.0	74.8	3.8	3.4	**45.3**	17.7	73.3	3.3	5.8	**49.0**
	P	0	42.1	16.9	41.0	**7.8**	1.3	41.4	13.3	44.0	**3.7**
M5	fcc	6.2	72.2	11.6	10.0	**17.7**	7.1	68.7	15.7	8.5	**17.6**
	$L1_2$	18.0	74.6	4.2	3.2	**75.0**	17.2	74.0	3.9	5.0	**78.4**
	P	0	41.8	18.2	40.0	**7.3**	1.3	36.8	20.5	41.4	**4.0**

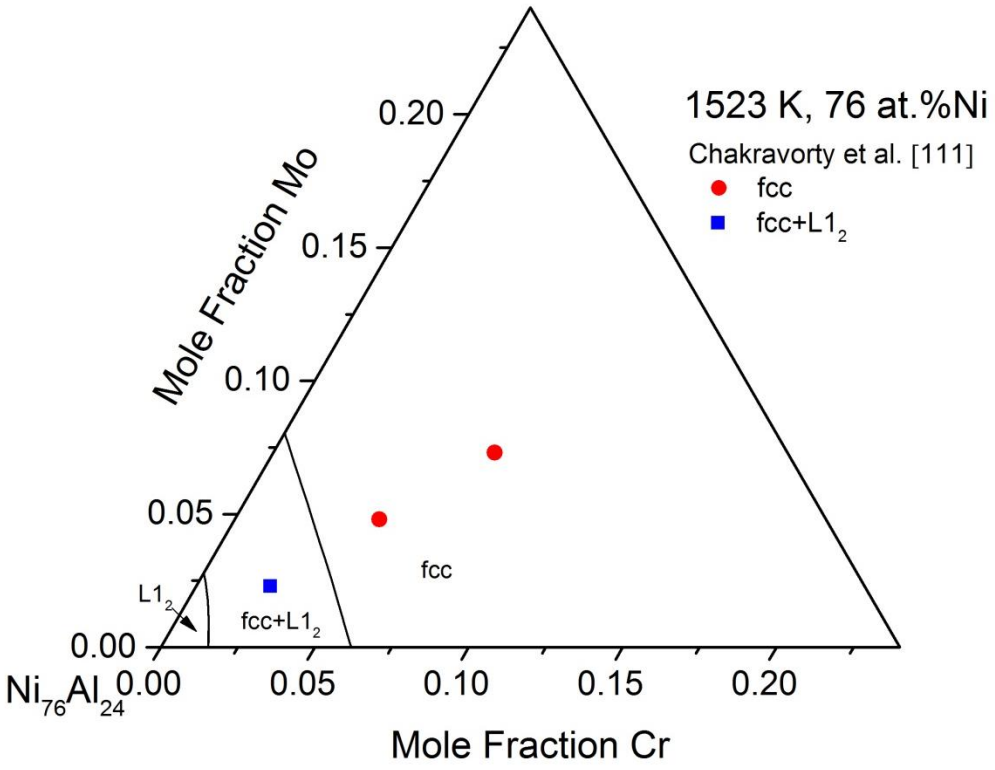

Fig. 8-10 Calculated 76 at.% Ni section of the system Al-Cr-Mo-Ni at 1523K in comparison with the experimental data from Chakravorty et al. [111].

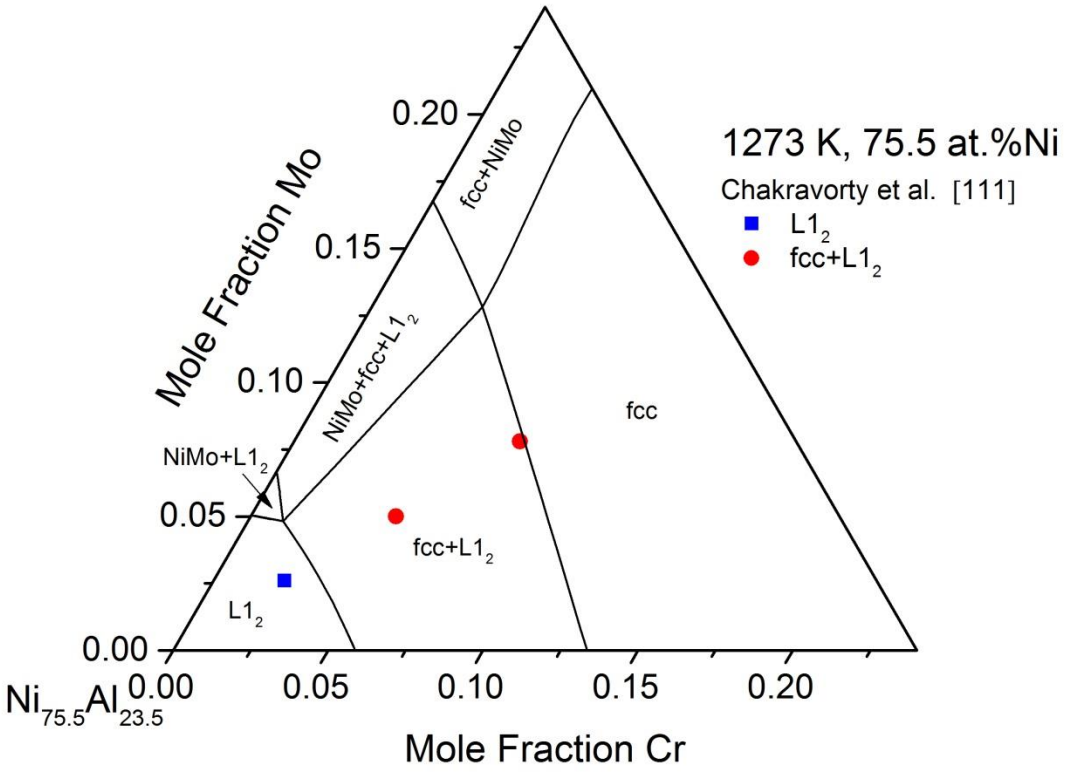

Fig. 8-11 Calculated 75.5 at.% Ni section of the system Al-Cr-Mo-Ni at 1273K in comparison with the experimental data from Chakravorty et al. [111].

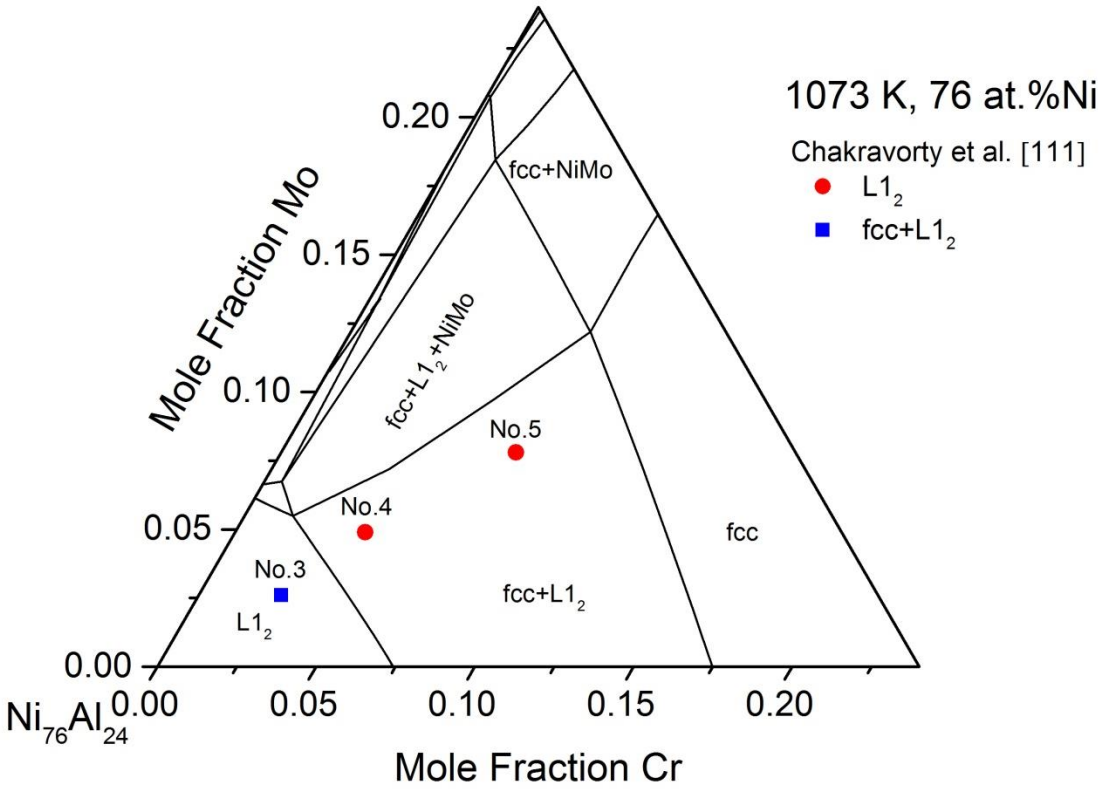

Fig. 8-12 Calculated 76 at.% Ni section of the system Al-Cr-Mo-Ni at 1073K in comparison with the experimental data from Chakravorty et al. [111].

Table 8-4 Calculated phase compositions in comparison with experimental data from Chakravorty et al. [111].

Alloys No.	Temperature, K	Phases	Calculated results				Experimental results			
			Al	Ni	Cr	Mo	Al	Ni	Cr	Mo
3	1523	fcc	17.1	76.7	3.3	2.9	16.6	76.6	3.6	3.2
		$L1_2$	21.5	74.7	1.9	1.9	20.8	74.8	2.2	2.2
	1273	$L1_2$	19.9	75.2	2.3	2.6	19.9	75.2	2.3	2.6
	1073	$L1_2$	18.9	75.9	2.6	2.6	18.9	75.9	2.6	2.6
4	1523	fcc	14.2	76.3	4.7	4.8	14.2	76.3	4.7	4.8
	1273	fcc	9.6	76.4	6.9	7.1	11.4	76.1	6.5	6.0
		$L1_2$	18.5	75.3	2.9	3.3	17.2	74.7	3.6	4.5
	1073	fcc	5.1	78.1	7.9	8.9	10.6	77.3	6.3	5.8
		$L1_2$	16.9	75.8	3.3	4.0	16.3	76.0	3.5	4.2
5	1523	fcc	9.5	76.0	7.2	7.3	9.5	76.0	7.2	7.3
	1273	fcc	9.2	75.5	7.4	7.9	8.2	76.2	7.6	8.0
		$L1_2$	18.6	75.1	3.0	3.3	17.9	74.2	3.5	4.4
	1073	fcc	4.6	76.1	9.4	9.9	6.8	76.4	8.5	8.3
		$L1_2$	16.9	75.5	3.7	3.9	12.9	75.3	5.6	6.2

Figs. 8-10 to 8-12 compare the calculated 76 at.% Ni sections of the system Al-Cr-Mo-Ni at 1523, 1273 and 1073 K with the experimental data from Chakravorty and West [111]. The calculated compositions of phases were also compared with the experimental data and the results are listed in Table 8-4. As we can see, the present thermodynamic description can predict the compositions of the phases very well. The fcc+$L1_2$ two-phase region or $\gamma+\gamma'$ region in this system, which is very important for the development of Ni-based alloys, is described satisfactorily. The present calculated partial isopleths differ considerably from these in Ref. [111], because more sophisticated thermodynamic descriptions of the sub-systems were adopted in the present work.

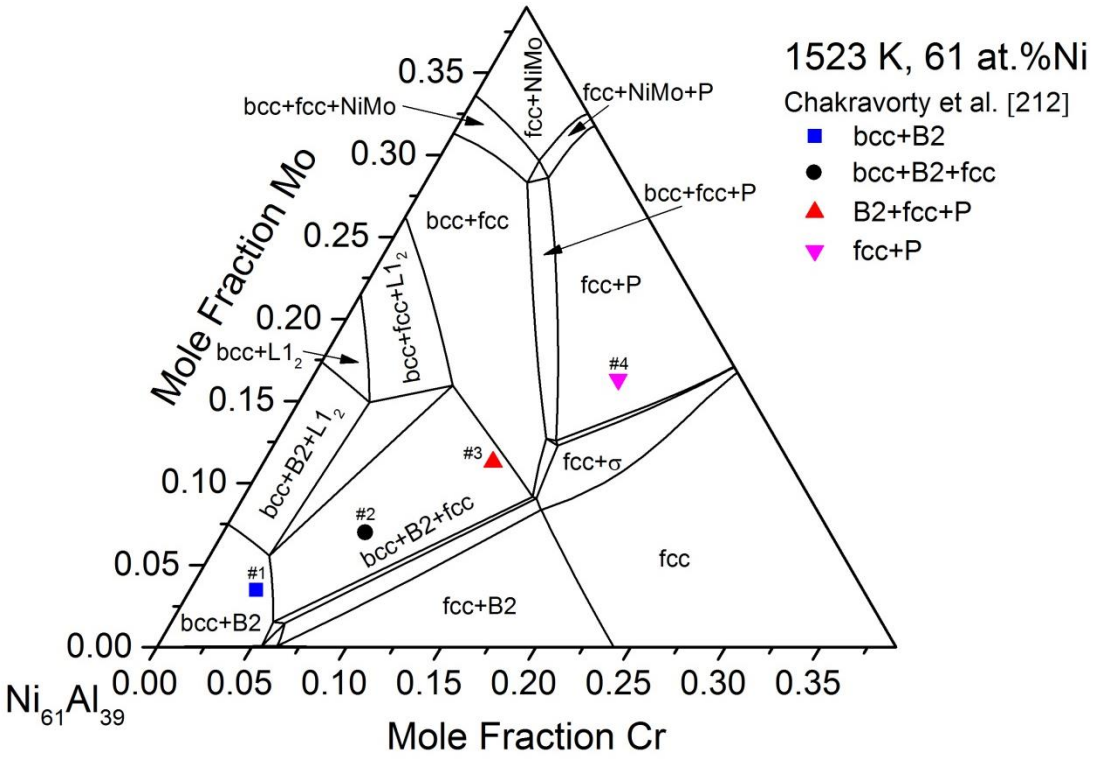

Fig. 8-13 Calculated 61 at.% Ni section of the system Al-Cr-Mo-Ni at 1523K in comparison with the experimental data from Chakravorty et al. [212].

Fig. 8-13 shows the calculated 61 at.% Ni section of the system Al-Cr-Mo-Ni at 1523 K. The experimental data from Chakravorty et al. [212] were superimposed for comparison. The present description can reproduce the experimental data very well except alloy #3.

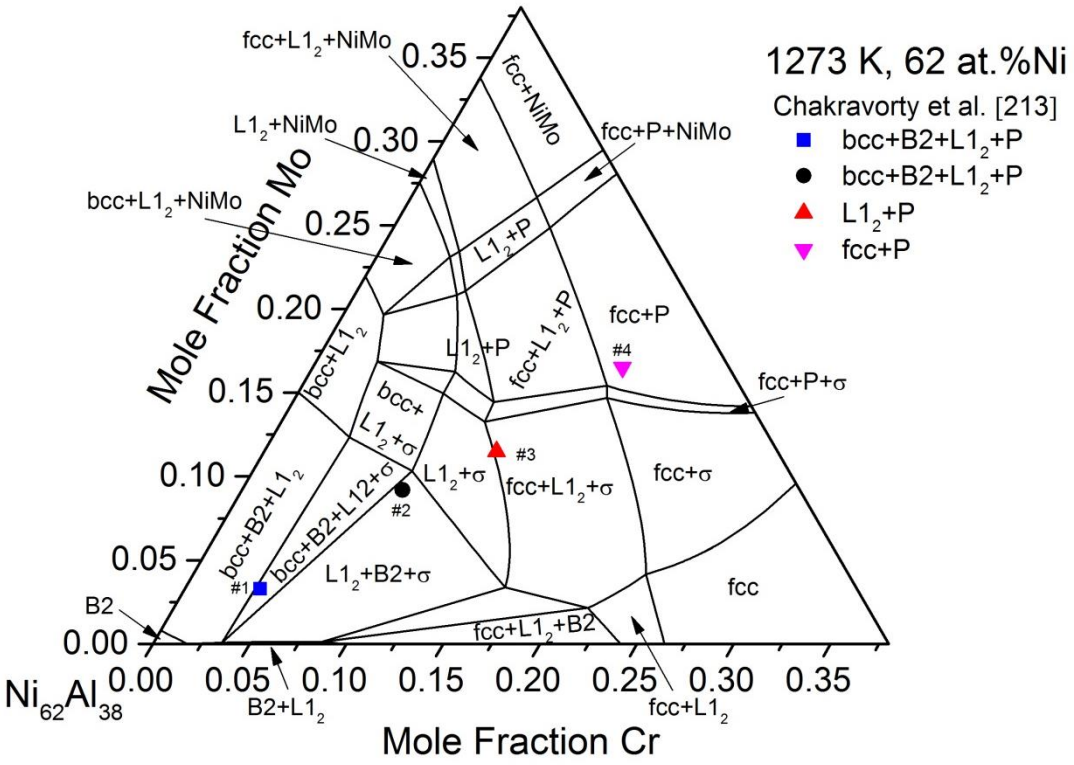

Fig. 8-14 Calculated 62 at.% Ni section of the system Al-Cr-Mo-Ni at 1273K in comparison with the experimental data from Chakravorty et al. [213].

Fig. 8-14 shows the calculated 62 at.% Ni section of the system Al-Cr-Mo-Ni at 1273 K in comparison with the experimental data from Chakravorty et al. [213]. The predicted phases in alloy #4 are in accord with the experimental data, while those in alloys #1, #2 and #3 show some deviations from the experimental data. According to the calculation, in these alloys, the σ phase should be stable instead of the P phase. Chakravorty et al. [213] reported that some σ phase particles were present besides P after alloy# 3 was annealed for three weeks at 1273 K, which indicated alloy #3 may consist of the $L1_2$, σ or $L1_2$, σ and P phases in its equilibrium state. In Fig. 8-14, the location of alloy #3 is very close to the $L1_2$+σ or $L1_2$+σ+P regions, which coincides reasonably with the experimental results of Chakravorty et al. [213].

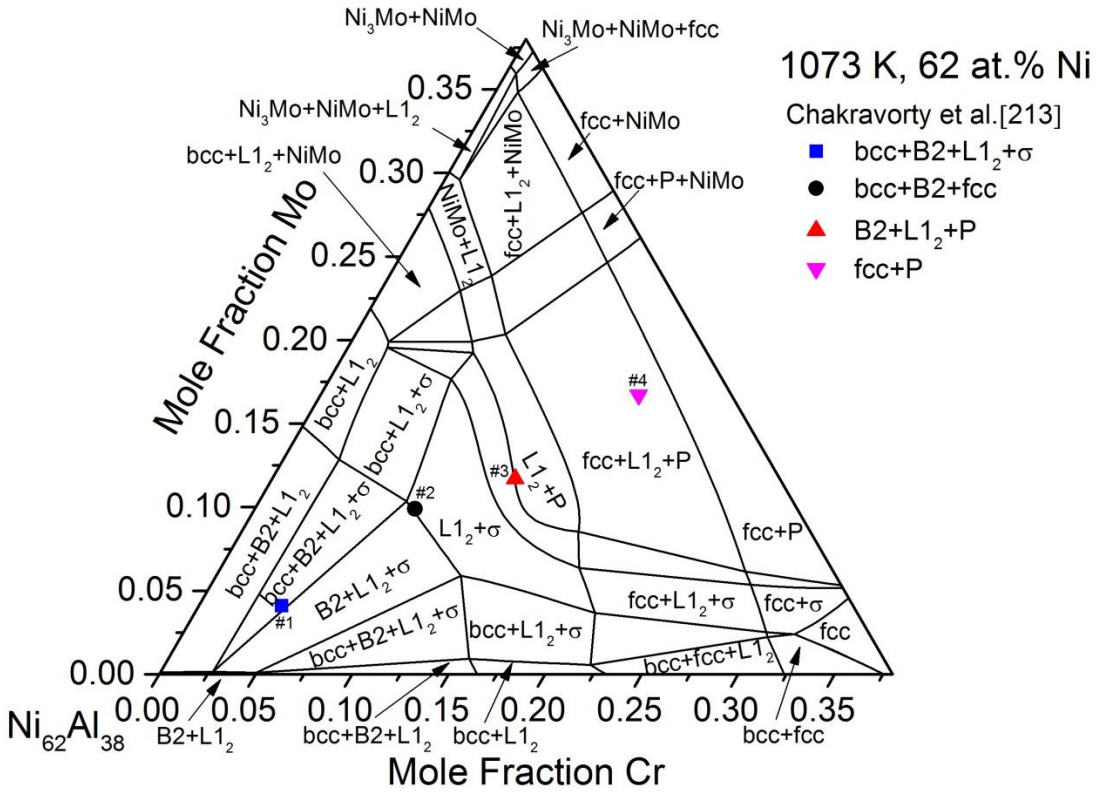

Fig. 8-15 Calculated 62 at.% Ni section of the system Al-Cr-Mo-Ni at 1073K in comparison with the experimental data from Chakravorty et al. [213].

Fig. 8-15 shows the calculated 62 at.% Ni section of the system Al-Cr-Mo-Ni at 1073 K in comparison with the experimental data from Chakravorty et al. [213]. The phases in alloy #1 are consistent with the experimental data, while deviations were found between calculation and experiment for alloys #2, #3 and #4. This deviation may be caused by the unsufficient annealing. Chakravorty et al. [213] stated that the studies on the phases and compositions of the alloys were made based on local equilibrium, because long range equilibrium was not achieved after the alloys were annealed at 1273 and 1073 K.

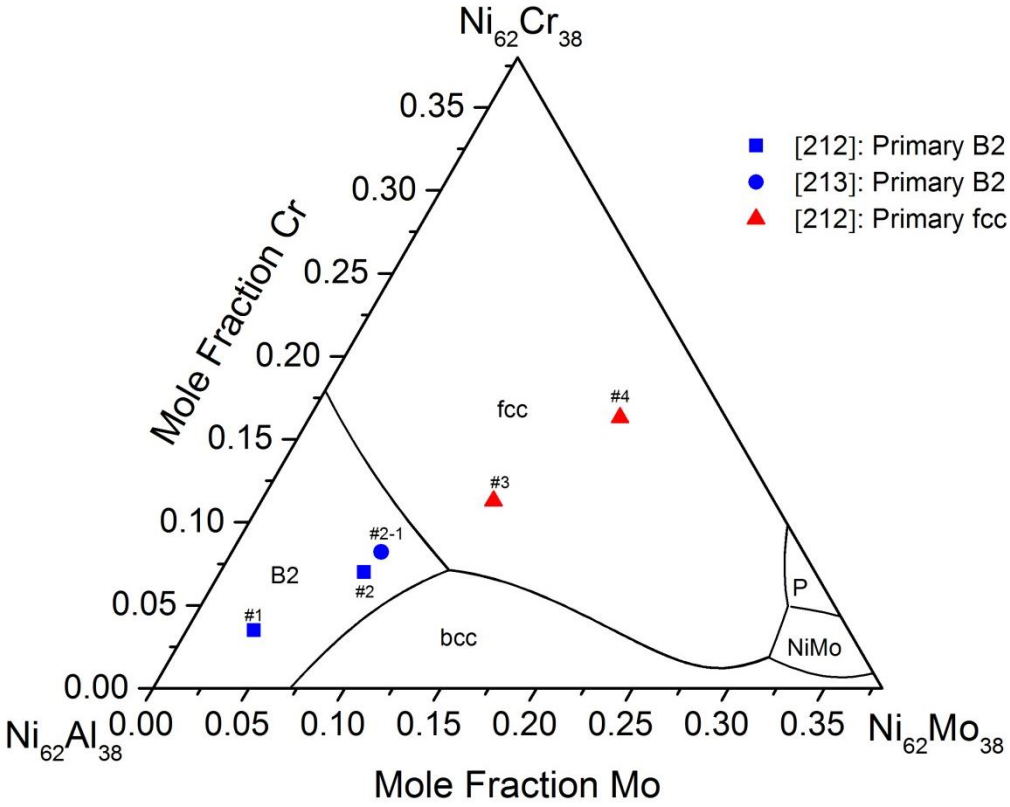

Fig. 8-16 Calculated liquidus surface projection of the 62 Ni at.% section of the Al-Cr-Mo-Ni system using the present description in comparison with the experimental data.

Since all binary and ternary interaction parameters for the liquid phase of the system Al-Cr-Mo-Ni are known, the liquidus projection in the quaternary system can be calculated. Fig. 8-16 shows the calculated liquidus projection of the 62 Ni at.% section of the Al-Cr-Mo-Ni system using the present thermodynamic description in comparison with the experimental data from the literature [212, 213]. It can be seen that our calculated results are in good agreement with the experimental data. By using Scheil module in the software package Thermo-Calc, the solidification process of the alloys can be simulated qualitatively. It assumes during solidification, the diffusion in the liquid phase is infinite but the diffusion in solid phases is zero. The Scheil simulation indicates around 76 mole percent of B2 phase will be obtained in alloy #1 while around 50 mole percent of B2 phase will present in alloy #2, which is in consistence with the report of Chaktavorty et al. [212] that larger amount of B2 phase was obtained in alloy #1 than alloy #2.

9. Summary and future work

9.1. Summary

In this thesis, experimental investigation and thermodynamic modeling (CALPHAD method) were combined to investigate the Al-Cr-Mo-Ni system and its sub-systems. It particularly focused on the binary systems Al-Ni and Al-Mo, ternary systems Al-Cr-Ni, Al-Mo-Ni and Cr-Mo-Ni, and the quaternary system NiAl-Cr-Mo.

In chapter 1, the motivation of the present work is presented. A brief introduction of the advantage of the NiAl-based superalloys as well as the project that the author involved is introduced.

Chapters 2 and 3 focus on the CALPHAD method and the experimental method, respectively. The advantages and scheme of the CALPHAD method are introduced. Different Gibbs energy models were also presented. In chapter 3, the devices employed in the present work to prepare and measure the samples are briefly introduced.

Chapters 4 to 7 concern with the literature review, experimental investigation and thermodynamic modeling of the ternary systems and the related binary sub-systems.

Chapter 4 focuses on the Al-Mo-Ni system. The thermodynamic description of system Al-Ni from Dupin et al. [28] was refined, in which the compound energy of thermal vacancies G_{Va}^{bcc} in the bcc phase was taken into account. G_{Va}^{bcc} was set to be 0.2·RT to ensure that a global equilibrium state can be achieved. Accordingly, the coefficients $\alpha_{\mathrm{Al,Va}}$ and $\alpha_{\mathrm{Ni,Va}}$ of the A2/B2 phases were adjusted. The same results as the original dataset of Dupin et al. [28] can be obtained from the revised dataset. The same method was also applied to other binary sub-systems to compensate the contribution of the compound energy of vacancies. Again, the same results as the original datasets were obtained after the revision. The Al-Mo system was reassessed. The topological constraint method of Malakhov and Balakumar was adopted. A grid of auxiliary equilibria, QF(liquid)>0, were applied in the POP file during optimization to suppress the occurrence of the miscibility gap in the liquid phase. The artificial inverse miscibility gap of the liquid phase and an artificial stabilization of the bcc phase above the liquidus line in the Al-Mo system from literature were removed. The new description of the Al-Mo system from the present work can reproduce the experimental data very well. The congruent melting of the AlMo phase was replaced by a peritectic reaction. A series of NiAl-Mo alloys up to 40 at.% Mo was prepared and annealed. The normal spectral emissivity of the NiAl and the liquidus and solidus temperatures of these alloys were measured by a laser heating-fast pyrometry apparatus. The present results agree well with the data from literature. The microstructure of the NiAl-0.1 at.% Mo and -0.3 at.% Mo alloys were observed in the as-cast state and after annealing at 1773 K. The solubility of Mo in NiAl at 1773 K was determined to be less than 0.1 at.%, which is smaller than the predictions in previous thermodynamic modeling. These results expand our understanding of the NiAl-Mo system and were successfully used in the

thermodynamic modeling of the Al-Mo-Ni system. A new dataset of the Al-Mo-Ni system was established. The A2 and B2 phases were modeled with a single Gibbs energy function as well as the A1 and $L1_2$ phases. Two ternary phases N and X were included in the modeling. Very good agreement between the calculated phase diagrams and the experimental data was obtained. The descriptions of the Ni-rich corner, the subsystem NiAl-Mo and the liquidus projection were considerably improved. There is no quasi-binary nature in the NiAl-Mo system. There is no quasi-binary nature in the NiAl-Mo system.

Chapter 5 focuses on the Al-Cr-Ni system. The NiAl-Cr eutectic composition was clarified by own experiment. The thermodynamic description of the Al-Ni-Cr system was refined regarding to the modeling of the liquid phase and thermal vacancies. The description of the sub-system NiAl-Cr is considerably improved. The ternary phases in the Al-rich corner were not included beacuse of the large discrepancy of the homogeneity ranges determined by different authors.

Chapter 6 focuses on the Cr-Mo-Ni system. A new thermodynamic description of the Cr-Mo-Ni covering the whole composition range was created. The up-to-date thermodynamic description of the Mo-Ni system from literature was adopted to ensure the reliability and the comparability with other ternary databases. In the present work, ternary phases, σ and P, were included but the μ phase was excluded because of the discrepancy at lower temperature. The new dataset can reproduce the experimental data well.

Chapter 7 focuses on the Al-Cr-Mo system. A critical review of the Al-Cr-Mo system was performed. Since the lack of experimental data, it is not possible to thermodynamically assess this system. However, some calculated isothermal sections as well as the liquidus projection were presented in the present work to support the investigations of this system in the future.

Chapter 8 further extends the present work to the quaternary Al-Cr-Mo-Ni system. Firstly, it focused on experimental investigation and modeling of the NiAl-Cr-Mo system. Next, the NiAl-Cr-Mo was further extended to the complete quaternary system with necessary modeling of the fcc and $L1_2$ phases.

A series of NiAl-Cr-Mo alloys were prepared and the microsturctures were observed. The primary solidified phases of these alloys were determined. Two types of primary solidified phases, B2 and bcc, were determined. The experimental results agree well with the data in the literature. With these new data and data from the literature, the ternary interaction parameters of the Al-Cr-Mo system was optimized, because it can contribute to the behavior of the liquid phase in the Al-Cr-Mo-Ni quaternary system. A quaternary database for the system Al-Cr-Mo-Ni was established. The calculated eutectic trough of the NiAl-Cr-Mo system fits well with the experimental data. Moreover, the eutectic temperatures and the phase fractions of the NiAl and the bcc phases have been calculated along the quaternary eutectic trough.

The NiAl-Cr-Mo database was further extended to the Al-Cr-Mo-Ni system by completing the modeling the fcc and $L1_2$ phases in this system. The constraints for the ordered $L1_2$ phase were

introduced into the Cr-Mo, Mo-Ni, Al-Mo-Ni, Al-Cr-Mo, Cr-Mo-Ni and Al-Cr-Mo-Ni systems to ensure that its disordered A1 (fcc) parent phase now can be properly disordered in the Al-Cr-Mo-Ni system and all sub-systems. The calculation results were compared with experimental data. A satisfactory agreement between them was obtained. The fcc+$L1_2$ two phases region, which is very important for the development of the Ni-based superalloys can be described satisfactorily.

The present thermodynamic description of the Al-Cr-Mo-Ni system can provide satisfactory descriptions of the regions related to NiAl-based superalloys as well as Ni-based superalloys. Thus, it can support the selection of alloy compositions and simulations of both NiAl-based and Ni-based superalloys.

9.2. Future work

To further improve the thermodynamic description of the Al-Ni-Cr-Mo system developed in the present work, the following works should be carried out in the future:

As reviewed in chapter 4.1.2, there is no experimental evidence on the character of the AlMo phase melting. In the present work, the AlMo phase was modeled as an extension of the Mo solid solution with A2 structure. However, the ab initio calculation of the bcc Al-Mo phase diagram by Gonzales-Ormeño et al. [221] indicates only the B32 AlMo superlattice should be found in this system. Therefore, more experimental work on the crystal structure and the melting behavior of the AlMo phase should be carried out in the future.

As stated in chapters 5.1.1 and 5.2, a sophisticated thermodynamic description of the Al-Cr system is available from Witusiewicz et al. [144] and the description of the Al-Cr-Ni system [28] adopted in this study only considers the NiAl-Ni-Cr section of the Al-Cr-Ni system. Therefore, it is necessary to re-assess the Al-Cr-Ni system with the complete composition range by adopting up-to-date dataset of the Al-Cr system in the future.

The investigations regarding on ternary phases of the Al-Cr-Mo do not agree well with each other. Further investigation is required to clarify the existence of the λ and ε phase and the polytypes of the Φ, λ and ρ phases as well as the homogeneity ranges of these ternary phases.

When the author is writing this thesis, a new assessment of the Al-Ni-Cr system covering the complete composition range was published by Wang and Cacciamani [222]. In Ref. [222], the binary descriptions of Al-Cr from Hu et al. [143], Al-Ni from Dupin et al. [28] and Cr-Ni from Gustafson [154]. Binary phases, Cr_4Al_{11}, $CrNi_2$ and Ni_3Al_4, and three ternary compounds in the Al-rich region were included for the first time. Indeed, some improvements were achieved in [222], but the up-to-date assessment of the Al-Cr system by Witusiewicz et al. [144] was not adopted. Further work on this system should clarify the stability ranges of the ternary phases by experiments and thermodynamically re-assess this system.

The adjustment of the Cr-Mo-Ni system in the present work is based on the assessment of Frisk [157]. However, the following things should be improved. Firstly, more experimental investigation should be performed to accurately determine the phase equilibria of this system. Secondly, the μ phase should be concluded in the modeling.

For the Al-Cr-Mo system, experimental works regarding on the phase equilibria is necessary. With the outcomes, this system should be assessed thermodynamically.

Appendix. The thermodynamic dataset of the Al-Cr-Mo-Ni system.

```
 ELEMENT /-   ELECTRON_GAS              .0000E+00   .0000E+00   .0000E+00!
 ELEMENT VA   VACUUM                    .0000E+00   .0000E+00   .0000E+00!
 ELEMENT AL   FCC_A1                   2.6982E+01  4.5773E+03  2.8322E+01!
 ELEMENT CR   BCC_A2                   5.1996E+01  4.0500E+03  2.3560E+01!
 ELEMENT NI   FCC_A1                   5.8690E+01  4.7870E+03  2.9796E+01!
 ELEMENT MO   BCC_A2                   9.5940E+01  4.5890E+03  2.8560E+01!

 SPECIES AL2                    AL2!
 SPECIES CR2                    CR2!
 SPECIES NI2                   NI2!

 FUNCTION UNASS      298.15  0;,,N !

 TYPE_DEFINITION % SEQ *!
 DEFINE_SYSTEM_DEFAULT E 2 !
 DEFAULT_COMMAND DEF_SYS_ELEMENT VA !

 DATABASE_INFO '"
 BASE TC-Ni, version 29-09-99'

 '
 ELEMENTS : Al, Cr, Ni'
 '
 ASSESSED SYSTEMS :'
 '
 BINARIES'
      Al-Cr, Al-Ni, Cr-Ni'
 TERNARIES'
      Al-Cr-Ni'
'
 MODELLING ORDER/DISORDER:'
'
 A1 and L12 phases are modelled with a single Gibbs energy curve.'
 They are FCC_L12#1 (A1) based on (Ni) and FCC_L12#2 (L12) based on'
 Ni3Al, differing by their site occupation.'
```

```
 The same type of relation exists for the A2 and B2 phases. There are'
 several possible sets for the phase named BCC_B2. They are either'
 disordered (A2) and correspond to the solid solution based on Cr,'
 or ordered based on the B2 compound AlNi.'
 !

ASSESSED_SYSTEMS
 AL-CR(;G5 MAJ:BCC_B2/CR:CR:VA ;P3 STP:.75/1200/1)
 AL-NI(;P3 STP:.75/1200/1)
 CR-NI(;G5 MAJ:BCC_B2/CR:CR:VA C_S:BCC_B2/NI:NI:VA
        ;P3 STP:.5/1200/2)
 AL-CR-NI(;G5 MAJ:BCC_B2/CR:CR:VA C_S:BCC_B2/AL:NI:VA
        ;P3 STP:.01/.8/2)
           !

 PHASE GAS:G %  1  1.0  !
 CONST GAS:G :AL,AL2,CR,CR2,NI,NI2 :  !

 PHASE LIQUID:L %  1  1.0  !
 CONST LIQUID:L :AL,CR,NI,MO :  !

 PHASE FCC_A1  %A  2 1   1 !
 CONST FCC_A1  :AL,CR,MO,NI% : VA% :  !

 PHASE BCC_A2  %B  2 1   3 !
 CONST BCC_A2  :AL,CR%,NI,MO,VA : VA :  !

 PHASE BCC_B2  %BCW  3 .5 .5    3 !
 CONST BCC_B2  :AL,CR,MO,NI%,VA : AL%,CR,MO,NI,VA : VA: !

 PHASE FCC_L12  %ADG  3 .75   .25   1 !
 CONST FCC_L12  :AL,CR,MO,NI : AL,CR,MO,NI : VA :  !

 PHASE CUB_A15  %  2 .75   .25 !
 CONSTITUENT CUB_A15  :AL,MO : AL,MO :  !

 TYPE_DEFINITION A GES A_P_D @ MAGNETIC  -3.0 .28 !
 TYPE_DEFINITION B GES A_P_D @ MAGNETIC  -1.0 .40 !

 TYPE_DEFINITION C GES A_P_D BCC_B2 DIS_PART BCC_A2 !
 TYPE_DEFINITION D GES A_P_D FCC_L12 DIS_PART FCC_A1 !
```

```
TYPE_DEFINITION G IF (AL AND NI) THEN
        GES A_P_D FCC_L12 C_S 2 NI:AL:VA !
TYPE_DEFINITION G IF (NI) THEN
        GES A_P_D FCC_L12 MAJ 1 NI:NI:VA !

TYPE_DEFINITION W IF (CR AND AL AND NI) THEN
        GES A_P_D BCC_B2 C_S,, NI:AL:VA !

TYPE_DEFINITION W IF (CR) THEN
        GES A_P_D BCC_B2 MAJ 1 CR:CR:VA !

FUNCTION ZERO       298.15  0;,,N !
FUNCTION DP         298.15  +P-101325;,,N !
FUNCTION TROIS 298.15 3;,,N !
FUNCTION UNTIER 298.15 TROIS**(-1);,,N !
FUNCTION GHCPAL  298.15  +5481-1.8*T+GHSERAL;   6.00000E+03   N !
TYPE_DEFINITION + GES A_P_D HCP_A3 MAGNETIC  -3.0    2.80000E-01 !
PHASE HCP_A3  %+  2 1   .5 !
CONSTITUENT HCP_A3  :AL,MO : VA :  !
PARAMETER G(HCP_A3,AL:VA;0) 298.15  +5481-1.8*T+GHSERAL; 6000  N 10Cup !
PARAMETER G(HCP_A3,MO:VA;0) 298.15  +GHCPMO;  5.00000E+03  N 10Cup !
PARAMETER G(HCP_A3,AL,MO:VA;0)  298.15  -85570+25*T; 6.00000E+03 N 10Cup !
PARAMETER G(HCP_A3,NI:VA;0)     298.15 +1046+1.255*T+GHSERNI; 3000 N 91DIN !
PARAMETER TC(HCP_A3,NI:VA;0)    298.15 +633;                6000 N 91DIN !
PARAMETER BMAGN(HCP_A3,NI:VA;0) 298.15 +0.52;               6000 N 91DIN !

$**************************************************************************
$
$                                   UNARY PARAMETERS
$
$--------------------------------------------------------------------------
$
$                                       Al
$
$                                   FUNCTIONS
$
FUNCTION F154T      298.15
  +323947.58-25.1480943*T-20.859*T*LN(T)
  +4.5665E-05*T**2-3.942E-09*T**3-24275.5*T**(-1);
```

```
            4300.0  Y
   +342017.233-54.0526109*T-17.7891*T*LN(T)+6.822E-05*T**2
   -1.91111667E-08*T**3-14782200*T**(-1);
            8200.0  Y
   +542396.07-411.214335*T+22.2419*T*LN(T)-.00349619*T**2
   +4.0491E-08*T**3-2.0366965E+08*T**(-1);  1.00000E+04  N !
$
 FUNCTION F625T      298.15
   +496408.232+35.479739*T-41.6397*T*LN(T)
   +.00249636*T**2-4.90507333E-07*T**3+85390.3*T**(-1);
            900.00  Y
   +497613.221+17.368131*T-38.85476*T*LN(T)-2.249805E-04*T**2
   -9.49003167E-09*T**3-5287.23*T**(-1);  2.80000E+03  N !
$
 FUNCTION GHSERAL    298.15
   -7976.15+137.093038*T-24.3671976*T*LN(T)
   -.001884662*T**2-8.77664E-07*T**3+74092*T**(-1);
            700.00  Y
   -11276.24+223.048446*T-38.5844296*T*LN(T)
   +.018531982*T**2-5.764227E-06*T**3+74092*T**(-1);
            933.60  Y
   -11278.378+188.684153*T-31.748192*T*LN(T)
   -1.231E+28*T**(-9);,,  N !
$
 FUNCTION GHCPAL     298.15  +5481-1.8*T+GHSERAL;,,N !
$
 FUNCTION GBCCAL     298.15  +10083-4.813*T+GHSERAL;,,N !
$
 FUNCTION GLIQAL     298.14
   +11005.029-11.841867*T+7.934E-20*T**7+GHSERAL;
            933.59  Y
   +10482.282-11.253974*T+1.231E+28*T**(-9)+GHSERAL;,,N !
$
$                                          GAS PHASE
$
 PARAMETER G(GAS,AL;0)  298.15  +F154T+R*T*LN(1E-05*P);,,N REF184 !
 PARAMETER G(GAS,AL2;0)  298.15  +F625T+R*T*LN(1E-05*P);,,N REF448 !
$
$                                        LIQUID PHASE
$
 PARAMETER   G(LIQUID,AL;0)   298.13
```

```
    +11005.029-11.841867*T+7.934E-20*T**7+GHSERAL;
                    933.60  Y
    +10482.382-11.253974*T+1.231E+28*T**(-9)
    +GHSERAL;,,N 91DIN !
$
$                                       FCC_A1 PHASE
$
 PARAMETER G(FCC_A1,AL:VA;0)  298.15  +GHSERAL;,,N 91DIN !
$
$                                       BCC_A2 PHASE
$
 PARAMETER G(BCC_A2,AL:VA;0)  298.15  +GBCCAL;,,N 91DIN !
  PARAMETER G(BCC_A2,VA:VA;0)  298.15  +0.2*R*T;,,N 14Fra !
$ the following function had to be amended in order to compensate the effect
$ of the vacancy parameter on the invariant B2+L=Al3Ni2 and the phase diagram
$ FUNCTION B2ALVA 295.15 10000-T;,,N !
 FUNCTION B2ALVA 295.15 10000-T-0.2*R*T;,,N !
   FUNC LB2ALVA 298.15 150000;,,N !
 PARAMETER L(BCC_A2,AL,VA:VA;0)  298.15  B2ALVA+LB2ALVA;,,N 99DUP !
$
$                                       BCC_B2 PHASE
$
 PARAMETER G(BCC_B2,AL:AL:VA;0) 298.15 0; 6000 N!
 PARAMETER G(BCC_B2,AL:VA:VA;0)  298.15  .5*B2ALVA-.5*LB2ALVA;,,N 99DUP !
 PARAMETER G(BCC_B2,VA:AL:VA;0)  298.15  .5*B2ALVA-.5*LB2ALVA;,,N 99DUP !

 PARAMETER G(CUB_A15,AL:AL;0)  298.15  +10000+GHSERAL;   6000 N 10Cup !
$
$---------------------------------------------------------------------
$
$                                           Cr
$
$                                         FUNCTIONS
$
 FUNCTION F7454T     298.15
   +390765.331-31.5192154*T-21.36083*T*LN(T)
   +7.253215E-04*T**2-1.588679E-07*T**3+10285.15*T**(-1);
              1100.0  Y
   +393886.928-44.107465*T-19.96003*T*LN(T)+.001513089*T**2
   -4.23648333E-07*T**3-722515*T**(-1);
              2000.0  Y
```

```
   +421372.003-231.888524*T+5.362886*T*LN(T)-.00848877*T**2
   +2.984635E-07*T**3-6015405*T**(-1);
                3300.0  Y
   +305164.698+251.019831*T-55.20304*T*LN(T)+.005324585*T**2
   -2.850405E-07*T**3+34951485*T**(-1);
                5100.0  Y
   +1069921.1-1708.93262*T+175.0508*T*LN(T)-.025574185*T**2
   +4.94447E-07*T**3-4.4276355E+08*T**(-1);
                7600.0  Y
   -871952.838+1686.47356*T-204.5589*T*LN(T)+.007475225*T**2
   -4.618745E-08*T**3+1.423504E+09*T**(-1);  1.00000E+04  N !
$
 FUNCTION F7735T     298.15  +598511.402+41.5353219*T-40.56798*T*LN(T)
   +.004961847*T**2-1.61216717E-06*T**3+154422.85*T**(-1);
                800.00  Y
   +613345.232-104.20799*T-19.7643*T*LN(T)-.007085085*T**2
   -4.69883E-07*T**3-1738066.5*T**(-1);
                1400.0  Y
   +642608.843-369.286259*T+17.64743*T*LN(T)-.02767321*T**2
   +1.605906E-06*T**3-5831655*T**(-1);
                2300.0  Y
   +553119.895+159.188556*T-52.07969*T*LN(T)-.004229401*T**2
   +1.5939925E-07*T**3+14793625*T**(-1);
                3900.0  Y
   +347492.339+623.137624*T-105.0428*T*LN(T)+3.9699545E-04*T**2
   +1.51783483E-07*T**3+1.4843765E+08*T**(-1);
                5800.0  Y
   -484185.055+2598.25559*T-334.7145*T*LN(T)+.028597625*T**2
   -4.97520167E-07*T**3+7.135805E+08*T**(-1);  6.00000E+03  N !
$
 FUNCTION GHSERCR    298.14
   -8856.94+157.48*T-26.908*T*LN(T)
   +.00189435*T**2-1.47721E-06*T**3+139250*T**(-1);
                2180.0  Y
   -34869.344+344.18*T-50*T*LN(T)-2.88526E+32*T**(-9);,,N !
$
 FUNCTION GCRLIQ     298.15
   +24339.955-11.420225*T+2.37615E-21*T**7+GHSERCR;
                2180.0  Y
   -16459.984+335.616316*T-50*T*LN(T);,,N !
$
```

```
 FUNCTION GFCCCR     298.15  +7284+.163*T+GHSERCR;,,N !
$
 FUNCTION GHCPCR     298.15  +4438+GHSERCR;,,N !
$
 FUNCTION ACRBCC     298.15  +1.7E-05*T+9.2E-09*T**2;,,N !
 FUNCTION BCRBCC     298.15  +1+2.6E-11*P;,,N !
 FUNCTION CCRBCC     298.15  2.08E-11;,,N !
 FUNCTION DCRBCC     298.15  +1*LN(BCRBCC);,,N !
 FUNCTION VCRBCC     298.15  +7.188E-06*EXP(ACRBCC);,,N !
 FUNCTION ECRBCC     298.15  +1*LN(CCRBCC);,,N !
 FUNCTION XCRBCC     298.15  +1*EXP(.8*DCRBCC)-1;,,N !
 FUNCTION YCRBCC     298.15  +VCRBCC*EXP(-ECRBCC);,,N !
 FUNCTION ZCRBCC     298.15  +1*LN(XCRBCC);,,N !
 FUNCTION GPCRBCC    298.15  +YCRBCC*EXP(ZCRBCC);,,N !
$
 FUNCTION ACRLIQ     298.15  +1.7E-05*T+9.2E-09*T**2;,,N !
 FUNCTION BCRLIQ     298.15  +1+4.65E-11*P;,,N !
 FUNCTION CCRLIQ     298.15  3.72E-11;,,N !
 FUNCTION DCRLIQ     298.15  +1*LN(BCRLIQ);,,N !
 FUNCTION VCRLIQ     298.15  +7.653E-06*EXP(ACRLIQ);,,N !
 FUNCTION ECRLIQ     298.15  +1*LN(CCRLIQ);,,N !
 FUNCTION XCRLIQ     298.15  +1*EXP(.8*DCRLIQ)-1;,,N !
 FUNCTION YCRLIQ     298.15  +VCRLIQ*EXP(-ECRLIQ);,,N !
 FUNCTION ZCRLIQ     298.15  +1*LN(XCRLIQ);,,N !
 FUNCTION GPCRLIQ    298.15  +YCRLIQ*EXP(ZCRLIQ);,,N !
$
$                                        GAS PHASE
$
 PARAMETER G(GAS,CR;0)  298.15  +F7454T+R*T*LN(1E-05*P);,,N REF4465 !
 PARAMETER G(GAS,CR2;0)  298.15  +F7735T+R*T*LN(1E-05*P);,,  N REF4591 !
$
$                                      LIQUID PHASE
$
 PARAMETER G(LIQUID,CR;0)  298.15  +GCRLIQ+GPCRLIQ;,,  N 91DIN !
$
$                                      FCC_A1 PHASE
$
 PARAMETER G(FCC_A1,CR:VA;0)  298.15  +GFCCCR+GPCRBCC;,,N 89DIN !
 PARAMETER TC(FCC_A1,CR:VA;0)  298.15  -1109;,,N 89DIN !
 PARAMETER BMAGN(FCC_A1,CR:VA;0)  298.15  -2.46;,,N 89DIN !
$
```

```
$                                        BCC_A2 PHASE
$
 PARAMETER G(BCC_A2,CR:VA;0)  298.15  +GHSERCR+GPCRBCC;,,N 91DIN !
 PARAMETER TC(BCC_A2,CR:VA;0)  298.15  -311.5;,,N 89DIN !
 PARAMETER BMAGN(BCC_A2,CR:VA;0)  298.15  -.008;,,N 89DIN !
$ following parameter amended in order to compensate the vacancy contribution
$ PARAMETER L(BCC_A2,CR,VA:VA;0)  298.15  100000;,,N 01DUP !
 PARAMETER L(BCC_A2,CR,VA:VA;0)  298.15  100000-0.2*R*T;,,N !
$
$                                        BCC_B2 PHASE
$
 PARAMETER G(BCC_B2,CR:VA:VA;0)  298.15  0;,,N 01DUP !
 PARAMETER G(BCC_B2,VA:CR:VA;0)  298.15  0;,,N 01DUP !
$
$---------------------------------------------------------------------
$
$                                           Ni
$
$                                        FUNCTIONS
$
 FUNCTION F13191T    298.15
   +417658.868-44.7777921*T-20.056*T*LN(T)
   -.0060415*T**2+1.24774E-06*T**3-16320*T**(-1);
                800.00  Y
   +413885.448+9.41787679*T-28.332*T*LN(T)+.00173115*T**2
   -8.399E-08*T**3+289050*T**(-1);
                3900.0  Y
   +440866.732-62.5810038*T-19.819*T*LN(T)+5.067E-04*T**2
   -4.93233333E-08*T**3-15879735*T**(-1);
                7600.0  Y
   +848806.287-813.398164*T+64.69*T*LN(T)-.00731865*T**2
   +8.71833333E-08*T**3-3.875846E+08*T**(-1);  10000.  N !
$
 FUNCTION F13265T    298.15
   +638073.279-68.1901928*T-24.897*T*LN(T)
   -.0313584*T**2+5.93355333E-06*T**3-14215*T**(-1);
                800.00  Y
   +611401.772+268.084821*T-75.25401*T*LN(T)+.01088525*T**2
   -7.08741667E-07*T**3+2633835*T**(-1);
                2100.0  Y
   +637459.339+72.0712678*T-48.587*T*LN(T)-9.09E-05*T**2
```

```
   +9.12933333E-08*T**3-1191755*T**(-1);
                4500.0 Y
   +564540.781+329.599011*T-80.11301*T*LN(T)+.00578085*T**2
   -1.08841667E-07*T**3+29137900*T**(-1);  6000.0  N !
$
 FUNCTION GHSERNI    298.14
   -5179.159+117.854*T-22.096*T*LN(T)
   -.0048407*T**2;
                1728.0  Y
   -27840.655+279.135*T-43.1*T*LN(T)+1.12754E+31*T**(-9);,,  N   !
$
 FUNCTION GHCPNI     298.15  +1046+1.2552*T+GHSERNI;,,N !
$
 FUNCTION GBCCNI     298.15  +8715.084-3.556*T+GHSERNI;,,,   N !
$
$                                          GAS PHASE
$
 PARAMETER G(GAS,NI;0)  298.15  +F13191T+R*T*LN(1E-05*P);,,N REF7504 !
 PARAMETER G(GAS,NI2;0)  298.15 +F13265T+R*T*LN(1E-05*P);,,N REF7553 !
$
$                                          LIQUID PHASE
$
 PARAMETER G(LIQUID,NI;0) 298.13
     +16414.686-9.397*T-3.82318E-21*T**7+GHSERNI;
                   1728.0  Y
     +18290.88-10.537*T-1.12754E+31*T**(-9)
     +GHSERNI;,,N 91DIN !
$
$                                          FCC_A1 PHASE
$
 PARAMETER G(FCC_A1,NI:VA;0)  298.15  +GHSERNI;,,N 91DIN !
 PARAMETER TC(FCC_A1,NI:VA;0)  298.15  633;,,N 89DIN !
 PARAMETER BMAGN(FCC_A1,NI:VA;0)  298.15  .52;,,N 89DIN !
$
$                                          BCC_A2 PHASE
$
 PARAMETER G(BCC_A2,NI:VA;0)  298.15  +GBCCNI;,,N 91DIN !
 PARAMETER TC(BCC_A2,NI:VA;0)  298.15  575;,,N 89DIN !
 PARAMETER BMAGN(BCC_A2,NI:VA;0)  298.15  .85;,,N 89DIN !
$ the following function had to be amended in order to compensate the effect
$ of the vacancy parameter on the invariant B2+L=Al3Ni2 and the phase diagram
```

```
$ FUNCTION B2NIVA 295.15 +162397.3-27.40575*T;,,N !
 FUNCTION B2NIVA 295.15 +162397.3-27.40575*T-0.2*R*T;,,N !
  FUNC LB2NIVA 298.15 -64024.38+26.49419*T;,,N !
 PARAMETER L(BCC_A2,NI,VA:VA;0)  298.15  B2NIVA+LB2NIVA;,,N 99DUP !
$
$                                        BCC_B2 PHASE
$
 PARAMETER G(BCC_B2,VA:NI:VA;0)  298.15  .5*B2NIVA-.5*LB2NIVA;,,N 99DUP !
 PARAMETER G(BCC_B2,NI:VA:VA;0)  298.15  .5*B2NIVA-.5*LB2NIVA;,,N 99DUP !
$---------------------------------------------------------------------
$                                          Mo
 FUNCTION GHSERMO    2.98150E+02  -7746.302+131.9197*T-23.56414*T*LN(T)
    -.003443396*T**2+5.66283E-07*T**3+65812*T**(-1)-1.30927E-10*T**4;
    2.89600E+03  Y
     -30556.41+283.559746*T-42.63829*T*LN(T)-4.849315E+33*T**(-9);
    5.00000E+03  N !
 FUNCTION GFCCMO  298.15  +7453.698+132.5497*T-23.56414*T*LN(T)
    -.003443396*T**2+5.66283E-07*T**3+65812*T**(-1)-1.30927E-10*T**4;
    2.89600E+03  Y
    -15356.41+284.189746*T-42.63829*T*LN(T)-4.849315E+33*T**(-9);
    5.00000E+03  N !
 FUNCTION GHCPMO  298.15  +3803.698+131.9197*T-23.56414*T*LN(T)
    -.003443396*T**2+5.66283E-07*T**3+65812*T**(-1)-1.30927E-10*T**4;
    2.89600E+03  Y
    -19006.41+283.559746*T-42.63829*T*LN(T)-4.849315E+33*T**(-9);
    5.00000E+03  N !

 FUNCTION GLIQMO     2.98150E+02  +34085.045+117.224788*T-23.56414*T*LN(T)
    -.003443396*T**2+5.66283E-07*T**3+65812*T**(-1)-1.30927E-10*T**4
    +4.24519E-22*T**7;  2.89600E+03  Y
    +3538.963+271.6697*T-42.63829*T*LN(T);  5.00000E+03  N !
$ following parameter amended in order to compensate the vacancy contribution
$ FUNC B2MOVA 298.15 10000-T; 6000 N !
 FUNC B2MOVA 298.15 10000-T-0.2*R*T; 6000 N !
 FUNC LB2MOVA 298.15 150000; 6000 N !
 PARAMETER G(LIQUID,MO;0)  298.15  +GLIQMO;   6000   N 91DIN !
 PARAMETER G(BCC_A2,MO:VA;0)  298.15  +GHSERMO;  5000  N  REF0 !
 PARAMETER L(BCC_A2,MO,VA:VA;0)  298.15  B2MOVA+LB2MOVA;,,N  FRA !
 PARAMETER G(BCC_B2,VA:MO:VA;0)  298.15  .5*B2MOVA-.5*LB2MOVA;,,N FRA !
 PARAMETER G(BCC_B2,MO:VA:VA;0)  298.15  .5*B2MOVA-.5*LB2MOVA;,,N FRA !
 PARAMETER G(BCC_B2,MO:MO:VA;0)  298.15  0; 6000 N!
```

```
 PARAMETER G(FCC_A1,MO:VA;0)     298.15 +GFCCMO;  5.00000E+03  N REF0 !
 PARAMETER G(HCP_A3,MO:VA;0) 298.15  +GHCPMO;  5.00000E+03  N 10Cup !
 PARAMETER G(CUB_A15,MO:MO;0)  298.15  +10000+GHSERMO; 6000 N   10Cup !

$**************************************************************************
$
$                                  BINARY PARAMETERS
$
$--------------------------------------------------------------------------
$
$                                        Al-Cr
$                    Mainly from Saunders (COST507)
$                    Metastable B2 and L12 from revision of Al-Cr-Ni
$
$                                     LIQUID PHASE
$
 PARAMETER L(LIQUID,AL,CR;0)  298.15  -29000;,,N 91SAU1 !
 PARAMETER L(LIQUID,AL,CR;1)  298.15  -11000;,,N 91SAU1 !
$
$                                     FCC_A1 PHASE
$
 PARAMETER G(FCC_A1,AL,CR:VA;0)  298.15  -45900+6*T;,,N 91SAU1 !
$
$                                     BCC_A2 PHASE
$
 PARAMETER G(BCC_A2,AL,CR:VA;0)  298.15  -54900+10*T;,,N 91SAU1 !
$
$                                     BCC_B2 PHASE
$                                       metastable
$
$ phase is not stabilized enough to become stable in the Al-Cr. It is
$ thus not in agreement with "T. Helander, and O. Tolochko, J. of Phase
$ Eq, 20 (1) 1999, 57-60." Further study on the extension of the B2 phase
$ towards AlCr in Al-Cr-Ni would be desirable.
 PARAMETER G(BCC_B2,AL:CR:VA;0)  298.15  -2000;,,N 01DUP  !
 PARAMETER G(BCC_B2,CR:AL:VA;0)  298.15  -2000;,,N 01DUP !
$
$                                    FCC_L12 PHASE
$                                      metastable
$
    FUN U1ALCR  298.15 -830;,,N  01DUP !
```

```
   FUN U3ALCR  298.15 0.0; 6000.00   01DUP !
   FUN U4ALCR  298.15 0.0; 6000.00 N  01DUP !
  FUNCTION L04ALCR 298.15 U3ALCR;,,N !
  FUNCTION L14ALCR 298.15 U4ALCR;,,N !
  FUNCTION ALCR3 298.15 3*U1ALCR;,,N !
  FUNCTION AL2CR2 298.15 4*U1ALCR;,,N !
  FUNCTION AL3CR 298.15 3*U1ALCR;,,N !
 PARAMETER G(FCC_L12,CR:AL:VA;0)  298.15  +ALCR3;,,  N  01DUP !
 PARAMETER G(FCC_L12,AL:CR:VA;0)  298.15  +AL3CR;,,  N  01DUP !
 PARAMETER L(FCC_L12,AL,CR:AL:VA;0) 298.15
   -1.5*ALCR3+1.5*AL2CR2+1.5*AL3CR;,,N 01DUP !
 PARAMETER L(FCC_L12,AL,CR:CR:VA;0) 298.15
   +1.5*ALCR3+1.5*AL2CR2-1.5*AL3CR;,,N 01DUP !
 PARAMETER L(FCC_L12,AL,CR:AL:VA;1) 298.15
   +0.5*ALCR3-1.5*AL2CR2+1.5*AL3CR;,,N 01DUP !
 PARAMETER L(FCC_L12,AL,CR:CR:VA;1) 298.15
   -1.5*ALCR3+1.5*AL2CR2-0.5*AL3CR;,,N 01DUP !
 PARAMETER L(FCC_L12,*:AL,CR:VA;0) 298.15 +L04ALCR;,,N 01DUP !
 PARAMETER L(FCC_L12,*:AL,CR:VA;1) 298.15 +L14ALCR;,,N 01DUP !
 PARAMETER L(FCC_L12,AL,CR:*:VA;0) 298.15 +3*L04ALCR;,,N 01DUP !
 PARAMETER L(FCC_L12,AL,CR:*:VA;1) 298.15 +3*L14ALCR;,,N 01DUP !
$
$                                        AL11CR2 PHASE
$
 PHASE AL11CR2  %  3 10   1   2 !
 CONST AL11CR2  :AL : AL : CR : !
 PARAMETER G(AL11CR2,AL:AL:CR;0)  298.15
   +11*GHSERAL+2*GHSERCR-175500+25.805*T;,,N 91SAU1 !
$
$                                        AL13CR2 PHASE
$
 PHASE AL13CR2  %  2 13   2 !
 CONST AL13CR2  :AL : CR :  !
 PARAMETER G(AL13CR2,AL:CR;0)  298.15
   +13*GHSERAL+2*GHSERCR-174405+22.2*T;,,N 91SAU1 !
$
$                                         AL4CR PHASE
$
 PHASE AL4CR  %  2 4   1 !
 CONST AL4CR  :AL : CR :  !
 PARAMETER G(AL4CR,AL:CR;0)  298.15
```

```
   +4*GHSERAL+GHSERCR-89025+19.05*T;,,N 91SAU1 !
$
$                                        AL8CR5_H PHASE
$
 PHASE AL8CR5_H  %  2 8   5 !
 CONST AL8CR5_H  :AL : CR :  !
 PARAMETER G(AL8CR5_H,AL:CR;0)  298.15
   +8*GHSERAL+5*GHSERCR-147732-58.5*T;,,N 91SAU1 !
$
$                                        AL8CR5_L PHASE
$
 PHASE AL8CR5_L  %  2 8   5 !
 CONST AL8CR5_L  :AL : CR :  !
 PARAMETER G(AL8CR5_L,AL:CR;0)  298.15
   +8*GHSERAL+5*GHSERCR-229515;,,N 91SAU1 !
$
$                                        AL9CR4_H PHASE
$
 PHASE AL9CR4_H  %  2 9   4 !
 CONST AL9CR4_H  :AL : CR :  !
 PARAMETER G(AL9CR4_H,AL:CR;0)  298.15
   +9*GHSERAL+4*GHSERCR-134433-56.16*T;,,N 91SAU1 !
$
$                                        AL9CR4_L PHASE
$
 PHASE AL9CR4_L  %  2 9   4 !
 CONST AL9CR4_L  :AL : CR :  !
 PARAMETER G(AL9CR4_L,AL:CR;0)  298.15
   +9*GHSERAL+4*GHSERCR-230750+16.094*T;,,N 91SAU1 !
$
$                                          ALCR2 PHASE
$
 PHASE ALCR2  %  2 1   2 !
 CONST ALCR2  :AL : CR :  !
 PARAMETER G(ALCR2,AL:CR;0)  298.15
   +GHSERAL+2*GHSERCR-32700-8.79*T;,,N 91SAU1 !
$
$---------------------------------------------------------------------
$
$                                              Al-Ni
$              Mainly from ND thesis,
```

```
$                slighly revised to get better solvus at low temperature
$
$                                        LIQUID PHASE
$
 PARAMETER L(LIQUID,AL,NI;0)  298.15 -207109.28+41.31501*T;,,N 95DUP3 !
 PARAMETER L(LIQUID,AL,NI;1)  298.15 -10185.79+5.8714*T;,,N 95DUP3 !
 PARAMETER L(LIQUID,AL,NI;2)  298.15 +81204.81-31.95713*T;,,N 95DUP3 !
 PARAMETER L(LIQUID,AL,NI;3)  298.15  +4365.35-2.51632*T;,,N 95DUP3 !
 PARAMETER L(LIQUID,AL,NI;4)  298.15  -22101.64+13.16341*T;,,N 95DUP3 !
$
$                                        FCC_A1 PHASE
$
 PARAMETER TC(FCC_A1,AL,NI:VA;0)  298.15  -1112;,,N 95DUP3 !
 PARAMETER TC(FCC_A1,AL,NI:VA;1)  298.15  1745;,,N 95DUP3 !
 PARAMETER G(FCC_A1,AL,NI:VA;0)  298.15  -162407.75+16.212965*T;,,N 95DUP3 !
 PARAMETER G(FCC_A1,AL,NI:VA;1)  298.15  +73417.798-34.914168*T;,,N 95DUP3 !
 PARAMETER G(FCC_A1,AL,NI:VA;2)  298.15  +33471.014-9.8373558*T;,,N 95DUP3 !
 PARAMETER G(FCC_A1,AL,NI:VA;3)  298.15  -30758.01+10.25267*T;,,N 95DUP3 !
$
$                                        BCC_A2 PHASE
$                                         metastable
$
  FUNC B2ALNI 295.15 -152397.3+26.40575*T;,,N !
  FUNC LB2ALNI 298.15 -52440.88+11.30117*T;,,N !
 PARAMETER L(BCC_A2,AL,NI:VA;0)  298.15  B2ALNI+LB2ALNI;,,N 99DUP!
$
$                                        BCC_B2 PHASE
$
 PARAMETER G(BCC_B2,AL:NI:VA;0)  298.15  .5*B2ALNI-.5*LB2ALNI;,,N 99DUP !
 PARAMETER G(BCC_B2,NI:AL:VA;0)  298.15  .5*B2ALNI-.5*LB2ALNI;,,N 99DUP !
$
$                                        FCC_L12 PHASE
$
    FUN UALNI 298.15 -22212.8931+4.39570389*T;,,,N 01DUP !
    FUN U1ALNI 298.15 2*UNTIER*UALNI;,,,N 01DUP !
    FUN U3ALNI 298.15 0;,,,N 01DUP !
    FUN U4ALNI 298.15 7203.60609-3.74273030*T;,,,N 01DUP !
  FUNCTION L04ALNI 298.15 U3ALNI;,,N 01DUP !
  FUNCTION L14ALNI 298.15 U4ALNI;,,N 01DUP !
  FUNCTION ALNI3   298.15 +3*U1ALNI;,,,N 01DUP !
  FUNCTION AL2NI2  298.15 +4*U1ALNI;,,,N 01DUP !
```

```
  FUNCTION AL3NI   298.15 +3*U1ALNI;,,,N 01DUP !
 PARAMETER G(FCC_L12,NI:AL:VA;0)  298.15  +ALNI3;,,N 01DUP !
 PARAMETER G(FCC_L12,AL:NI:VA;0)  298.15  +AL3NI;,,N 01DUP !
 PARAMETER L(FCC_L12,AL,NI:AL:VA;0) 298.15
    -1.5*ALNI3+1.5*AL2NI2+1.5*AL3NI;,,N 01DUP !
 PARAMETER L(FCC_L12,AL,NI:NI:VA;0) 298.15
    +1.5*ALNI3+1.5*AL2NI2-1.5*AL3NI;,,N 01DUP !
 PARAMETER L(FCC_L12,AL,NI:AL:VA;1) 298.15
    +0.5*ALNI3-1.5*AL2NI2+1.5*AL3NI;,,N 01DUP !
 PARAMETER L(FCC_L12,AL,NI:NI:VA;1) 298.15
    -1.5*ALNI3+1.5*AL2NI2-0.5*AL3NI;,,N 01DUP !
 PARAMETER L(FCC_L12,*:AL,NI:VA;0) 298.15 +L04ALNI;,,N 01DUP !
 PARAMETER L(FCC_L12,*:AL,NI:VA;1) 298.15 +L14ALNI;,,N 01DUP !
 PARAMETER L(FCC_L12,AL,NI:*:VA;0) 298.15 +3*L04ALNI;,,N 01DUP !
 PARAMETER L(FCC_L12,AL,NI:*:VA;1) 298.15 +3*L14ALNI;,,N 01DUP !
$
$                                        AL3NI1 PHASE
$
 PHASE AL3NI1  %  2 .75   .25 !
 CONST AL3NI1  :AL : NI :  !
 PARAMETER G(AL3NI1,AL:NI;0)  298.15
 -48483.73+12.29913*T
 +.75*GHSERAL+.25*GHSERNI;,,N 95DUP3 !
$
$                                        AL3NI2 PHASE
$
 PHASE AL3NI2  %  3 3   2   1 !
 CONST AL3NI2  :AL : AL,NI% : NI,VA% :  !
 PARAMETER  G(AL3NI2,AL:AL:NI;0)  298.15  +5*GBCCAL+GBCCNI
    -39465.978+7.89525*T;,,N 95DUP3 !
 PARAMETER G(AL3NI2,AL:NI:NI;0)  298.15  +3*GBCCAL+3*GBCCNI
    -427191.9+79.21725*T;,,N 95DUP3 !
 PARAMETER  G(AL3NI2,AL:AL:VA;0) 298.15  +5*GBCCAL
    +30000-3*T;,,N 95DUP3 !
 PARAMETER  G(AL3NI2,AL:NI:VA;0)  298.15  +3*GBCCAL+2*GBCCNI
    -357725.92+68.322*T;,,N 95DUP3 !
 PARAMETER  L(AL3NI2,AL:AL,NI:*;0)  298.15
    -193484.18+131.79*T;,,N 95DUP3 !
 PARAMETER  L(AL3NI2,AL:*:NI,VA;0)  298.15
    -22001.7+7.0332*T;,,N 95DUP3 !
$
```

```
$                                        AL3NI5 PHASE
$
 PHASE AL3NI5  %  2 .375   .625 !
 CONST AL3NI5  :AL : NI :  !
 PARAMETER G(AL3NI5,AL:NI;0)  298.15  +.375*GHSERAL+.625*GHSERNI
    -55507.7594+7.2648103*T;,,N 95DUP3 !
$
$---------------------------------------------------------------------------
$
$                                           Cr-Ni
$                    Mainly from SSOL
$                    Metastable B2 and L12 from revision of Al-Cr-Ni
$
$                                        LIQUID PHASE
$
 PARAMETER L(LIQUID,CR,NI;0)  298.15  +318-7.3318*T;,,N 91LEE !
 PARAMETER L(LIQUID,CR,NI;1)  298.15  +16941-6.3696*T;,,N 91LEE !
$
$                                        FCC_A1 PHASE
$
 PARAMETER G(FCC_A1,CR,NI:VA;0)  298.15  +8030-12.8801*T;,,N 91LEE !
 PARAMETER G(FCC_A1,CR,NI:VA;1)  298.15  +33080-16.0362*T;,,N 91LEE !
 PARAMETER TC(FCC_A1,CR,NI:VA;0)  298.15  -3605;,,N 86DIN !
 PARAMETER BMAGN(FCC_A1,CR,NI:VA;0)  298.15  -1.91;,,N 86DIN !
$
$                                        BCC_A2 PHASE
$
 PARAMETER G(BCC_A2,CR,NI:VA;0)  298.15  +17170-11.8199*T;,,N 91LEE !
 PARAMETER G(BCC_A2,CR,NI:VA;1)  298.15  +34418-11.8577*T;,,N 91LEE !
 PARAMETER TC(BCC_A2,CR,NI:VA;0)  298.15  2373;,,N 86DIN !
 PARAMETER TC(BCC_A2,CR,NI:VA;1)  298.15  617;,,N 86DIN !
 PARAMETER BMAGN(BCC_A2,CR,NI:VA;0)  298.15  4;,,N 86DIN !
$
$                                        BCC_B2 PHASE
$                                          metastable
$
$
 PARAMETER G(BCC_B2,CR:NI:VA;0)  298.15  4000;,,N 01DUP !
 PARAMETER G(BCC_B2,NI:CR:VA;0)  298.15  4000;,,N 01DUP !
$
$                                        FCC_L12 PHASE
```

```
$                                        metastable
$
$ The L12 phase is metastable in the binary Cr-Ni while it was stable in NDTH.
    FUN U1CRNI 298.15 -1980;,,,N 01DUP !
$    FUN U1CRNI 298.15 -7060+3.63*T;,,,N 01DUP !
    FUN U3CRNI 298.15 0;,,,N 01DUP !
    FUN U4CRNI 298.15 0;,,,N 01DUP !
  FUNCTION L04CRNI 298.15 U3CRNI;,,N 01DUP !
  FUNCTION L14CRNI 298.15 U4CRNI;,,N 01DUP !
  FUNCTION CRNI3   298.15 +3*U1CRNI;,,,N 01DUP !
  FUNCTION CR2NI2  298.15 +4*U1CRNI;,,,N 01DUP !
  FUNCTION CR3NI   298.15 +3*U1CRNI;,,,N 01DUP !
 PARAMETER G(FCC_L12,NI:CR:VA;0)  298.15  +CRNI3;,,  N 01DUP !
 PARAMETER G(FCC_L12,CR:NI:VA;0)  298.15  +CR3NI;,,  N 01DUP !
 PARAMETER L(FCC_L12,CR,NI:CR:VA;0) 298.15
    -1.5*CRNI3+1.5*CR2NI2+1.5*CR3NI;,,N 01DUP !
 PARAMETER L(FCC_L12,CR,NI:NI:VA;0) 298.15
    +1.5*CRNI3+1.5*CR2NI2-1.5*CR3NI;,,N 01DUP !
 PARAMETER L(FCC_L12,CR,NI:CR:VA;1) 298.15
    +0.5*CRNI3-1.5*CR2NI2+1.5*CR3NI;,,N 01DUP !
 PARAMETER L(FCC_L12,CR,NI:NI:VA;1) 298.15
    -1.5*CRNI3+1.5*CR2NI2-0.5*CR3NI;,,N 01DUP !
 PARAMETER L(FCC_L12,*:CR,NI:VA;0) 298.15 +L04CRNI;,,N 01DUP !
 PARAMETER L(FCC_L12,*:CR,NI:VA;1) 298.15 +L14CRNI;,,N 01DUP !
 PARAMETER L(FCC_L12,CR,NI:*:VA;0) 298.15 +3*L04CRNI;,,N 01DUP !
 PARAMETER L(FCC_L12,CR,NI:*:VA;1) 298.15 +3*L14CRNI;,,N 01DUP !
$----------------------------------------------------------------------
$
$                                      Al-Mo, Peng
$
 PARAMETER G(LIQUID,AL,MO;0)  298.15 -102047.625+3.77803026E+01*T;
   6000 N Peng !
 PARAMETER G(LIQUID,AL,MO;1) 298.15  1.37544909E+04-1.88870075E+00*T;
   6000 N Peng !
 PARAMETER G(LIQUID,AL,MO;2)  298.15 -3.73262997E+04+1.04018453E+01*T;
   6000 N Peng !

 PARAMETER G(BCC_A2,AL,MO:VA;0) 298.15 -73113.2883+22.7704371*T; 6000 N 10Cup
!
 PARAMETER G(BCC_A2,AL,MO:VA;1)  2.98150E+02  -16584.5446;   6000 N 10Cup !
 PARAMETER G(BCC_A2,AL,MO:VA;2)  2.98150E+02  -18877.1914;   6000 N 10Cup !
```

```
 PARAMETER G(BCC_B2,MO:AL:VA;0)  298.15  -14100+2*T; 6000   N 10Cup !
 PARAMETER G(BCC_B2,AL:MO:VA;0)  298.15  -14100+2*T; 6000   N 10Cup !
 PARAMETER G(FCC_A1,AL,MO:VA;0) 298.15 -146174.503+75.6992933*T; 6000 N 10Cup
!
 FUNCTION U1ALMO  298.15 0;,,N  01DUP !
 FUNCTION U3ALMO  298.15 0.0; 6000.00   01DUP !
 FUNCTION U4ALMO  298.15 0.0; 6000.00 N  01DUP !
 FUNCTION L04ALMO 298.15 U3ALMO;,,N !
 FUNCTION L14ALMO 298.15 U4ALMO;,,N !
 FUNCTION ALMO3   298.15 3*U1ALMO;,,N !
 FUNCTION AL2MO2  298.15 4*U1ALMO;,,N !
 FUNCTION AL3MO   298.15 3*U1ALMO;,,N !
 PARAMETER G(FCC_L12,MO:AL:VA;0)  298.15  +ALMO3;,,  N  01DUP !
 PARAMETER G(FCC_L12,AL:MO:VA;0)  298.15  +AL3MO;,,  N  01DUP !
 PARAMETER L(FCC_L12,AL,MO:AL:VA;0) 298.15
-1.5*ALMO3+1.5*AL2MO2+1.5*AL3MO;,,N 01DUP !
 PARAMETER L(FCC_L12,AL,MO:MO:VA;0) 298.15
+1.5*ALMO3+1.5*AL2MO2-1.5*AL3MO;,,N 01DUP !
 PARAMETER L(FCC_L12,AL,MO:AL:VA;1) 298.15
+0.5*ALMO3-1.5*AL2MO2+1.5*AL3MO;,,N 01DUP !
 PARAMETER L(FCC_L12,AL,MO:MO:VA;1) 298.15
-1.5*ALMO3+1.5*AL2MO2-0.5*AL3MO;,,N 01DUP !
 PARAMETER L(FCC_L12,*:AL,MO:VA;0) 298.15 +L04ALMO;,,N 01DUP !
 PARAMETER L(FCC_L12,*:AL,MO:VA;1) 298.15 +L14ALMO;,,N 01DUP !
 PARAMETER L(FCC_L12,AL,MO:*:VA;0) 298.15 +3*L04ALMO;,,N 01DUP !
 PARAMETER L(FCC_L12,AL,MO:*:VA;1) 298.15 +3*L14ALMO;,,N 01DUP !

 PARAMETER G(CUB_A15,MO:AL;0)  298.15  -21180.9741+3.3394361*T
+.75*GHSERMO+.25*GHSERAL;   6.00000E+03   N 10Cup !
 PARAMETER G(CUB_A15,AL:MO;0)  298.15  +10000+.75*GHSERAL
+.25*GHSERMO;   6.00000E+03   N 10Cup !
 PARAMETER G(CUB_A15,AL,MO:AL;0) 298.15  +0.455738495*T; 6000 N 10Cup !
 PARAMETER G(CUB_A15,MO:AL,MO;0) 298.15  -2.63250337*T; 6000 N  10Cup !

 PHASE AL12MO  %  2 12   1 !
   CONSTITUENT AL12MO  :AL : MO :  !
  PARAMETER G(AL12MO,AL:MO;0)  298.15 -1.47884522E+05+33*T
  +12*GHSERAL#+GHSERMO#; 6000 N Peng !

 PHASE AL17MO4  %  2 17   4 !
   CONSTITUENT AL17MO4  :AL : MO :  !
```

```
 PARAMETER G(AL17MO4,AL:MO;0)    298.15 -5.96728081E+05+1.60445888E+02*T
 +17*GHSERAL#+4*GHSERMO#; 6000 N Peng !

PHASE AL22MO5  %  2 22   5 !
  CONSTITUENT AL22MO5  :AL : MO :  !
 PARAMETER G(AL22MO5,AL:MO;0)   298.15 -7.45899148E+05+1.98500000E+02*T
 +22*GHSERAL#+5*GHSERMO#; 6000 N Peng !

PHASE AL3MO  %  2 3   1 !
  CONSTITUENT AL3MO  :AL : MO :  !
 PARAMETER G(AL3MO,AL:MO;0)    298.15 -1.43801421E+05+4.09326635E+01*T+
 3*GHSERAL#+GHSERMO#; 6000 N Peng !

PHASE AL4MO  %  2 4   1 !
  CONSTITUENT AL4MO  :AL : MO :  !
 PARAMETER G(AL4MO,AL:MO;0)    298.15 -1.42202145E+05+3.54152656E+01*T
 +4*GHSERAL#+GHSERMO#; 6000 N Peng !

PHASE AL5MO  %  2 5   1 !
  CONSTITUENT AL5MO  :AL : MO :  !
 PARAMETER G(AL5MO,AL:MO;0)    298.15 -1.48908113E+05+38.3*T
 +5*GHSERAL#+GHSERMO#; 6000 N Peng !

PHASE AL63MO37  %  2 63   37 !
  CONSTITUENT AL63MO37  :AL : MO :  !
 PARAMETER G(AL63MO37,AL:MO;0)  298.15 -1.51552361E+06-1.76057703E+02*T
 +63*GHSERAL#+37*GHSERMO#; 6000 N Peng !

PHASE AL8MO3  %  2 8   3 !
CONSTITUENT AL8MO3  :AL : MO :  !
PARAMETER G(AL8MO3,AL:MO;0)  2.98150E+02  -432300+128.341056*T+8*GHSERAL
+3*GHSERMO;   6.00000E+03   N 10Cup !
$----------------------------------------------------------------------
$
$                                    Mo-Ni, 05Zhou
$
PARAMETER L(LIQUID,MO,NI;0)  298.15  -39597+15.935*T;  6000  N 05Zho !
PARAMETER L(LIQUID,MO,NI;1)  298.15  -7373+4.102*T;    6000  N 05Zho !
PARAMETER L(LIQUID,MO,NI;2)  298.15  -12123+5.551*T;   6000  N 05Zho !
PARAMETER L(BCC_A2,MO,NI:VA;0)   298.15  27691; 6000  N  05Zho !
PARAMETER L(BCC_A2,MO,NI:VA;1)   298.15  18792; 6000  N  05Zho !
```

```
 PARAMETER L(FCC_A1,MO,NI:VA;0)  298.15  -8916+3.591*T; 6000  N 05Zho !
 PARAMETER L(FCC_A1,MO,NI:VA;1)  298.15  5469-0.249*T; 6000   N 05Zho !
 PARAMETER L(FCC_A1,MO,NI:VA;2)  298.15  -1549-2.741*T; 6000  N 05Zho !
$MO-Ni metastable
$FUNCTION U1CRNI  298.15 -1980;,,,N 01DUP !
 FUNCTION U1MONI  298.15 0;,,,N 01DUP !
$FUNCTION U1CRNI  298.15 -7060+3.63*T;,,,N 01DUP !
 FUNCTION U3MONI  298.15 0;,,,N 01DUP !
 FUNCTION U4MONI  298.15 0;,,,N 01DUP !
 FUNCTION L04MONI 298.15 U3MONI;,,N 01DUP !
 FUNCTION L14MONI 298.15 U4MONI;,,N 01DUP !
 FUNCTION MONI3   298.15 +3*U1MONI;,,,N 01DUP !
 FUNCTION MO2NI2  298.15 +4*U1MONI;,,,N 01DUP !
 FUNCTION MO3NI   298.15 +3*U1MONI;,,,N 01DUP !
 PARAMETER G(FCC_L12,NI:MO:VA;0)  298.15  +MONI3;,,  N 01DUP !
 PARAMETER G(FCC_L12,MO:NI:VA;0)  298.15  +MO3NI;,,  N 01DUP !
 PARAMETER L(FCC_L12,MO,NI:MO:VA;0) 298.15
 -1.5*MONI3+1.5*MO2NI2+1.5*MO3NI;,,N 01DUP !
 PARAMETER L(FCC_L12,MO,NI:NI:VA;0) 298.15
 +1.5*MONI3+1.5*MO2NI2-1.5*MO3NI;,,N 01DUP !
 PARAMETER L(FCC_L12,MO,NI:MO:VA;1) 298.15
 +0.5*MONI3-1.5*MO2NI2+1.5*MO3NI;,,N 01DUP !
 PARAMETER L(FCC_L12,MO,NI:NI:VA;1) 298.15
 -1.5*MONI3+1.5*MO2NI2-0.5*MO3NI;,,N 01DUP !
 PARAMETER L(FCC_L12,*:MO,NI:VA;0) 298.15 +L04MONI;,,N 01DUP !
 PARAMETER L(FCC_L12,*:MO,NI:VA;1) 298.15 +L14MONI;,,N 01DUP !
 PARAMETER L(FCC_L12,MO,NI:*:VA;0) 298.15 +3*L04MONI;,,N 01DUP !
 PARAMETER L(FCC_L12,MO,NI:*:VA;1) 298.15 +3*L14MONI;,,N 01DUP !

 PHASE NIMO  %  3  24   20   12 !
 CONSTITUENT NIMO  :CR,NI : CR,AL,MO,NI : MO :  !
 PARAMETER G(NIMO,NI:MO:MO;0)  298.15  -169981+1154.981*T-155.484*T*LN(T)
 +24*GHSERNI+32*GHSERMO;            6000  N 05Zho !
 PARAMETER G(NIMO,NI:NI:MO;0)  298.15  -154106+2855.001*T-394.923*T*LN(T)
 +24*GHSERNI+20*GBCCNI+12*GHSERMO;   6000  N 05Zho !
 PARAMETER L(NIMO,NI:MO,NI:MO;0)  298.15  -829211+825.923*T; 6000  N 05Zho !
 PARAMETER L(NIMO,NI:MO,NI:MO;1)  298.15  -417368+326.504*T; 6000  N 05Zho !

 PHASE NI3MO  %  3  4  2  2 !
 CONSTITUENT NI3MO  :MO,NI : NI: MO,NI,AL :  !
```

```
 PARAMETER G(NI3MO,MO:NI:MO;0)  298.15
136480+4*GFCCMO+2*GHSERNI+2*GHSERMO;
 6000  N  05Zho !
 PARAMETER G(NI3MO,NI:NI:MO;0)  298.15  -81055.2+465.054*T-58.929*T*LN(T)
 +4*GHSERNI+2*GHSERNI+2*GHSERMO;  6000  N  05Zho !
 PARAMETER G(NI3MO,NI:NI:NI;0)  298.15
22720+4*GHSERNI+2*GHSERNI+2*GBCCNI;
 6000  N  05Zho !
 PARAMETER L(NI3MO,MO,NI:NI:MO;0)  298.15  -69324;   6000  N  05Zho !
 PARAM G(NI3MO,NI:NI:AL;0) 298.15 -309000+31.2*T
 +4*GHSERNI+2*GHSERNI+2*GBCCAL; 6000 N Peng !

 PHASE NI2MO  %  2   2  1 !
 CONSTITUENT NI2MO  :NI : MO,AL :  !
 PARAMETER G(NI2MO,NI:MO;0)  298.15  -28263+148.653*T-18.693*T*LN(T)
 +2*GHSERNI+GHSERMO; 6000  N 05Zho !

 PHASE NI4MO  %  2  4   1 !
 CONSTITUENT NI4MO  :NI : MO,AL :  !
 PARAMETER G(NI4MO,NI:MO;0)  298.15  -45105+275.020*T-35.4*T*LN(T)
 +4*GHSERNI+GHSERMO; 6000  N  05Zho !


 PHASE NI8MO  %  2   8   1 !
 CONSTITUENT NI8MO  :NI : MO :  !
 PARAMETER G(NI8MO,NI:MO;0)  298.15  -55035+299.322*T-36.765*T*LN(T)
 +8*GHSERNI+GHSERMO;  6000  N 05Zho !

$----------------------------------------------------------------------
$
$                                       Cr-Mo
$
  PARAMETER G(LIQUID,CR,MO;0)  2.98150E+02  +15810-6.714*T;   6.00000E+03
 N 88Fri !
  PARAMETER G(LIQUID,CR,MO;1)  2.98150E+02  -6220;   6.00000E+03   N 88Fri !
  PARAMETER G(BCC_A2,CR,MO:VA;0)  2.98150E+02  +28890-7.962*T;
 6.00000E+03   N 88Fri !
  PARAMETER G(BCC_A2,CR,MO:VA;1)  2.98150E+02  +5974-2.428*T;   6.00000E+03
   N 88Fri !
```

```
$**************************************************************************
$
$                                TERNARY PARAMETERS
$
$--------------------------------------------------------------------------
$
$                                    Al-Cr-Ni
$                        July 1999, ND
$                        Revision. Main changes:
$                        - description of the A2/B2
$                        - new liquidus data taken into account
$                        - simpler ternary interaction parameters
$
$                                  LIQUID PHASE
$
 PARAMETER L(LIQUID,AL,CR,NI;0)  298.15  38000;,,N Peng !
 PARAMETER L(LIQUID,AL,CR,NI;1)  298.15  6000;,,N Peng !
 PARAMETER L(LIQUID,AL,CR,NI;2)  298.15  16000;,,N Peng !
$
$                                  FCC_A1 PHASE
$
 PARAMETER G(FCC_A1,AL,CR,NI:VA;0)  298.15  30300;,,N 01DUP !
$
$                                  BCC_A2 PHASE
$
 PARAMETER G(BCC_A2,AL,CR,NI:VA;0)  298.15  42500;,,N 01DUP !
$
$                                  FCC_L12 PHASE
$
  FUN U1ALCRNI 298.15 6650;,,N 01DUP !
  FUN U2ALCRNI 298.15 0;,,N 01DUP !
  FUN U3ALCRNI 298.15 0;,,N 01DUP !
  FUN ALCRNI2 298.15 U1ALCR+2*U1ALNI+2*U1CRNI+U1ALCRNI;,,N 01DUP !
  FUN ALCR2NI 298.15 2*U1ALCR+U1ALNI+2*U1CRNI+U2ALCRNI;,,N 01DUP !
  FUN AL2CRNI 298.15 2*U1ALCR+2*U1ALNI+U1CRNI+U3ALCRNI;,,N 01DUP !
 PARA L(FCC_L12,AL,CR,NI:AL:VA;0) 298.15
    -1.5*ALCRNI2-1.5*ALCR2NI+ALCR3+ALNI3+6*AL2CRNI
    -1.5*AL2CR2-1.5*AL2NI2-1.5*AL3CR-1.5*AL3NI;,,N 01DUP !
 PARA L(FCC_L12,AL,CR,NI:CR:VA;0) 298.15
    -1.5*ALCRNI2+6*ALCR2NI-1.5*ALCR3-1.5*AL2CRNI
    -1.5*AL2CR2+AL3CR+CRNI3-1.5*CR2NI2-1.5*CR3NI;,,N 01DUP !
```

```
 PARA L(FCC_L12,AL,CR,NI:NI:VA;0) 298.15
    +6*ALCRNI2-1.5*ALCR2NI-1.5*ALNI3-1.5*AL2CRNI
    -1.5*AL2NI2+AL3NI-1.5*CRNI3-1.5*CR2NI2+CR3NI;,,N 01DUP !
 PARA L(FCC_L12,AL,CR:NI:VA;0) 298.15
    +1.5*ALCR2NI+1.5*AL2CRNI-1.5*AL3NI-1.5*CR3NI;,,N 01DUP !
 PARA L(FCC_L12,AL,NI:CR:VA;0) 298.15
    +1.5*ALCRNI2+1.5*AL2CRNI-1.5*AL3CR-1.5*CRNI3;,,N 01DUP !
 PARA L(FCC_L12,CR,NI:AL:VA;0) 298.15
    +1.5*ALCRNI2+1.5*ALCR2NI-1.5*ALCR3-1.5*ALNI3;,,N 01DUP !
 PARA L(FCC_L12,AL,CR:NI:VA;1) 298.15
    -1.5*ALCR2NI+1.5*AL2CRNI-0.5*AL3NI+0.5*CR3NI;,,N 01DUP !
 PARA L(FCC_L12,AL,NI:CR:VA;1) 298.15
    -1.5*ALCRNI2+1.5*AL2CRNI-0.5*AL3CR+0.5*CRNI3;,,N 01DUP !
 PARA L(FCC_L12,CR,NI:AL:VA;1) 298.15
    -1.5*ALCRNI2+1.5*ALCR2NI-0.5*ALCR3+0.5*ALNI3;,,N 01DUP !
$

$----------------------------------------------------------------------
$
$                                                Al-MO-Ni
 PARAMETER L(LIQUID,AL,MO,NI;0) 298.15 0;  6000  N Peng !
 PARAMETER L(LIQUID,AL,MO,NI;1) 298.15 0;  6000  N Peng !
 PARAMETER L(LIQUID,AL,MO,NI;2) 298.15 144400;  6000  N Peng !
 PARAMETER L(BCC_A2,AL,MO,NI:VA;0)  298.15  280000;,,N Peng !

$ AL-NI-MO
$FUNCTION U1ALCRNI 298.15 6650;,,N 01DUP !
 FUNCTION U1ALMONI 298.15 13000;,,N Peng !
 FUNCTION U2ALMONI 298.15 0;,,N 01DUP !
 FUNCTION U3ALMONI 298.15 5000;,,N Peng !
 FUNCTION ALMONI2 298.15 U1ALMO+2*U1ALNI+2*U1MONI+U1ALMONI;,,N 01DUP
!
 FUNCTION ALMO2NI 298.15 2*U1ALMO+U1ALNI+2*U1MONI+U2ALMONI;,,N 01DUP
!
 FUNCTION AL2MONI 298.15 2*U1ALMO+2*U1ALNI+U1MONI+U3ALMONI;,,N 01DUP
!
 PARAMETER L(FCC_L12,AL,MO,NI:AL:VA;0) 298.15
  -1.5*ALMONI2-1.5*ALMO2NI+ALMO3+ALNI3+6*AL2MONI
 -1.5*AL2MO2-1.5*AL2NI2-1.5*AL3MO-1.5*AL3NI;,,N 01DUP !
 PARAMETER L(FCC_L12,AL,MO,NI:MO:VA;0) 298.15
 -1.5*ALMONI2+6*ALMO2NI-1.5*ALMO3-1.5*AL2MONI
```

```
-1.5*AL2MO2+AL3MO+MONI3-1.5*MO2NI2-1.5*MO3NI;,,N 01DUP !
PARAMETER L(FCC_L12,AL,MO,NI:NI:VA;0) 298.15
+6*ALMONI2-1.5*ALMO2NI-1.5*ALNI3-1.5*AL2MONI
-1.5*AL2NI2+AL3NI-1.5*MONI3-1.5*MO2NI2+MO3NI;,,N 01DUP !
PARAMETER L(FCC_L12,AL,MO:NI:VA;0) 298.15
+1.5*ALMO2NI+1.5*AL2MONI-1.5*AL3NI-1.5*MO3NI;,,N 01DUP !
PARAMETER L(FCC_L12,AL,NI:MO:VA;0) 298.15
+1.5*ALMONI2+1.5*AL2MONI-1.5*AL3MO-1.5*MONI3;,,N 01DUP !
PARAMETER L(FCC_L12,MO,NI:AL:VA;0) 298.15
+1.5*ALMONI2+1.5*ALMO2NI-1.5*ALMO3-1.5*ALNI3;,,N 01DUP !
PARAMETER L(FCC_L12,AL,MO:NI:VA;1) 298.15
-1.5*ALMO2NI+1.5*AL2MONI-0.5*AL3NI+0.5*MO3NI;,,N 01DUP !
PARAMETER L(FCC_L12,AL,NI:MO:VA;1) 298.15
-1.5*ALMONI2+1.5*AL2MONI-0.5*AL3MO+0.5*MONI3;,,N 01DUP !
PARAMETER L(FCC_L12,MO,NI:AL:VA;1) 298.15
-1.5*ALMONI2+1.5*ALMO2NI-0.5*ALMO3+0.5*ALNI3;,,N 01DUP !

PARAM L(FCC_A1,AL,MO,NI:VA;0) 298.15 8543-13.5*T; 6000 N !
PARAM L(FCC_A1,AL,MO,NI:VA;1) 298.15 81408-44.64*T; 6000 N !
PARAM L(FCC_A1,AL,MO,NI:VA;2) 298.15 173588-32.53*T; 6000 N !


PARAM G(NIMO,NI:AL:MO;0) 298.15 -3140000+895*T
+24*GHSERNI+20*GBCCAL+12*GHSERMO; 6000 N Peng!

PARAM G(NI3MO,NI:NI:AL;0) 298.15 -309000+31.2*T
+4*GHSERNI+2*GHSERNI+2*GBCCAL; 6000 N Peng !

PARAM G(NI4MO,NI:AL;0) 298.15 -161200+19.7*T+4*GHSERNI+GBCCAL; 6000 N  Peng!

  PHASE X  %  3 .75   .11   .14 !
CONSTITUENT X  :AL : MO : NI :  !
 PARAMETER G(X,AL:MO:NI;0)            298.15 -39464.2+6.521*T
 +.75*GHSERAL#+.14*GHSERNI#+.11*GHSERMO#; 6000 N 14Zhou !

PHASE N  %  3 2   1   1 !
CONSTITUENT N  :AL,NI : AL,NI : MO :  !
 PARAMETER G(N,AL:AL:MO;0)            298.15 -108760+22.128*T+3*GHSERAL#
 +GHSERMO#; 6000 N 14Zhou !
 PARA G(N,NI:AL:MO;0) 298.15 +0; 6000 N!
 PARAMETER G(N,AL:NI:MO;0)            298.15 -119040+2*GHSERAL#+GHSERNI#
```

```
 +GHSERMO#; 6000 N 14Zhou !
  PARAMETER G(N,NI:NI:MO;0)            298.15 -29600+32.028*T+3*GHSERNI#
 +GHSERMO#; 6000 N 14Zhou !
  PARAMETER G(N,AL:AL,NI:MO;0)         298.15 -140870; 6000 N 14Zhou !
  PARAMETER G(N,AL:AL,NI:MO;1)         298.15 -60570; 6000 N 14Zhou !
$-----------------------------------------------------------------------
$
$                                          Al-Cr-Mo
$                                           Liquid
 PARAMETER L(LIQUID,AL,Cr,MO;0) 298.15 27000;  6000  N Peng !

$***************************************************************************
$                                          Cr-Mo-Ni

 PHASE Sigma  %  3 8  4   18 !
   CONSTITUENT Sigma  :NI :CR,MO : CR,MO,NI :  !

  PARAMETER G(Sigma,NI:CR:CR;0)  298.15 173460-188*T
  +8*GHSERNI+4*GHSERCR+18*GHSERCR; 6000 N 90Fri !
  PARAMETER G(Sigma,NI:MO:CR;0)  298.15 386423
  +8*GHSERNI+4*GHSERMO+18*GHSERCR; 6000 N 90Fri !
  PARAMETER G(Sigma,NI:CR:MO;0)  298.15 -110000
  +8*GHSERNI+4*GHSERCR+18*GHSERMO; 6000 N Peng !
  PARAMETER G(Sigma,NI:MO:MO;0)  298.15 85662
  +8*GHSERNI+4*GHSERMO+18*GHSERMO; 6000 N 90Fri !
  PARAMETER G(Sigma,NI:CR:NI;0)  298.15 100000
  +8*GHSERNI+4*GHSERCR+18*GBCCNI; 6000 N Peng !
  PARAMETER G(Sigma,NI:MO:NI;0)  298.15 -16385
  +8*GHSERNI+4*GHSERMO+18*GBCCNI; 6000 N 90Fri !

   PHASE P  %C  3 24  20  12 !
   CONSTITUENT P  :CR,NI :CR,NI,MO : MO :  !

  PARAMETER G(P,CR:CR:MO;0)  298.15 252300-100*T
  +24*GFCCCR+20*GHSERCR+12*GHSERMO; 6000 N 90Fri !
  PARAMETER G(P,NI:CR:MO;0)  298.15 -341858
  +24*GHSERNI+20*GHSERCR+12*GHSERMO; 6000 N 90Fri !
  PARAMETER G(P,CR:MO:MO;0)  298.15 95573-200*T
  +24*GFCCCR+20*GHSERMO+12*GHSERMO; 6000 N 90Fri !
  PARAMETER G(P,NI:MO:MO;0)  298.15 26739-90*T
  +24*GHSERNI+20*GHSERMO+12*GHSERMO; 6000 N Peng !
```

```
 PARAMETER G(P,CR:NI:MO;0)  298.15 0
 +24*GFCCCR+20*GBCCNI+12*GHSERMO; 6000 N Peng !
PARAMETER G(P,NI:NI:MO;0)  298.15 208845-60*T
 +24*GHSERNI+20*GBCCNI+12*GHSERMO; 6000 N Peng !


PARAM G(NIMO,NI:CR:MO;0) 298.15 -200000
+24*GHSERNI+20*GHSERCR+12*GHSERMO; 6000 N 90Fri!
PARAM G(NIMO,CR:NI:MO;0) 298.15 -200000
+24*GFCCCR+20*GBCCNI+12*GHSERMO; 6000 N 90Fri!
 PARAM G(NIMO,CR:CR:MO;0) 298.15 50000
 +24*GFCCCR+20*GHSERCR+12*GHSERMO; 6000 N 90Fri!
 PARAM G(NIMO,CR:MO:MO;0) 298.15 100000
 +24*GFCCCR+20*GHSERMO+12*GHSERMO; 6000 N 90Fri!

 PARAM L(FCC_A1,Mo,CR,NI:VA;0)  298.15 6*T;  6000  N Peng !

$**********************************************************************
$ To make fcc phase correctly disordered in quaternary system,
$ constraints were added into Cr-Mo, Al-Cr-Mo, Cr-Mo-Ni and AL-Ni-Cr-Mo
$**********************************************************************
$                                        Cr-Mo, Peng


FUNCTION U1CRMO  298.15 0;,,,N Peng !
FUNCTION U3CRMO  298.15 0;,,,N Peng !
FUNCTION U4CRMO  298.15 0;,,,N Peng !
FUNCTION L04CRMO 298.15 U3CRMO;,,N Peng !
FUNCTION L14CRMO 298.15 U4CRMO;,,N Peng !
FUNCTION CRMO3   298.15 +3*U1CRMO;,,,N Peng!
FUNCTION CR2MO2  298.15 +4*U1CRMO;,,,N Peng !
FUNCTION CR3MO   298.15 +3*U1CRMO;,,,N Peng !
PARAM G(FCC_L12,MO:CR:VA;0) 298.15 CRMO3; 6000 N Peng !
PARAM G(FCC_L12,CR:MO:VA;0) 298.15 CR3Mo; 6000 N Peng !

PARAM  L(FCC_L12,CR,MO:CR:VA;0) 298.15 -1.5*CRMO3+1.5*CR2MO2+1.5*CR3MO
; 6000 N Peng !
PARAM  L(FCC_L12,CR,MO:CR:VA;1) 298.15 +.5*CRMO3-1.5*CR2MO2+1.5*CR3MO
; 6000 N Peng !
PARAM  L(FCC_L12,CR,MO:MO:VA;0) 298.15 +1.5*CRMO3+1.5*CR2MO2-1.5*CR3MO
; 6000 N Peng !
```

```
 PARAM  L(FCC_L12,CR,MO:MO:VA;1) 298.15 -1.5*CRMO3+1.5*CR2MO2-.5*CR3MO
; 6000 N Peng !
 PARAM  L(FCC_L12,*:CR,MO:VA;0) 298.15 +L04CRMO ; 6000 N Peng !
 PARAM  L(FCC_L12,*:CR,MO:VA;1) 298.15 +L14CRMO ; 6000 N Peng !
 PARAM  L(FCC_L12,CR,MO:*:VA;0) 298.15 +3*L04CRMO ; 6000 N Peng !
 PARAM  L(FCC_L12,CR,MO:*:VA;1) 298.15 +3*L14CRMO ; 6000 N Peng !

$**********************************************************************
$                              Al-Cr-Mo, Peng
 FUNCTION U1ALCRMO 298.15 0;,,N Peng !
 FUNCTION U2ALCRMO 298.15 0;,,N Peng !
 FUNCTION U3ALCRMO 298.15 0;,,N Peng !
 FUNCTION ALCRMO2 298.15 U1ALCR+2*U1ALMO+2*U1CRMO+U1ALCRMO;,,N Peng
!
 FUNCTION ALCR2MO 298.15 2*U1ALCR+U1ALMO+2*U1CRMO+U2ALCRMO;,,N Peng
!
 FUNCTION AL2CRMO 298.15 2*U1ALCR+2*U1ALMO+U1CRMO+U3ALCRMO;,,N Peng
!
 PARAM L(FCC_L12,AL,CR,MO:AL:VA;0) 298.15 -1.5*ALCRMO2-
1.5*ALCR2MO+ALCR3+ALMO3
 +6*AL2CRMO-1.5*AL2CR2-1.5*AL2MO2-1.5*AL3CR-1.5*AL3MO; 6000 N Peng !
 PARAM L(FCC_L12,AL,CR,MO:CR:VA;0) 298.15 -1.5*ALCRMO2+6*ALCR2MO-
1.5*ALCR3
 -1.5*AL2CRMO-1.5*AL2CR2+AL3CR+CRMO3-1.5*CR2MO2-1.5*CR3MO; 6000 N Peng !
 PARAM L(FCC_L12,AL,CR,MO:MO:VA;0) 298.15 +6*ALCRMO2-1.5*ALCR2MO-
1.5*ALMO3
 -1.5*AL2CRMO-1.5*AL2MO2+AL3MO-1.5*CRMO3-1.5*CR2MO2+CR3MO; 6000 N Peng !
 PARAM L(FCC_L12,CR,MO:AL:VA;0) 298.15 +1.5*ALCRMO2+1.5*ALCR2MO-
1.5*ALCR3
 -1.5*ALMO3; 6000 N Peng !
 PARAM L(FCC_L12,CR,MO:AL:VA;1) 298.15 -1.5*ALCRMO2+1.5*ALCR2MO-.5*ALCR3
 +.5*ALMO3; 6000 N Peng !
 PARAM L(FCC_L12,AL,MO:CR:VA;0) 298.15 +1.5*ALCRMO2+1.5*AL2CRMO-
1.5*AL3CR
 -1.5*CRMO3; 6000 N Peng !
 PARAM L(FCC_L12,AL,MO:CR:VA;1) 298.15 -1.5*ALCRMO2+1.5*AL2CRMO-.5*AL3CR
 +.5*CRMO3; 6000 N Peng !
 PARAM L(FCC_L12,AL,CR:MO:VA;0) 298.15 +1.5*ALCR2MO+1.5*AL2CRMO-
1.5*AL3MO
 -1.5*CR3MO; 6000 N Peng !
 PARAM L(FCC_L12,AL,CR:MO:VA;1) 298.15 -1.5*ALCR2MO+1.5*AL2CRMO-.5*AL3MO
```

+.5*CR3MO; 6000 N Peng !

$**
$ Cr-Mo-Ni, Peng

FUNCTION U1CRMONI 298.15 0;,,N Peng !
FUNCTION U2CRMONI 298.15 0;,,N Peng !
FUNCTION U3CRMONI 298.15 0;,,N Peng !
FUNCTION CRMONI2 298.15 U1CRMO+2*U1CRNI+2*U1MONI+U1CRMONI;,,N Peng !
FUNCTION CRMO2NI 298.15 2*U1CRMO+U1CRNI+2*U1MONI+U2CRMONI;,,N Peng !
FUNCTION CR2MONI 298.15 2*U1CRMO+2*U1CRNI+U1MONI+U3CRMONI;,,N Peng !

PARAM L(FCC_L12,CR,MO,NI:CR:VA;0) 298.15 -1.5*CRMONI2-
1.5*CRMO2NI+CRMO3+CRNI3
+6*CR2MONI-1.5*CR2MO2-1.5*CR2NI2-1.5*CR3MO-1.5*CR3NI; 6000 N Peng !
PARAM L(FCC_L12,CR,MO,NI:MO:VA;0) 298.15 -1.5*CRMONI2+6*CRMO2NI-
1.5*CRMO3
-1.5*CR2MONI-1.5*CR2MO2+CR3MO+MONI3-1.5*MO2NI2-1.5*MO3NI; 6000 N Peng !
PARAM L(FCC_L12,CR,MO,NI:NI:VA;0) 298.15 +6*CRMONI2-1.5*CRMO2NI-1.5*CRNI3
-1.5*CR2MONI-1.5*CR2NI2+CR3NI-1.5*MONI3-1.5*MO2NI2+MO3NI; 6000 N Peng !
PARAM L(FCC_L12,MO,NI:CR:VA;0) 298.15 +1.5*CRMONI2+1.5*CRMO2NI-1.5*CRMO3
-1.5*CRNI3; 6000 N Peng !
PARAM L(FCC_L12,MO,NI:CR:VA;1) 298.15 -1.5*CRMONI2+1.5*CRMO2NI-.5*CRMO3
+.5*CRNI3; 6000 N Peng !
PARAM L(FCC_L12,CR,NI:MO:VA;0) 298.15 +1.5*CRMONI2+1.5*CR2MONI-1.5*CR3MO
-1.5*MONI3; 6000 N Peng !
PARAM L(FCC_L12,CR,NI:MO:VA;1) 298.15 -1.5*CRMONI2+1.5*CR2MONI-.5*CR3MO
+.5*MONI3; 6000 N Peng !
PARAM L(FCC_L12,CR,MO:NI:VA;0) 298.15 +1.5*CRMO2NI+1.5*CR2MONI-1.5*CR3NI
-1.5*MO3NI; 6000 N Peng !
PARAM L(FCC_L12,CR,MO:NI:VA;1) 298.15 -1.5*CRMO2NI+1.5*CR2MONI-.5*CR3NI
+.5*MO3NI; 6000 N Peng !

$**
$ Al-Cr-Mo-Ni
FUNCTION ALCRMONI 298.15
U1ALNI+U1ALCR+U1ALMO+U1CRMO+U1CRNI+U1MONI;,,N Peng !

PARAM L(FCC_L12,AL,CR,MO:NI:VA;0) 298.15 AL3NI+CR3NI+MO3NI-1.5*ALCR2NI
-1.5*ALMO2NI-1.5*AL2CRNI-1.5*AL2MONI
-1.5*CRMO2NI-1.5*CR2MONI+6*ALCRMONI; 6000 N Peng !

```
 PARAM L(FCC_L12,AL,CR,NI:MO:VA;0) 298.15 AL3MO+CR3MO+MONI3-
1.5*ALCR2MO
 -1.5*ALMONI2-1.5*AL2CRMO-1.5*AL2MONI
 -1.5*CRMONI2-1.5*CR2MONI+6*ALCRMONI; 6000 N Peng !
 PARAM L(FCC_L12,AL,MO,NI:CR:VA;0) 298.15 AL3CR+CRMO3+CRNI3-1.5*ALCRMO2
 -1.5*ALCRNI2-1.5*AL2CRMO-1.5*AL2CRNI
 -1.5*CRMONI2-1.5*CRMO2NI+6*ALCRMONI; 6000 N Peng !
 PARAM L(FCC_L12,CR,MO,NI:AL:VA;0) 298.15 ALCR3+ALMO3+ALNI3-1.5*ALCRMO2
 -1.5*ALCRNI2-1.5*ALCR2MO-1.5*ALCR2NI
 -1.5*ALMONI2-1.5*ALMO2NI+6*ALCRMONI; 6000 N Peng !




 LIST_OF_REFERENCES
 NUMBER  SOURCE
  86DIN     'A. Dinsdale, T. Chart, MTDS NPL, Unpublished work (1986); CR-NI'
  89DIN     'Alan Dinsdale, SGTE Data for Pure Elements,
        NPL Report DMA(A)195 September 1989'
  91DIN     'Alan Dinsdale, SGTE Data for Pure Elements, NPL Report
        DMA(A)195 Rev. August 1990'
  91LEE     'Byeong-Joo Lee, unpublished revision (1991); C-Cr-Fe-Ni'
  91SAU1    'Nigel Saunders, 1991, based on
          N. Saunders, V.G. Rivlin
          Z. metallkde, 78 (11), 795-801 (1987); Al-Cr'
  91DIN     'Alan Dinsdale, SGTE Data for Pure Elements,
        Calphad Vol 15(1991) p 317-425,
        also in NPL Report DMA(A)195 Rev. August 1990'
  95DUP3     'N. Dupin, Thesis, LTPCM, France, 1995;
        Al-Ni,
        also in I. Ansara, N. Dupin, H.L. Lukas, B. SUndman
        J. Alloys Compds, 247 (1-2), 20-30 (1997)'
  99DUP      'N. Dupin, I. Ansara,
        Z. metallkd., Vol 90 (1999) p 76-85;
        Al-Ni'
  01DUP    ' N. Dupin, I. Ansara, B. Sundman
        Thermodynamic Re-Assessment of the Ternary System Al-Cr-Ni,
        Calphad, 25 (2), 279-298 (2001); Al-Cr-Ni'
   REF184   'AL1<G> CODATA KEY VALUES SGTE **
        ALUMINIUM <GAS>
```

Cp values similar in Codata Key Values and IVTAN Vol. 3'
REF448 'AL2<G> CHATILLON(1992)
Enthalpy of formation for Al1<g> taken from Codata Key Values.
Enthalpy of form. from TPIS dissociation energy mean Value
corrected with new fef from Sunil K.K. and Jordan K.D.
(J.Phys. Chem. 92(1988)2774) ab initio calculations.'
REF4465 'CR1<G> T.C.R.A.S. Class: 1
CHROMIUM <GAS>'
REF4591 'CR2<G> T.C.R.A.S. Class: 6'
REF7504 'NI1<G> T.C.R.A.S Class: 1
Data provided by T.C.R.A.S. October 1996'
REF7553 'NI2<G> T.C.R.A.S Class: 5
Data provided by T.C.R.A.S. October 1996'
FRA 'present work, Introduced by Dr. Franke'
10Cup 'D. Cupid, O. Fabrichnaya, F. Ebrahimi, H.J. Seifert,
Intermetallics 18 (2010) 1186-1196'
REF0 ' '
Peng 'present work,
(1) Al-Mo-Ni, Journal of Alloys and Compounds 674:305–314, 2016
and (2) NiAl-Cr-Mo, J. Phase Equilib. Diffus. 37: 592-600, 2016.'
05Zho 'S.H.Zhou, Mater. Sci. Eng. A, 397(2005)288; Ni-Mo'
90Fri 'Report TRITA-MAC 429, Stockholm, Sweden, 1990'
14Fra 'J. Phase Equilib. Diffus. 35 (2014) 780–787'
88Fri 'Calphad 12 (1988) 247-254.'
!

References

[1] R.D. Noebe, W.S. Walston, Prospects for the development of structural NiAl alloys, in: M.V. Nathal, R. Darolia, C.T. Liu, P.L. Martin, D.B. Miracle, R. Wagner, M. Yamaguchi, (Eds.), Structural Intermetallics 1997, The Minerals, Metals Materials Society, Champion, 1997, pp. 573-584.

[2] D.B. Miracle, Overview No. 104 the physical and mechanical properties of NiAl, Acta Metall. 41 (1993) 649-684.

[3] R.D. Noebe, R.R. Bowman, M.V. Nathal, Physical and mechanical properties of the B2 compound NiAl, Int. Mater. Rev. 38 (1993) 193-232.

[4] E.P. George, C.T. Liu, Brittle fracture and grain boundary chemistry of microalloyed NiAl, J. Mater. Res. 5 (1990) 754-762.

[5] C.A. Barrett, Effect of 0.1 at.% Zirconium on the cyclic oxidation resistance of β-NiAl, Oxid. Met. 30 (1988) 361-390.

[6] F. Ebrahimi, S. Shrivastava, Brittle-to-ductile transition in NiAl single crystal, Acta Mater. 46 (1998) 1493-1502.

[7] J. L. Walter, H. E. Cline, The effect of solidification rate on structure and high-temperature strength of the eutectic NiAl-Cr, Metall. Mater. Trans. 1 (1970) 1221-1229.

[8] P. Ferrandini, W.W. Batista, R. Caram, Influence of growth rate on the microstructure and mechanical behaviour of a NiAl-Mo eutectic alloy, J. Alloys Compd. 381 (2004) 91-98.

[9] H. Bei, E.P. George, Microstructures and mechanical properties of a directionally solidified NiAl-Mo eutectic alloy, Acta Mater. 53 (2005) 69-77.

[10] J.F. Zhang, J. Shen, Z. Shang, Z.R. Feng, L.S. Wang, H.Z. Fu, Microstructure and room temperature fracture toughness of directionally solidified NiAl-Mo eutectic in situ composites, Intermetallics 21 (2012) 18-25.

[11] S. Bogner, L. Hu, S. Hollad, W. Hu, G. Gottstein, A. Bührig-Polaczek, Microstructure of a eutectic NiAl-Mo alloy directionally solidified using an industrial scale and a laboratory scale bridgman furnace, Int. J. Mat. Res. 103 (2012) 17-23.

[12] L. Hu, W. Hu, G. Gottstein, S. Bogner, S. Hollad, A. Bührig-Polaczek, Investigation into microstructure and mechanical properties of NiAl-Mo composites produced by directional solidification, Mater. Sci. Eng. A 539 (2012) 211-222.

[13] X.F. Chen, D.R. Johnson, R.D. Noebe, B.F. Oliver, Deformation and fracture of a directionally solidified NiAl-28Cr-6Mo eutectic alloy, J. Mater. Res. 10 (1995) 1159-1170.

[14] M. Dudová, K. Kuchařová, T. Barták, H. Bei, E.P. George, C. Somsen, A. Dlouhý, Creep in directionally solidified NiAl-Mo eutectics, Scripta Mater. 65 (2011) 699-702.

[15] H.L. Lukas, S.G. Fries, B. Sundman, Computational thermodynamics: The CALPHAD method, Cambridge University Press, Cambridge, 2007.

[16] D. Furrer, S. L. Semiatin, ASM Handbook Volume 22B: Metals process simulation, ASM International, Materials Park, Ohio, 1990.

[17] J. Allison, M. Li, C. Wolverton, X. Su, Virtual aluminum castings: An industrial application of ICME, JOM 58 (2006) 28-35.

[18] U.R. Kattner, The calphad method and its role in material and process development, Tecnol. Metal. Mater. Miner. 13 (2016) 3-15.

[19] H.J. Seifert, F. Aldinger, Applied phase studies, Z. Metallkde. 87 (1996) 841-853.

[20] A. Dinsdale, SGTE data for pure elements, Calphad 15 (1991) 317-425.

[21] Y. Fei, S.K. Saxena, G. Eriksson, Some binary and ternary silicate solution models, Contr. Mineral. Petrol. 94 (1986) 221-229.

[22] O. Redlich, A.T. Kister, Algebraic representation of thermodynamic properties and the classification of solutions, Ind. Eng. Chem. 40 (1948) 345-348.

[23] M. Hillert, M. Jarl, A model for alloying in ferromagnetic metals, Calphad 2 (1978) 227-238.

[24] M. Hillert, The compound energy formalism, J. Alloys Compd. 320 (2001) 161-176.

[25] X. Lu, Y. Cui, Z. Jin, Experimental and thermodynamic investigation of the Ni-Al-Mo system, Metall. Mater. Trans. A 30 (1999) 1785-1795.

[26] S.H. Zhou, Y. Wang, L.Q. Chen, Z.-K. Liu, R.E. Napolitano, Solution-based thermodynamic modeling of the Ni-Al-Mo system using first-principles calculations, Calphad 46 (2014) 124-133.

[27] W. Huang, Y.A. Chang, Thermodynamic properties of the Ni-Al-Cr system, Intermetallics 7 (1999) 863-874.

[28] N. Dupin, I. Ansara, B. Sundman, Thermodynamic re-assessment of the ternary system Al-Cr-Ni, Calphad 25 (2001) 279-298.

[29] N. Dupin, Contribution a l'eveluation thermodynamique des alliages polyconstitutes a base de nickel, Ph. D. Thesis, l'Institut National Polytechnique de Grenoble, France, 1995.

[30] B. Jansson, Ph.D. thesis, Royal Institute of Technology, Stockholm, 1983.

[31] J.-O. Andersson, T. Helander, L. Höglund, P. Shi, B. Sundman, Thermo-Calc & DICTRA, computational tools for materials science, Calphad 26 (2002) 273-312.

[32] B. Sundman, B. Jansson, J.-O. Andersson, The Thermo-Calc databank system, Calphad 9 (1985) 153-190.

[33] W. Zhou, R.P. Apkarian, Y. Wang, D. Joy, Fundamentals of Scanning Electron Microscopy in: Z. Wang, W. Zhou (eds.), Scanning Microscopy for Nanotechnology-Techniques and Applications, Springer, New York, 2006, pp. 1-39.

[34] W.J. Boettinger, U.R. Kattner, K.-W. Moon and J. H. Perepezko, DTA and Heat-flux DSC measurements of alloy melting and freezing, in: J.-C. Zhao (Ed.), Methods for Phase Diagram Determination, Elsevier, 2007, pp. 151-222.

[35] F.D. Bruycker, K. Boboridis, P. Pöml, R. Eloirdi, R.J.M. Konings, D. Manara, The melting behaviour of Plutonium dioxide: A laser-heating study, J. Nucl. Mater. 416 (2011) 166-172.

[36] D. Manara, M. Sheindlin, W. Heinz, C. Ronchi, New techniques for high temperature melting measurements in volatile refractory materials via laser surface heating, Rev. Sci. Instrum. 79 (2008) 113901.

[37] M. Planck, The theory of heat radiation, M. Masius (transl.) (2nd ed.). P. Blakiston's Son & Co. Philadelphia, 1914.

[38] M. Massoud, Engineering thermofluids: thermodynamics, fluid mechanics, and heat transfer, Springer, College Park, 2005.

[39] D. Manara, H.F. Jackson, C. Perinetti-Casoni, K. Boboridis, M.J. Welland, L. Luzzi, P.M. Ossi, W.E. Lee, The ZrC-C eutectic structure and melting behaviour: A high-temperature radiance spectroscopy study, J. Eur. Ceram. Soc. 33 (2013) 1349-1361.

[40] P. Saltykov, L. Cornish, G. Cacciamani, Al-Ni binary phase diagram evaluation, in MSI Eureka, G. Effenberg (Ed.), MSI, Materials Science International Services GmbH, Stuttgart (2004), Document ID: 20.10238.1.2.

[41] M. Turchanin, N. Kolchugina, D. Smagulov, Mo-Ni binary phase diagram evaluation, in MSI Eureka, G. Effenberg (Ed.), MSI, Materials Science International, Stuttgart (2015), Document ID: 20.13805.1.9.

[42] P. Nash, M.F. Singleton, J.L. Murray, Al-Ni (Aluminum-Nickel), in: Phase diagrams of binary Nickel alloys, ASM International, Materials Park, OH, 1991.

[43] H. Okamoto, Al-Ni (Aluminum-Nickel), J. Phase Equilib. Diffus. 25 (2004) 394.

[44] H. Okamoto, Al-Ni (Aluminum-Nickel), J. Phase Equilib. 14 (1993) 257-259.

[45] Y. Ma, A.J. Ardell, The (γ+γ′)/γ′ phase boundary in the Ni-Al phase diagram from 600 to 1200 ºC, Z. Metallkde. 94 (2003) 972-975.

[46] L. Kaufman, Coupled phase diagrams and thermochemical data for transition metal binary systems -V, Calphad 2 (1978) 117-146.

[47] I. Ansara, B. Sundman, P. Willemin, Thermodynamic modeling of ordered phases in the Ni-Al system, Acta Metall. 36 (1988) 977-982.

[48] Y. Du, N. Clavaguera, Thermodynamic assessment of the Al-Ni system, J. Alloys Compd. 237 (1996) 20-32.

[49] I. Ansara, N. Dupin, H.L. Lukas, B. Sundman, Thermodynamic assessment of the Al-Ni system, J. Alloys Compd. 247 (1997) 20-30.

[50] W. Huang, Y.A. Chang, A thermodynamic analysis of the Ni-Al system, Intermetallics 6 (1998) 487-498.

[51] W. Huang, Y.A. Chang, Corrigendum to "A thermodynamic analysis of the Ni-Al system" [Intermetallics, 6 (1998) 487-498], Intermetallics 7(1999) 625-626.

[52] N. Dupin, I. Ansara, On the sublattice formalism applies to the B2 phase, Z. Metallkde. 90 (1999) 76-85.

[53] J.C. Schuster, Al-Mo binary phase diagram evaluation, in MSI Eureka, G. Effenberg (Ed.), MSI, Materials Science International Services GmbH, Stuttgart (2005), Document ID: 20.12123.1.3.

[54] K. Yamaguchi, K. Simizu, The equilibrium diagram of the Al-Mo system, Nippon. Kinzoku Gakkaishi 4 (1940) 390-392.

[55] V.N. Yerembnko, Ya.V. Natanzon, V.I. Dybkov, Interaction of the refractory metals with liquid aluminium, J. Less Comm. Met. 50 (1976) 29-48.

[56] R.R. Malinovskii, Position of the liquidus in the Al-Mo system, Tekhnol. Legk. Splavov 1 (1980) 60-61.

[57] L.E. Mondolfo, The Al-Mo system, Metallography of aluminium alloys, John Wiley & Sons, 1943, pp. 30-31.

[58] V.N. Vigdorovich, V.M. Glazov, N.N. Glagoleva, An investigation of the solubility of Cr, Mo, and W in Al by the microhardness method, Izv. Vyss. Uchebn. Zaved. Tsvet. Met. 2 (1960) 143-146.

[59] J. Adam, J.B. Rich, The crystal structure of WAl_{12}, $MoAl_{12}$ and (Mn, Cr)Al_{12}, Acta Cryst. 7 (1954) 813-816.

[60] L.K. Walford, The structure of the intermetallic phases $MoAl_{12}$, $ReAl_{12}$ and $TcAl_{12}$, Acta Cryst. 17 (1964) 57-59.

[61] F. Sperner, Das Zweistoffsystem Aluminum-Molybdän, Z. Metallkde. 50 (1959) 588-591.

[62] J.W.H. Clare, Compounds present in Aluminum-rich alloys of the Aluminum-Molybdenum system, J. Inst. Met. 89 (1960) 232-234.

[63] M. Pötzschke, K. Schubert, Zum Aufbau einiger zu T_4-B_3 homologer und quasihomologer Systeme, Z. Metallkde. 53 (1962) 548-561.

[64] M. Eumann, G. Sauthoff, M. Palm, Re-evaluation of phase equilibria in the Al-Mo system, Int. J. Mater. Res. 97 (2006) 1502-1511.

[65] J.C. Schuster, H. Ipser, The Al-Al_8Mo_3 section of the binary system Aluminum-Molybdenum, Metall. Mater. Trans. A 22 (1991) 1729-1736.

[66] K. Kamei, T. Ninomiya, S. Terauchi, Aluminume-Molybdenum binary phase diagram, Technol. Rept. Kansai Univ. 13 (1972) 93-106.

[67] G.V. Tenderloo, J.V. Landuyt, S. Amelinckx, The defect structure of Aluminum rich Al-Mo alloys, Mat. Res. Bull. 10 (1975) 941-948.

[68] F. Wöhler, F. Michel, Über krystallisirte Verbindungen von Aluminium mit Metallen, Liebigs Ann. Chem. Pharm. 115 (1860) 102-105.

[69] J.A. Leake, The refinement of the crystal structure of the intermetallic phase Al_4Mo, Acta Cryst. 17 (1964) 918-924.

[70] G. Petzow, J. Rexer, Melting equilibria in the system U-UAl_2-Al_8Mo_3-Mo, Z. Metallkde. 60 (1969) 449-453.

[71] J. Rexer, Die Phasengleichgewichte im System Aluminium-Molybdän oberhalb 1400 °C, Z. Metallkde. 62 (1971) 844-848.

[72] I. Shilo, H.F. Franzen, High temperature thermodynamic study of the Molybdenum-rich regions of the Mo-Al system, J. Electrochem. Soc. 129 (1982) 2613-2617.

[73] R.C. Hansen, A. Aravamudhan, Alloy chemistry of σ related phases III. σ phases with non-transition metals, Z. Metallkde. 61 (1970) 115-120.

[74] J.B. Forsyth, G. Gran, The structure of the intermetallic phase γ(Mo-Al)-Mo_3Al_8, Acta Crystallogr. 15 (1962) 100-104.

[75] N. Saunders, System Al-Mo, in: I. Ansara, A. T. Dinsdale, M. H. Rand (Eds.), Binary Alloy Systems, COST 507: Thermochemical database for light metal alloys Vol. 2, Office for Official Publications of the European Communities, Luxembourg, 1998, pp. 59-64.

[76] N. Saunders, The Al-Mo system (Aluminum-Molybdenum), J. Phase Equilib. 18 (1997) 370-378.

[77] J.L. Ham, A.J. Herzig, First and second annual reports on project NR 031-331, Climax Molybdenum Co. 1950 and 1951, respectively; see also J.L. Ham, Introduction to arc-cast Molybdenum and its alloys, Trans. Am. Soc. Mech. Eng. 73 (1951) 727-732.

[78] G.I. Belyaeva, N.G. Ilyuhchenko, A.I. Anfmogenov, Thermodynamics of solid alloys of the Mo-Al system, Tr. Inst. Elektrokhim, Akad. Nauk SSSR, Ural. Filial 10 (1967) 85-89.

[79] A.S. Dubrovin, O.S. Gorelkin, Yu.Ya. Demidov, N.A. Chirkov, L.S. Kostylev, and O.D. Kolesnikova, Calorimetric study of heats of solution of Si and Al in Aluminothermic alloys, Metalloterm. Protsessy Khim. Metall. Mater. Konf., A.T. Dogvinenko, Ed., Nauk. Sib. Otd. Novosibirsk 121, 1971.

[80] S.V. Meschel, O.J. Kleppa, Standard enthalpies of formation of 4d aluminides by direct synthesis calorimetry, J. Alloys Compd. 191 (1993) 111-116.

[81] V.S. Sudavtsova, G.I. Batalin, V.S. Tutevich, Thermodynamic properties of molten binary alloys in systems Al-(Zr, Nb, Mo), Izvestiya Akademii, Nauk SSSR. Metally 5 (1985) 183-185.

[82] L. Kaufman, H. Nesor, Calculation of superalloy phase diagrams: Part II, Metall. Trans. 5 (1974) 1623-1629.

[83] Z. Du, C. Guo, C. Li, W. Zhang, Thermodynamic description of the Al-Mo and Al-Fe-Mo systems, J. Phase Equilib. Diffus. 30 (2009) 487-501.

[84] D.M. Cupid, O. Fabrichnaya, F. Ebrahimi, H.J. Seifert, Thermodynamic assessment of the Al-Mo system and of the Ti-Al-Mo System from 0 to 20 at.% Ti, Intermetallics 18 (2010) 1185-1196.

[85] L. Brewer, R.H. Lemoreaux, Molybdenum: Physico-chemical properties of its compounds and alloys, At. Energy Rev. Spec. Issue 7 (1980) 195-356.

[86] H. Okamoto, Mo-Ni (molybdenum-nickel), J. Phase Equilib. 12 (1991) 703.

[87] M.F. Singleton, P. Nash, Mo-Ni (Molybdenum-Nickel), Phase diagrams of binary nickel alloys, ed. by P. Nash, ASM Intl., Materials Park, OH, 1991, pp. 207-212.

[88] L. Kaufman, H. Nesor, Coupled phase diagrams and thermochemical data for transition metal binary systems -II, Calphad 2 (1978) 81-108.

[89] K. Frisk, A thermodynamic evaluation of the Mo-Ni system, Calphad 14 (1990) 311-320.

[90] Y. Cui, Z. Jin, X. Lu, Experimental study and thermodynamic assessment of the Ni-Mo-Ta ternary system, Metall. Mat. Trans. A 30 (1999) 2735-2744.

[91] Y. Wang, C. Woodward, S.H. Zhou, Z.-K. Liu, L.-Q. Chen, Structural stability of Ni-Mo compounds from first-principles calculations, Scripta Mater. 52 (2005)17-20.

[92] S.H. Zhou, Y. Wang, C. Jiang, J.Z. Zhu, L.-Q. Chen, Z.-K. Liu, First-principles calculations and thermodynamic modeling of the Ni-Mo system, Mater. Sci. Eng. A 397 (2005) 288-296.

[93] P. Franke, Modeling of thermal vacancies in metals within the framework of the compound energy formalism, J. Phase Equilib. Diffus. 35 (2014) 780-787.

[94] W. Xiong, H. Xu, Y. Du, Thermodynamic investigation of the galvanizing systems, II: Thermodynamic evaluation of the Ni-Zn system, Calphad 35 (2011) 276-283.

[95] R.M. Peçanha, F. Ferreira, G.C. Coelho, C.A. Nunes, B. Sundman, Thermodynamic modeling of the Nb-B system, Intermetallics 15 (2007) 999-1005.

[96] G. Kaptay, A new equation for the temperature dependence of the excess Gibbs energy of solution phases, Calphad 28 (2004) 115–124.

[97] G. Kaptay, On the abilities and limitations of the linear, exponential and combined models to describe the temperature dependence of the excess Gibbs energy of solutions, Calphad 44 (2014) 81-94.

[98] D.V. Malakhov, T. Balakumar, Post-optimization elimination of inverted miscibility gaps, Int. J. Mater. Res. 98 (2007) 786-796.

[99] D.V. Malakhov, T. Balakumar, Re-optimization of the Mg-Sb system under topological constraints, Z. Metallkde. 97 (2006) 517-525.

[100] D.A. Porter, K.E. Easterling, M. Sherif, Phase transformations in metals and alloys, 3rd ed., CRC press, London, 2009.

[101] P. Roentgen, W. Koch, The influence of heavy metals on Al alloys, Z. Metallkde. 25 (1930) 182-185.

[102] B. Grushko, S. Mi, J.G. Highfield, A study of the Al-rich region of the Al-Ni-Mo alloy system, J. Alloys Compd. 334 (2002) 187-191.

[103] S.B. Maslenkov, N.N. Burova, V.A. Rodimkina, Ni-NiAl-Mo phase diagram in the 1200-700 °C temperature range, Izv. Akad. Nauk SSSR, Met. 6 (1988) 183-190.

[104] D.B. Miracle, K.A. Lark, V. Srinivas, H.A. Lipsitt, Nickel-Aluminum-Molybdenum phase equilibria, Metall. Trans. A 15 (1984) 481-486.

[105] R.W. Cutler, The 1200 °C isothermal sections of the Ni-Al-Cr and the Ni-Al-Mo ternary phase diagrams, Master thesis, The Ohio State University, United States, 2011.

[106] P. Nash, S. Fielding, D.R.F. West, Phase equilibria in Nickel rich Ni-Al-Mo and Ni-Al-W alloys, Metal Science 17 (1983) 192-194.

[107] S.B. Maslenkov, A.L. Udovskii, N.N. Burova, V.A. Rodimkina, The Ni-Al-Mo phase diagram in the 1300-2000 °C range, Izv. Akad. Nauk SSSR, Met. 1 (1986) 198-205.

[108] C.C. Jia, K. Ishida, T. Nishizawa, Partition of alloying elements between γ(A1), γ' (L12), and β (B2) phases in Ni-Al base systems, Metall. Mater. Trans. A 25 (1994) 473-485.

[109] S.B. Maslenkov, V.A. Rodimkina, Phase equilibrium of the system Ni-Al-Mo for the Ni-NiAl-Mo composition range, Izv. Akad. Nauk SSSR, Met. 3 (1986) 218-223.

[110] K. Wakashima, K. Hoguchi, T. Suzuki, S. Umekawa, Reinvestigation of phase equilibria in the system Ni-Al-Mo and its implication to the elevated temperature stability of γ/γ'-Mo aligned eutectics, Acta Metall. 11 (1983) 1937-1944.

[111] S. Chakravorty, D.R.F. West, The Ni_3Al-Ni_3Cr-Ni_3Mo section of the Ni-Cr-Al-Mo system, J. Mater. Sci. 19 (1984) 3574-3587.

[112] S.B. Maslenkov, V.A. Rodimkina, Phase transformations in Ni-NiAl-Mo alloys, Izv. Akad. Nauk SSSR, Met. 1 (1989) 194-198.

[113] Y.M. Hong, H. Nakajima, Y. Mishima, T. Suzuki, The γ solvus surface in Ni-Al-X (X= Cr, Mo and W) ternary systems, ISIJ International 29 (1989) 78-84.

[114] Y.M. Hong, Y. Mishima, T. Suzuki, Accurate determination of γ' solvus in Ni-Al-X ternary systems, Mat. Res. Soc. Symp. Proc. 733 (1989) 429-440.

[115] M. Yamamoto, J. Iada, S. Nenno, The microstructure of a two-phase mixture in a $Ni_{75}Mo_{20}Al_5$ alloy, J. Mat. Sci. Lett. 9 (1990) 34-35.

[116] O. Paris, M. Fährmann, E. Fährmann, T.M. Pollock, P. Fratzl, Early stages of precipitate rafting in a single crystal Ni-Al-Mo model alloy investigated by small-angle X-ray scattering and TEM, Acta Mater. 45 (1997) 1085-1097.

[117] M. Fährmann, P. Fratzl, O. Paris, E. Fährmann, W.C. Johnson, Influence of coherency stress on microstructural evolution in model Ni-Al-Mo alloys, Acta Metall. Mater. 43 (1995) 1007-1022.

[118] M. Fährmann, E. Fährmann, T.M. Pollock, W.C. Johnson, Element partitioning during coarsening of (γ-γ′) Ni-Al-Mo alloys, Metall. Mater. Trans. A 28 (1997) 1943-1945.

[119] D.D. Pearson, F.D. Lemkey, Solidification and properties of γ/γ′-α Mo ductile/ductile eutectic superalloy, Proc. Conf. Solidification and Casting of Metals, Metals Soc. London, Sheffield, U.K., 1977, pp. 526-532.

[120] E. R. Stover, Tech. Reprint No. WADC TDR60-184, Sept. 1966.

[121] L.I. Pryakhina, K.P. Myasnikova, V.Ya. Markiv, V.V. Burnasheva, Investigation of the Molybdenum-Nickel-Aluminium ternary system, phase diagrams of metal systems, Nauka, Moscow, 1971, pp. 112-116.

[122] H. Yoshizawa, K. Wakashima, S. Umekawa, T. Suzuki, Elevated temperature stability of the phases in a γ(Ni)/γ′ (Ni_3Al)-α(Mo) aligned eutectic composite, Scr. Metall. 15 (1981) 1091-1096.

[123] E.R. Aigeltinger, S.R. Bates, R.W. Gould, J.J. Hren, F.N. Rhines, Phase equilibria in rapidly solidified Nickel-rich Ni-Mo-Al alloys, Proc. Int. Conf. Rapid Solidification Processing. Principles and Technologies, Reston, Virginia, Claitor's Publishing Div., Baton Rouge, 1977, pp. 291-299.

[124] L.N. Nesterovich, G.V. Kupchenko, N.P. Ivanov, V.T. Budnikov, Structure and properties of some directionally crystallized eutectics based on nickel, Phys. Met. Metallogr. 42 (1976) 117-123.

[125] M.F. Henry, Precipitation of γ′ in γ-α (Ni-Al-Mo) eutectics, Scr. Metall. 10 (1976) 955-957.

[126] H. Sprenger, H. Richter, J.J. Nickel, Unidirectional solidification of Ni-Mo-Al eutectic alloys, J. Mater. Sci. 11 (1976) 2075-2081.

[127] K. Kováčová, Undirectional solidification of Ni-Al-Mo alloy, J. Cryst. Growth 66 (1984) 426-430.

[128] I.L. Svetlov, A.L. Udovski, E.V. Monastyrskaya, I.V. Oldakovskii, M.P. Nazarova, Monovariant line L/(L+γ+α) in the Ni-Mo-Al system and crystallization with a plane front of alloy γ/γ′-α, Izv. Akad. Nauk SSSR, Met. 6 (1987) 183-189.

[129] R.W. Guard, E.A. Smith, Constitution of Nickel-base ternary alloys, J. Inst. Metals 88 (1960) 283-287.

[130] A.V. Virkar, A. Raman, Alloy chemistry of σ (β-U)-related phases II. The characteristics of σ and other σ-related phases in some Mo-NiX systems, Z. Metallkde. 60 (1969) 594-600.

[131] K. Schubert, A. Raman, W. Rossteutscher, Einige Strukturdaten Metallischer Phasen (10), Die Naturwissenschaften 24 (1964) 506-507.

[132] A. Raman, K. Schubert, On the constitution of alloys related to $TiAl_3$, III. Investigations in some T-Ni-Al and T-Cu-Al systems, Z. Metallkde. 56 (1965) 99-104.

[133] V.Y. Markiv, V.V. Burnashova, L.I. Pryakhina, K.P. Myasnikova, Phase equilibria in the Mo-Ni-Al system, Izv. Akad. Nauk SSSR Metally 5 (1969) 180-185.

[134] A.V Khvan, A. Watson, Al-Cr binary phase diagram evaluation, in MSI Eureka, G. Effenberg (Ed.), MSI, Materials Science International Services GmbH, Stuttgart (2013), Document ID: 20.12106.1.1.

[135] J.L. Murray, The Al-Cr (Aluminum-Chromium) system, J. Phase Equilib. 19 (1998) 368-375.

[136] H. Okamoto, Al-Cr (Aluminum-Chromium), J. Phase Equilib. Diffus. 29 (2008) 112-113.

[137] H. Chen, Crystal structure, phase diagram determination and thermodynamic assessment of the Al-Cr-Si, Al-Cr-Ti, Al-Cu-Fe, Al-Cu-Ni and Nb-Ni systems, Ph.D. Thesis, Central South University, China, 2008.

[138] B. Grushko, B. Przepiórzyński, D. Pavlyuchkov, On the constitution of the high-Al region of the Al-Cr alloy system, J. Alloys Compd. 454(2008) 214-220.

[139] N. Saunders, V.G. Rivlin, A Critical review and thermodynamic calculation for the Al rich portion of the Al-Cr-Fe phase diagram, Z. Metallkde. 78 (1987) 795-801.

[140] N. Saunders, V.G. Rivlin, Thermodynamic characterization of Al-Cr, Al-Zr, and Al-Cr-Zr alloy systems, Mater. Sci. Technol. 2 (1986) 521-527.

[141] T. Tokunaga, H. Ohtani, M. Hasebe, Thermodynamic assessment of the Al-Cr system by combining the first principles and CALPHAD methods, Materials Science Forum 539-543 (2007) 2407-2412, 2007,

[142] Y. Liang, C. Guo, C. Li, Z. Du, Thermodynamic modeling of the Al-Cr system, J. Alloys Compd. 460 (2008) 314-319.

[143] B. Hu, W.-W. Zhang, Y. Peng, Y. Du, S. Liu, Y. Zhang, Thermodynamic reassessment of the Al-Cr-Si system with the refined description of the Al-Cr system, Thermochim. Acta 561 (2013) 77-90.

[144] V.T. Witusiewicz, A.A. Bondar, U. Hecht, T. Velikanova, Thermodynamic re-modelling of the ternary Al-Cr-Ti system with refined Al-Cr description, J. Alloys Compd. 644 (2015) 939-958.

[145] COST 507, Thermodynamic database for light metal alloys, Vol. 2, EUR 18499, I. Ansara, A.T. Dinsdale, M.H. Rand, (eds.), European Comission, Luxembourg, 1998.

[146] B. Grushko, E. Kowalska-Strzęciwilk, B. Przepiórzyński, M. Surowiec, Investigation of the Al-Cr γ-range, J. Alloys Compd. 402 (2005) 98–104.

[147] F. Stein, C. He, I. Wossack, The liquidus surface of the Cr-Al-Nb system and re-investigation of the Cr-Nb and Al-Cr phase diagrams, J. Alloys Compd. 598 (2014) 253-265.

[148] P. Nash, The Cr-Ni (Chromium-Nickel) system, Bulletin of Alloy Phase Diagrams 7 (1986) 466-476.

[149] A.L. Udovsky, E.A. Kozodaeva, An optimized calculation of phase diagram and thermodynamic properties of the Ni-Cr system, Calphad 17 (1993) 17-34.

[150] J. Tomiska, K. Kopecky, M.S. Belegratis, C. Myers, Thermodynamic mixing functions and phase equilibria in the Nickel-Chromium system by high-temperature Knudsen cell mass spectrometry, Metall. Mater. Trans. A 26 (1995) 259-265.

[151] T.B. Massalski, H. Okamoto, P.R. Subramanian, L. Kacprzak, Binary alloy phase diagrams (Second edition), ASM International, Materials Park, Ohio, USA, 1990.

[152] P. Saltykov, V. T. Witusiewicz, I. Arpshofen, H. J. Seifert, F. Aldinger, Enthalpy of mixing of liquid Al-Cr and Cr-Ni alloys, J. Mater. Sci. Technol. 18 (2002) 167-170.

[153] T. Chart, NPL, Tedington, UK, unpublished work (quoted in [157]).

[154] P. Gustafson, A thermodynamic evaluation of the Cr-Ni-W system, Calphad 12 (1988) 277-292.

[155] B. Lee, On the stability of Cr carbides, Calphad 16 (1992) 121-149.

[156] P. Turchi, L. Kaufman, Z.-K. Liu, Modeling of Ni-Cr-Mo based alloys: Part I-phase stability, Calphad 30 (2005) 70-87.

[157] K. Frisk, Report TRITA-MAC 429, Stockholm, Sweden, 1990.

[158] T. Velikanova, K. Korniyenko, V. Sidorko, Al-Cr-Ni ternary phase diagram evaluation, in MSI Eureka, G. Effenberg, (Ed.), MSI, Materials Science International Services GmbH, Stuttgart (2004), Document ID: 10.12731.2.8.

[159] D.C. Tu, L.L. Seigle, Kinetics of formation and microstructure of Aluminide coatings on Ni-Cr alloys, Thin Solid Films 95 (1982) 47-56.

[160] E. Rosell-Laclau, M. Durand-Charre, M. Audier, (Al rich) Liquid-solid equilibria in the Aluminium-rich corner of the Al-Cr-Ni system, J. Alloys Compd. 233(1996) 246-263.

[161] X.Z. Li, K. Hiraga, A. Yamamoto, Icosahedral cluster in the structure of an Al-Cr-Ni κ-phase, Philos. Mag. A 76 (1997) 657-666.

[162] A. Sato, A. Yamamoto, X.Z. Li, K. Hiraga, T. Haibach, W. Steurer, A new hexagonal κ phase of Al-Cr-Ni, Acta Cryst. C53 (1997) 1531-1533.

[163] D.N. Compton, L.A. Cornish, M.J. Witcomb, The effect of microstructure on hardness measurements in the Aluminium-rich corner of the Al-Ni-Cr system, J. Alloys Compd. 317-318 (2001) 372-378.

[164] B. Grushko W. Kowalski, D. Pavlyuchkov, B. Przepiórzyński, M. Surowiec, A contribution to the Al-Ni-Cr phase diagram, J. Alloys Compd. 460 (2008) 299-304.

[165] F. Weitzer, W. Xiong, N. Krendelsberger, S. Liu, Y. Du, J.C. Schuster, Reaction scheme and liquidus surface in the Al-rich section of the Al-Cr-Ni system, Metall. Mat. Trans. A 39 (2008) 2363-2369.

[166] B. Grushko, W. Kowalski, D. Pavlyuchkov, S. Mi, M. Surowiec, Al-rich region of the Al-Ni-Cr alloy system below 900 °C, J. Alloys Compd. 485 (2009) 132-138.

[167] I. I. Kornilov, R.S. Mints, Phase diagram of the Cr-Ni-Al system, Izv. Sekt. Fiz.-Khim. Anal., Inst. Obschch. Neorg. Khim., Akad. Nauk. SSSR 22 (1953) 111-116.

[168] A. Taylor, R.W. Floyd, The constitution of nickel-rich alloys of the Nickel-Chromium-Aluminium system, J. Inst. Met. 81 (1952-1953) 451-464.

[169] Yu.A. Bagaryatskiy, The Cr corner of the Cr-Ni-Al system and the Cr-NiAl pseudobinary section, Zh. Neorg. Khim. 3 (1958) 722-728.

[170] Yu.A. Bagaryatskiy, Z.M. Petrova, L.M. Utevskiy, The phase diagram of the Ni-Cr-NiAl system, Problemy Metalloved. i Fizika Metallov 5 (1958) 235-240.

[171] V.V. Volkov, Y. Akshertsev, L.V. Smirnov, T.P. Krinitsina, L.P. Voronina, Features of directional crystallization of eutectic alloys Ni-Ni_3Ti, Fe-Fe_2Ti and NiAl-Cr, Phys. Met. Metallogr. 45 (1978) 146-151.

[172] J.L. Walter, H.E. Cline, Stability of the directionally solidified eutectics NiAl-Cr and NiAl-Mo, Metall. Trans. 4 (1973) 33-38.

[173] H.E. Cline and J.L. Walter, E.F. Koch, L.M. Osika, The Variation of interface dislocation networks with lattice mismatch in eutectic alloys, Acta. Metall. 19 (1971) 405-414.

[174] H.E. Cline and J.L. Walter, The effect of alloy additions on the rod-plate transition in the eutectic NiAl-Cr, Metall. Trans. 1 (1970) 2907-2917.

[175] P.K. Sung, D. R. Poirier, Liquid-solid partition ratios in Nickel-base alloys, Metall. Mater. Trans. A 30 (1999) 2173-2181.

[176] W.H. Tian, C.S. Han, M. Nemoto, Precipitation of α-Cr in B2-ordered NiAl, Intermetallics 7 (1999) 59-67.

[177] P. Saltykov, V.T. Witusiewicz, I. Arpshofen, O. Fabrichnaya, H.J. Seifert, F. Aldinger, Thermodynamics of liquid and undercooled liquid Al-Cr-Ni alloys, Scand. J. Metall. 30 (2001) 297-301.

[178] B. Tang, D.A. Cogswell, G. Xu, S. Milenkovic, Y. Cui, Formation mechanism of eutectic microstructures in NiAl-Cr composites, Phys. Chem. Chem. Phys. 18 (2016) 19773-19786.

[179] J. Peng, P. Franke, D. Manara, T. Watkins, R.J.M. Konings, H.J. Seifert, Experimental investigation and thermodynamic re-assessment of the Al-Mo-Ni system, J. Alloys Compd. 674 (2016) 305-314.

[180] M. Venkatraman, J.P. Neumann, The Cr-Mo (Chromium-Molybdenum) system, Bull. Alloy Phase Diagr. 8 (1987) 216-220.

[181] L. Kaufman, H. Nesor, Couple phase diagram and thermochemical data for the transition metal binary system-I, Calphad 2 (1978) 55-80.

[182] S.S. Balakrishna, A.K. Mallik, Synthesis of azeotropic and two terminal solid solution type binary diagrams, Calphad 3 (1979) 109-118.

[183] A.G. Lesnik, V.V. Nemoshkalenko, A.A. Ovcharenko, Computer calculation of phase diagrams of some binary alloys in the subregular solution approximation, Metallofizika 75 (1979) 20-31.

[184] K. Frisk, P. Gustafson, An Assessment of the Cr-Mo-W system, Calphad 12 (1988) 247-254.

[185] K.Y. Shunyaev, Calculations of phase diagrams in associated solution model, J. Phase Equilib. Diffus. 26 (2005) 613-615.

[186] V. Jindal, B.N. Sarma, S. Lele, A thermodynamic assessment of the Cr-Mo system using CE-CVM, Calphad 43 (2013) 80-85.

[187] E. Rudy, Ternary phase equilibria in transition metal-boron-carbon-silicon systems: part V. compendium of phase diagram data, Techn. Rep. AFML-TR-65-2, Contact No. USAF 33(615)-1249 and 33(615)-67-C-1513, Air Force Materials Laboraty, Wright-Patterson Air Force Base, OH, 1969.

[188] Y.A. Kocherzhinskii and V.I. Vasilenko, Fusibility diagram of Molybdenum-Chromium, Russ. Metall. 4 (1979) 183-185.

[189] O. Kubaschewski, T.G. Chart, Calculation of metallurgical equilibrium diagrams from thermochemical data, J. Inst. Met. 93 (1964-1965) 329-338.

[190] K.P. Gupta, Phase diagrams of ternary Nickel alloys, The Indian Institute of Metals, Calcutta, 1990, 26-48.

[191] H. Lukas, Cr-Mo-Ni ternary phase diagram evaluation, in MSI Eureka, G. Effenberg (Ed.), MSI, Materials Science International Services GmbH, Stuttgart (2010), Document ID: 10.12385.1.7.

[192] R. Mathieu, N. Dupin, J.C. Crivello, K. Yaqoob, A. Breidi, J.-M. Fiorani, N. David, J.-M. Joubert, CALPHAD description of the Mo-Re system focused on the sigma phase modeling, Calphad 43 (2013) 18-31.

[193] D. S. Bloom, N. J. Grant, An investigation of the systems formed by Chromium, Molybdenum, and Nickel, J. Metals 200 (1952) 261-268.

[194] M. Raghavan, R. Mueller, G.A. Vaughn, S. Floreen, Determination of isothermal sections of Nickel rich portion of Ni-Cr-Mo system by analytical electron microscopy, Metall. Trans. A 15 (1984) 783-792.

[195] S. Rideout, W.D. Manly, E.L.Kamen, B.S. Lement, P.A. Beck, Intermediate phases in ternary alloy systems of transition elements, Trans. AIME 191 (1951) 872-876.

[196] I. Class, H. Gräften, E. Scheil, Entwicklung einer ausscheidungsträgen korrosionbeständigen Nickel-Chrom-Molybdän-Legierung, Z. Metallkde. 53 (1962) 283-293.

[197] A.A. Kodentzov, S.F. Dunaev, E.M. Slusarenko, Diffusion paths and phase equilibria in the Mo-Ni-Cr system at 1425 K, J. Less Comm. Met. 141 (1998) 225-234.

[198] C. Morizot, A. Vignes, Study of the Ni-Co-Cr-Mo diagram from the point of view of predicting the appearence of sigma phase in super-refractory alloys, Mem. Sci. Rev. Met. 70 (1973) 857-874.

[199] M. Selleby, Bachelor thesis, Division of physical metallurgy, Royal Insitute of Technology. Stockholm, Sweden.

[200] H.J. Goldschmidt, Metallurgy of rare metals I. Chrimium, Ed. A.H. Shully, Butterworths Publishing Company, London, 1954.

[201] A.P. Smiryagin, A.Ya. Potenkin, R.P. Martinuk, The Ni-Mo-Cr phase diagram, Zhur, Neorg, Khim 3 (1958) 853-859.

[202] E. Siedschlag, Das Dreistoffsystem Chrom-Nickel-Molybdän, Z. Metallkde. 17 (1925) 53-56.

[203] L. Kaufman and H. Nesor, Calculation of superalloy phase diagrams Part I, Metall. Trans. 5 (1974) 1617-1721.

[204] SSOL Database, Thermo-Calc version N, Foundation of computational thermodynamics, Royal Institute of Technology, Stockholm, Sweden, 1998.

[205] A. Raman, K. Schubert, Über die Verbreitung des Zr_2Cu-Type und Cr_2Al-Type, Z. Metallkde. 55 (1964) 798-804.

[206] A.F. Polesya, A.I. Stepina, Formation of supersaturated ternary solid solution from melts cooled at high rates, Fiz. Metal. Metalloved. 27 (1969) 885-889.

[207] P.M. Natishan, E. McCafferty, G.K. Hubler, The corrosion behavior of Mo-Al, Cr-Al and Cr-Mo-Al surface alloys produced by ion beam mixing and ion implantation, Corros. Sci. 32 (1991) 721-731.

[208] A. García-Escorial, B. Sánchez, M.C. Cristina, G. Caruana, M. Torralba, Rapidly solidified Al-3Cr-X (Ni, Mo) ribbons: structure and decomposition behavior, Mater. Sci. Eng., A 134 (1991) 1204-1207.

[209] B. Sánchez, A. García-Escorial, G. Caruana, M.C. Cristina, J. Ibáñez, M. Torralba, Microstructure and mechanical properties of rapidly solidified Al-3Cr-0.3Mo alloys, Welding International 6 (1992) 539-547.

[210] B. Sánchez, A. García-Escorial, M. C. Cristina, G. Caruana , M. Torralba, Microstructure and thermal stability of Al–Cr–X (X=Ni, Mo, Si) powders obtained by centrifugal atomisation, Mats. Sci. Tech. 12 (1996) 794-801.

[211] E. Akiyama, A. Kawashima, K. Asami, K. Hashimoto, The effects of alloying elements on the passivity of sputter-deposited amorphous Al-Cr-Mo alloys in 1M HCl, Corros. Sci. 38 (1996) 1281-1294.

[212] S. Chakravorty S. Sadiq, D.R.F. West, Equilibria involving P- and (σ-phases in Ni-Cr-Al-Mo system, Mater. Sci. Technol. 2 (1986) 110-121.

[213] S. Chakravorty S. Sadiq, D.R.F. West, Intermetallic compound precipitation in Ni-Cr-Al-Mo system, Mats. Sci. Tech. 3(1987) 629-641.

[214] J. Havránková, J. Buršík, A. Kroupa, P. Brož, Experimental study and thermodynamic assessment of the Ni-Al-Cr-Mo system at 1173 K, Scr. Mater. 45 (2001) 121-126.

[215] J.D. Whittenberger, S.V. Raj, I.E. Locci, J.A. Salem, Elevated temperature strength and room-temperature toughness of directionally solidified Ni-33Al-33Cr-1Mo, Metall. Mat. Trans. A 33(2002) 1385-1397.

[216] Z. Zhang, X. Liu, S. Gong, H. Xu, Microstructure and properties of the β NiAl and its eutectic alloy with Cr and Mo addtions, Trans. Nonferrous Met. Soc. China 16 (2006) s2046-s2049.

[217] J. Wang, G. Zhang, S. Li, Investigation of microstructure and corrosive behavior of NiAl-31Cr-3Mo alloy at high temperature, Min. and Metall. Eng. 30 (2010) 93-96.

[218] Z. Shang, J. Shen, L. Wang, Y. Du, Y. Xiong, H. Fu, Investigations on the microstructure and room temperature fracture toughness of directionally solidified NiAl-Cr(Mo) eutectic alloy, Intermetallics 57 (2015) 25-33.

[219] J. Buršík, M. Svoboda, The existence of P phase and Ni_2Cr superstructure in Ni-Al-Cr-Mo system, Scr. Mater. 39 (1998) 1107-1112.

[220] J. Peng, P. Franke, H.J. Seifert, Experimental investigation and CALPHAD assessment of the eutectic trough in the system NiAl-Cr-Mo, J. Phase Equilib. Diffus. 37 (2016) 592-600.

[221] P.G. Gonzales-Ormeño, H.M. Petrilli , C.G. Schön, Ab initio calculation of the bcc Mo-Al (molybdenum-aluminium) phase diagram: Implications for the nature of the ζ-MoAl phase, Scr. Mater. 53(2005) 751-756.

[222] Y. Wang, G. Cacciamani, Thermodynamic modeling of the Al-Cr-Ni system over the entire composition and temperature range, J. Alloys Compd. 688 (2016) 422-435.